ITER-TN-BL-5-0-3

U.S. Technical Report

for the

ITER Blanket/Shield

A. Blanket

July - November 1990

Garching, Federal Republic of Germany

Contributors

Argonne National Laboratory - ANL

Y. Gohar
H. Attaya
M. Billone
C. Lin
C. Johnson
S. Majumdar
D.L. Smith

Oak Ridge National Laboratory - ORNL

P.L. Goranson
B.E. Nelson
D.E. Williamson
C.C. Baker

University of California, Los Angeles - UCLA

A.R. Raffray
A. Badawi
Z. Gorbis
A. Ying
M.A. Abdou

University of Wisconsin, Madison - WI

I.N. Sviatoslavsky
J.P. Blanchard
E.M. Mogahed
M. Sawan
G. Kulcinski

TABLE OF CONTENTS

TABLE OF CONTENTS
(continued)

1.0 INTRODUCTION

Three solid-breeder water-cooled blanket concepts have been developed for ITER based on a multilayer configuration. The primary difference among the concepts is in the fabricated form of breeder and multiplier. All the concepts have beryllium for neutron multiplication and solid-breeder temperature control. The blanket design does not use helium gaps or insulator material to control the solid breeder temperature. Lithium oxide (Li_2O) and lithium zirconate (Li_2ZrO_3) are the primary and the backup breeder materials, respectively. The lithium-6 enrichment is 95%. The use of high lithium-6 enrichment reduces the solid breeder volume required in the blanket and consequently the total tritium inventory in the solid breeder material. Also, it increases the blanket capability to accommodate power variation. The multilayer blanket configuration can accommodate up to a factor of two change in the neutron wall loading without violating the different design guidelines. The accommodation capability depends on the form of the solid breeder material. The blanket material forms are sintered products and packed bed of small pebbles. The first concept has a sintered product material (blocks) for both the beryllium multiplier and the solid breeder (Fig. 1-1). The second concept, the common ITER blanket, uses a packed bed breeder and beryllium blocks. The last concept is similar to the first except for the first and the last beryllium zones. Two small layers of beryllium pebbles are located behind the first wall and the back of the last beryllium zone to reduce the total inventory of the beryllium material and to improve the blanket performance.

The design philosophy adopted for the blanket is to produce the necessary tritium required for the ITER operation and to operate at power reactor conditions as much as possible. Also, the reliability and the safety aspects of the blanket are enhanced by using low-pressure water coolant and the separation of the tritium purge flow from the coolant system by several barriers. The other criteria used to guide the design process are mechanical simplicity, predictability, performance, cost, and minimum R&D requirements.

The inboard blanket has a single breeder zone (Fig. 1-2) embedded in a beryllium zone. Poloidal-flow water coolant of the first wall and the shield behind the blanket were used to cool the inboard blanket by conducting the

nuclear heating to these zones. This results in a simple design. The outboard blanket has two breeder zones with toroidal coolant flow (Fig. 1-3), which improves the performance and the mechanical design of the blanket. An additional coolant panel is used in the beryllium zone between the two breeder plates to get the appropriate temperature profile for the blanket materials.

The net tritium breeding ratio estimated based on three-dimensional analysis is in the range of 0.8 to 0.9 depending on whether two or three breeder zones are used in the outboard blanket. These values do not account for any tritium generated from the test sections. The analysis uses very detailed models for the different reactor components including the divertor zones, the sector side walls, the assembly gaps, the copper stabilizer, and the spatial source distribution.

The blanket box is designed to accommodate the plasma disruption conditions without exceeding the stress limits for the Type 316 austenitic steel (SA). The analyses have been performed for two sets of conditions: one using a saddle coil stabilizer and the other using a twin loop stabilizer. The electromagnetic pressure distributions on the first wall from these two sets of conditions are significantly different. The saddle coil generates approximately linear pressure distribution in the toroidal direction with a net integrated force of approximately zero across any toroidal section. The peak pressure is about 0.5 MPa at the poloidal location where the copper coil begins. The twin loop creates uniform pressure distributions in the toroidal directions with a peak value of about 0.9 MPa at the midplane. The accommodation of the electromagnetic load of the twin loop insures a maximum first-wall deformation of less than 100 μm during normal operation from the helium purge gas and the surface heat flux. This results in a satisfactory thermal blanket performance. If the saddle loop option is used, additional first wall stiffening is required to limit the maximum deformation to less than 100 μm. The third blanket concept is more tolerant to first wall deformation, and it does not require this additional stiffening.

Each breeder layer is purged by He with 0.2% H_2. The protium is added to the purge gas to reduce solubility and adsorption, important at higher temperatures, and to enhance desorption kinetics, important at lower temperatures. The average H/T ratio in the blanket is 28. The He flow rate is chosen to be high enough to keep the total moisture (H_2O + HTO + T_2O)

pressure to <10 Pa throughout the whole blanket. The tritium inventory is calculated to be <14 g in the Li_2O for both physics and technology phase pulsed operation. Based on very limited data and conservative estimations which include the chemical and irradiation-induced trapping of tritium in Be, the end-of-life tritium inventory in the beryllium multiplier is ~1.2 kg. The blanket design does allow for purging of tritium from the beryllium multiplier zones.

The major blanket performance parameters are summarized in Table 1-1 for the Be/Li_2O sintered product design (first concept). The results for the third concept (sintered Li_2O with sintered and pebble Be) are essentially the same as those in the table. The main improvements associated with this third concept are reduced Be mass (~25% decrease) and ability to accommodate blanket and first wall deformations. Most of the parameters also apply to the second concept (Li_2O pebble bed) with the exception of the Li_2O maximum temperature. For the technology phase, T_{max} = 675°C for the single-size pebble bed and 600°C for the binary pebble bed. The Li_2O tritium inventories for the pebble beds are lower than for the sintered product because of the higher T_{max}. However, the single size bed has less power variation accommodation and a smaller TBR. The binary-size bed has a relatively large pressure drop (~0.1 MPa) associated with it.

The third blanket concept is the recommended blanket design for ITER. This concept is not sensitive to the deformation of the first wall or the swelling of the blanket materials. It uses less beryllium and has the potential for a higher tritium breeding ratio relative to the other blanket concepts. Also, it has all the advantages of the first concept. The common ITER design with single size pebbles has less capability for tritium breeding and power variation accommodation. The use of lithium oxide pebbles with two sizes improves the blanket performance but is causes a high pressure drop in the breeder zone.

Table 1-1.
Summary of Blanket Performance Parameters for Sintered-Product Li_2O/Be Concept 1[a] with One Inboard and Two Outboard Breeder Zones

Parameter	Technology Phase
Fusion power, MW	860
Net 3-D TBR	0.81
Tritium generation rate, g/day	106
Minimum/maximum temperature, °C:	
H_2O coolant	60/100
steel	60/472
Be	92/457
Li_2O	450/536
H_2O coolant:	
flow rate, liters/h	1.0
system pressure	1.5
pressure drop, MPa:	
outboard	0.014
inboard	0.56
He - 0.2% H_2 purge:	
average pressure, MPa	0.1
flow rate, moles/s	3.24
maximum moisture pressure, Pa	10
maximum tritium pressure, Pa	20
pumping power, MW	0.016
Tritium inventory, g	
Li_2O	14
Be (end of phase)	1200

a- These performance parameters are essentially the same for the other two breeder concepts except the Li_2O maximum temperature which is higher for the ITER common (pebble-bed) design.

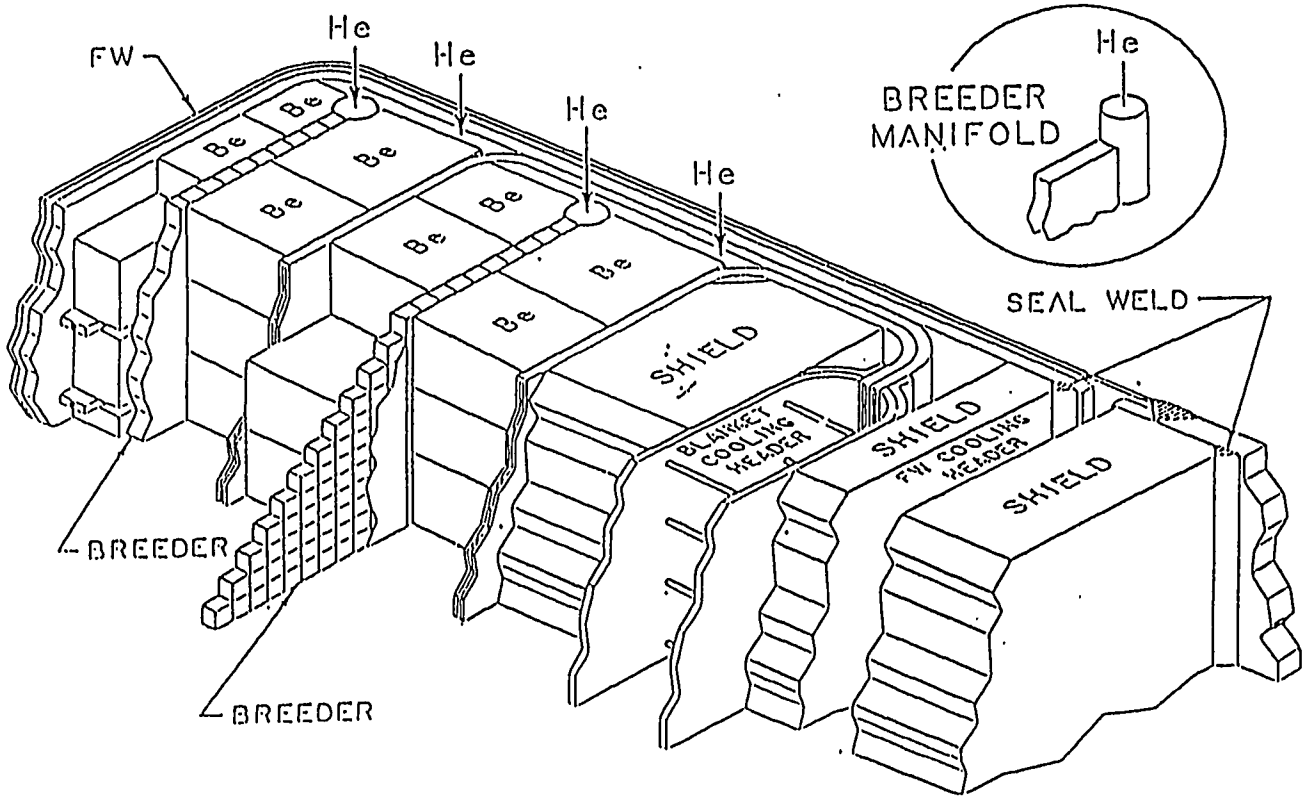

Figure 1-1. Isometric view of the outboard blanket internals.

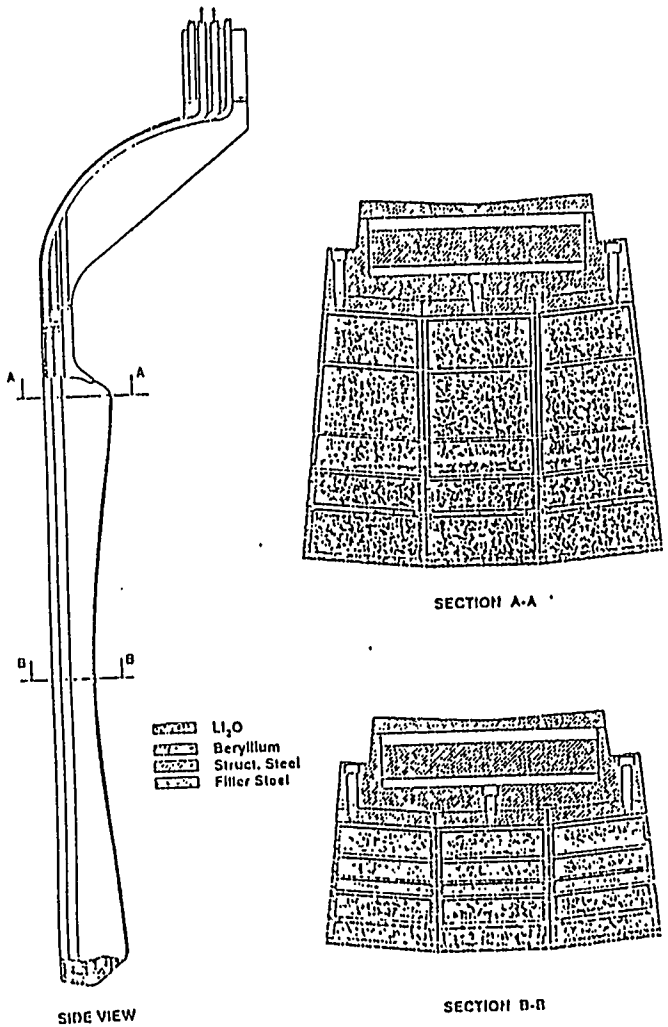

Fig. 1-2. Schematic of the inboard blanket at the core midplane and the top of the blanket.

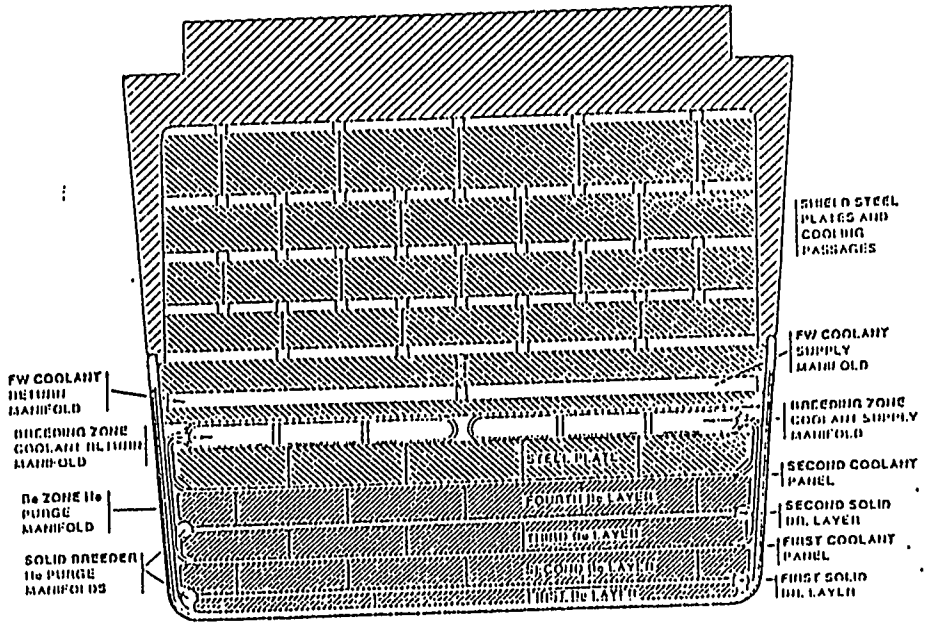

Fig. 1-3. Outboard side module midplane cross section.

2.0 OPERATING CONDITIONS

2.1 Design Parameters

This section provides the design parameters used for the blanket and shield analyses.

- Reactor Power

Physics phase	
Fusion power	1100 MW
Flat burn time	400 s
Minimum total pulse time	600 s
Startup/shutdown time	20 s
Number of DT pulses	5000
Technology phase	
Fusion power	860 MW
Flat burn time	2290 s
Minimum total pulse time	2490 s
Startup/shutdown time	20 s
Number of DT pulses per MWa/m^2	

- Fluence Design Goal
  (51000 DT pulses with 2290 s plus 1.5 Ms of DT burn)

- First Wall Protection
  2 cm carbon tile for the physics phase
  0.05 cm tungsten coating

- Water Coolant Conditions

Coolant temperature	60/100°C
Coolant inlet pressure	<1.5 MPa

- Double Null Divertor Configuration

- Number of Blanket Segments

Outboard	(3 segments per TF coil; 32 side segments, 16 upper central segments, and 16 lower central segments)	64 segments
Inboard	(2 segments per TF coil, each is divided to three subsegments which are electrically insulated)	96 subsegments

- Number of Shield Segments

Outboard	(3 segments per TF coil; 32 side segments, 16 upper central segments, and 16 lower central segments)	64 segments
Inboard	(2 segments per TF coil)	32 segments

- Type 316 SA Steel Structural Material
- Integrated FW/B/S Design
- Twin Loop or Saddle Copper Stabilizer with FW/B/S
- Vertical Coolant Manifolds at the Top Except the Lower Segments Under the Sixteen Ports are Cooled by Vertical Coolant Manifolds from the Bottom

2.2 Neutron Wall Loading Distribution

The neutron wall loading poloidal distribution for ITER has been calculated with the NEWLIT code [1]. The neutron source is given by $n^2\langle\sigma v\rangle$ where n is the plasma density and $\langle\sigma v\rangle$ is the fusion reaction rate which depends on the plasma temperature T. Based on the plasma simulation calculations, the plasma density changes as $(1-(r/a)^2)^{.5}$ and the temperature T is proportional to $(1-(r/a)^2)$. For the temperature range used in ITER $\langle\sigma v\rangle$ changes as T^2. Accordingly the neutron source profile changes as $(1-(r/a)^2)^{\varepsilon}$, where ε equals 3.

A schematic of the ITER first wall, the neutron source at midplane, and the neutron wall loading is shown in Fig. 2-1. The poloidal distribution of the neutron wall loadings in the physics and the technology phases are shown in Fig. 2-2. In Fig. 2-3 and Fig. 2-4, The accumulated power and surface area as a function of the vertical height are shown for the outboard and the inboard first walls.

It has been argued, based on other plasma simulation, that the neutron source profile changes as $(1-(r/a)^2)^{6.35}$. In this case, as seen in Fig. 2-5, the values of the neutron wall loading in and near the midplane increase slightly. This increase is balanced by smaller decrease in the neutron wall loading everywhere else.

Reference

[1] H. Attaya, "NEWLIT - A General Code for Neutron Wall Loading Distribution in Toroidal Reactors," Fusion Tech. 8, 1 (1985) 608.

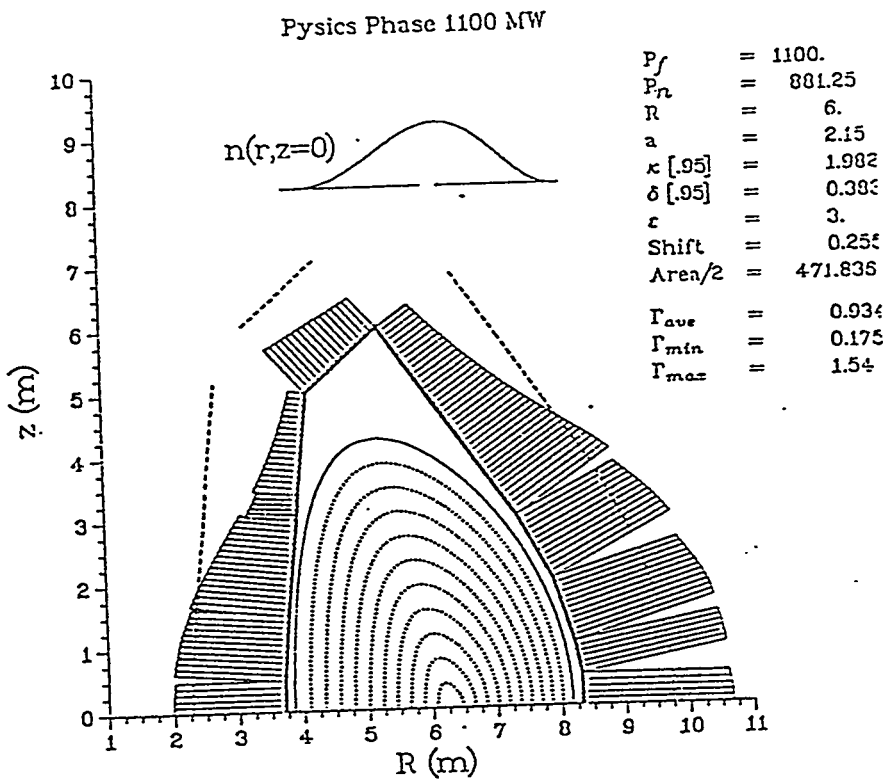

Figure 2-1. ITER neutron wall loading distribution.

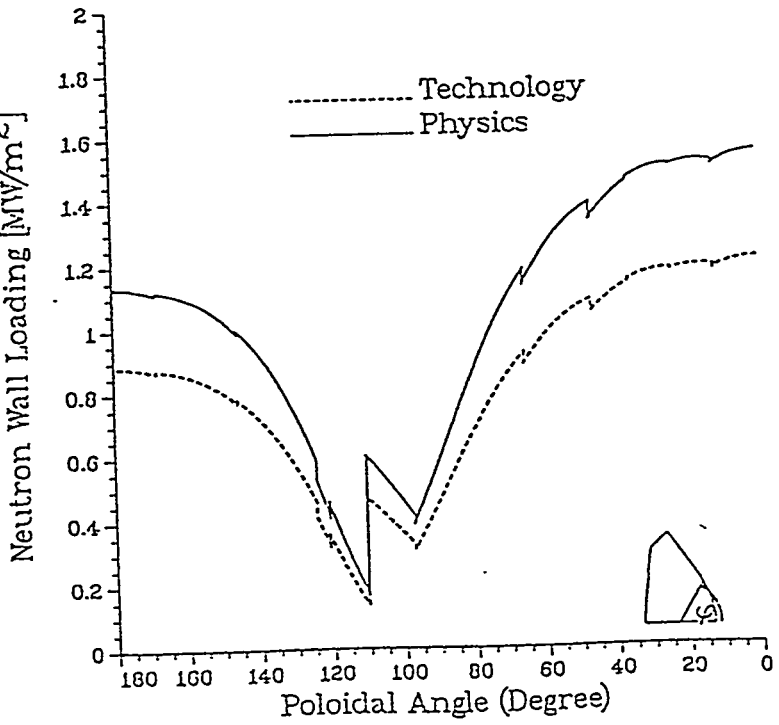

Figure 2-2. ITER neutron wall loading distribution.

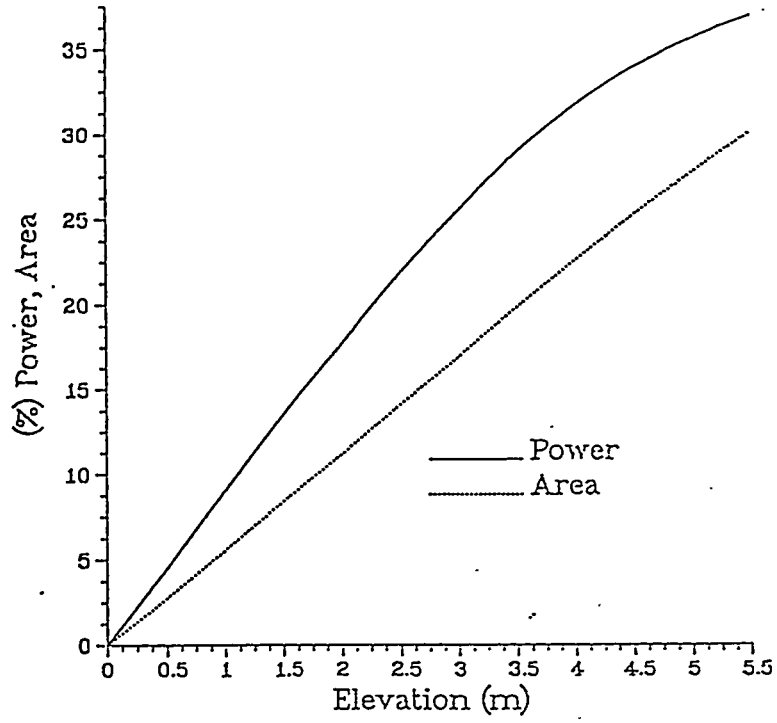

Figure 2-3. ITER outboard neutron power distribution.

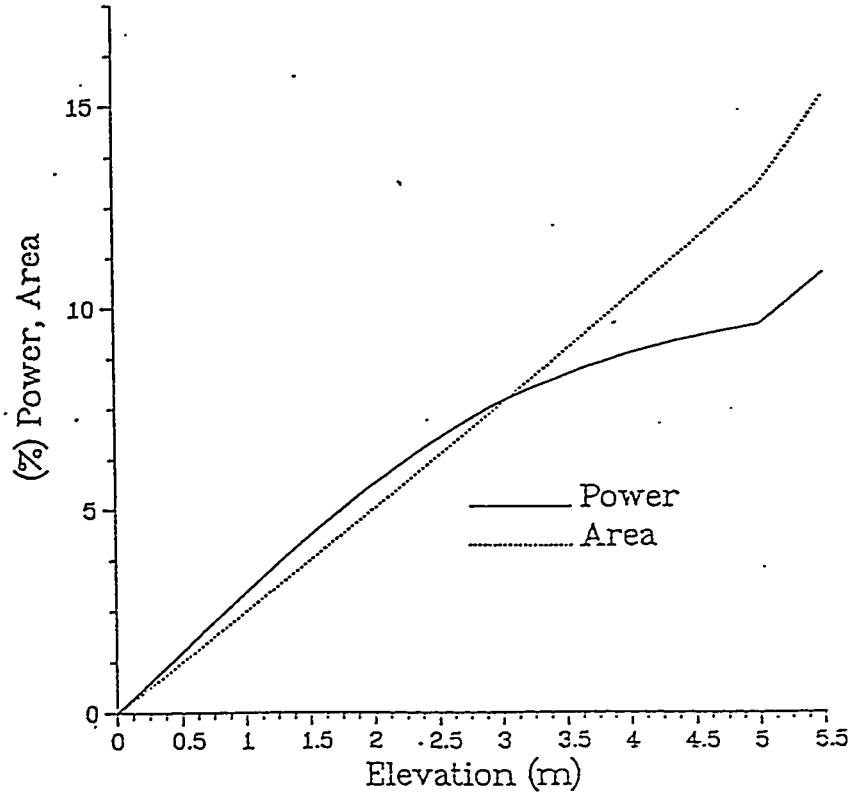

Figure 2-4. ITER inboard neutron power distribution.

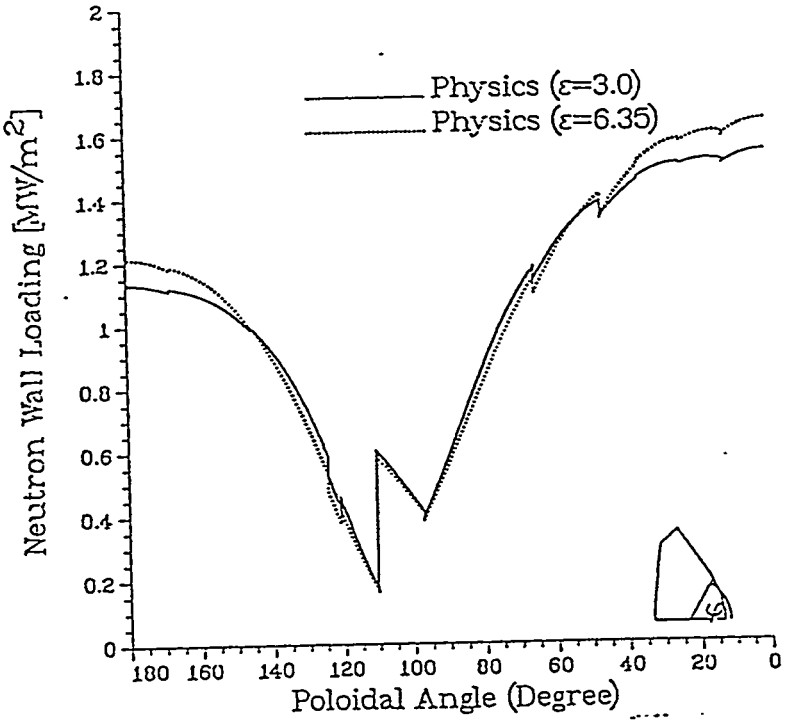

Figure 2-5. ITER neutron wall loading distribution.

3.0 DESIGN GUIDELINES

Design guidelines and limits were established for blanket components to satisfy the ITER mission and insure satisfactory performance. The different limits for structural steel and shield components (with a short clarification note if it is needed) are listed below:

Design Limits

Maximum load structural temperature during normal operation for annealed Type 316 Stainless Steel[1], °C	400
Maximum load structural temperature during off-normal conditions for annealed Type 316 Stainless Steel[2], °C	800
Allowable stress intensity[3], S_m, for annealed Type 316 Stainless Steel at 400°C, MPa	110
Structural temperature for annealed Type 316 Stainless Steel at H_2O interface[4], °C	<150 or >250
Maximum operating temperature for shielding material, °C	
W[5]	2670
B_4C[6]	1900
TiH_2[6]	300
Pb[5]	210
Steel[5]	1050

Radiation Dose Limits

Maximum total operating personnel doses under normal conditions, rem/y-person	1
Maximum dose level during operation and after shutdown in radiation zones for normal personnel operation (no maintenance), mrem/h	0.5

Maximum dose level one day after shutdown for planned personnel access, mrem/h	2.5

Outboard Shield Design Criterion

Complete remote maintenance operation

No consideration for the radiation dose inside the reactor hall after shutdown

Use the available space between the first wall and the outboard TF coils for shielding

Insure no significant increase in the TF coil nuclear heating

Remote maintenance operation with personnel access to the reactor hall

Maximum dose level one day after shutdown with all shields in place, mrem/h	2.5

Tritium

A net tritium breeding ratio close to unity is the design goal

Tritium concentration in the water coolant[7], Ci/ℓ	
Average over time	10
Peak	30
Maximum tritium loss from first wall/blanket/shield, Ci/D	40
Maximum total tritium loss, Ci/D[8]	50
Maximum tritium inventory in the water coolant (to satisfy 1 rem off-site accidental prompt dose assuming 2-10% release), g	1000-200

Toroidal Field Coils Design Limits

Maximum insulator dose[9], rads	
Polyimides	10^{10}
Epoxy-type G10-CR or G11-CR	5×10^{9}

Maximum insulator dose for polyimides, assuming only a static compression load, rads	4×10^{11}
Maximum fast neutron fluence (E > 0.1 MeV) in the Nb_3Sn superconductor,(10) n/cm^2	10^{19}
Maximum total nuclear heating,(11) kW	<65
Maximum nuclear heating in winding pack, MW/cm^3	2
Maximum total copper stabilizer resistance including radiation contribution,(12) $\Omega \cdot cm$	3×10^{-7}

---

(1) Swelling consideration defines this limit.

(2) Structure deformation at this temperature is the limiting factor.

(3) Use 1.5 S_m for primary membrane plus bending stress intensity; and 3 S_m for primary membrane, plus bending, plus secondary stress intensity. Use Von Mises effective stress on the stress intensity for multiaxial stress.

(4) Stress corrosion cracking is the basis for this limit.

(5) The maximum temperature is taken to be 0.8 the melting point.

(6) The dissociation of TiH_2 and B_4C is the basis for the temperature limit.

(7) The maximum off-site dose due to 100% release of vulnerable tritium and the tritium system cost are the basis for these limits.

(8) The off-site dose to the public is the basis for this tritium loss.

(9) A 25% decrease in the mechanical properties is the basis for this limit.

(10) No change in the critical current density and 0.9 the original value of the critical temperature are the basis for this limit.

(11) Heat removal considerations are the basis for this limit.

(12) The conductor design requires this limit.

In the following section, temperature limits are defined for the non-structural components of the blanket: solid-breeder candidates, Be multiplier, and stainless steel cladding separating Be/breeder zones. The temperature limits are based on tritium retention/recovery, materials stability, mass transfer, and compatibility. It should be emphasized that the design guidelines and limits give general target ranges based on materials performance. Within these target ranges, detailed thermal, mechanical, tritium and mass-transfer analyses need to be done to answer design-dependent issues and insure satisfactory performance for a particular design configuration and set of operating parameters.

3.1 Bulk Temperatures

Table 3-1 summarizes the upper and lower temperature limits for the bulk materials (excluding interfaces) during long-time operation. The lower limit (T_{min}) for the solid breeders is based on experimental data corresponding to a tritium residency time of one day. Under the conditions of the experiments, at temperatures lower than T_{min}, the tritium retention was greater than one-day's generation of tritium. Detailed tritium inventory calculations are, however, required even for $T > T_{min}$ because the inventory depends on many other parameters, such as generation rate, purge flow rate and composition, and purge impurity levels. No minimum temperature is specified for the steel and Be. While some tritium is generated in the Be, the limited data which exist suggest that tritium retention is high for temperatures below 600°C.

Table 3-1. Summary of Long-Time, Steady-State Temperature Limits for Non-Structural Blanket Components

Material	T_{min}, °C	Basis	T_{max}, °C	Basis
Solid Breeders				
Li_2O	320	tritium transport	1000	mass transfer/ sintering
Li_2ZrO_3	320	tritium transport	1000	sintering
$LiAlO_2$	450	tritium transport	900	sintering
Li_4SiO_4	390	tritium transport	900	sintering/mass transfer
Be Multiplier	none	---	600	swelling
Steel	none	---	550	integrity
Be/steel	none	---	480	≤0.1 mm wastage
Li_2O/steel	none	---	500	≤0.1 mm wastage
Li_4SiO_4/steel	none	---	600	≤0.1 mm wastage
$LiAlO_2$/steel	none	---	<750	<0.1 mm wastage
Li_2ZrO_3/steel	none	---	<750	<0.1 mm wastage

The maximum breeder temperatures listed in Table 3-1 are chosen based on mass transfer and/or sintering concerns. Both of these phenomena depend on the level of moisture in the breeder and in the gas phase. The numbers in the table assume relatively dry breeder materials (<<0.1 wppm H_2O) and relatively dry gas environments (<100 Pa H_2O). The Be limit is based on He induced-swelling in the Be. Data are available which suggest that for $T \leq 500°C$, Be swelling is moderately low even up to the maximum end-of-life helium content in ITER Be. Other data exist which show significant swelling for $T \geq 700°C$ even at relatively low He levels. Be swelling in the temperature range of $500 < T < 700°C$ depends strongly on the He content. Thus, the 600°C is meant as an intermediate guide. The actual temperature limit is design-dependent and is to be determined by detailed analysis. Finally, the stainless steel cladding limit is set somewhat arbitrarily at 550°C. The thin (~1 mm) cladding layers are not designed as load-bearing members. Rather they are barriers to inhibit Be/breeder interaction. Basically, the cladding has a very small temperature gradient, and its limits are based on surface temperatures and reaction rates.

3.2 Surface Temperatures

While there are no constraints on T_{min} at the material interfaces, Be/steel and breeder/steel interaction rates determine T_{max} at the interfaces. Figure 3-1 shows the long-time extrapolations based on relatively short-time tests for Be/steel, Be/Li_2O, and Be/Li_4SiO_4 wastage. A limit of 0.1 mm is chosen somewhat arbitrarily assuming a total steel cladding thickness of 1 mm. The corresponding temperatures are 480°C for Be, 500°C for Li_2O, and 600°C for Li_4SiO_4. Very little interaction was observed experimentally between $LiAlO_2$/steel and Li_2ZrO_3/steel pairs. Thus, the 750°C limits in Table 3-1 are somewhat arbitrary.

3.3 General Comments on Long-Time, Steady-State Criteria

The correlations used to establish temperature limits based on tritium transport and compatibility are presented in Section 4.2. The correlation for Li_2O/steel is based on a wide range of data for stagnant and flowing gas environments in the temperature range of 500-800°C and times ranging from 100-5600 h. The correlation is considered conservative because the reported data

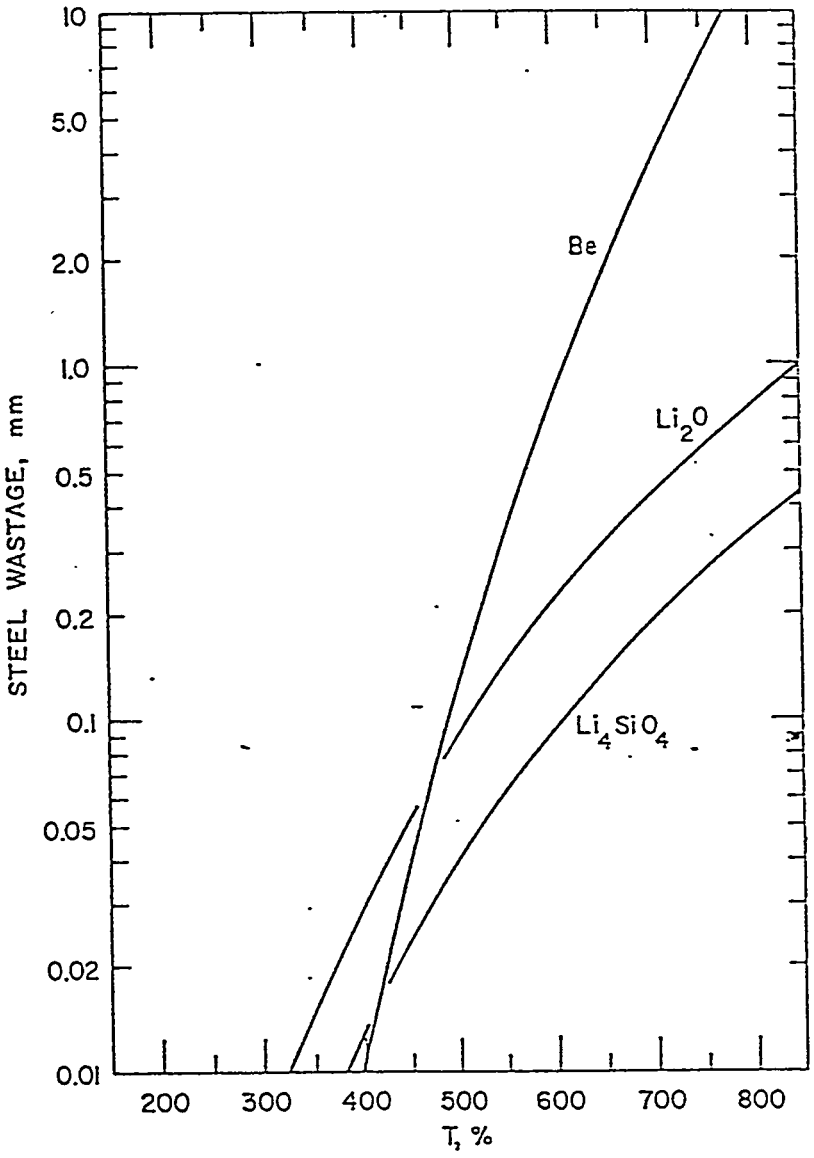

Figure 3-1. Extrapolation of wastage correlations to an ITER lifetime of 3 MW-y/m^2 (3.792 full power years). Correlations are conservative (i.e., upperbound) in that they match the reaction zone thickness (> steel layer consumed); the Be/steel correlation is extrapolated linearly in time; and Li_2O/steel correlation is an upperbound to data from Li_2O with a wide range (≤ 0.5 wt. %) of initial moisture contents.

are for "interaction" or "reaction" zone thickness (which tends to be larger than the steel layer consumed) and because the correlation bounds the measured wastages for a wide range of initial Li_2O moisture levels (<0.1 wt. % to 0.5 wt. %) and moisture content of the gas environment.

The correlation for Be/steel interaction is based on data in the range of 600-900°C and 100-3000 hours. It is conservative (i.e., upper bound) from two viewpoints: the measured interaction layer thickness used is larger than the steel consumed; and a linear extrapolation in time is used from 3000 hours to ~4 years. The reaction products may inhibit further interaction, causing a decrease in the wastage rate with time.

Some of the temperature limits are more restrictive than the ones listed in the ITER design guidelines [1]. This is based on new data and better correlations to old data than were available at the time Ref. [1] was written.

References

[1] ITER Concept Definition, Vol. 2, ITER Documentation Series, No. 3, IAEA, Vienna (1989).

4. MATERIAL SELECTION

4.1 Comparison of Solid Breeders

Table 4-1 shows a comparison of four solid breeders (Li_2O, Li_4SiO_4, Li_2ZrO_3, and $LiAlO_2$) which was used in the early screening of solid breeder candidates. Li_2O was chosen as the reference breeder material because of its excellent thermal and tritium transport properties. Li_2ZrO_3, which has as good tritium properties, good stability, and low thermal and in-reactor swelling, but poor thermal conductivity, was chosen as the backup material. $LiAlO_2$ has good stability, low thermal and in-reactor swelling, good thermal conductivity, but poor tritium release characteristics below 450°C. Thus, it was not considered seriously for ITER application. Finally, Li_4SiO_4, which has very low thermal conductivity and is not superior in any category, was eliminated for ITER application.

The thermal properties of the four breeders are shown in Figs. 4-1 through 4-3 as a function of temperature. The corresponding properties of the other blanket materials (steel and Be) are also shown. Figure 4-4 is a comparison plot of the tritium residency times for the breeders based on correlation fits to experimental data. It is used as a guide in comparing the tritium performance of solid breeders under similar experimental conditions. While the experimental results are used to validate models for tritium analysis, the results cannot be applied directly to ITER conditions because of differences in generation rates and purge flow rates.

Table 4-1.
Thermophysical Properties of ITER Candidate Breeder Materials at 80% Density and 90% Enrichment

Property	Li_2O	Li_4SiO_4	Li_2ZrO_3	$LiAlO_2$
Li-6 density, g/cm^3	0.587	0.346	0.235	0.172
T_{melt}, °C	1432	1255	1695	1750
T_{phase}, °C	none	655	none	none
$(\Delta V/V_o)_{phase}$, %	none	0	none	none
Thermal conductivity at 600°C, W/m-K	3.54	0.82	1.42	2.83
Thermal diffusivity at 600°C, mm^2/s	0.857	0.300	0.357	0.715
Thermal expansion at 600°C, %	1.50	1.41	0.57	0.62
T_{min} (°C) for 1-day tritium residency time	320	390	320	450
In-reactor volume change[a]	high	intermediate	low	low
Incompatibility and Li mass transport[a]	high	intermediate	low	low
Activation and afterheat[a]	low	intermediate	high	intermediate
Mechanical response[a]	intermediate	poor	good	intermediate

a- Relative ranking.

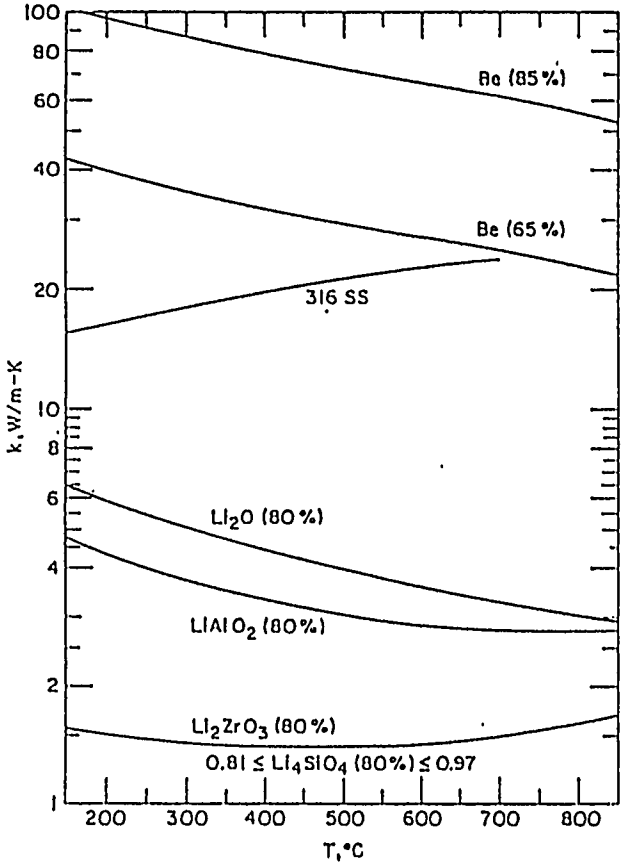

Fig. II-1. Comparison of thermal conductivities of solid breeder ceramics, Be, and 316 SS.

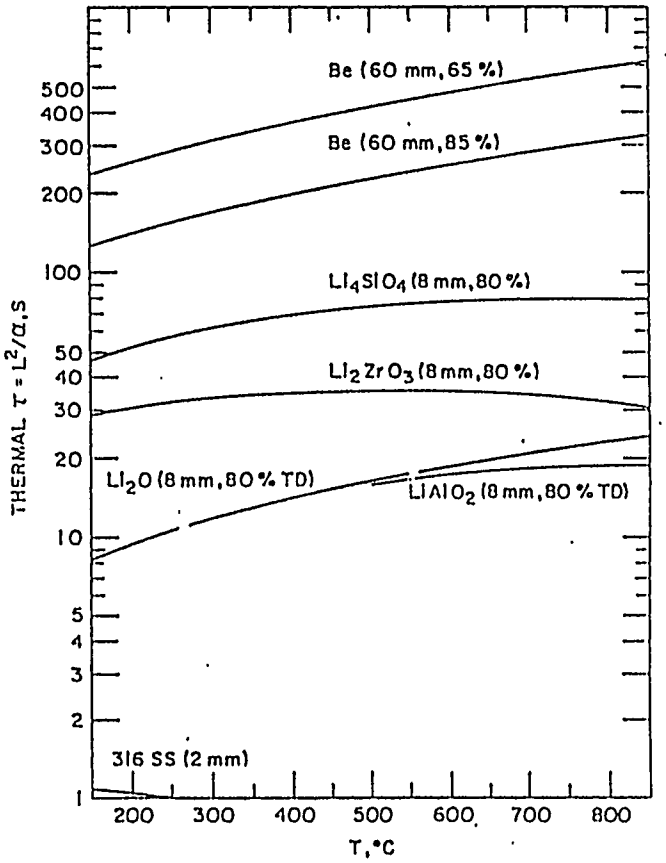

Fig. II-2. Comparison of thermal time constants of solid breeder ceramics, Be, and 316 SS.

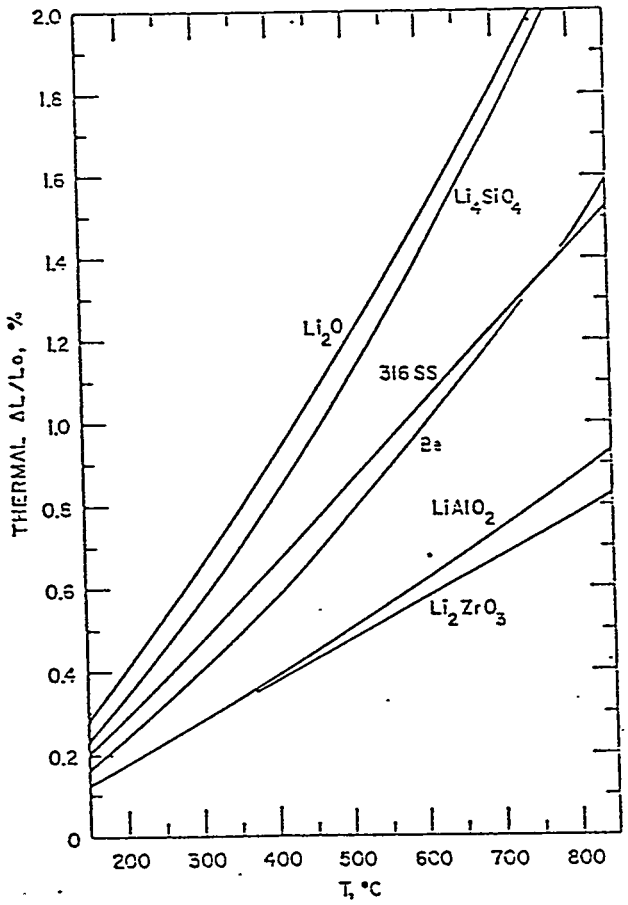

Fig. 4-3. Comparison of the linear thermal expansion strain (referenced to 25°C) for ceramic breeders, Be, and 316 SS.

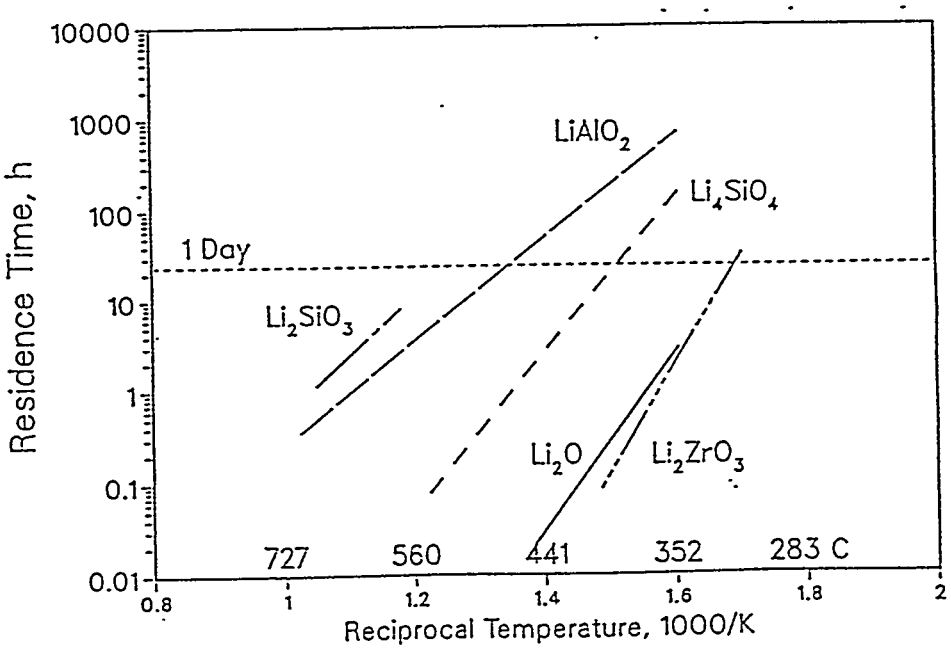

Fig. 4-4. Comparison of tritium residency times for solid breeders based on extrapolations from tritium release experiments.

4.2 Design Data Base

Reference material properties correlations for ITER solid breeder materials, Be, and annealed 316 stainless steel were established at the ITER Specialists' Meetings on Blanket and Structural Materials Data Bases (February 7-9, 1990). These correlations were used to perform the thermal, tritium, structural, and materials analyses for blanket components. Tables I (Li_2O), III (Li_2ZrO_3), and V (Be) are reprinted, along with references, from the Summary Report for the ITER Specialists' Meeting on Blanket Materials Data Base. Table 4-2 (316 SS) was generated basically from correlations presented in ANL/FPP/88-1.

Additional correlations were used in the detailed design analysis. For both solid breeder and Be, heat transfer coefficients were developed to describe the heat transfer at interfaces with stainless steel. Also, as the conductivities listed in the tables are for sintered products, correlations were developed for the effective conductivity of sphere-pac beds and their associated wall heat-transfer coefficients. Finally, correlations were developed for the He-induced swelling and irradiation creep of Be.. These are listed below.

4.2.1 Effective thermal conductivity of packed beds

The Hall and Martin model [1] is used for the effective thermal conductivity of a sphere-pac or pebble bed with one particle size and packing fractions in the range of $0.524 \le P_f \le 0.635$:

$$k_{eff} = \frac{P_f}{0.524}\left\{\frac{(\pi/2)(1-\lambda)}{\delta(1-\lambda)-1} - \frac{(\pi/2)(1+m)}{[\delta(1-\lambda)-1]^2}\ln\left[\frac{\delta(1+\lambda m)+m}{(1+\delta\lambda)(1+m)}\right] + (1-\pi/4)(1+\lambda)\right\} k_g \qquad (4.2\text{-}1)$$

where

$$k_g = \text{He conductivity} = 3.366 \times 10^{-3}\, T^{0.668},\ W/m\text{-}K \qquad (4.2\text{-}1a)$$

T = temperature in K

$\delta = k_g/k_b$ (4.2-1b)

k_b = conductivity of Li_2O (Table I), Li_2ZrO_3 (Table III), or Be (Table V)

$m = 2\ g/D_p = 3.0833 \times 10^{-4}\ T^{1.168}/(P_g D_p)$ 4.2-1c)

P_g = He pressure in MPa

D_p = particle diameter in μm

$\lambda = 4.4919786 \times 10^{-11}\ T^{2.332}\ D_p$ (4.2-1d)

Equation (4.2-1) was developed by Hall and Martin for an idealized cubic packing array of spheres with a packing fraction of 0.524. Larger packing fractions can be achieved, with hexagonal packing giving the theoretical limit of 0.635. The ratio of the sphere diameter (D_p) to the bed thickness is an important parameter in determining what packing fraction can be achieved. The correction factor of ($P_f/0.524$) is imposed on the Hall and Martin model to allow extrapolation in the range of $0.524 \leq P_f \leq 0.635$. Also, based on sensitivity studies and comparisons to data, the model is limited in application to $D_p \leq 1000$ μm (1 mm) because the irradiation term enhances k_{eff} too much for $D_p > 1000$ μm.

To achieve higher packing fractions than 0.635, a binary mixture of large (D_p) and small (d_p) particles may be used. Ideally, 0.87 packing fraction may be achieved. However, a more practical limit is ~0.80-0.85. Based on sensitivity studies with more complicated models than the one proposed by Hall and Martin, the effective thermal conductivity increases by a factor of ~2 in going from a single-particle packed bed of packing fraction ~0.52 to a binary packed bed of packing fraction ~0.82. Thus, for the binary case, $P_f/0.524$ is set to 2 for design analysis calculations.

4.2.2 Wall heat transfer coefficients

At the interface between the stainless steel cladding and either sintered Li_2O, Li_2ZrO_3, or Be, the model used for the heat transfer coefficient is the same as the one developed and validated for fission reactor materials. It consists of a gas conductance term which includes a hot gas gap (G), the rms roughness height (r) and the jump distance (g); a solid-solid conductance term; and a radiation conductance term. The model and modeling parameters are described in detail in Refs. [2] and [3]. It is repeated in the following:

$$h = \frac{k_g}{(r_1 + r_2) + (g_1 + g_2) + G} + \frac{2k_1k_2}{k_1 + k_2} \frac{1}{Ar_{12}^{1/2}} \frac{P_{12}}{H_s}$$

$$+ \{\sigma/[1/\varepsilon_1 + 1/\varepsilon_2 - 1]\} (T_1^2 + T_2^2)(T_1 + T_2) \quad , \qquad (4.2\text{-}2)$$

where

k_g = He conductivity
$= 3.366 \times 10^{-3} T_g^{0.668}$ W/m-K (4.2-2a)

r_1 = root-mean-square (rms) roughness height of the steel (10^{-6} m)

r_2 = rms roughness height of breeder or Be
$= 1 + 110\ P$, 10^{-6} m (4.2-2b)

P = porosity volume fraction of breeder or Be

g_1+g_2 = sum of the temperature jump distances
$= 4.625 \times 10^{-11} T_g^{1.168} (1/a_1 + 1/a_2)/P_g$, m (4.2-2c)

P_g = He pressure in MPa

a_1 = accommodation coefficient for steel (0.12)

a_2 = accommodation coefficient for Li_2O (0.2), Li_2ZrO_3 (0.2), or Be (0.145)

G = hot gap, m

k_1 = steel thermal conductivity (Table 4-2)

k_2 = thermal conductivity of 100% dense Li_2O (Table I), Li_2ZrO_3 (Table III), or Be (Table V)

A = 0.05 $m^{1/2}$

ε_1 = steel thermal emissivity (0.9)

ε_2 = emissivity of Li_2O (0.8), Li_2ZrO_3 (0.8), or Be (0.6)

σ = the Stephan-Boltzmann constant (5.67×10^{-8} $W/m^2 - K^4$)

T_1 = steel surface temperature, K

T_2 = breeder or Be surface temperature, K

T_g = $(T_1 + T_2)/2$ = average gap temperature, K

P_{12} = contact pressure, MPa

r_{12} = $[(r_1^2 + r_2^2)/2]^{1/2}$, m

and

$$H_s = 2.25 \times 10^3 \, (1 - 7.94 \times 10^{-4} \, T_1), \text{ MPa} \qquad (4.2\text{-}2d)$$

Table 4-3 shows typical gap-conductance values from Eq. (4.2-2) for a Be/steel interface as a function of hot gas gap, gas pressure and temperature.

In the case of the sphere-pac or pebble bed, models and data are available [4] for the wall heat-transfer coefficient for both high and low conducting spheres encased in stainless steel. The uncertainty in model parameters and raw data is quite high. In particular, the direct measurement of wall heat transfer coefficient is quite difficult. The approach taken in this design analysis is to use the ratio of h/k_{eff} from the data base. For example, based on Li_4SiO_4 particles of diameter 0.5 mm and packing fraction of 62%, the ratio is 2700 ± 2300 m^{-1}. This would correspond to wall heat transfer coefficient of ~3100 W/m^2-K for an equivalent Li_2O single size bed and ~5700 W/m^2-K for an Li_2O binary bed in the He pressure range of 0.05-0.10 MPa. Design sensitivity studies were performed in the lower range of 1600-3100 W/m^2-K for a Li_2O sphere-pac bed to add additional conservatism to the analysis.

For a Be pebble bed, the heat transfer coefficient should be at least as high as for the Li_2O bed but no higher than for the conductance for sintered Be/steel interface at nominal contact. Thus, the values recommended are between 3100 W/m^2-K and the values listed in Table 4-3.

4.2.3 Be swelling and irradiation creep

While the ITER Specialists on Blanket Materials did not recommend swelling and irradiation creep rates for Be, it is important to the design analysis that such correlations be developed. The major problem with developing a swelling correlation is the uncertainty in the conversion factor for appm (He)/10^{22} n/cm^2 fast (E > 1 MeV) fluence. This conversion factor has been measured for EBR-II-tested samples (1540) and has recently been measured for ATR-tested samples (6000). Using these two data sets, the following swelling correlation was developed for T < 773 K and He contents $G_\alpha < 3 \times 10^4$ appm [5]:

$$\Delta V/V_o = 8.6 \times 10^{-2} \left(G_\alpha/10^3\right)^{1.035} \cdot \left[1 + 22.2 \left(G_\alpha/10^3\right)^{1/2} T^{3/2} \exp(-9322/T)\right], \% \qquad (4.2\text{-}3)$$

The comparison between predicted and measured swelling for EBR-II samples (427-487°C) and ATR post-irradiation anneal samples (200-500°C for one hour) is shown in Fig. 4-5. Not shown in the figure is the large data base for 75°C ATR samples for which the low temperature branch of Eq. 4.2-3 is an excellent fit.

There is only one literature value [6] reported for the irradiation creep constant for Be. Using this constant for irradiation creep (ε_{ic}) gives

$$\varepsilon_{ic} = 3.2 \times 10^{-4} \; D \; \sigma, \; \% \qquad (4.2\text{-}4)$$

where D is damage in dpa and σ is stress in MPa.

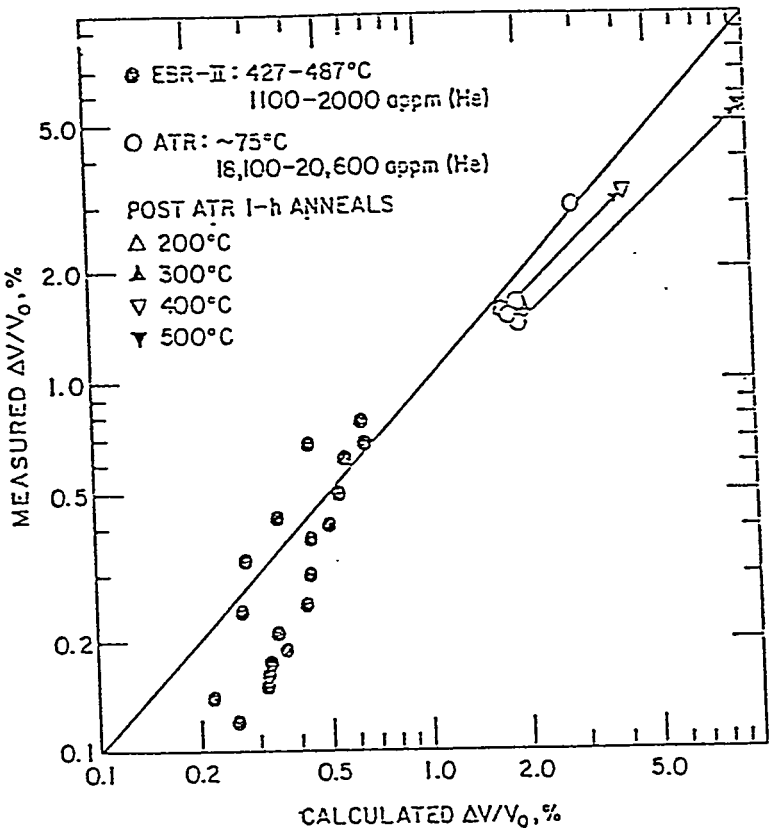

Fig. 4-5. Comparison of proposed swelling correlation to EBR-II and ATR data.

References

[1] R.O.A. Hall and D.G. Martin, "The Thermal Conductivity of Powder Beds," J. Nucl. Mater. 101 (1981) 172-183.

[2] M.C. Billone, "Gap Conductance Modeling and Data," ANL intra-lab memo to Y. Gohar,, November 25, 1987.

[3] M.C. Billone, personal communication with A.R. Raffray, November 10, 1988.

[4] G. Sordan, Uber den Warmetransport in Kugelschuttungen," doctoral dissertation, University of Karlsruhe, July 5, 1988.

[5] M.C. Billone, "Thermomechanical Calculations for the U.S. Layered Blanket Design Concept for ITER," ANL intra-lab memo to S. Majumdar, May 2, 1990.

[6] R.V. Hesketh, "Collapse of Vacancy Cascades to Dislocation Loop," Battelle Northwest Laboratories Report BNL-50083 (1967) p. 389.

Table I. Li_2O

		References
Baseline physical properties		
Molecular weight, g/g-mol	30.0314-2.002 δ, δ = atom fraction ^6Li in Li	[1]
Crystalline structure	Anti-CaF_2 (cubic)	[1]
Density, g/cm^3	2.0338 (1-0.06665 δ)	[2]
Li density, g/cm^3	0.815 δ for ^6Li, 0.950 (1-δ) for ^7Li	[2]
Melting point, °C	1432 ± 6	[1]
Thermal properties		
Vapor pressure, Pa	$\log P_{Li} = -(18.19\times10^3/T) + 12.09$ $\log P_{LiO} = -(19.85\times10^3/T) + 11.21$ $\log P_{Li_2O} = -(20.60\times10^3/T) + 13.40$ $1352 \leq T \leq 1663$ K	[3]
Specific heat, kJ/kg-K	$C_p = 2.5179 + 3.328\times10^{-4} T - 8.382\times10^4/T^2$ $306 \leq T \leq 1073$ K	[2]
Thermal conductivity, W/m-K	$k = (1-P)^{1.96} [39.79 (1+7.067\times10^{-3} T)^{-1}]$ $0.066 \leq P$ (Porosity) ≤ 0.292; $473 \leq T \leq 1173$ K	[4] (Fig. 1-1)
Thermal expansion		
Linear expansion, %	$\Delta L/L_o = 1.87\times10^{-3} (1 + 4.49\times10^{-4} T)(T-298)$	[2]
Instantaneous coef., 1/K	$\alpha = 1.605\times10^{-5} (1 + 1.072\times10^{-3} T)$	(Fig. 1-2a,b)
Mean coefficient, 1/K	$\alpha_m = 1.87\times10^{-5} (1 + 4.49\times10^{-4} T)$ $298 \leq T \leq 1223$ K	

Table I. Li_2O (Cont'd.)

		References
Mechanical Properties		
Young's modulus, GPa	$E = 141 \exp(-3.5P)\,[1-2.3\times10^{-4}\,(T-293)]$ $0.07 \leq P \leq 0.20$, $T = 293$ K	[5]
Poisson's ratio	$\nu = 0.19$ (93% dense pellet), 0.16 (single crystal)	[5,6]
Ultimate compressive strength, MPa	$\sigma_c = 800\ dg^{-0.5} \exp(-10P)\ \ell n(2000/T)$ dg = grain diameter in μm, NO DATA	[5] (Fig. 1-3)
Ultimate bending strength, MPa	$\sigma_b = 195\ dg^{-0.5} \exp(-4.3P)\ \ell n\ (2000/T)$ dg = 10 μm, P = 0.2, T = 293 K	[5] (Fig. 1-4)
Thermal creep rate, 1/s	$\dot{\varepsilon}_c = 8.8\times10^{2}\ (1-P^{2/3})^{-n} \exp(-4.04\times10^{4}/T)\ \sigma^{n}$ $n = 5.9$ for $T < 973$ K $n = 5.9\ [1-1.1\times10^{-3}\ (T - 293)]$, $973 \leq T \leq 1123$K $n = 4.9$ for $T > 1123$ K $0.07 \leq P \leq 0.21$, $973 \leq T \leq 1223$ K, $4 \leq \sigma \leq 45$ MPa	[5]
Interaction with Hydrogen (solubility), (H) ppm (Li_2O)	$S_H = 173 \exp(-2950/T)\ P_{H_2}^{0.5}$ $30 \leq P_{H_2} \leq 6.7\times10^{4}$ Pa, $476 \leq T \leq 963$ K Factor of 4 uncertainty	[7] (Fig. 1-6)

Table I. Li_2O (Cont'd.)

		References
Interaction with (cont'd.)		
Water		
Liquid	$Li_2O + H_2O \rightarrow 2LiOH + 125$ kJ/mole LiOH	[1]
Vapor (solubility), (OH) ppm (Li_2O)	$S_{OH} = 10^{-A} (9.864 \times 10^{-6} P_{H_2O})^B$	[8]
	$A = 23.667 - 2.502 \times 10^{-2} T + 9.62 \times 10^{-6} T^2$	(Fig. 1-6)
	$B = 0.427 + 1.7 \times 10^{-4} T$	
	$2 \leq P_{H_2O} \leq 2000$ Pa, $713 \leq T \leq 1123$ K	
316 stainless steel (wastage), μm	$d = 1.06 \times 10^3 \exp(-5920/T)\ t^{0.5}$	[9,10,11]
	$773 \leq T \leq 1073$ K, $100 \leq t \leq 5600$ h	
Be	NO DATA	
Irradiation effects		
Physical integrity	Fair for 500, 700, 900°C (< 3 at.% ^6Li burnup)	[12,13,14]
	Fair for 550-1000°C (4 at.% ^6Li burnup)	(Fig. 1-9), [15]
Swelling		[13]

	$\Delta V/V_o$, %		
Bu, at.%	500°C	700°C	900°C
1	-1.0	5.0	6.0
2	-3.5	7.5	6.0
3	-2.8	7.0	6.0

(Fig. 1-10)

Grain growth	at 1 at.% ^6Li burnup	[16]
	and 500°C: 3.5 → 3.5 μm	(Fig. 1-11)
	700°C: 3.5 → 7.0 μm	
	900°C: 3.5 → 17.0 μm	

Table I. Li_2O (Cont'd.)

					References
Helium retention		Retained/Generated, %			[14]
	Bu, at.%	500°C	700°C	900°C	(Fig. 1-13)
	1	25	25	10	
	2	14	22	5	
	3	13	23	7	
Li transport, g/h	$W = (29.9/2)\, F/\overline{K \cdot P_{H_2O}}/P_{total}$				[17]
	F = He sweep gas flow rate (mol/h)				(Figs. 1-7/1-8)
	$K = (P_{LiOH})^2/P_{H_2O}$, equilibrium constant for $Li_2O(s) + H_2O(g) \rightarrow 2LiOH(g)$				
	P_{H_2O} = water vapor pressure in atm.				
	P_{total} = total sweep gas pressure, atm.				
Thermal conductivity	Slight decrease at low temperature due to fast neutron irradiation				[18] (Fig. 1-12)
Young's modulus	NO DATA				
Compressive strength	NO DATA				
Bending strength	NO DATA				
Tritium diffusivity, cm^2/s	$D = 6.81 \times 10^{-3} \exp[-84.8\ (kJ/mol)/RT]$				[19]
	$550 \leq T \leq 1000$ K				(Figs. 1-14/1-15)
	Single crystal diffusivity decreases with irradiation				
Tritium residency time, h	$\tau = \exp(2.273 \times 10^4/T - 34.83)$				[20] (Fig. 1-16)
	dg ~ 16 μm, P ~ 20%, $593 \leq T \leq 773$				
	He + 0.1% H_2 purge				

References for Table I

1. D.J. Suiter, "Lithium Based Oxide Ceramics for Tritium Breeding Applications," McDonnell Douglas, MDC E2677 (1983).
2. Materials Handbook for Fusion Energy Systems, Hanford Engineering and Development Laboratory, DOE/TIC-10122 (1980-).
3. H. Kudo, C.H. Wu, and H.R. Ihle, J. Nucl. Mater. 78 (1978) 380.
4. T. Takahachi and T. Kikuchi, "Porosity Dependence on Thermal Diffusivity and Thermal Conductivity of Li_2O from 200 to 900°C," J. Nucl. Mater. 91 (1980) 93.
5. M.C. Billone and W.T. Grayhack, "Summary of Mechanical Properties Data and Correlations for Li_2O, Li_4SiO_4, $LiAlO_2$, and Be," Argonne National Laboratory, ANL/FPP/TM-218 (1988).
6. S. Hull et al, J. Nucl. Mater. 160 (1988) 125.
7. S. O'Hira, T. Hayashi, K. Okuno, and H. Kudo, "Tritium Dissolution in and Release from Li_2O," Fusion Eng. and Design 8 (1989) 335.
8. M. Tetenbaum, A.K. Fischer, and C.E. Johnson, "An Investigation of the Solubility of LiOH in Solid Li_2O," Fusion Techn. 7 (1985) 53.
9. D.L. Porter, J.R. Krsul, M.T. Lang, L.C. Walters, and M. Tetenbaum, "Neutron Irradiation and Compatibility Testing of Li_2O," J. Nucl. Mater. 122-123 (1984) 929.
10. P. Hofmann and W. Dienst, "Chemical Compatibility Between Lithium-Based Oxide Ceramics and Stainless Steels," J. Nucl. Mater. 141-143 (1986) 289.
11. O.K. Chopra and D.L. Smith, Oak Ridge National Laboratory Report, DOE/ER-0045/8 (1982) 507-513.
12. G.W. Hollenberg, J. Nucl. Mater. 123 (1984) 986.
13. G.W. Hollenberg and D.L. Baldwin, J. Nucl. Mater. 133-134 (1985) 242.
14. D.L. Baldwin and G.W. Hollenberg, J. Nucl. Mater. 141-143 (1986) 305.
15. O.D. Slagle and G.W. Hollenberg, Proc. 2nd Int. Specialist's Workshop on Modeling Tritium Behavior in Fusion Ceramic Blankets (1989) pp. 181-199.
16. G.W. Hollenberg, "Irradiation Effects on Li_2O, $LiAlO_2$, Li_4SiO_4, and Li_2ZrO_3," in Sixth Annual Progress Report on Special Purpose Materials for Magnetically Confined Fusion Reactors, DOE/ER-0113/3, May 1984, pp. 12-16.
17. T. Kobayashi et al., JAERI-M 87-219 (1988).
18. J.L. Ethridge, D.E. Baker, A.D. Miller, J. Am. Ceram. Soc. 71(6) (1988) C-294.
19. T. Tanifugi et al., to be published.
20. M. Briec, J.J. Abassin, C.E. Johnson, M. Masson, N. Roux, and H. Watanabe, "The MOZART Experiment: In-Pile Tritium Extraction from Lithium Oxide, Aluminate, Zirconates," Proc. 15th SOFT Conf. (1988).

Table III. Li_2ZrO_3

		References
Baseline physical properties		
Molecular weight, g/g-mol	153.25 (1 - 1.31×10^{-2} δ), δ = ^{6}Li fraction in Li	[6]
Crystalline structure	Monoclinic	[6]
Density, g/cm^3	ρ = 4.1573 (1 - 1.31×10^{-2} δ)	[6]
Li density, g/cm^3	0.3264 δ for ^{6}Li, 0.3807 (1 - δ) for ^{7}Li	[6]
Melting point, °C	1695 ± 15	[2,3]
Thermal properties		
Vapor pressure, Pa	Log P_{Li} = - 18.39 $10^3/T$ + 10.59 1032 ≤ T ≤ 1642 K	[6]a
Specific heat, kJ/kg-K	Cp = 1.022 - 3.696×10^{-5} T - 2.791×10^{4} T^{-2} 350 ≤ T ≤ 1012 K	[4]
Thermal conductivity, W/m-K	K = $(1 - P)^{5/3}$ [3.643 $(1 + 1.549\times10^{-3}$ T$)^{-1}$ + 7.579×10^{-10} T^3] 0.187 ≤ P (porosity) ≤ 0.211 373 ≤ T ≤ 1063 K	[5] (Fig. 3-1)
Thermal expansion		
Linear expansion, %	$\Delta L/Lo = 9.89\times10^{-4}$ $(1 + 1.13\times10^{-5}$ T)(T - 298)	[6]b
Instantaneous coef., 1/K	$\alpha = 9.86\times10^{-6}$ $(1 + 2.27\times10^{-5}$ T)	
Mean coefficient, 1/K	$\alpha_m = 9.89\times10^{-6}$ $(1 + 1.13\times10^{-5}$ T)	

Table III. i_2ZrO_3 (Cont'd.)

		References
Mechanical properties		
Young's modulus, GPa	$E = 203.35\ (1 - P)(1 - 1.286\ P)^2 \cdot [1 - 2.40 \times 10^{-4}\ (T - 293)]$ $T = 293$ K	[1]g
Poisson's ratio	$\nu = 0.2$	[1]h
Ultimate compressive strength, MPa	$\sigma_c = 396$ (dg = 0.8 μm, 80% TD) $\sigma_c = 230 \pm 31$ (dg = 2 μm, 80% TD)	[1]g [4]
Ultimate bending strength, MPa	$\sigma_b = 65 \pm 15$ (25°C), 60 ± 20 (400°C), 63 ± 1 (600°C), (dg = 2 μm, 80% TD)	[4]
Thermal creep rate, s^{-1}	2×10^{-6} (26 MPa), 8×10^{-6} (75 MPa), 4×10^{-5} (144 MPa) at 900°C	[1]i
Interaction with		
Hydrogen: solubility	NO DATA	
adsorption	NO DATA	
Water		
Liquid	Hydrolyses at 25°C and 100°C	[4,9]
Vapor: solubility	NO DATA	
adsorption	NO DATA	
Steels	No significant interaction in conditions explored: up to 700°C in vacuum	[12]
Beryllium	No significant interaction up to 650°C in vacuum, slight oxidation of beryllium in wet helium	[12]

Table III. Li_2ZrO_3 (Cont'd.)

		References
Irradiation effects		
Physical integrity	Very good	[4,10]
Swelling	Less than 0.7%	[13] (Fig. 3-2)
Grain growth	No	[14]
Li transport	No	[18]
Thermal conductivity	No significant change	[18]
Thermal expansion	No significant change	[18]
Young's modulus	~30% increase	[18]
Compressive strength	Significant decrease, not in agreement with bending strength behavior	[18]
Bending strength	Scattered values available	[15]
Helium retained	Very low	(Fig. 3-3)
Tritium diffusivity	No single crystal data	(Fig. 3-4)
Tritium residency time, h	$\tau = 1.089 \times 10^{-19} \exp(230.5\ kJ \cdot mol^{-1}/RT)$ $T \geq 583K$, $0.5 \leq dg \leq 1\ \mu m$, $20 \leq P \leq 25\%$ He + 0.1% H_2 purge	(Table 3-1)

References for Table III

1. M. Kuchle, "Material Data Base for the NET Test Blanket Studies," April 1989.
1a. W. Dienst, "Properties and Comparison of Ceramic Oxide Breeder Materials for Fusion Reactors," Internal KfK Report 03 06 02 PO 1B (1987).
1b. Y. Ikeda, H. Ito, G. Matsumoto, and H. Hayashi, J. Nucl. Mater. 97 (1981) 47-58.
1c. A.U. Christensen, K.C. Conway, and K.K. Kelby, U.S. Bureau of Mines RI 5565 (1969) 1-7.
1d. B. Rasneur, "Tritium Breeding Material: $LiAlO_2$," 6th Topical Meeting on the Technology of Fusion Energy, San Francisco, 1985.
1e. H. Zimmermann and M. Blumhofer, "Mechanical Properties of $LiAlO_2$ Pellets of CEA Production," KfK/IMF 124 (1986).
1f. M.C. Billone and W.T. Grayhack, "Summary of Mechanical Properties Data and Correlations for Li_2O, Li_4SiO_4, $LiAlO_2$, and Be," Argonne National Laboratory Report, ANL/FPP/TM 218 (1988).
1g. B. Rasneur, "Determination of Chemical Characteristics of $LiAlO_2$ and Li_2ZrO_3 for a Fusion Reactor Blanket," 15th SOFT, Fusion Technology (1988).
1h. P. Kennedy, "The Preparation, Characterization and Properties of Lithium Oxide and Metazirconate Specimens Irradiated in HFR Petten in the Second and Third EXOTIC Experiments," 14th SOFT, Fusion Technology (1986) 1013.
1i. W. Dienst, "Contribution of the Data Base for the International Fusion Materials Handbook: Mechanical Properties and Compatibility of Ceramic Breeding Materials," IMF-Notiz 129 (1989).
2. "Semi-Annual Report of KfK/Euratom April-September 1989," KfK Report 4677, November 1989.
3. G.P. Wyers and E.H.P. Gordfunke, "Phase Relations in the System Li_2OZrO_2," J. Nucl. Mater. 168 (1988) 24.
4. D.A. Moore, "A Compilation of Data and a Review of the Properties of Lithium Monoxide and Lithium Zirconates Relevant to Their Use as Tritium Breeder Material in Fusion Reactors," NRL-R-2014 (S) to be published.
4a. G.W. Hollenberg and D.E. Baker, DOE/ER/013/3.
5. W. Dienst and H. Zimmerman, "Investigation of the Mechanical Properties of Ceramic Breeder Materials," J. Nucl. Mater. 155-157 (1988) 476.
6. D.J. Suiter, "Lithium Based Oxide Ceramics for Tritium Breeding Applications," MDC Report E2677 UC-20, June 1983.
6a. A. Neubert and D. Guggi, J. Chem. Thermo. 10 (1978) 297-306.
6b. G.W. Hollenberg, "Thermal Properties of Lithium Ceramics for Fusion Application," 84th Meeting of the Am. Ceram. Soc., Cincinnati, 1982.
7. A.M. Lejus, "Revue des Hautes Températures et Réfractaires Li," (1964), p. 72.
8. B. Rasneur and J. Charpin, "Chemical Properties of Lithium Ceramics: Reactivity with Water and Water Vapour," J. Nucl. Mater. 461 (1988) 155-157.
9. B. Rasneur, "Fabrication, Mechanical and Chemical Properties of $LiAlO_2$ and Li_2ZrO_3 as Tritium Breeders for a Solid Blanket," presented at the 91st Annual Meeting of the American Ceramic Society, Indianapolis, April 1989.
10. M. Broc, T. Flament, P. Fauvet, and J. Sannier, "Compatibility of 316L Stainless Steel with Liquid and Solid Tritium Breeding Materials," J. Nucl. Mater. 611 (1986) 141-143.
11. A. Terlain, D. Herpin, P. Perodeaud, T. Flament, and J. Sannier, "Compatibility Problems with Beryllium in Ceramic Blankets," 15th SOFT, Fusion Technology (1988) 1179.
12. M. Broc, T. Flament, A. Terlain, and J. Sannier, "Compatibility Problems in Tritium Breeding Blankets," ICFRM 4, to be published.

13. G.W. Hollenberg, "Pellet Integrity and Swelling of Lithium Ceramics," Report HEDL 7643, January 1987.
14. G.W. Hollenberg, D.L. Baldwin, R. Wisner, and B. Carlson, "Lithium Transport Within Closed Irradiation Capsules Containing Lithium Ceramics," Report HEDL 7644, January 1987.
15. G.W. Hollenberg and D.L. Baldwin, "Tritium and Helium Retained in Fast Neutron Irradiated Lithium Ceramics as Measured by High Temperature Vacuum Extraction," Report HEDL 7645, January 1987.
16. J.L. Ethridge and D.E. Baker, "Effects of Fast Neutron Irradiation on the Thermal Conductivity of Li_2O and $LiAlO_2$," Advances in Ceramics 25 (19) 165.
17. F. Botter, B. Rasneur, and E. Roth, "Irradiation Behaviour of a Tritium Breeding Material $LiAlO_2$. Results of Two In-pile Experiments Alice I and Alice II," J. Nucl. Mater. 160 (1988) 48-57.
18. S.D. Preston, AEA Technology, Springfields, private communication.
19. R.G. Clemmer, "The TRIO Experiment," ANL 8455 (1984).
20. T. Kurasawa, J. Nucl. Mater. 141-143 (1986) 265.
21. M. Briec, J. Nucl. Mater. 155-157 (1988) 549.
22. T. Kurasawa, J. Nucl. Mater. 155-157 (1988) 544.
23. M. Briec, 15th SOFT, Fusion Technology (1988).
24. S. Casadio and M. Briec, to be published.
25. H. Kwast, 15th SOFT, Fusion Technology (1988).
26. H. Werle and M. Briec, to be published.

Table V. Beryllium

		References
Baseline Physical Properties		
Molecular weight, g/g-mol	9.01	[1]
Crystalline structure	HCP	[1]
Density, g/cm^3	1.85	[1]
Melting point, °C	1283	[1]
Heat of melting, kJ/kg	1303	[1]
Thermal Properties		
Vapor presure, Pa	$\text{Log}(P_{Be}) = 11.192 + 1.454 \times 10^{-4} T - 1.6734 \times 10^{4}/T$ $1173 \leq T \leq 1556$ K	[1]
Specific heat, kJ/kg-K	$C_p = 2.432 + 6.378 \times 10^{-4} T - 7.11 \times 10^{4} T^{-2}$ $300 \leq T < 1556$ K	[2]
Thermal conductivity, W/m-K	$k = f_p [291 (1 - 1.650 \times 10^{-3} T + 1.464 \times 10^{-6} T^2 - 5.125 \times 10^{-10} T^3)]$	[3]
	$f_p = (1 - P)(1 + 11 P^2)^{-1}$	[4]
	P = porosity fraction	(Figs. 5-1,5-2)
	$300 \leq T \leq 823$ K	

Table V. Beryllium (continued)

		Reference(s)
Thermal expansion		[5]
Linear expansion, %	$\Delta L/L_o = 8.43 \times 10^{-4} (1 + 1.36 \times 10^{-3} T - 3.53 \times 10^{-7} T^2)(T - 298)$	(Figs. 5-3)
Instantaneous coeff., 1/K	$\alpha = 5.01 \times 10^{-6} (1 + 3.451 \times 10^{-3} T - 1.979 \times 10^{-7} T^2)$ $298 \leq T \leq 1500$ K	
Mean coefficient, 1/K	$\alpha_m = 8.43 \times 10^{-6} (1 + 1.36 \times 10^{-3} T - 3.53 \times 10^{-7} T^2)$ $298 \leq T \leq 1500$ K	
Thermal accommodation coeff.	0.0925 ± 0.0525	[6]
Thermal emissivity	0.6 for unpolished surface	[7]
Mechanical Properties		
Young's modulus, GPa	$E = 297 \exp(-3.5 P)[1 - 1.9 \times 10^{-4} \cdot (T - 293)]$ $P = 0$, $293 \leq T \leq 1088$ K	[8] (Fig. 5-4)
Poisson's ratio	$\nu = 0.07 \pm 0.06$	[8]

Table V. Beryllium (continued)

		Reference(s)
Ultimate compressive strength, MPa	$\sigma_c = 450\ dg^{-1/2} \exp(-5\ P)\ \ln(9200/T)$ dg = grain diameter, μm $0 \le P \le 0.2,\ 293 \le T \le 773$ K	[8] (Fig. 5-5)
Bending strength, MPa	$\sigma_b = 700\ dg^{-1/2} \exp(-5\ P)\ \ln(9200/T)$ $P = 0,\ T = 293$	[14]
Ultimate tensile strength, Mpa	$\sigma_t = 450\ dg^{-1/2} \exp(-5\ P)\ \ln(9200/T)$	[8] (Fig. 5-6)
Thermal creep rate, s^{-1}	$\dot{\varepsilon}_c = 0.751\ (1 - P^{2/3})^{-3.6}$ $\cdot \exp(-2.60 \times 10^4/T)\ \sigma^{3.6}$ $P = 0,\ 673 \le T \le 973$ K $14 \le \sigma \le 21$ MPa	[8] (Fig. 5-7)
Ductility, %	$\varepsilon_u = (1.0 \pm 0.5)$ $\cdot \exp(2.71 - 7.13 \times 10^{-3}\ \lvert T - 673 \rvert)$ $P \ge 0.1,\ 293 \le T \le 873$ K	[7,9] (Fig. 5-8,5-9)

Table V. Beryllium (continued)

		Reference(s)
Interaction with		
Hydrogen		
Solubility, appm	$S = 1.9 \times 10^{-2} (P_{H_2}/Pa)^{1/2}$	[15]
Adsorption	NO DATA	
Water:		
Liquid:	Slow and self-limiting for T < 873 K because of formation of BeO protective layer	[2]
Vapor:		
Solubility	NO DATA	
Adsorption	NO DATA	
Stainless steel (316), μm	$d = 6.58 \times 10^{4} \exp(-1.29 \times 10^{4}/T)t$ $100 \leq T \leq 3000$ h $823 \leq T \leq 1173$ K	[10,11,12]
Radiation Effects		
Physical properties	No change in physical properties is anticipated for irradiation above room temperature. However, the $\Delta V/V_o$ due to He-induced swelling must be added to P in the porosity correction factor for thermal conductivity.	[13]
Mechanical properties	He embrittlement causes a decrease in ductility for 100% dense Be tested (post-irradiation) at room temperature. In the absence of data on porous Be, the lower bound on the ductility of unirradiated Be is recommended.	[7]

Table V. Beryllium (continued)

		Reference(s)
Mechanical properties (continued)		
	$\varepsilon_u = 0.5 \exp(2.71 - 7.13 \times 10^{-3} \lvert T - 673 \rvert)$, %	
	The room temperature compressive strength increases significantly with fast fluence up to ~2×10^{22} n/cm^2 and then decreases. The flexure and tensile strengths decrease with fluence at room temperature by ~50 MPa/10^{22} n/cm^2 up to 3×10^{22} n/cm^2. For irradiation of porous Be ($P \geq 0.1$) at temperature ($T > 100$°C), unirradiated properties are recommended.	
Tritium Retention/Release		
Diffusivity, cm^2/s	$D = 1.73 \times 10^{-5} \exp(-18.5\ \text{kJ} \cdot \text{mol}^{-1}/RT)$	[15,16]
Solubility, appm	$S = 1.9 \times 10^{-2} (P_{T_2}/\text{Pa})^{1/2}$	[15]
Trapping	Very little tritium (<2%) is released from irradiated Be for T < 600°C. Above 600°C, tritium release may be enhanced by He swelling. For two samples with high He content (~24×10^3 appm), ~95% of the tritium was released after 5 hours at 611°C.	[17]

Table V. Beryllium (continued)

Radiation Effects (continued)

Reference(s)

[14,18-20]

Swelling

Parameter	ATR [14]	BR2 [18]	EBR-II [19]
Irradiation Temperature, °C	75	45	427-487
ϕt, 10^{22} n/cm^2 (E > 1 MeV)	1.4-3.4	0.7-2.9	0.8-1.3
appm He/10^{22} n/cm^3	4440	2205-3730	1540
Maximum He concentration, appm	15000	6600/11200	2000
Maximum swelling $\Delta V/V_o$, %	1.5	2.6	0.9
Post-irradiation anneals			
Time, h	1	24	
T = 200-300°C	slight effect		
T = 400-500°C	3.2-5.5%		
T = 400-600°C		3.5-6.0%	
T > 600°C	1-h anneals have resulted in significant swelling at fluences as low as 10^{21} n/cm^2 [20].		

References for Table V

1. G.E. Darwin and J.H. Buddery, Beryllium, Butterworth Scientific Publications, London (1960).
2. Y.S. Touloukian and E.H. Buyco, "Specific Heat: Metallic Elements and Alloys," Vol. 4, Thermophysical Properties of Matter, IFI Plenum (New York) 1970.
3. Y.S. Touloukian, R.W. Powell, C.Y. Ho, and P.G. Klemmens, "Thermal Conductivity: Metallic Elements and Alloys," Vol. 1, Thermophysical Properties of Matter, IFI/Plenum (New York) 1970.
4. J.C.Y. Koh and A. Fortini, "Prediction of Thermal Conductivity and Electrical Resistivity of Porous Metallic Materials," Heat Transfer 16 (1973) 2013-2022.
5. Y.S. Touloukian, R.K. Kirby, R.E. Taylor, and P.D. Dasai, "Thermal Expansion: Metallic Elements and Alloys," Vol. 12, Thermophysical Properties of Matter, IFI/Plenum (New York) 1975.
6. Y.S. Touloukian, C.Y. Ho, S.C. Saxena, and R.K. Joshi, Thermal Accommodation and Adsorption Coefficients of Gases, Vol. II-1, McGraw-Hill/CINDAS Data Series on Material Properties (New York) 1981.
7. J.M. Beeston, "Beryllium Metal as a Neutron Moderator and Reflector Material," Nucl. Eng. Design 14 (1970) 445-474.
8. M.C. Billone and W.T. Grayhack, "Summary of Mechanical Properties Data and Correlations for Li_2O, Li_4SiO_4, $LiAlO_2$, and Be," ANL/FPP/TM-218 (1988).
9. D.M. Goddard, M.J. Hoven, and S.N. Rosenwasser, "Development of Porous Be," McDonell Douglas Astronautics Company, AFML-TR-241 (1972).
10. W. Vickers, The Metallurgy of Beryllium, Proc. Int. Conf., Institute of Metals Monograph and Report Series No. 28 (1961).
11. M. Broc, T. Flament, A. Terlain, and J. Sannier, "Compatibility Problems in Tritium Breeding Blankets," ICFRM-4, Kyoto (Japan) 4-8 December 1989 (to be published in J. Nucl. Mater. 1990).
12. P. Hofmann and W. Dienst, "Chemical Interactions of Be with Li-Based Oxides and Stainless Steel," to be published in J. Nucl. Mater. (1990).
13. G.J. Dienes and A.C. Damask, J. Nucl. Mater. 3(1) (1961) 16-20.
14. J.M. Beeston, "Properties of Irradiated Beryllium, Statistical Evalua-tion," EG&G Report, TREE-1063 (October 1976).
15. P.M.S. Jones and R. Gibson, "Hydrogen in Beryllium," J. Nucl. Mater. 21 (1967) 353.
16. M.C. Billone, "Tritium Retention in Be," ANL memo to C.E. Johnson, September 8, 1988.
17. D.L. Baldwin, O.D. Slagle, and D.S. Gelles, "Tritium Release from Irradiated Beryllium at Elevated Temperatures," ICFRM-4, Kyoto (Japan) 4-8 December 1989 (to be published in J. Nucl. Mater. 1990).
18. P. Lorenzetto, presentation at the ITER Workshop on Blanket/Shield, Garching, FRG, January-February 1990.
19. J.M. Beeston, L.G. Miller, E.L. Wood, and R.W. Moir, "Comparison of Compression Properties and Swelling of Beryllium Irradiated at Various Temperatures," J. Nucl. Mater. 122-123 (1984) 802-809.
20. J. Rich, G.B. Redding, and R.S. Barnes, "The Effects of Heating Neutron Irradiated Beryllium," J. Nucl. Mater. 1 (1959) 96-105.

Table 4-2. Annealed 316 Stainless Steel

			References
Baseline physical properties			
Density, g/cm^3		7.965	2
Melting point, °C		1375	1
Latent heat of melting, kJ/kg		268	1
Thermal properties			
Specific heat, kJ/kg•K	C_p	$= 0.448799+4.54793\times10^{-4}\ (T-255.4) - 5.96555\times10^{-7}\ (T-255.4)^2+3.51261\times10^{-10}\ (T-255.4)^3$	1
Thermal conductivity, W/m-K	k	$= 12.7001+1.73467\times10^{-2}\ (T-255.4) - 2.53038\times10^{-6}\ (T-255.4)^2 - 1.92401\times10^{-10}\ (T-255.4)^3$	1
Thermal expansion			
Linear expansion, %	$\Delta L/L_o$	$= 1.269\times10^{-3}\ (1+8.9606\times10^{-4}T - 5.5032\times10^{-7}\ T^2 +1.02458\times10^{-10}\ T^3)(T-333)$	1
Mean coefficient, 1/K	α_m	$= 1.269\times10^{-5}\ [1+8.9606\times10^{-4}\ T - 5.5032\times10^{-7}\ T^2 +1.02458\times10^{-10}\ T^3]$	1
Thermal emissivity	ε	$= 0.9$	2

Table 4-2. Annealed 316 Stainless Steel (continued)

Mechanical properties

Young's modulus, GPa	E	$= 195.4255 - 3.577917\times10^{-2}\,(T-255.4) - 8.262780\times10^{-5}\,(T-255.4)^2 + 3.100689\times10^{-8}\,(T-255.4)^3$	1
Poisson's ratio	ν	$= 0.2428705 + 7.678417\times10^{-5}\,T$	1
Shear modulus, GPa	G	$= 77.56966 - 2.039276\times10^{-2}\,(T-255.4) - 2.973692\times10^{-5}\,(T-255.4)^2 + 1.434864\times10^{-8}\,(T-255.4)^3$	1

Irradiation properties

Swelling, %	$\Delta V/V_o$	$= R\left[\phi t + \frac{1}{\alpha}\,\mathrm{Ln}\left\{\frac{1+\exp\left[\alpha(\tau-\phi t)\right]}{1+\exp\left(\alpha\tau\right)}\right\}\right]$	1

where:

ϕt = fluence, 1 unit = 10^{22} n/cm^2 (E > 0.1 MeV)

$R = \exp\left(-49.8592 + 0.195283T_c - 1.87409\times10^{-4}\,T_c^2\right)$

$\alpha = -1.117 + 6.889\times10^{-3}\,T_c$

$\tau = 1.0/\left(7.98769 - 2.98448\times10^{-2}\,T_c + 2.87279\times10^{-5}\,T_c^2\right)$

T_c = temperature, °C

Table 4-2. Annealed 316 Stainless Steel (continued)

Irradiation creep, %

$$\bar{\varepsilon} = A_1 [1-\exp(-3\Phi)] \bar{\sigma} + A_2 (2.78 \times 10^{-4} t)^{0.5} \bar{\sigma}^{4.5} + A_3 (\sinh \bar{\sigma}/\sigma_1 H)^3 (2.78 \times 10^{-4} t)^3 + A_4 \Phi \bar{\sigma} + 2.2 (A_5/A_6) \Omega^2 \log_e (\cosh \Phi/\Omega) \bar{\sigma} . \quad (2)$$

where:

$\bar{\varepsilon}$ = effective strain expressed in %

$\bar{\sigma}$ = effective stress expressed in MPa,

Φ = fast fluence expressed in units of 10^{22} n/cm^2 (E > 0.1 MeV)

t = time expressed in s,

ϕ = fast flux expressed in units of 10^{15} n/cm^2 • s

T = temperature expressed in K,

σ_1 = 47.76, expressed in units of MPa

H = $1 + (\Phi)^{0.5}$

A_1 = 134 exp (-9461/T) for biaxial loading

= 268 exp (-9461/T) for condition of bending

A_2 = exp (-1.41 - 24,000/T)

A_3 = exp (77.84 - 95,000/T)

A_4 = 7.25×10^{-4}

A_5 = exp (2.91 - 8052/T)

A_6 = 1 + exp (45 - 40,262/T)

Ω = τ (from swelling equation)

Note: Valid for temperature range 300-750°C and strain rates less than 10^{-5}/s.

References for Table 4-2

1. C.C. Baker et al., "ITER Shield and Blanket Work Package Report," Argonne National Laboratory Report ANL/FPP/88-1, June 1988.

2. Nuclear Systems Materials Handbook, Vol. 1: Design Data, Oak Ridge National Laboratory, TID26666.

Table 4-3.
Sample Values of Be/Steel Heat Transfer Coefficient as a Function of Be Porosity (P), He Pressure (P_g), Hot Gap Size (G) and Gap-Temperature (T)

P	P_g, MPa	T, °C	h, W/m^2-K		
			G = 0 μm	40 μm	80 μm
0.15	0.1014	100	6892	2684	1666
		200	7425	3041	1912
		300	7788	3342	2128
		400	8033	3599	2319
		500	8193	3818	2489
	0.0507	100	5407	2424	1562
		200	5569	2676	1761
		300	5624	2869	1925
		400	5617	3017	2063
		500	5573	3132	2179
0.35	0.1014	100	3700	2009	1379
		200	4141	2296	1588
		300	4498	2544	1773
		400	4788	2760	1939
		500	5026	2951	2089
	0.0507	100	3225	1860	1307
		200	3492	2081	1482
		300	3680	2260	1630
		400	3810	2405	1757
		500	3901	2524	1866

4.3 Material Specifications

4.3.1 Annealed 316 stainless steel

The stainless steel cladding between Be and breeder is nominally 1 mm thick. From a heat transfer perspective, it is desirable to have the surfaces relatively smooth (1-2 μm surface roughness). However, this is not a critical specification in that the larger roughnesses of the porous Be and breeder will dominate.

The first-wall/back-wall unit and the coolant channel steel have box-like geometries. While these require special fabrication procedures, there are no additional materials specifications required.

4.3.2 Be

The Be layers consist of cubic blocks of porous Be with thicknesses ranging from 30 mm to 190 mm. The densities are either 85% or 65%. The fabrication technique is cold-isostatic pressing followed by sintering. From the tritium transport point of view, it is desirable to have a finished product with <1 wt. % BeO, 10-30 μm grain diameter, and an average pore diameter >1 μm. Green densities in the range of 68-82% of theoretical have been achieved with cold-isostatic pressing, depending on pressing pressure, technique (single-pressed vs. double-pressed), and starting powder size. Thus, only a small amount of densification by sintering is required to achieve 85% density [1]. The resulting grain sizes, BeO content, and average pore diameters are within the desirable range. A central issue for the 85% dense finished product is the desirable vs. achievable surface roughness. In the design analysis, it is assumed that the finished product has a mean rms surface roughness of $1 + 110\ P$, μm, where P is the porosity volume fraction. Thus, the assumed roughness for contact heat conductance is 17.5 μm. It would be desirable, but not necessary, to have the surface finish be 1-10 μm. It is more important to know what the roughness is for the fabricated blocks with no polishing than it is to specify a roughness. The main issue is the uncertainty in the heat transfer calculation due to the uncertainty in roughness of the fabricated blocks.

The 65% dense blocks represent a special case in that this density is below the green density of isostatically-pressed blocks with pressing pressure

≥276 MPa. It may be necessary to press at lower pressure or to use a vibratory technique to produce a green density of 55-60% and then sinter to achieve 65% density in order to have enough strength in the blocks to withstand differential thermal stresses. Again, knowledge of the surface roughness is important in minimizing the uncertainty in the heat transfer calculations.

A design alternative is to use Be balls or spheres in the diameter range of 0.1-1 mm for some of the layers. These spheres would be 100% dense. No fabrication difficulties are anticipated and no detailed material specifications are needed. The final product could have diameter variations of ±10% and surface roughnesses in the range of 1-5 μm with little impact on the heat transfer analysis.

4.3.3 Solid breeder

In the sintered-product design, the Li_2O is 80% dense with radial thicknesses of 8 mm (outboard) and 10 mm (inboard). It is assumed that the Li_2O layers are made up of cubic Li_2O blocks with quarter-circular cylindrical grooves at four edges forming purge flow channels in the toroidal direction. The minimum radius for these grooves is 0.23 mm. The grooves can be larger with the net effect of increasing the permeability and decreasing the pressure drop.

The assumed grain diameter is 20 μm and the assumed average pore diameter 5 μm. Tolerances of ±25% can be allowed without adversely affecting the tritium performance.

As Li_2O is very hygroscopic, it is important that the Li_2O be relatively dry ($<<0.1$ wt. % H_2O). This moisture will be driven out of the material at operating temperatures. However, the presence of large initial moisture contents could enhance densification, grain growth, and LiOH mass transport. It would be desirable to dry the Li_2O to $<10^{-2}$ wt. %.

If Li_2ZrO_3 is used in place of Li_2O, the grain diameter should be on the order of 1-5 μm. Experimentally, Li_2ZrO_3 with this range of grain diameters has been shown to have excellent tritium release properties.

For the common design, a binary mixture of spheres or pebbles is called for. The large pebble diameter is in the range of 0.5-1.5 mm while the small

pebble diameter is in the range of 0.1-0.5 mm. Packing fractions of 0.80-0.82 can easily be achieved with such binary mixtures as long as the ratio of large-to-small particles is >5 and the ratio of large particle diameter to layer thickness is >3. Within each particle, the porosity volume fraction is 0-15% depending on tritium release performance and desired swelling accommodation. Li_2O pebbles with 15% porosity and 1-5 mm diameter have been made in Japan. No fabrication problems are anticipated in this area. If Li_2ZrO_3 is used instead of Li_2O, the same range of particle sizes should be used.

References

[1] S.N. Rosenwasser, D.M. Goddard, and M.J. Hovan, "Development of Porous Beryllium," McDonnell Douglas Report AFML-TR-71-241, January 1972.

4.4 Impurities

Impurity levels are important in the activation and afterheat analyses. Values have been established for stainless steel and Li_2O based on experience in manufacturing these materials. Table 4-4 lists the composition, including impurities, for stainless steel. Table 4-5 lists the impurity levels for 80% dense Li_2O.

Table 4-4.
Composition for Annealed Type 316 SS

Comp.	wt.%	Comp.	wt.%	Comp.	wt.%	Comp.	wt.%
H	-	B	0.001	C	0.018	N	0.07
O	0.002	Na	-	Mg	-	Al	0.3
Si	0.46	P	0.026	S	0.01	K	0.0005
Ca	-	Ti	0.04	V	0.004	Cr	17.1
Mn	1.7	Fe	64.4265	Co	0.03	Ni	13.2
Cu	0.1	As	0.0005	Zr	0.002	Nb	0.002
Mo	2.5	Ag	0.0002	Cd	0.0002	Sn	0.002
Sb	0.0005	Ba	0.0005	Tb	0.0005	Ta	0.0005
W	0.001	Ir	0.0005	Pb	0.0008	Bi	0.0008

Table 4-5.
Impurity Levels in 80% Dense Li_2O.

Imp.	wppm	Imp.	wppm	Imp.	wppm	Imp.	wppm
Be	1.0	B	1.0	C	100.0	N	2.0
F	0.1	Na	60.0	Mg	10.0	Al	50.0
Si	50.0	P	1.0	S	0.1	Cl	10.0
K	20.0	Ca	100.0	Sc	0.1	Ti	10.0
V	1.0	Cr	1.0	Mn	1.0	Fe	50.0
Co	0.2	Ni	10.0	Cu	10.0	Zn	10.0
Ga	1.0	Ge	0.1	As	0.1	Br	0.1
Rb	0.1	Sr	1.0	Zr	1.0	Mo	0.1
Cd	0.1	In	0.03	Sn	1.0	Sb	1.0
Ba	5.0	La	0.1	Au	0.0005	Pb	0.1
U	0.1						

5.0 MECHANICAL DESIGN

5.1 Outboard Section

5.1.1 General description

The outboard (OB) blanket is divided into 48 segments of equal toroidal extent, three segments for each toroidal field (TF) coil sector. The three segments consist of a central segment and two side segments. The side segments extend the full height of the reactor and will henceforth be called side modules. The central segment is located between TF coils and is divided into an upper and lower module. A penetration is situated at midplane between the upper and lower central modules. Each side module lies partially in the shadow of a TF coil. Thus, the back of each side module has part of it rounded to fit the contour of the vacuum chamber within the TF coil and part of it straight from top to bottom to fit the vacuum chamber between the TF coils. Central modules have straight backs and come out of the reactor vertically without circumferential displacement. Side modules, require a circumferential translation before they can be extracted through the upper maintenance port. Side modules and upper central modules have service connections at the top, while the lower central module has service connections at the bottom.

The OB solid breeder blanket module design is of slab configuration consisting of Be plates interleaved with solid breeder zones and coolant panels, all contained within a stainless steel box. Figure 5-1 shows a view of a side module with cross sections at midplane and at the upper extremity. Figure 5-2 is also a midplane cross section but with the zones identified. From Fig. 5-1 it will be noted that the multiplier zone thickness increases from midplane to the upper extremity. This is done as part of the solid breeder temperature control system. As the neutron wall loading decreases at the extremities, the Be zones are increased in thickness in order to maintain the solid breeder within the desired temperature window. There are two solid breeder zones and two blanket coolant panels extending the full height of the module. The present design can accommodate three solid breeder zones and three coolant panels with minimal impact on the complexity. This can result in a substantial increase in the tritium breeding ratio. It should be noted

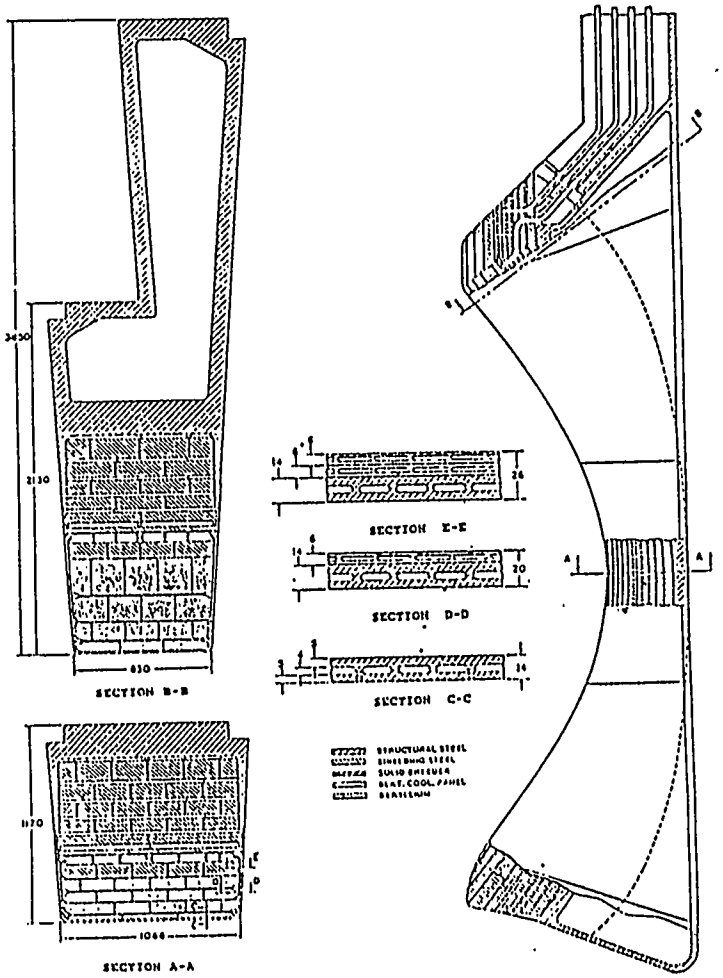

Fig. 5-1. Outboard side module at the midplane and the upper blanket extremity.

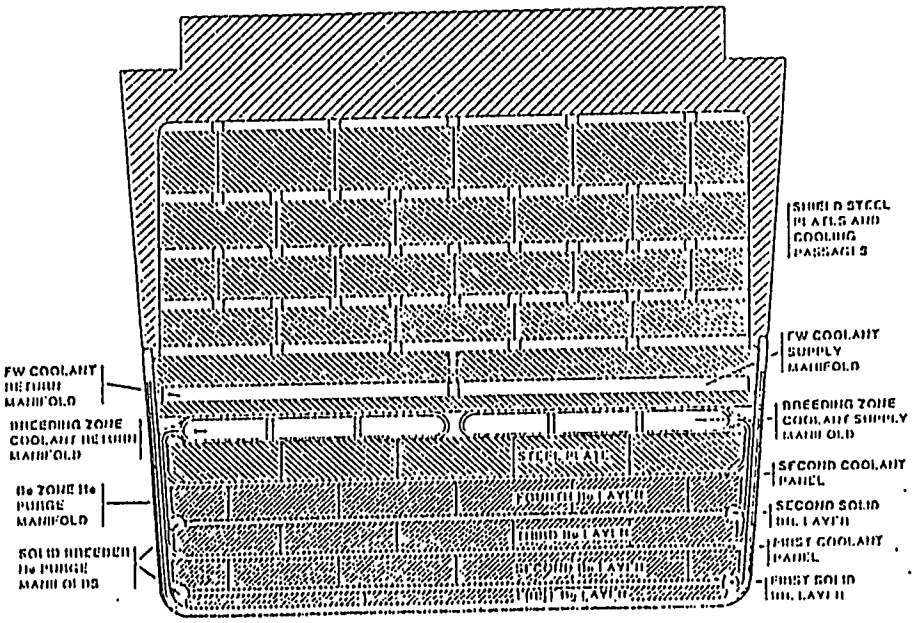

Fig. 5-2. Midplane cross section of outboard side blanket module.

that the solid breeder zones and coolant panels are of constant thickness regardless of their poloidal location. There are four Be zones. The first is immediately behind the first wall; the second immediately behind the 1st solid breeder zone; the third behind the first coolant panel; and the fourth behind the 2nd solid breeder zone. The last layer in the front breeding part consists of steel plates and is located immediately behind the 2nd coolant panel. It is followed by the oblong manifolds which supply the blanket coolant panels. Figures 5-1 and 5-2 show the details of the described zones and Table 5-1 gives the radial build at midplane and at the extremities.

The toroidal width of the OB modules also varies from top to midplane, with the nominal dimensions shown in Fig. 5-1. The Be plates are segmented in the toroidal and poloidal direction to prevent excessive distortion due to temperature gradients. Since control of the solid breeder temperature depends on the Be thickness and the gap resistances, it is imperative to insure that the Be and solid breeder surface conform to the coolant panel surfaces. The formation of distortion gaps and their consequences are discussed in Sections 8.4 and 8.5. The Be plate zones are designed with the option of purging with He gas to prevent accumulation of tritium in this area. This is accomplished by providing spaces at the interfaces between the Be plates and the side walls as shown in Fig. 5-1. These spaces act like manifolds for distributing He gas poloidally. This gas then flows toroidally across the Be plates and comes out on the other side of the module. Precautions must be taken to prevent short circuits of the gas at the top and bottom of the module.

The solid breeder consists of Li_2O panels, 0.8 cm thick, clad in 0.1 cm thick SS sheets. The panels are continuous from top to bottom and have built in manifolds on the sides running in the poloidal direction. Purge gas flows poloidally through the manifold, then toroidally across the panel through machined grooves and finally back out through the return manifold. This purge gas carries with it the tritium which is bred in the solid breeder.

The first wall (FW) consists of a 1.4 cm thick plate with built-in rectangular channels, 0.4 cm × 2 cm separated by 0.3 cm walls. It is

Table 5-1. Radial Build of OB Blanket

Zone	Material	Function	Dimension (cm) Midplane	Extremity
1	SS	First Wall	0.5	0.5
2	H_2O	FW Coolant	0.4	0.4
3	SS	First Wall	0.5	0.5
4	Cu	Stabilizer Coil	0	0.5
5	Be	Multiplier	3.4	7.3
6	SS	Cladding	0.1	0.1
7	Li_2O	Breeder	0.8	0.8
8	SS	Cladding	0.1	0.1
9	Be	Multiplier	5.9	12.8
10	SS	Panel Wall	0.2	0.2
11	H_2O	Blanket Coolant	0.2	0.2
12	SS	Panel Wall	0.2	0.2
13	Be	Multiplier	5.7	19.4
14	SS	Cladding	0.1	0.1
15	Li_2O	Breeder	0.8	0.8
16	SS	Cladding	0.1	0.1
17	Be	Multiplier	7.1	19.0
18	SS	Panel Wall	0.2	0.2
19	H_2O	Blanket Coolant	0.2	0.2
20	SS	Panel Wall	0.2	0.2
21	SS	Filler	8.0	8.0
22	SS	Manifold Wall	0.2	0.2
23	H_2O	Blanket Manifold	5.0	5.0
24	SS	Manifold Wall	0.2	0.2
25	SS	Steel Plate	3.2	3.2
26	H_2O	FW Manifold	3.0	3.0
27	SS	Steel Plate	6.0	6.0
28	H_2O	Shield Coolant	2.0	2.0
29	SS	Shield	7.0	7.0
30	H_2O	Shield Coolant	2.0	2.0
31	SS	Shield	8.0	8.0
32	H_2O	Shield Coolant	2.0	2.0
33	SS	Shield	9.0	9.0
34	H_2O	Shield Coolant	2.0	2.0
35	SS	Shield	11.8	11.8
36	H_2O	Shield Coolant	2.0	2.0
37	SS	Rear Plate	2.0	2.0

assembled from two extruded SS plates, each with one half channel embossed on one side. The two sheets are assembled with the channel wall separations making contact and continuously spot welded, thus forming the plate with the built-in channels. Section C-C, D-D and E-E of Fig. 5-1 show a cross section of the first wall. The plate orientation is such that the channels run along one side wall, then toroidally through the FW and back along the other side wall. This insures good cooling of the side walls and the FW. The FW also has blind holes drilled and tapped for attachement of graphite tiles during the physics phase of operation. Section DD of Fig. 5-1 shows the FW followed by a single blanket coolant panel and section EE, by two blanket coolant panels. These coolant panels are made the same as the FW but are only 0.6 cm overall thickness and have 0.2 cm × 2 cm coolant channels separated by 0.2 cm thick walls. The panels are welded/brazed to oblong supply and return manifolds which extend poloidally the full length of the module and are reinforced by through studs to prevent transfer of pressure to the blanket components.

The next two steel plates play an important role in the blanket design. These plates which are 3.2 cm and 6 cm thick, respectively, and are separated by a 3 cm gap, are continuous top to bottom and are welded to the module side wall all around. They serve three main functions:

[1] The first plate completely seals the front breeding zone from the FW coolant manifolds. No water can be allowed to permeate the breeding zone materials which operate at very high temperatures.

[2] The 3-cm space between the two plates defines the supply and return manifolds for the FW coolant (See Fig. 5-2).

[3] The two plates act as structural elements tying the two sidewalls of the blanket module together and effectively creating a box for the breeding zone materials.

The poloidal extent of the OB breeding blanket is ±4.1 m. The actual first wall extends somewhat further. These zones which extend beyond the breeding blanket consist of steel plates and cooling panels instead of Be and solid breeder plates. The sidewall and first wall configuration is, however, the same.

Figure 5-3 shows several views of an upper central module. On the right is a side view with the sidewall removed to show the internal details of the blanket. Section A-A is a cross section near the lower end of the blanket (nearest to the penetration) and section B-B of the upper extremity. In contrast with Fig. 5-1, what is immediately obvious is that the back of the module extends straight out, and does not have a step as in the side module. The step in the side module is needed so that it can be inserted circumferentially into the bore of the TF coil. Both figures show the outline of the copper stabilizing coil which will be discussed later in this chapter.

5.2 Inboard Section

There are four important differences between the inboard (IB) and the outboard (OB) blanket, which are:

[1] IB blanket has poloidal coolant flow

[2] IB blanket has only one solid breeder zone

[3] IB module is subdivided into three electrically insulated parts

[4] Fabrication and assembly of the IB blanket is radically different from the OB blanket.

The IB blanket is divided into 32 toroidally equal modules, or two modules per TF coil. The centerlines of the modules never coincide with the centerlines of the TF coils. Thus the two modules fit between two TF coil centerlines.

Figure 5-4 has a side view of an IB module with cross sections at midplane and at the top extremity (Z= ±3.4 m). The FW, side walls and blanket coolant panels are fabricated the same as in the OB blanket; however, the coolant channels run in the poloidal direction. As in the OB blanket, the radial build is smaller at midplane than at the extremities. Water and purge gas connections are all at the top.

To reduce disruption effects, each module is subdivided into three parts electrically insulated from each other. The insulated zone extends 27 cm at

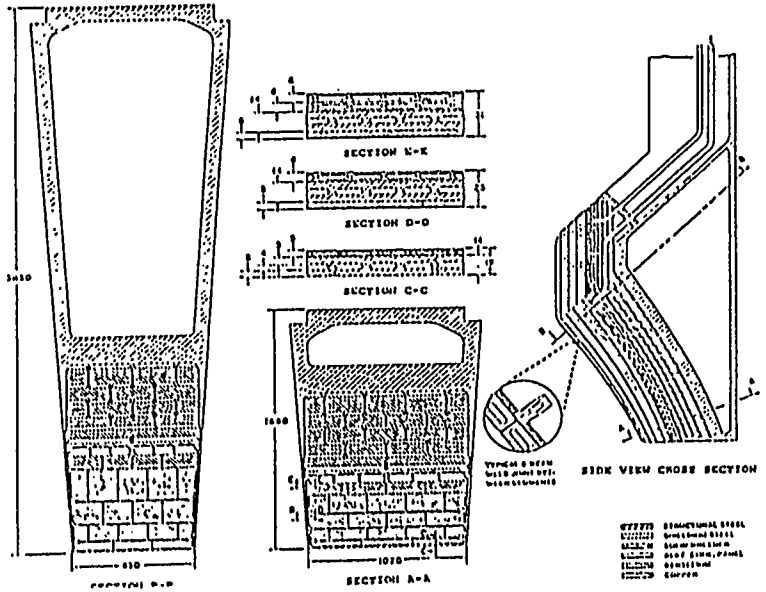

Fig. 5-3. Poloidal cross section of the upper central module.

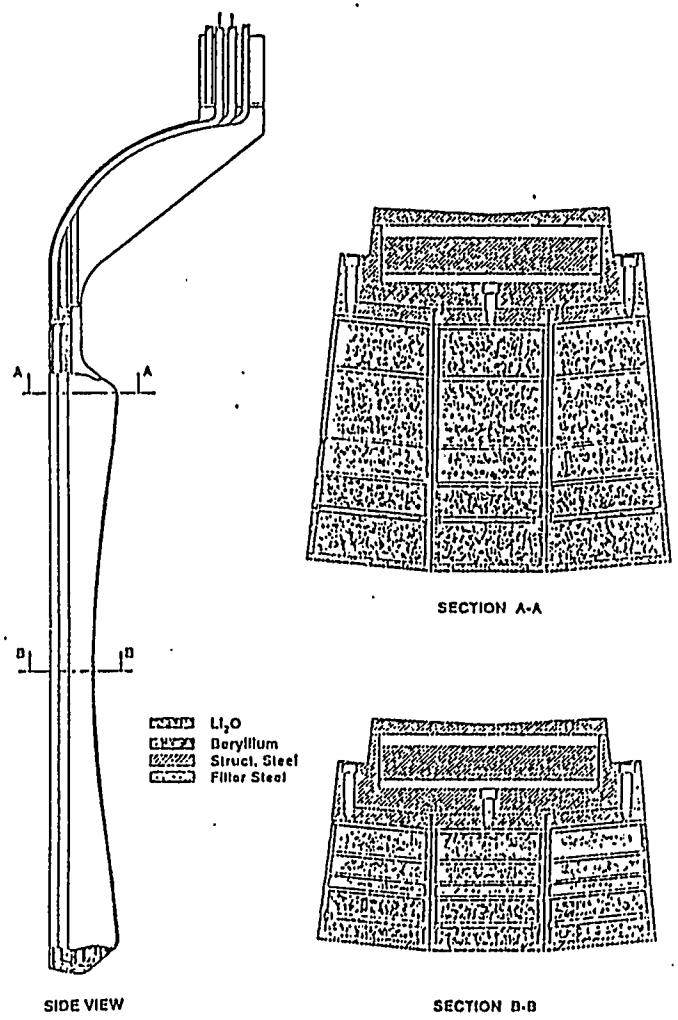

Fig. 5-4. Inboard module with cross sections at midplane and the top extremity.

midplane and 53 cm at the extremities. The three parts of the module are then E-beam welded together in the back and then bolted to a common shield backing. The solid breeder and the Be zone are purged with He gas.

The FW is 1.5 cm thick and has 0.5 cm × 3.48 cm coolant channels spaced 2 mm apart. These spaces are increased in some places to allow room for fasteners needed to attach graphite tiles during the physics phase of operations. Side walls are 1.0 cm thick and have 0.3 cm × 3.8 cm channels spaced every 1.2 cm. Table 5-2 gives the radial build of the IB blanket/shield.

Table 5-2. Radial Build of IB Blanket

Zone	Material	Function	Dimension (cm) Midplane	Extremity
1	SS	FW Structure	0.5	0.5
2	H_2O	FW Coolant	0.5	0.5
3	SS	FW Structure	0.5	0.5
4	Be	Multiplier	3.4	9.0
5	SS	Cladding	0.1	0.1
6	Li_2O	Breeder	1.0	1.0
7	SS	Cladding	0.1	0.1
8	Be	Multiplier	4.8	6.5
9	SS	Panel Wall	0.2	0.2
10	H_2O	Blanket Coolant	0.5	0.5
11	SS	Panel Wall	0.2	0.2
12	SS	Shield	2.5	7.4
13	H_2O	Shield Coolant	0.6	0.6
14	SS	Shield	4.0	14.0
15	H_2O	Shield Coolant	0.8	0.8
16	SS	Shield	6.0	10.4
17	H_2O	Shield Coolant	1.0	1.0
18	SS	Shield	8.8	8.8
19	H_2O	Shield Coolant	2.0	2.0
20	SS	Shield	7.5	7.5
21	H_2O	Shield Coolant	2.5	2.5
22	SS	Rear Plate	2.5	2.5

5.3 First Wall Support

The FW has two loads which it must deal with, He gas pressure from the blanket and disruption loads. The analysis related to the maximum toroidal span that can be tolerated is given in Section 8. In this section we will address the impact of such a requirement on the mechanical design.

Toroidal stiffeners which were originally contemplated for the FW must now be attached to the back shield structure in order to provide the required support against disruption loads. The attachment can be in the form of rods which are welded to the stiffeners and then to the front plate of the FW cooling manifold. Figure 5-5 shows how this can be accomplished. Sealed penetrations have to be provided through the breeder panels, the cooling panels and through the blanket coolant manifolds. This is a minor complication in the design and has minimal impact on the total material fraction in the blanket and will not reduce the breeding ratio appreciably.

Preliminary analysis indicates that these rods can be cooled by conduction if they can be adequately grounded to the cooling panels as they go through them. Another interesting idea is to make these rods as double ended heat pipes with sinks at either end.

5.4 Copper Stabilizer Coil Integration

The side view in Fig. 5-1 shows the outline of the passive stabilizer coils. They are located on the upper and lower third of the side module, starting at z = ±2.7 m extending to ±4.3 m at the first wall and to ±5.0 m at the rear. These coils cover the entire poloidal span of the center modules. The coils are in the form of 0.5-cm thick copper plates which subtend the blanket module on all four sides. Section B-B of Fig. 5-1 shows the copper plates on the outside of the side walls but on the inside of the first wall. The plates are bonded/brazed to the blanket wall structure and thus do not require separate cooling.

5.5 Penetration Accommodation

Each space between TF coils at the midplane has penetrations which are used for various functions such as test module placement, RF heating modules and neutral beam tubes. Test module penetrations which are nominally 1 m

in toroidal extent and ±1.7 m in poloidal extent are easy to accommodate. The central part is split into an upper and a lower module, providing the space needed for the penetration at midplane. The upper module has service connections at the top and the lower module at the bottom.

The more difficult penetration to accommodate is the neutral beam tube, which comes in tangent to the circumferential centerline of the plasma and thus sweeps across two side modules and one central module as shown in Fig. 5-6. The neutral beam tube is 0.8 m wide and extends ±1.7 m in the poloidal direction from midplane. For the purpose of discussion we number the two side modules as S-1 and S-2, and the central module as C-1.

There are two ways to accommodate the neutral beam penetration. In both ways, modules C-1 and S-2 are modified in the same way, but module S-1 is modified differently. Module C-1 is made to be continuous from top to bottom but with the rear corner modified to make room for the neutral beam tube. Likewise module S-2 is modified to have a front corner missing. These modifications are shown in Figs. 5-7 and 5-8 respectively. The two ways in which module S-1 can be modified are the following:

[1] Tunnel through module S-1 at the midplane, with the upper and lower segments attached to each other by the two triangular segments, and duct coolant and purge gas through these triangular segments. In this way, the service connections remain at the top.

[2] Split S-1 into an upper and lower module with one sealed off triangular segment connected to one and the second to the other. In this case, the lower module will have service connections from the bottom. When the two halves are assembled in the reactor, they appear continuous.

In either case, the triangular connecting segments will have to be fabricated from FW panels, since they would be exposed to surface heat loads from the plasma.

Figure 5-9 shows module S-1 as continuous with the penetration tunneled through. The cross sections show the triangular connecting pieces with the

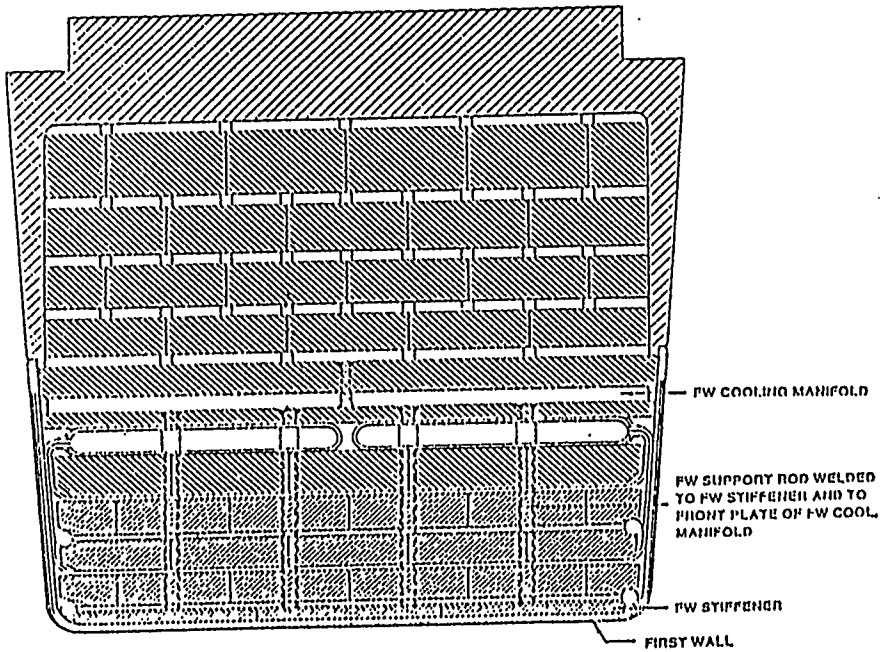

Fig. 5-5. First wall support to the back shield.

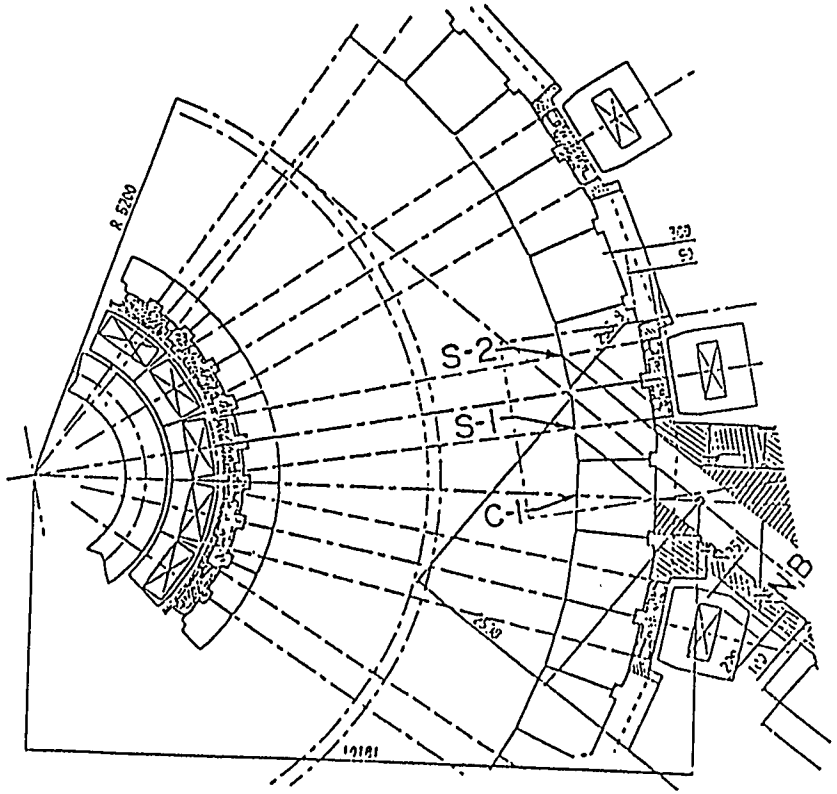

Fig. 5-6. Layout of a neutral beam tube at midplane and its effect on the blanket modules.

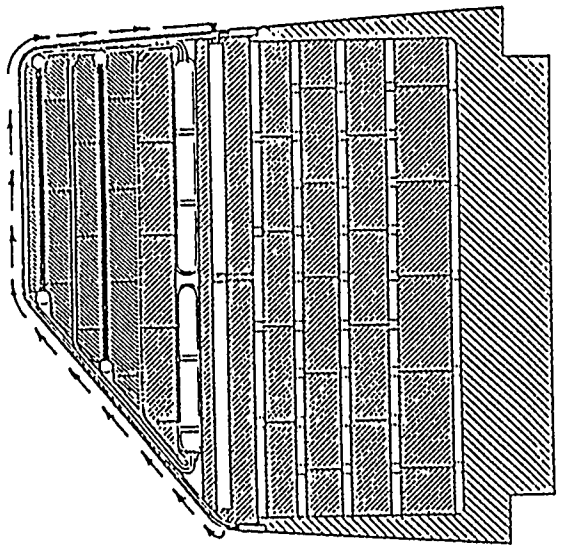

Fig. 5-7. Modification of module S-2. (Arrows indicate water flow in first wall.)

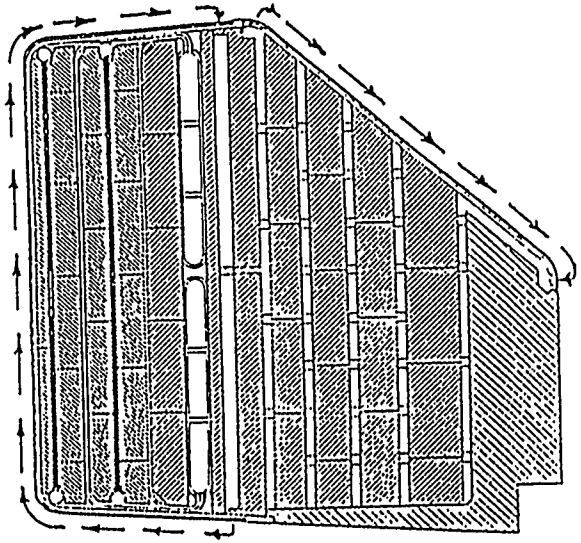

Fig. 5-8. Modification of module C-1. (Arrows indicate water flow in first wall.)

coolant and purge gas lines ducted through. Note that the surfaces exposed to the plasma are cooled as if they are part of the first wall.

Figure 5-10 shows the S-1 module split into an upper and lower half with the service connections for the lower half provided from the bottom. Although this method simplifies the blanket design, it complicates the bottom coolant connection due to the fact that the module has to be translated circumferentially in the reactor to fit inside the TF coil bore

5.6 Blanket/Shield Integration

In the solid breeder design, the blanket and shield are integrated both structurally and thermal hydraulically. This means that both blanket and shield are assembled outside the reactor into a single unit which is called a module. When loaded into the reactor as a module, a single set of cooling and purge gas connections have to be made to provide the service for that module.

Figure 5-1 and 5-3 show this integration for the OB side and center modules respectively. It can be seen that the breeding zone which occupies the front part of the blanket shares the same structural box as the shield which makes up the rear part. There is one distinction which must be kept in mind: the breeding part is sealed off from the shield part by the front plate of the FW cooling manifold. No water can be allowed to permeate into the breeding part except in the cooling panels, where it is isolated, and will never come in contact with the hot Be plates or the solid breeder cladding. In the shield part, the water flows through gaps between the steel plates and is not contained within sealed channels. The Hydraulics Section details the flow paths of the water through the OB blanket and shield.

The IB side also has the blanket and shield integrated into a single unit. Figure 5-4 shows the IB module as consisting of a front part which is made up of three electrically insulated boxes, attached to a single rear part. Breeding and shielding material fill the front part, while the rear part consists of water-cooled steel. As in the case of the OB blanket, the same coolant loop is used for the blanket and shield, while the first wall is separately cooled. The flow path and thermal hydraulics parameter are given in Section 9.0.

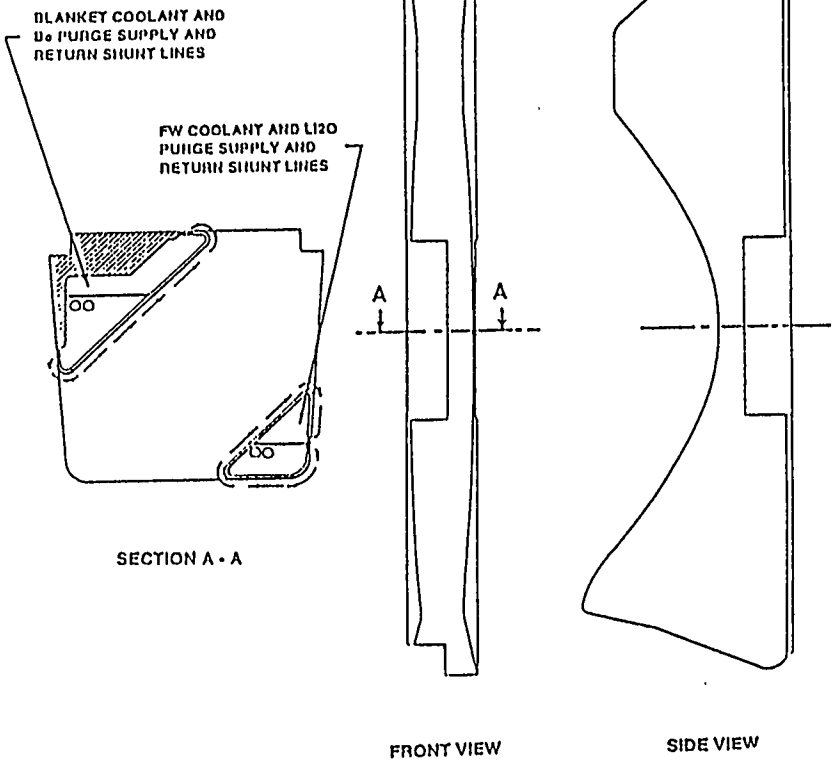

Fig. 5-9. Module S-1 with upper service connections.

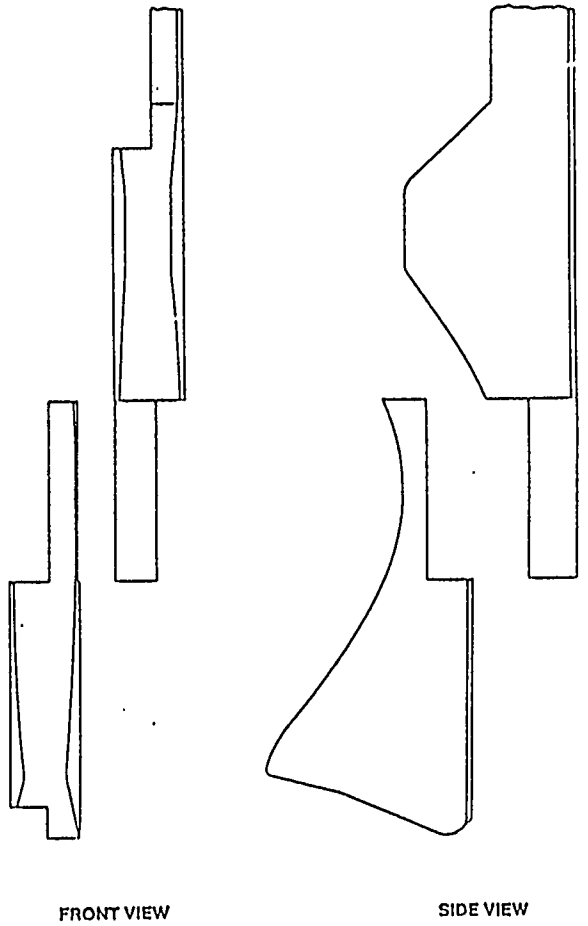

Fig. 5-10. Module S-1 with upper and lower service connections.

5.7 Coolant Manifolds

Each OB and IB blanket/shield module has the following service connections:

[1] FW coolant supply
[1] FW coolant return
[3] Blanket/shield coolant supply
[4] Blanket/shield coolant return
[5] Be zone He purge gas supply
[6] Be zone He purge gas return
[7] Solid breeder He purge gas supply
[8] Solid breeder He purge gas return

Figures 5-1, 5-3, and 5-4 show the service connections at the top of the OB side, OB upper central and IB blanket modules, respectively. The OB lower central module and possibly the OB lower side modules which bracket a neutral beam penetration will need service connections at the bottom (not shown in any figures).

The OB blanket modules have connection pipes coming through the upper chimney and connecting to manifolds within the modules. The FW manifolds distribute the coolant poloidally from which individual channels carry water toroidally across the FW collecting into the return manifold and exiting the module through the return connecting pipe. The OB blanket has similar manifolding, however, as the water exits the return manifold, it is directed through the coolant channels in the shield before coming out of the module through the return connection.

In the IB blanket the FW supply connections feed water into a short toroidal manifold (shown as a circle at the top in Fig. 5-4) from which the water flows poloidally through the FW within each of the three boxes. At the bottom of the module, the water is divided into two parts and each flows back through one side wall in the box. Thus, the closed circuit cools the FW and side walls. At the top the water collects into a return toroidal manifold and then out of the module through a return connecting pipe. The blanket coolant supply connecting pipe feeds water simultaneously to the two extreme rear channels in the rear of the shield. The water in the rear channel flows down

through the shield in the poloidal direction, then makes a transition into each of the three boxes at the bottom and flows back up through the blanket coolant panel. The water in the second to last channel also flows down through the shield then makes several transits through the shield ending up at the top. From there both coolant streams are dumped into the divertor shield zone flowing up to a bulkhead and out through a return connecting pipe. Table 5-3 gives the dimensions of the connecting pipes for each of the various modules.

Table 5-3. Dimension of Connecting Pipes

OB Blanket/shield	Inner Dimension (cm)
Side Modules	
FW supply and return	14.2
Blanket supply and return	16.1
Central Modules	
FW supply and return	10.0
Blanket supply and return	11.4
IB Modules	
FW supply and return	7.8
Blanket supply and return	8.3

5.8 Fabrication and Assembly

Fabrication of both OB and IB blanket modules is based on the ability to make cooling panels with built in channels and then forming them into the needed shapes. Although the particular shape of panels used in the design of the blanket are not available from the shelf, the processes used in fabricating many shapes of cooling panels can be used to produce them.

Dean Products Inc. of Brooklyn, NY produces a product called Panelcoil. These panelcoils are fabricated from two sheets of metal, usually stainless steel, where either one, or both sheets are embossed with a pattern and then seam-welded (continuously spot-welded) together. The pattern then forms coolant channels in different configurations. These panels are then formed into various shapes such as cones, spheres, cylinders and rectangular boxes.

The panels can be bent both parallel and perpendicular to the direction of the channels.

In the present design, the FW and the blanket panels are made of plates with flat sides which have coolant channels built in. We propose that such panels can be fabricated as shown in Fig. 5-11. Sheets of stainless steel are hot rolled or extruded with the imprint of one half of the coolant channels on one side. The sheets are then assembled to form the complete channels and continuously spot welded across the channel separations. The panels are then bent into the proper shapes needed to form a module. A module can be made out of several segments and then E-beam welded together into a complete unit as long as the weld does not cut across any coolant channels. At a meeting with technical representatives from Dean Products Inc., we were assured that such procedures were entirely possible, although for them to produce such panels today, would require special tooling of their production line and the sheets would have to be extruded at the steel mill.

The OB blanket module boxes present a fabrication challenge, because of their unusual shape and the required toroidal cooling. As presently envisaged, the panels can be shaped by drawing and bending operations, but care must be exercised to insure that the channels remain properly directed. As mentioned earlier, the front boxes will most likely be made out of several sections which are subsequently E-beam welded together. Figure 5-12 shows a sequence of operations resulting in a completed front box for a side module. Figures 5-13 and 5-14 show how the rest of the module is assembled.

The IB module is also made of the same kind of panels. Because of the need for segmenting the module into three electrically insulated parts and because the coolant channels are running poloidally, it was decided to make the individual boxes out of E-beam welded segments. The cross sections A-A and B-B of Figure 5-4 show how this is accomplished. Figure 5-15 shows the sequence needed for assembling an IB blanket module.

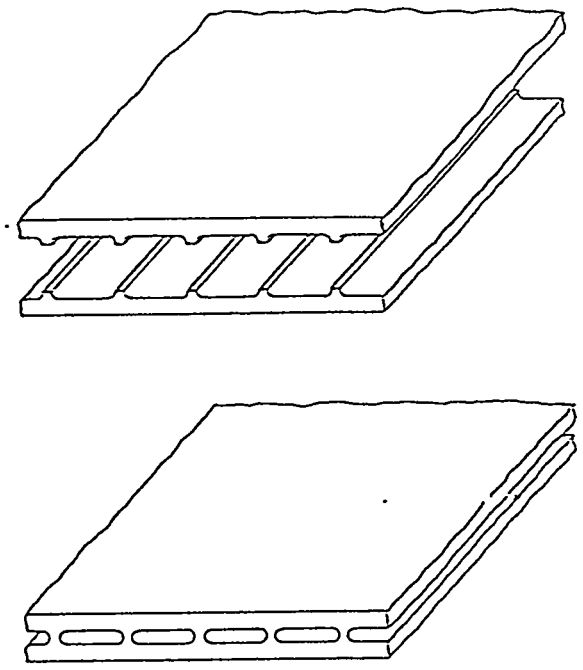

Fig. 5-11. First wall panels.

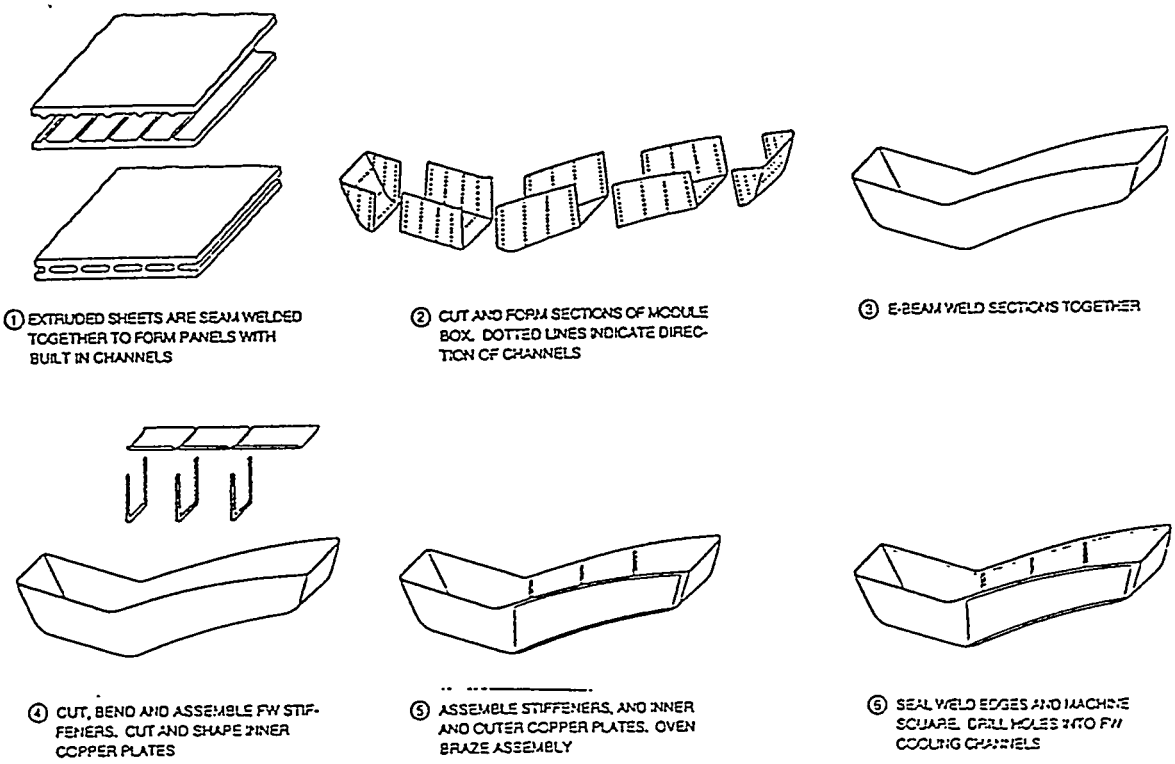

Fig. 5-12. Fabrication sequence of the front box of a side module.

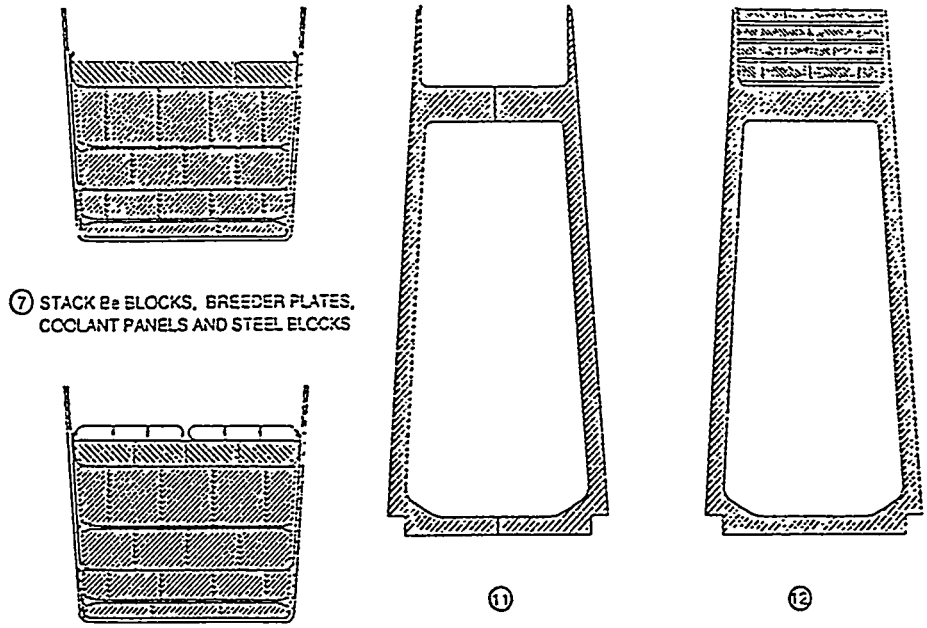

Fig. 5-13. Fabrication sequence of the side module.

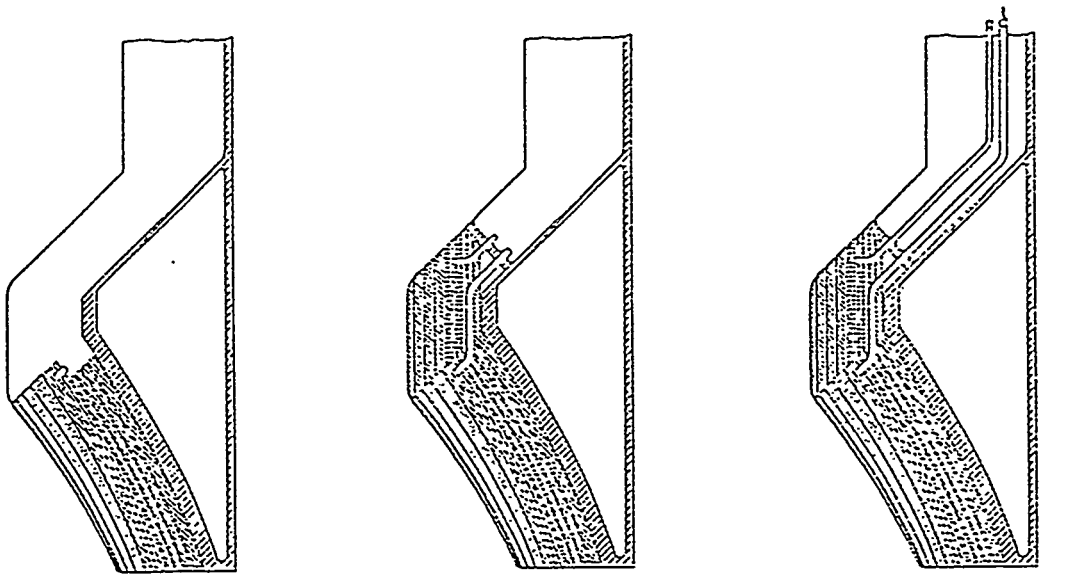

⑭ STAND MODULE UPRIGHT. CONNECT HELIUM PURGE LINES TO MANIFOLDS AT THE UPPER EXTREMITY

⑮ ASSEMBLE UPPER EXTREMITY SHIELD COMPONENTS. CONNECT MANIFOLDS AND EXTEND PIPES UP TO BULKHEAD. ASSEMBLE REMAINING SHIELD. WELD FRONT CLOSURE PLATE UP TO BULKHEAD. INSTALL BULKHEAD AND SEAL WELD TO MODULE SIDES AND TO PIPES

⑯ EXTEND PIPES ALL THE WAY. WELD REST OF FRONT CLOSURE PLATE.

Fig. 5-14. Fabrication sequence for the helium purge lines and manifolds for the side module.

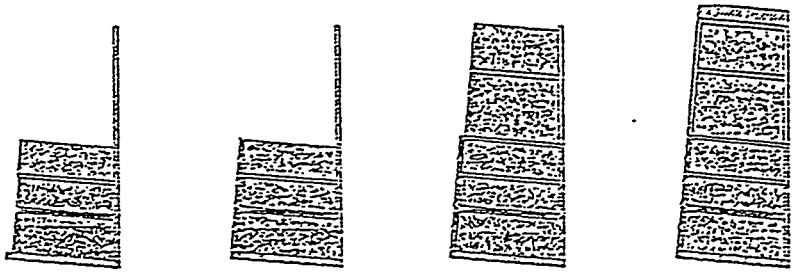

Because the end segments of the IB blanket module get narrower toward the back, they must be assembled in steps as shown above.

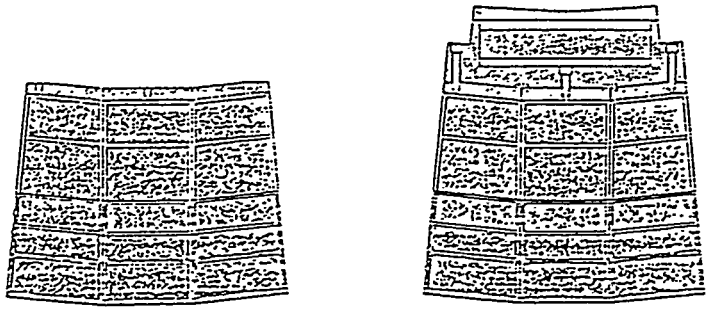

The three segments are then welded together and the assembly bolted to the back steel structure. Finally the rest of the shield is assembled and the last plate welded

Fig. 5-15. Fabrication sequence of the inboard module.

6.0 NEUTRONICS ANALYSIS

6.1 Introduction

The blanket design philosophy is to produce the necessary tritium required for the ITER operation and to operate at power reactor conditions as much as possible. This requires a continuous tritium recovery from the blanket during operation. To operate in such mode, the solid breeder material has to be within a specific temperature range (temperature window). The minimum temperature of this range is 320 to 450°C, which does not match the the water coolant temperature range of 60 to 100°C. The design approach is to use the beryllium material between the solid breeder and the water coolant to get the breeder temperature distribution within the required temperature window. This approach increases the confidence in the blanket performance because it does not make use of an adjustable gap conductance or helium gaps to adjust the solid breeder temperature. The blanket design uses the multilayer configuration [1-3]. The first wall/blanket/shield design and optimization system (BSDOS) [4] was used to carry out the neutronics and thermal-hydraulics analyses in an integrated manner.

This section gives the blanket neutronics analyses for ITER. The nuclear data base and the calculational methodology for the design analyses are briefly discussed. The parametric studies carried out to define the key blanket design parameters are presented. The change in the blanket performance due to the change in the first wall design is analyzed. The three-dimensional analysis of the net tritium breeding ratio is presented and compared to the one-dimensional result.

6.2 Calculational Methodology and Nuclear Data Base

The first step in the analysis is to define a blanket configuration that maximizes the tritium breeding ratio and satisfies the temperatures limits for the different materials. BSDOS use the one/two-dimensional discrete ordinates code ONE/TWODANT [5] to carry out the transport calculations. The analyses use a P_3 approximation for the scattering cross sections and an S_8 angular quadrature set. A 67-coupled group nuclear data library [6] (46 neutron and 21 gamma) based on ENDF/B-V is used for all the one-dimensional calculations. This library is based on VITAMIN-E [7] for the transport cross sections and KAOS/LIB [8] for the nuclear responses.

The calculational model uses a poloidal cross section with the plasma minor radius. The radial build of the blanket is defined at six locations to insure the accommodation of the poloidal distribution of the neutron wall loading. The radial build is defined at the midplane and the end of the blanket in the poloidal direction for the inboard and the outboard sections. The other two locations are at the starting point of the copper stabilizer in the poloidal direction. At each location, the calculated neutron wall loading is used to determine the radial build of the blanket.

Three blanket concepts have been developed based on the multilayer configuration. The first concept has sintered materials for the breeder and the multiplier. The second concept, the common ITER blanket uses lithium oxide pebbles and sintered beryllium blocks. The third concept is similar to the first except for the material form of the first and last beryllium zones. Two small layers of beryllium pebbles are located behind the first wall and the back of the last beryllium zone of the blanket.

The total inboard blanket and shield thickness is defined based on the global system studies. This thickness does not permit the use of a full blanket module and an adequate shield thickness to protect the inboard section of the toroidal field coils. Therefore, the inboard blanket thickness is minimized to provide an adequate radial space for the shield. The inboard blanket has a single breeder zone embedded in a beryllium material, which uses a limited inboard space. On the outboard section, an adequate radial space does exist to accommodate a full blanket module. Two and three breeder zones are considered for this section of the blanket to maximize the tritium breeding.

6.3 Radial Blanket Build

The radial build of the first blanket concept is defined based on neutronics and thermal considerations. In the inboard section, the beryllium material is used with a 0.65 density factor to reduce the thermal conductivity of the sintered block. This reduces the beryllium thickness required to get the temperature distribution of the solid breeder material within the temperature window. On the contrary, the beryllium material of the first outboard breeder zone has a density factor of 0.85 to get high thermal conductivity. This permits the use of a thick beryllium zone in the front

section of the blanket where it is needed from the neutronics point of view. The beryllium material of the second breeder zone has a 0.65 density factor to reduce the required beryllium thickness similar to the inboard section. The range of the beryllium density factor of 0.65 to 0.85 is defined based on material considerations including swelling and mechanical properties.

The calculated radial build of the outboard and inboard blankets at the different locations for the first concept are given in Table 6-1 and 6-2 for the sintered product materials. The change in the beryllium material thickness in the poloidal direction is similar to the poloidal change of the neutron wall loading on the first wall. The local tritium breeding ratio for this concept varies from 1.375 at Z = 0.0 to 1.461 at Z = 2.7 where the copper stabilizer starts. The thickness of the copper stabilizer is 0.5 cm, and it is attached to the back of the first wall. The thickness of the first beryllium zone behind the copper stabilizer is reduced by 0.5 cm. This approach keeps the continuity of the different blanket zones in the poloidal direction. The loss in the local tritium breeding ratio due to the copper stabilizer is 7.7% at Z = 2.7 m. At the end of the blanket, the local tritium breeding ratio is 1.310. The blanket thickness varies from 26.5 cm at the midplane to 58.5 cm at the end. The local tritium breeding ratio of the inboard blanket changes from 0.755 at Z = 0 to 0.895 at the end of the blanket. The corresponding blanket thicknesses are 10.7 and 18.3 cm, respectively.

In the common ITER blanket design, the breeder zone is lithium oxide pebbles. First, the analysis was carried out for a breeder material with single size pebbles, the calculated radial build is given in Table 6-3. The values of the thermal conductivity of the pebbles and the gap conductance between the steel clad and the pebbles are low compared to the sintered block breeder. The thicknesses of the beryllium zones are reduced relative to the sintered product blanket to avoid the use of a large fraction of the temperature window of the solid breeder for normal operation. This results in a small blanket thickness and a lower tritium breeding ratio as shown in Table 6-3. To improve the performance of this blanket concept, a lithium oxide material with two pebble sizes is considered to improve the thermal characteristics of the breeder zone. The corresponding radial build is also shown in Table 6-3. The local poloidal tritium breeding ratio is 1.331 instead of 1.257 for the single size pebbles. The corresponding increase in the

Table 6-1

Outboard Radial Blanket Configuration with Two Breeder Zones at the Midplane, the Beginning of the Copper Stabilizer, and the End of the Blanket

ZONE	MATERIAL (DF)	THICKNESS (cm) 1.2 MW/m^2 Z = 0	0.958 MW/m^2 Z = ±2.7 m		0.6 MW/m^2 Z = ± 4.3 m
First Wall Layers					
Tile[a]	C	2.0	2.0	2.0	2.0
First wall	steel	0.5	0.5	0.5	0.5
Stabilizer	Cu	0.0	0.0	0.5	0.5
Coolant	H_2O	0.4	0.4	0.4	0.4
Back wall	steel	0.5	0.5	0.5	0.5
Blanket					
Multiplier	Be (0.85)	3.4	4.8	4.3	7.2
Clad	steel	0.1	0.1	0.1	0.1
Breeder	Li_2O (0.80)	0.8	0.8	0.8	0.8
Clad	steel	0.1	0.1	0.1	0.1
Multiplier	Be (0.85)	5.9	7.9	7.9	12.7
Coolant channel	steel	0.2	0.2	0.2	0.2
Coolant	H_2O	0.2	0.2	0.2	0.2
Coolant channel	steel	0.2	0.2	0.2	0.2
Multiplier	Be (0.65)	5.7	8.4	8.4	19.0
Clad	steel	0.1	0.1	0.1	0.1
Breeder	Li_2O (0.80)	0.8	0.8	0.8	0.8
Clad	steel	0.1	0.1	0.1	0.1
Multiplier	Be (0.65)	7.1	11.6	11.6	15.2
Coolant channel	steel	0.2	0.2	0.2	7.2[b]
Coolant	H_2O	0.2	0.2	0.2	0.2
Total first wall/blanket thickness		26.5	37.1	37.1	58.5
Local tritium breeding ratio		1.375	1.461	1.356	1.310

a- The carbon tile is used only in the physics phase analyses and it is not included in the total first wall/blanket thickness.

b- 7.0 cm of the steel in this zone is a part of the bulk shield and it is not included in the total first wall/blanket thickness.

Table 6-2
Inboard Radial Blanket Configuration with One Breeder Zone at the Midplane and the End of the Blanket

ZONE	MATERIAL (DF)	THICKNESS (cm)	
		0.884 MW/m^2 Z = 0	0.325 MW/m^2 Z = ±3.4 m
First Wall			
Tile[a]	C	2.0	2.0
First wall	steel	0.5	0.5
Coolant	H_2O	0.4	0.4
Back wall	steel	0.5	0.5
Blanket			
Multiplier	Be (0.65)	3.3	9.0
Clad	steel	0.1	0.1
Breeder	Li_2O (0.80)	1.0	1.0
Clad	steel	0.1	0.1
Multiplier	Be (0.65)	4.6	6.5
Coolant channel	steel	0.2	2.8[b]
Coolant	H_2O	0.2	0.2
Total first wall/blanket thickness		10.9	18.5
Local tritium breeding ratio		0.755	0.895

a- The carbon tile is used only in the physics phase analyses and it is not included in the total first wall/blanket thickness.

b- 2.6 cm of the steel in this zone is part of the bulk shield and it is not included in the total first wall/blanket thickness.

Table 6-3

Outboard Radial Midplane Blanket Configuration with Two Lithium Oxide Breeder Zones Using of One or Two Size Pebbles

ZONE	MATERIAL (DF)	THICKNESS (cm)	
		One Size	Two Sizes
First Wall Layers			
Tile[a]	C	2	2
First wall	steel	0.5	0.5
Coolant	H_2O	0.4	0.4
Back wall	steel	0.5	0.5
Blanket			
Multiplier	Be (0.85)	2.7	3.1
Clad	steel	0.1	0.1
Breeder pebbles	Li_2O[b]	0.8	0.8
Clad	steel	0.1	0.1
Multiplier	Be (0.85)	4.9	5.5
Coolant channel	steel	0.2	0.2
Coolant	H_2O	0.2	0.2
Coolant channel	steel	0.2	0.2
Multiplier	Be (0.65)	4.8	5.3
Clad	steel	0.1	0.1
Breeder pebbles	Li_2O[b]	0.8	0.8
Clad	steel	0.1	0.1
Multiplier	Be (0.65)	5.8	6.5
Coolant channel	steel	0.2	0.2
Coolant	H_2O	0.2	0.2
Total first wall/blanket thickness		22.6	24.8
Local tritium breeding ratio		1.257	1.331

a- The carbon tile is used only in the physics phase analyses and it is not included in the total first wall/blanket thickness.

b- The density factors for the one and two sizes lithium oxide pebbles are 0.6 and 0.8, respectively.

blanket thickness is 2.2 cm of beryllium. These results show that the use of two pebble sizes for the breeder zone improves the blanket breeding capability by 5.9%.

The third blanket concept has been developed to improve the performance and reduce the beryllium inventory relative to the other two concepts. A small zone of beryllium pebbles is used between the coolant panel and the beryllium blocks. This blanket concept can be optimized to maximize the tritium breeding ratio by adjusting the thicknesses of the beryllium zones without thermal consideration. The second step is to divide the beryllium zone, if it is needed, into two zones. The first zone next to the coolant panel has beryllium pebbles, the second zone has beryllium blocks (sintered products). The thicknesses of these two beryllium zones are adjusted to achieve the required temperature profile for the solid breeder material. An example of this configuration is given in Table 6-4 (it is not optimized for maximum tritium breeding) to show the reduction in the beryllium inventory relative to the other two concepts. It has a higher local tritium breeding ratio of 1.387 relative to the other two concepts, and it reduces the beryllium inventory by more than 26%.

At the end of this section, the net tritium breeding ratios for the different concepts are estimated based on one-dimensional analyses. The net tritium breeding ratio is given for the first blanket concept based on a detailed three-dimensional analysis. Also, the three-dimensional result is compared to the one-dimensional estimation. The thermal performance is given in Section 7 for these blanket concepts, as well as the comparison between the three concepts.

6.4 Blanket Performance Analyses

Several studies were carried out to improve the blanket performance including the tritium breeding capability. The other objective is to determine the blanket performance as a function of the different design parameters. The key parameters for these studies are the number of the breeder zones, the thickness of the breeder zone, the breeder clad thickness, the lithium-6 enrichment, the carbon tile thickness, and the thickness of the first wall materials. The thermal analyses of these studies are presented in the next section.

Table 6-4

Outboard Radial Blanket Configuration at the Midplane with Two Breeder Zones and Two Zones of Beryllium Pebbles at the Front and Back of the Blanket

ZONE	MATERIAL (DF)	THICKNESS (cm)	
		1.2 MW/m^2 Z = 0	0.958 MW/m^2 Z = ±2.7 m
First Wall Layers			
First wall	steel	0.5	0.5
Coolant	H_2O	0.4	0.4
Back wall	steel	0.5	0.5
Blanket			
Multiplier	Be pebbles (0.82)	0.7	0.9
Clad	steel	0.1	0.1
Breeder	Li_2O (0.80)	0.8	0.8
Clad	steel	0.1	0.1
Multiplier	Be blocks (0.85)	5.3	6.5
Coolant channel	steel	0.2	0.2
Coolant	H_2O	0.2	0.2
Coolant channel	steel	0.2	0.2
Multiplier	Be blocks (0.85)	8.3	11.0
Clad	steel	0.1	0.1
Breeder	Li_2O (0.80)	0.8	0.8
Clad	steel	0.1	0.1
Multiplier	Be blocks (0.85)	5.3	6.3
Multiplier	Be pebbles (0.82)	0.5	0.9
Coolant channel	steel	0.2	0.2
Coolant	H_2O	0.2	0.2
Total first wall/blanket thickness		24.5	30.0
Local tritium breeding ratio		1.387	1.336

Tritium Breeding Enhancement: The first blanket concept is reconfigured with three breeder zones and the same minimum breeder temperature. The calculated radial build of this blanket is shown in Table 6-5. The local poloidal tritium breeding ratio at the midplane for the new configuration is 1.634 compared to 1.375 for the blanket with two breeder zones, which is about 19% increase. However the blanket thickness is increased from 26.5 to 45.1 cm. This increase in thickness can be reduced significantly by a using small layer of beryllium pebbles for the third breeder zone similar to the approach of the third concept. The net tritium breeding ratio from the use of three breeder plates is estimated in the next subsection.

Breeder Zone Thicknesses: The breeder zone thicknesses of the first blanket concept are varied simultaneously from 0.4 to 1.6 cm to study the impact on the local tritium breeding ratio. The results are shown in Fig. 6-1. The tritium production from the second breeder plate is almost constant. This indicates that the thickness of the second breeder plate should be sized based on other considerations. The tritium production from the first plate is increased slightly to reach a saturation value as the breeder plate thickness increases. The local tritium breeding ratio is increased only by 4% when the thickness of the breeder plate is doubled from 0.8 to 1.6 cm. From the results shown in Fig. 6-1, a breeder zone thick of about 0.8 cm is adequate from the neutronics point of view.

Breeder Clad Thickness: The breeder clad thickness is based on the beryllium steel compatibility consideration. The thickness of the reaction layer for ITER conditions is less than 0.01 cm at the end-of-life. Therefore, a clad thickness of 0.1 cm is used for the blanket design. The impact of the breeder clad thickness on the tritium breeding capability is calculated. The thickness of the clad material for the breeder zones is varied from 0.05 to 0.3 cm in this sensitivity study. The tritium breeding ratio as a function of the clad thickness is shown in Fig. 6-2. It is not sensitive to the clad thickness. Doubling the clad thickness from 0.1 to 0.2 cm reduces the tritium breeding ratio by 2.6%.

Lithium-6 Enrichment: The blanket design has a 95% lithium-6 enrichment for the solid breeder, which helps the blanket performance in several ways. It reduces the solid breeder and tritium inventories in the blanket. It reduces the impact of the design parameters on the blanket performance such as the clad thickness and breeder zone thickness. Also, the use of a small

Table 6-5

Outboard Radial Blanket Configuration With Three Breeder Zones[a] at The Midplane and Z = 2.7 m from the Midplane

ZONE	MATERIAL (DF)	THICKNESS (cm)	
		1.2 MW/m^2 Z = 0	0.6 MW/m^2 Z = 2.7 m
First Wall Layers			
Tile[b]	C	2.0	2.0
First wall	steel	0.3	0.3
Coolant	H_2O	0.4	0.4
Back wall	steel	0.7	0.7
Blanket			
Multiplier	Be (0.85)	2.7	3.4
Clad	steel	0.1	0.1
Breeder	Li_2O (0.8)	0.8	0.8
Clad	steel	0.1	0.1
Multiplier	Be (0.85)	5.9	7.0
Coolant channel	steel	0.2	0.2
Coolant	H_2O	0.2	0.2
Coolant channel	steel	0.2	0.2
Multiplier	Be (0.65)	5.7	7.2
Clad	steel	0.1	0.1
Breeder	Li_2O (0.8)	0.8	0.8
Clad	steel	0.1	0.1
Multiplier	Be (0.65)	6.4	8.2
Coolant channel	steel	0.2	0.2
Coolant	H_2O	0.2	0.2
Coolant channel	steel	0.2	0.2
Multiplier	Be (0.65)	13.8	20.7
Clad	steel	0.1	0.1
Breeder	Li_2O (0.8)	0.8	0.8
Clad	steel	0.1	0.1
Multiplier	Be (0.65)	4.8	9.1
Coolant channel/shield	steel	5.0	8.0
Coolant	H_2O	0.2	0.2
Total first wall/blanket thickness[c]		45.1	61.8
Local tritium breeding ratio		1.634	1.650

a- The third breeder plate extends between the copper stabilizer loops in the poloidal direction.

b- Carbon tile is used only in the physics phase analyses and it is not included in the total blanket thickness.

c- Steel shield thickness is not included in the total first wall/blanket thickness.

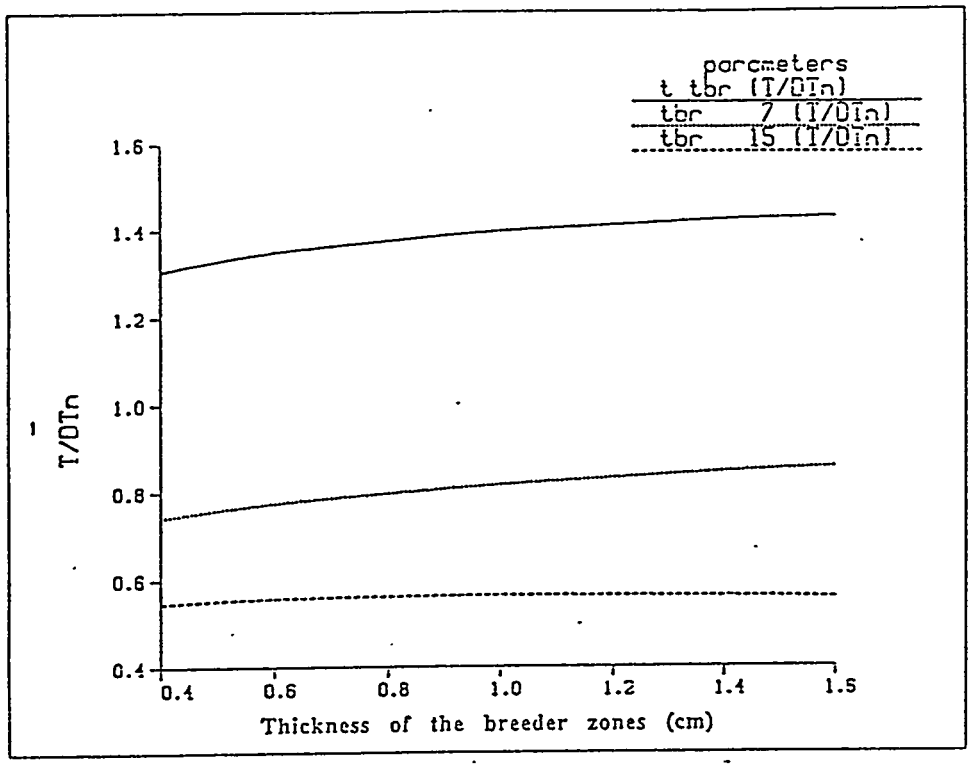

Fig. 6-1. Local tritium breeding ratio at the midplane as a function of the thickness of the two breeder zones.

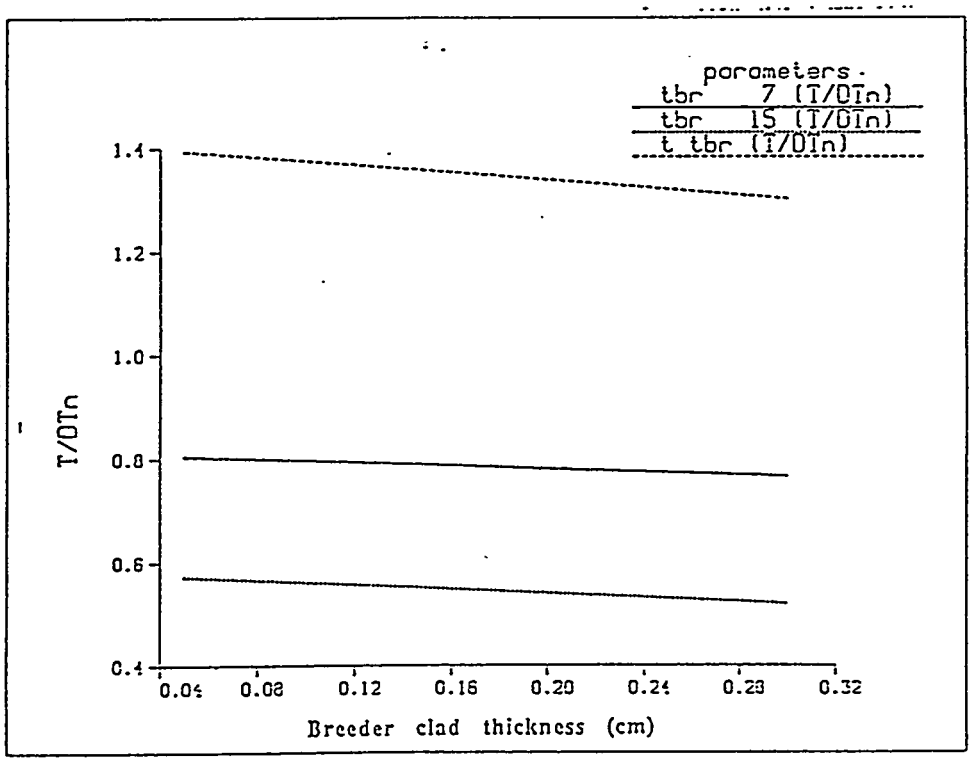

Fig. 6-2. Local tritium breeding ratio at the midplane as a function of the breeder clad thickness.

breeder zone thickness reduces its maximum temperature. This increases the blanket capability to accommodate a higher neutron wall loading. The lithium-6 enrichment is changed from the natural abundance to 95% for the blanket configuration of the first concept. The impact on the tritium breeding is shown in Fig. 6-3. The tritium breeding in both breeding zones increases fast and then slows down as the lithium-6 enrichment increases.

First Wall Design: The impact of the first wall design on the tritium breeding is assessed. The thickness of the carbon tile is varied from 0.0 to 2.5 cm for the blanket configuration of the first concept. In this range, the decrease in the tritium breeding ratio is almost linear. It is about 7% per centimeter of the carbon tile. Also, the steel thickness of the first wall is varied from 0.2 to 1.6 cm; the corresponding change in the tritium breeding ratio is 0.191. It is about 14% loss per centimeter of steel. The impact of the water-zone thickness in the first wall does account for 21% loss in the tritium breeding capability of the blanket per centimeter of water. These results encourage the use of as thin a first wall as permitted by the structural analysis.

Beryllium Density Factor: The last study examines the effect of the fabrication tolerance in the beryllium density factor on the tritium breeding capability of the blanket. The beryllium density factor is varied by ±0.05 from the designed values of 0.85 and 0.65 for the beryllium zones. The corresponding change in the tritium breeding ratio is 0.023. This result shows that the tritium breeding capability of the blanket can accommodate a .5% tolerance in the beryllium density factor in this blanket configuration.

References

[1] Y. Gohar et al., "Water-Cooled Solid-Breeder Blanket Concept for ITER," Fusion Technology, 15, March 1989.

[2] C. Baker et al., "U.S. Contribution to the Nuclear Design of ITER," Fusion Technology, 15, March 1989.

[3] Y. Gohar et al., "Low Technology, High Tritium Breeding Blanket Concept," Proceedings of 12th Symposium on Fusion Engineering, October 12-16, 1987, Monterey, California, IEEE Catalog No. 87CH2507-2.

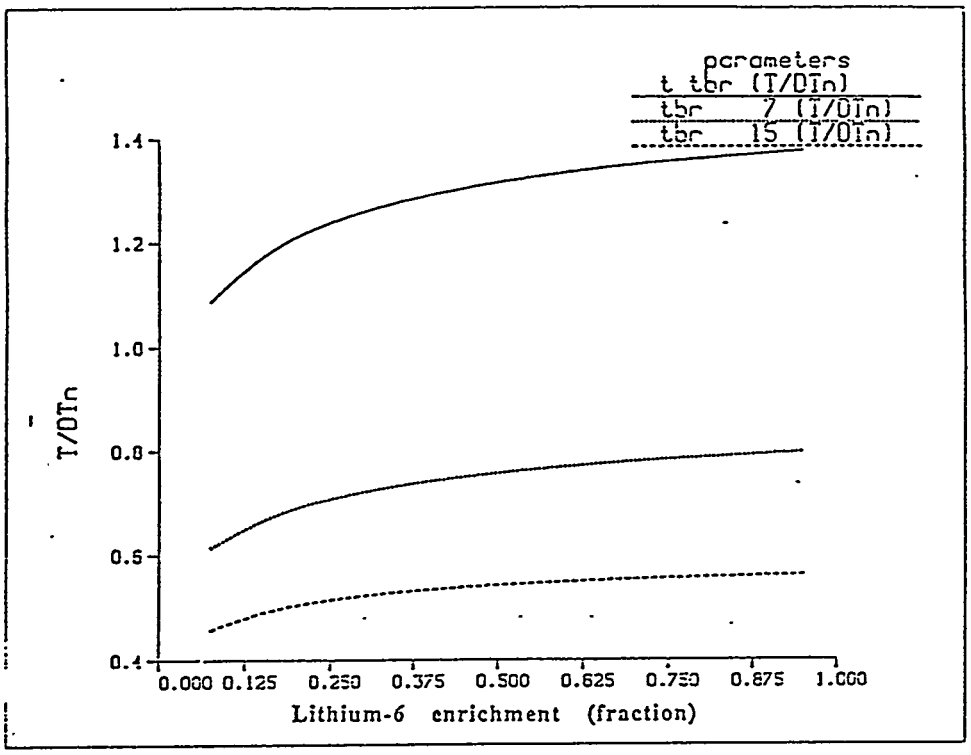

Fig. 6-3. Local tritium breeding ratio at the midplane as a function of the lithium-6 enrichment.

[4] Y. Gohar et al., "First Wall/Blanket/Shield Design and Optimization System," International Symposium on Fusion Nuclear Technology, Tokyo, Japan, April 10-15, 1988.

[5] R.D. O'Dell, F.W. Brinkley, and D.R. Marr, "User's Manual for ONEDANT: A Code Package for One-Dimensional Diffusion-Accelerated, Neutral-Particle Transport, Los Alamos National Laboratory Report LA-9184-M (February 1982).

[6] Y. Gohar "A Coupled 46-Neutron, 21 Gamma Ray Multigroup Nuclear Data Library for Fusion Analysis Based on ENDF/B-V," Argonne National Laboratory Report (to be published).

[7] R.W. Roussin et al., "VITAMIN-E: A Coupled 174 Neutron, 38 Gamma Ray Multigroup Cross-Section Library for Deriving Application Dependent Working Libraries for Radiation Transport Calculations," Oak Ridge National Laboratory Report ORNL/RSIC-XX (August 1984).

[8] Y. Farawila, Y. Gohar, and C. Maynard, "KAOS/LIB-V: A Library of Nuclear Response Functions Generated by KAOS-V Code from ENDF/B-V, Argonne National Laboratory Report ANL/FPP/TM-241 (April 1989).

6.5 Three-Dimensional Neutronics Analysis

Three-dimensional neutronics calculations have been performed for the solid-breeder water-cooled blanket design with sintered product materials to determine the overall tritium breeding ratio as well as tritium breeding and nuclear heating in the different components of the blanket. The continuous energy coupled neutron-gamma Monte Carlo Code MCNP, version 3B, [1] has been used with cross section data based on the ENDF/B-V evaluation. The outboard blanket is divided into 48 equally-wide modules. Three modules fit between adjacent TF coil center lines. Of the three, the central module is split into top and bottom modules by the 1.07 m × 3.4 m radial ports. The inboard blanket is divided into 32 identical modules with each module being divided into three electrically insulated segments. Because of symmetry, only 1/32 of the reactor was modeled with two vertical reflecting surfaces at azimuthal angles of 0° and 11.25°. The model includes one inboard blanket module, one outboard side blanket module, one-half of an outboard top central blanket module and one-half of an outboard bottom central blanket module.

The blanket modules were modeled in detail with the poloidally varying radial builds required for breeder temperature control. The sidewalls and detailed layered configuration of the FW and blanket are included in the model. The sidewalls are 1.4 cm thick in the outboard modules and 1 cm thick in the inboard modules. The vertical extents of the inboard and outboard blankets are -3.4 to 3.4 m and -4.8 to 4.3 m, respectively. The total inboard FW and blanket thickness increases from 11.6 cm at the midplane to 21.5 cm at the top. The total outboard FW and blanket thickness varies from 26.5 cm at the midplane to 69.2 cm at the top. The calculations have been performed for the U.S. design that utilizes a single Li_2O breeder plate in the inboard blanket and two breeder plates in the outboard blanket. The lithium in the Li_2O breeder is enriched to 95% ^6Li and the beryllium density factor ranges from 0.65 to 0.85.

The 2-cm-thick assembly gaps between blanket modules were included in the model. The copper stabilizer loops used in the outboard region were modeled. The thickness of the Cu shell is 0.5 cm and covers both sides of each outboard blanket module as well as the front of the blanket at the top and bottom with vertical distances beyond 2.7 m from the reactor midplane. The FW configuration in the inboard, outboard, and divertor regions was

modeled in detail. The divertor plates and vacuum pumping ducts in the lower divertor region were included in the model. The ITER divertor plate design consisting of tungsten, niobium, and water, was used. Sixteen standard 1.07 m × 3.4 m radial ports were used at the middle of the outboard region. These ports are utilized for testing, plasma heating, startup and maintenance. A typical Li/V blanket was used in the ports to represent a blanket test module. The test section used in the model is surrounded by a 25 cm thick steel buffer zone.

Figures 6-4 and 6-5 show vertical cross sections of the geometrical model used through central and side outboard blanket modules, respectively. A horizontal cross section at the reactor midplane is given in Fig. 6-6 with cross sections showing the details of the inboard, outboard side, and outboard central blanket modules given in Figs. 6-7, 6-8, and 6-9. The neutron source was sampled from the D-shaped toroidal plasma zone whose boundary was determined from the reference ITER plasma parameters. The plasma has a 6 m major radius, 2.15 m minor radius, 1.98 elongation, 0.383 triangularity, and 0.255 m magnetic axis shift. The location of the neutron source in the plasma zone was determined by sampling from the reference ITER source profile. The results were normalized to the technology phase fusion power of 860 MW. Several variance reduction techniques, including geometry splitting and weight cutoff with Russian roulette, were utilized to improve the accuracy of the calculations. Thirty thousand histories were used in the calculation yielding statistical uncertainties less than 0.8% in the calculated overall TBR and nuclear heating.

Table 6-6 gives the tritium breeding results in the different blanket zones. Numbers in parentheses represent the relative statistical error from the Monte Carlo calculation. The results indicate that the overall TBR is 0.81 with 15% of it contributed by the inboard blanket. The effect of using different materials in the radial ports on tritium breeding has been investigated by performing the 3-D calculation with 35% steel, 10% H_2O, 5% Cu, and 50% void in the outboard radial port. This is representative of a LH or RF port. The overall TBR calculated in this case is 0.802 implying that tritium breeding in the permanent breeding blanket is not sensitive to the material used in the ports. It is interesting to note that coupling the 1-D toroidal geometry results with coverage fractions of the different breeding

zones, the overall TBR was estimated to be 0.84 which is only 3.7% different from the value obtained from the detailed 3-D calculation. In addition, the 1-D analysis for the ITER common blanket design with two size breeder pebble bed resulted in 3.2% lower overall TBR compared to the sintered-product design implying that the 3-D calculation for the common blanket design is expected to yield 0.78 for net TBR. Furthermore, the 1-D analysis indicated that the overall TBR increases by 9.6% if three breeder plates are utilized in the outboard blanket in the zone $-2.7\ m < z < 2.7\ m$. Therefore, the overall TBR from the 3-D calculations is expected to increase to 0.89 and 0.86 with three breeder plates for the U.S. and common designs, respectively. Tritium breeding in each test module was determined to be 0.003 per DT fusion. Hence, if tritium bred in the 8 test modules is accounted for, the overall TBR will increase by 0.024. Table 6-7 gives the breakdown of nuclear heating in the different reactor regions. The total nuclear heating in the reactor excluding test modules is 996 MW, for the technology phase implying that the overall energy multiplication is 1.45. Adding the surface heating implies that the total reactor thermal power is 1150 MW.

References

[1] "MCNP - A General Monte Carlo Code for Neutron and Photon Transport, Version 3A," LA-7396-M, Rev. 2, Los Alamos National Laboratory (1986) and J. Briesmeister, "MCNP3B Newsletter," X-6-JFB-88-292, Los Alamos National Laboratory (July 1988).

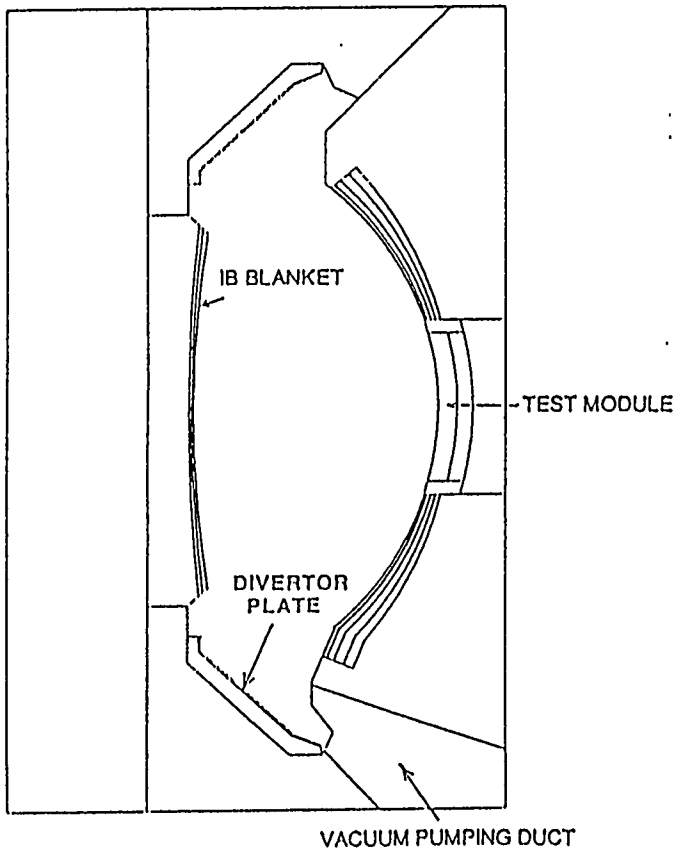

Figure 6-4. Vertical cross section through a central module.

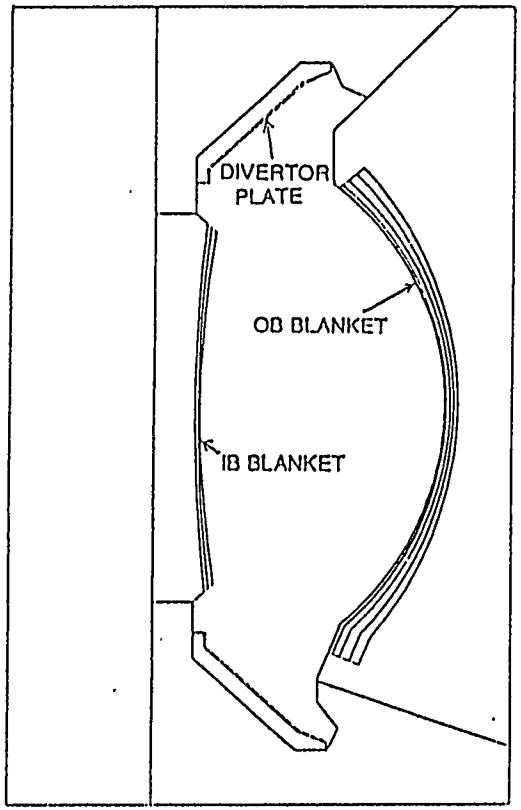

Figure 6-5. Vertical cross section through a side module.

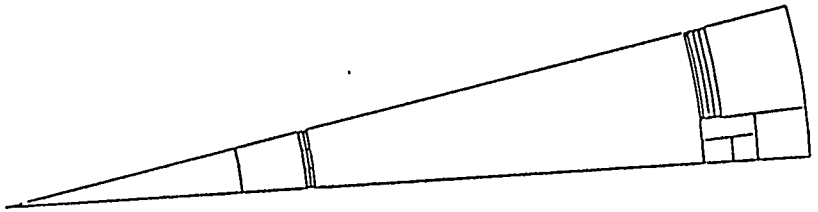

Figure 6-6. Horizontal cross section at midplane.

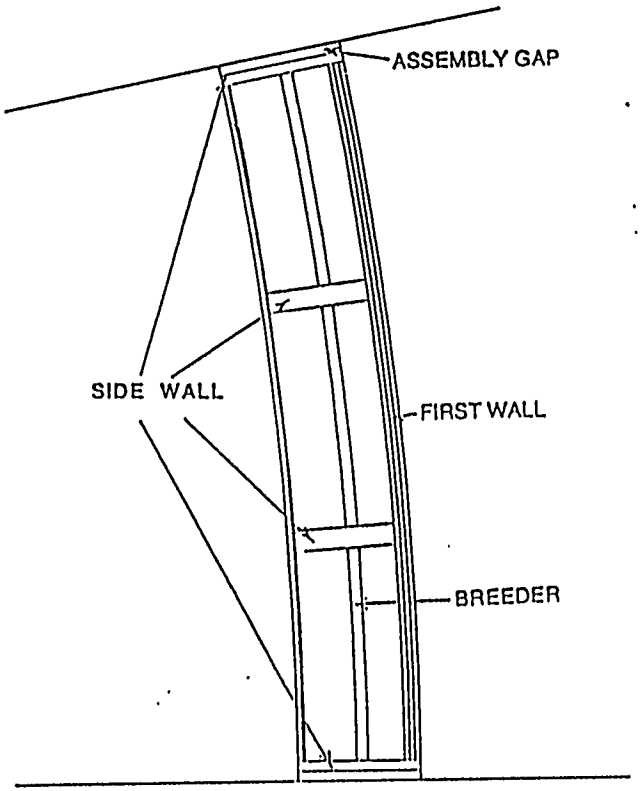

Figure 6-7. Horizontal cross section showing IB module details.

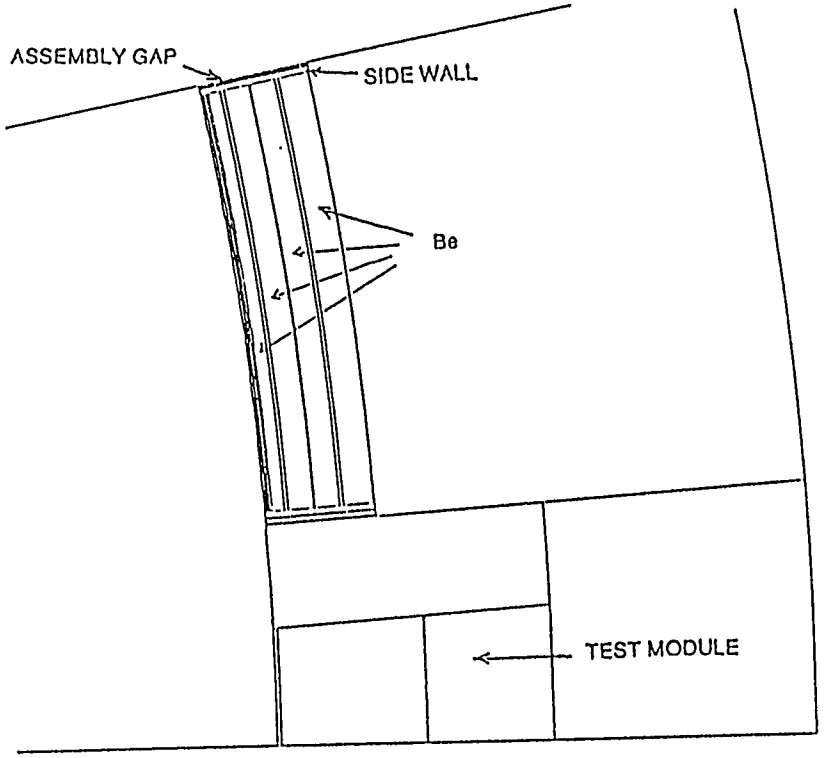

Figure 6-8. Horizontal cross section showing OB side module details.

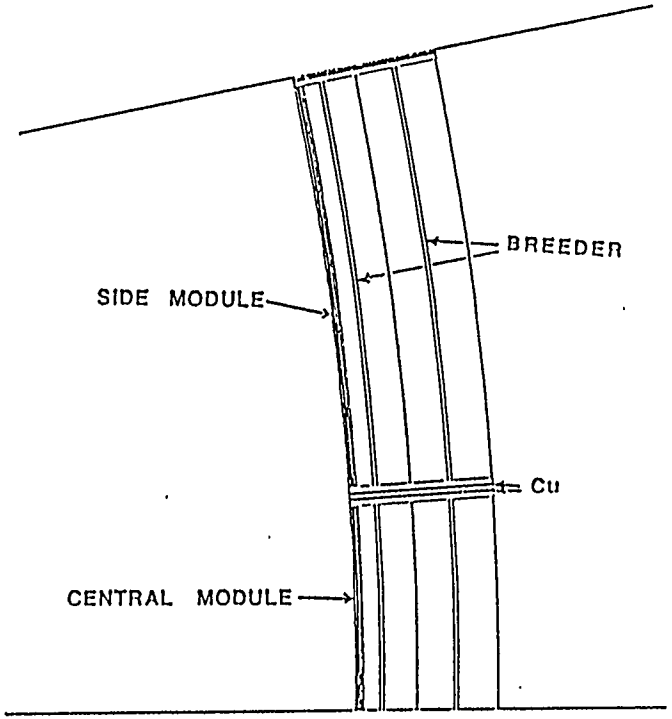

Figure 6-9. Horizontal cross section with OB side and central module details.

Table 6-6.
Tritium Breeding (Tritons per DT Fusion) in the Different Breeder Zones of the Sintered-Product Solid Breeder Blanket

Inboard Blanket		0.116 (0.021)*
Outboard Blanket		
Side Module:		
	Front breeder plate	0.331 (0.012)
	Back breeder plate	0.206 (0.017)
	Total	0.537 (0.010)
Top Central Module:		
	Front breeder plate	0.047 (0.032)
	Back breeder plate	0.028 (0.046)
	Total breeder plate	0.075 (0.026)
Bottom Central Module:		
	Front breeder plate	0.053 (0.031)
	Back breeder plate	0.028 (0.044)
	Total	0.081 (0.024)
Reactor Total		0.809 (0.008)

*Relative error

Table 6-7.
Nuclear Heating in the Different Reactor Regions (Technology Phase)

Region	Nuclear Heating (MeV/DT Fusion)	Nuclear Power (MW)
Divertor		
Divertor plates	0.425 (.03)*	21
Shield	3.201 (.02)	156
Total	3.626 (.02)	177
Inboard		
FW/Blanket	2.018 (.01)	99
Shield	1.642 (.03)	80
Total	3.660 (.01)	179
Outboard		
FW/Blanket	10.475 (.01)	512
Shield	2.617 (.02)	128
Total	13.092 (.02)	640
Reactor Total	20.378 (.007)	996

*Relative error

6.6 Estimate of Overall Tritium Breeding Ratio

Several one-dimensional toroidal cylindrical geometry calculations have been performed to determine tritium breeding in both the inboard and outboard blankets. In these calculations, the neutronics coupling (reflection and spectral effects) between the inboard and outboard blankets are taken into account. The overall TBR has been estimated by coupling the one-dimensional results with the coverage fractions of the different blanket regions. The coverage fraction corresponds to the solid angle fraction subtended by the particular region as seen by the source neutrons in the plasma and represents the fraction of source neutrons going directly to this region. The NEWLIT code [2] was used to determine the coverage fractions for the different reactor regions taking into account the actual source profile in the D-shaped plasma.

The inboard blanket extends vertically from z = -3.4 m to z = 3.4 m. The outboard side blanket module extends from z = -4.8 m to z = 4.4 m while the outboard top central blanket module extends from z = 1.7 m to z = 4.1 m and the outboard bottom central blanket module extends from z = -4.8 m to z = -1.7 m. The coverage fractions for the inboard and outboard regions have been determined to be 16.4% and 68.1%, respectively. Sixteen penetrations are used in the outboard region at the midplane. All penetrations are 3.4 m high. It is assumed that eight 1.07 m wide ports will be utilized for blanket and material testing in ITER with 4.9% of the source neutrons going directly to them. Other penetrations include two 1.3 m wide maintenance ports, one 1.07 m wide EC startup port and two 1.07 m wide LH ports. The coverage fractions for these three types of ports are 1.5%, 0.6% and 1.2%, respectively. In addition, three NBI ducts are used in ITER. Each NBI duct is 0.8 m wide and tangent to a 6.2 m radius circle implying that the port is 1.2 m wide at the first wall. The coverage fraction for the three NBI ports is 2.1%. The total coverage fraction of the 16 ports in the outboard region is 10.3%. The actual coverage fraction of the outboard blanket should be modified by subtracting the coverage fraction of the penetrations. This leads to a coverage fraction of 57.8% for the outboard blanket.

The radial build for the solid breeder blanket varies poloidally according to the poloidal neutron wall loading variation in order to maintain constant minimum breeder temperature in the poloidal direction. The

neutronics calculations have been performed for the blanket configurations at different poloidal locations. The thickness of the Be layer was assumed to vary linearly with the wall loading. The effect of the 0.5 cm thick copper stabilizer loops used at the top and bottom of the outboard blanket has been taken into account by performing the neutronics calculations with the Cu in the outboard region at distances more than 2.7 m vertically away from the reactor midplane. The results of the toroidal cylindrical geometry neutronics calculations are given in Table 6-8 for the first U.S. blanket concept with a single Li_2O zone in the inboard blanket and two breeder zones in the outboard blanket. The Li in the Li_2O breeder is enriched to 95% ^6Li. Taking into account the poloidal variation of the neutron wall loading and radial build, the poloidally averaged TBR was determined to be 0.21 for the inboard region and 1.003 for the outboard region.

Table 6-8.
Results of Toroidal Cylindrical Geometry Calculations for the Sintered-Product Blanket Design

Region	Z (m)	Wall Loading (MW/m^2)	Cu Thickness (cm)	TBR
Inboard				
	0	0.884	0	0.206
	3.4	0.325	0	0.217
Outboard				
	0	1.204	0	0.948
	2.7	0.958	0	1.070
	2.7	0.958	0.5	0.991
	4.3	0.600	0.5	0.966

In the one-dimensional toroidal cylindrical geometry model, 21.2% of the source neutrons go directly to the inboard region with the rest going to the outboard region. The results of the toroidal calculations have to be modified by the actual coverage of the inboard and outboard regions of ITER to determine the contribution to the net TBR. In addition, space taken by the assembly gaps and side walls amounting to 11% of the inboard region and 4.4% of the outboard region should be taken into account. Figure 6-10 illustrates

the estimation of the overall TBR for the sintered-product solid breeder blanket. The overall TBR is estimated to be 0.84 with 0.14 contributed from the inboard blanket modules. The overall TBR for the common ITER blanket design with a two-size breeder pebble bed is estimated to be 0.81 as indicated in Fig. 6-11.

An alternate blanket design that utilizes three breeder plates in the middle of the outboard blanket (-2.7 m < z < 2.7 m) has been considered. In this design, two breeder plates are used in the outboard blanket regions behind the Cu stabilizer shells. The impact on tritium breeding has been assessed. The poloidally-averaged outboard TBR determined from the one-dimensional toroidal calculations for the U.S. design is 1.113 and the overall TBR is 0.92. This implies that using three breeder plates instead of two in the middle of the outboard region results in 9.6% enhancement in TBR. The impact of the Cu stabilizer shells used in the outboard region has been investigated by performing the calculations for the blanket configuration with two breeder zones without the copper. This resulted in an overall TBR of 0.87 implying that the Cu stabilizer loops reduce the overall TBR by 3.4%. The overall TBR increases to 0.95 for the three breeder plate design if the Cu stabilizer loops are not used. It is, therefore, concluded that the overall TBR is in the range between 0.81 and 0.95 depending on the breeder form (pebble bed or sintered product), whether two or three breeder zones are used in the outboard blanket and whether Cu stabilizer loops are utilized.

References

[1] R. O'Dell et al., "User's Manual for ONEDANT: A Code Package for One-Dimensional, Diffusion Accelerated, Neutral Particle Transport," LA-9184-M, Los Alamos National Laboratory (1982).

[2] H. Attaya and M. Sawan, "NEWLIT - A General Code for Neutron Wall Loading Distribution in Toroidal Reactors," Fusion Technology, 8/1,608 (1985).

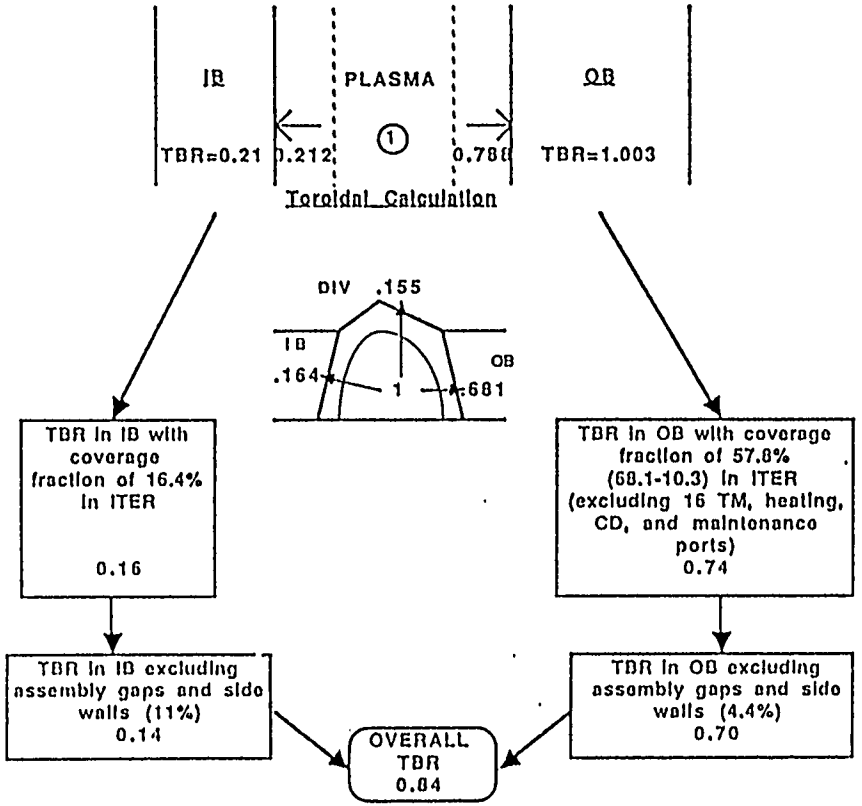

Figure 6-10. Estimation of overall TBR for the U.S. blanket design with two OB breeder plates.

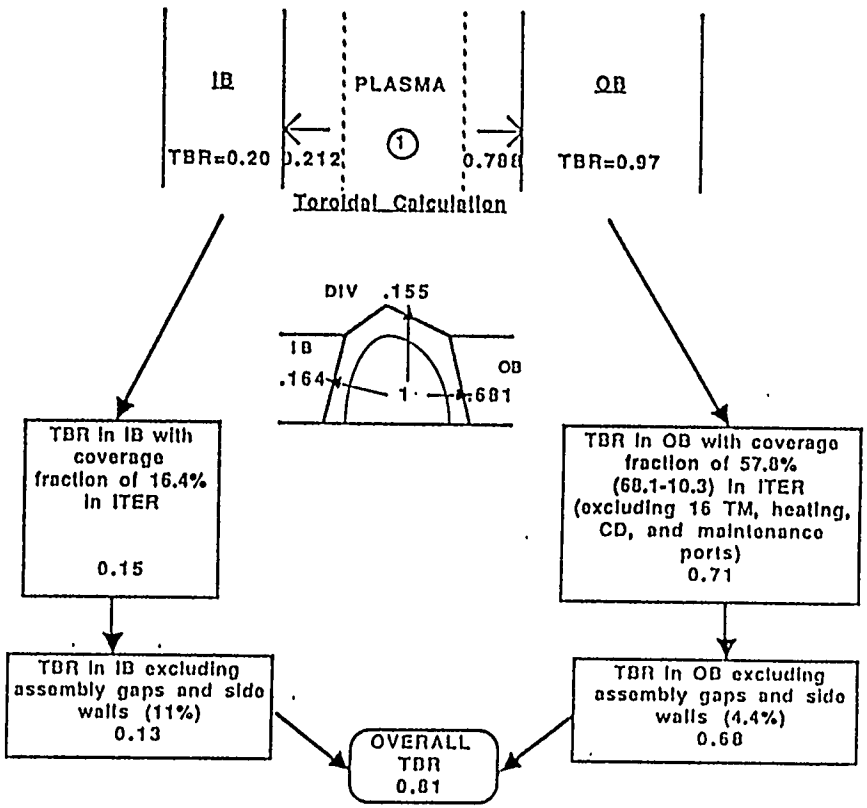

Figure 6-11. Estimation of overall TBR for the common blanket design with two OB pebble bed breeder plates.

7.0 THERMAL ANALYSES

7.1 Introduction

The thermal analysis is always performed for each blanket configuration after the neutronics analysis to insure the appropriate temperature profiles of the different materials. In all the blanket configurations, the zone dimensions and material density factors are defined to get 450°C as a minimum temperature for the solid breeder material for the technology phase. This choice results in a satisfactory tritium inventory for the physics and the technology phases. Also, it limits the maximum temperature at the clad beryllium interface to <430°C. Which results in a steel reaction layer of 0.03 mm at the ITER end-of-life.

This section gives the calculational procedure and the results of the thermal analyses. Steady state analyses are presented for the three blanket concepts. Transient analyses were performed for the first concept in detail, which is required for the tritium inventory analyses. Studies are given to show the blanket capability to accommodate changes in the neutron wall loading. The change in the blanket performance as a function of the different blanket parameters is analyzed in detail. The analyses include gap conductance, breeder zone thickness, breeder clad thickness, lithium-6 enrichment, and beryllium density factor.

7.2 Calculational Methodology

The BSDOS system gets the zone dimensions and the radial distribution of the nuclear heating over a fine mesh from the neutronics analysis. The internal size is about 0.1 to 0.2 cm for the breeder zones and ~0.5 cm for the beryllium zones. BSDOS pass these data to the three-dimensional mesh generator for modeling nonlinear systems, INGRID [1], to model the blanket module. Geometrical data, coolant conditions, and gap conductance model are included in the modeling process. INGRID generates a three-dimensional finite element model for the blanket module. The three-dimensional finite element heat transfer code TOPAZ3d [2] uses this model to calculate the temperature distribution profiles and the change in the coolant conditions. The physical properties of the different materials are evaluated at each node as a function of the temperature and the material density factor.

The blanket thermal analyses assume the value of the surface heat flux is 0.25 the neutron wall loading. The coolant inlet temperature is 60°C and the water pressure is 15 atm. The calculational model uses a poloidal cross section with the plasma minor radius. The coolant flow direction is included in the model. In the transient analyses, the fusion power during the start up and the shut down for the pulse is assumed linear. Also, the coolant is flowing continuously during the dwell time. The pulse parameters for the transient analyses are shown in Fig. 7-1.

7.3 Steady State and Transient Thermal Analyses

For the first design concept with sintered product, the neutronics and the thermal calculations are iterated. The purpose of this iteration is to get the minimum temperature of the solid breeder at 450°C for the technology phase. The results from these analyses give the radial build and the temperature distribution of the blanket. The neutronics section shows the radial build of the blanket at six poloidal locations for the first concept. The corresponding extreme temperatures are given in Table 7-1 for the outboard blanket. The minimum solid breeder temperatures for the different radial builds are 450 ± 5°C except for the outboard blanket at z = 2.7 m. The minimum solid breeder temperatures at this location are 484 and 476°C for the first and second breeder zones, respectively. At this location the cooper stabilizer replaces 0.5 cm of the beryllium material behind the first wall. The minimum solid breeder temperatures with the copper stabilizer are 455 and 452°C for the first and second breeder zone, respective
y. At this poloidal point, the calculations assume no change in the poloidal direction for the zone materials. Still, copper will be contacting beryllium in the poloidal direction. This results in minimum solid breeder temperatures in the range of 455-484°C and 449-465°C for the first and second breeder zones, respectively. The extreme temperatures of the inboard blanket at the midplane and the end of the blanket are given in Table 7-2. The solid breeder material in this concept uses only about 90°C of the 600°C temperature window (400 to 1000°C) for the lithium oxide.

In the physics phase, the reactor fusion power is 1100 instead of 860 MW for the technology phase, and carbon tiles are used for first wall protection. Also, the flat DT burn time is relatively short. It is 400 s instead of

2290 s for the technology phase. The neutronics and the thermal analyses are repeated for the physics phase. The extreme temperatures of the blanket materials assuming a continuous DT burn with the physics power level are shown in Tables 7-3 and 7-4. The minimum breeder temperatures are in the range 499 to 509°C except at z = 2.7 m as explained before. However, the physics pulse is short, which requires thermal transient analyses to provide realistic temperature profiles for the solid breeder material. Figures 7-2 through 7-5 give the temperature history of the solid breeder zones using a 1-mm interval for the outboard blanket. At the midplane section, the solid breeder temperatures reach very close to saturation during the second pulse, while the end of the blanket requires 3 to 10 pulses to reach saturation values. Also, the temperature history of the inboard solid breeder zone is shown in Figs. 7-6 and 7-7.

The steady state extreme temperatures for the common ITER blanket design are given in Table 7-5 for the technology phase. The lithium oxide with single size pebbles uses 222°C of the temperature window relative to 84°C for the lithium oxide blocks. The use of a large fraction of the temperature window of the solid breeder diminishes the blanket capability to accommodate power variation. To reduce this fraction, the thermal conductivity of the lithium oxide pebbles is improved by using pebbles with two sizes. This reduces the used fraction of the temperature window to 143°C. Also, it improves the tritium breeding capability as shown in the neutronics section. This leads to the recommendation of the use of two sizes of the lithium oxide pebbles for the common ITER design. The same thermal performance is obtained in the physics phase as shown in Table 7-6. The transient analyses show that the solid breeder temperatures reach very close to saturation values within two pulses at the midplane as shown in Fig 7-8 through 7-11. This performance insures a low tritium inventory similar to the lithium oxide blocks.

The extreme temperatures of the third blanket concept are given in Table 7-7. The lithium oxide breeder uses the same fraction of the temperature window as the first concept. However, the response time to reach the saturation temperature during the physics phase is less compared to the other two concepts because this blanket has less thickness.

7.4 Blanket Performance Analyses

Several studies were carried out to improve the blanket performance including the power variation accommodation. The other objective was to define the blanket performance as a function of the different design parameters. The main parameters for these studies are the number of the breeder zones, the thickness of the breeder zone, the lithium-6 enrichment, the breeder clad thickness, the fabrication tolerance in the beryllium density factor, and the gap conductance.

Blanket Configuration with Three Breeder Zones: The extreme temperatures for the first blanket concept with the three breeder zones during the technology phase are given in Table 7-8. The minimum temperatures of the three breeder plates are 452, 454, and 454. Similar to the design with two breeder zones, the solid breeder uses only 84°C of the temperature window. These results insure a satisfactory tritium inventory and power variation accommodation. Detail analyses on both points are given in this report.

Power Variation Accommodation: The extreme temperatures of the different materials in the outboard blanket at the midplane under a wide range of the neutron wall loading are shown in Figs. 7-12 through 7-14. This section of the blanket is designed to operate at 1.2 MW/m^2 neutron wall loading during the technology phase. For continuous operation, the lithium oxide material in this design has to operate within the temperature range of 350 to 1000°C. The upper end of this range is reached at a 2.1 MW/m^2 neutron wall loading as shown in Fig 7-12. The low end of this temperature range insures a low tritium inventory. However, operating for a full power day at low temperature will result in a tritium inventory of less than 130 g. So from the solid breeder point of view, a continuous operation in the range of 0.94 to 2.1 MW/m^2 is acceptable during the technology phase.

The temperature limit of the steel clad is set based on the thickness of the reaction layer at the end-of-life. For example, the thickness of the reaction layer is 0.01 mm at the end of a full power day at 2.1 MW/m^2 relative to 0.1 mm expected at the end-of-life. So, the steel clad does not restrict the blanket operation.

The beryllium temperature limit is set to avoid helium-induced swelling. During the physics phase the helium concentration in the beryllium material is

very low, which allows the beryllium to operate at higher temperatures. As the beryllium accumulates neutron fluence, the temperature limit approaches the design limit of less than 700°C. This limit is corresponding to 1.88 MW/m^2 or 1350 MW of fusion power during the technology phase at the end-of-life. Also, the beryllium material in ITER is expected to show less swelling because of the low density factor (0.65 to 0.85) used for the design. The beryllium swelling data base is only for beryllium metal (at 1.0 density factor).

The blanket steel structure, the back wall of the first wall and the side walls are at less than the 400°C temperature limit because of the coolant conditions. This discussion shows that the blanket can operate over a wide range of neutron wall loading. It is expected that the other reactor components such as the divertor or the first wall will impose more restrictive limit on the upper end of the allowable range. Similar analyses were done for the physics phase where the same conclusion was reached.

The same analyses were performed for the common ITER design. Figures 7-15 and 7-16 show the extreme temperature of the lithium oxide pebbles as a function of the neutron wall loading. The maximum temperature of the lithium oxide material with one size pebbles reaches the 1000°C temperature limit at 1.89 neutron wall loading. The corresponding value for the lithium oxide material with two pebble sizes is 2.1 MW/m^2. Also, the tritium breeding ratio is higher for the two pebble sizes. Therefore, it is recommended to use two size pebbles for the common ITER blanket design.

The third blanket concept has sintered lithium oxide material for the breeder zones. It has the same thermal performance as the first concept.

In summary, the two forms of lithium oxide material, sintered product and two size pebbles in thin zones reach the 1000°C maximum temperature limit at 2.1 MW/m^2. At 1.2 MW/m^2, the maximum temperatures of the breeder material are 537 and 671 for the sintered product and the two size pebbles, respectively. The difference in the maximum temperature diminishes as the neutron wall loading increases. This difference does impact the thermo-mechanical performance of the breeder zone.

Breeder Plate Thickness: The breeder plate thicknesses of the first blanket concept are varied simultaneously from 0.4 to 1.6 cm to study the

impact on the blanket performance. Figure 7-17 shows the breeder extreme temperatures as a function of the breeder zone thicknesses. The maximum temperature of the first breeder zone increases sharply with thickness while its minimum temperature increases very slowly. This large increase reduces the breeder power variation accommodation capability. The second breeder zone is less sensitive. This leads to a recommendation of the use of the minimum breeder zone thickness, which has an adequate tritium breeding ratio. As discussed in the neutronics section, a 0.8-cm thick zone is adequate for this concept.

Lithium-6 Enrichment: The extreme temperatures of the solid breeder material as a function of the lithium-6 enrichment are shown in Fig. 7-18. The neutronics analyses in the previous section prove that a high lithium-6 enrichment is essential to get a high tritium breeding ratio. The breeder maximum temperatures in Fig. 7-18 have a very small increase of less than 10°C as the lithium-6 increase from 60 to 95%. Therefore, a 95% lithium-6 enrichment is used without penalizing the thermal performance of the blanket.

Breeder Clad Thickness: The extreme temperatures of the breeder and the steel clad are shown in Figs 7-19 and 7-20 as a function of the breeder clad thickness. The extreme temperatures of the breeder and clad materials of the first breeder zone increase about 16 and 20°C per mm of the clad thickness, respectively. The temperature distribution of the second breeder zone does not change with the clad thickness. The extreme temperatures of the clad material in the second breeder zone increase only by 3.6°C per mm. These results show that increasing the breeder clad thickness does not impact the blanket thermal performance or the tritium breeding ratio as shown in the neutronics section.

Beryllium Density Factor: The impact of the beryllium density factor on the thermal performance of the blanket is analyzed. The density factors of all the beryllium zones are varied ±0.05 from the design values. The calculated temperature distribution of the first breeding cell (beryllium, breeder, and clad materials) shows no impact due to this change as shown in Fig. 7-21. For the second breeder cell, the increase in the beryllium density factor decreases the minimum temperature of the solid breeder material. The decrease rate is 9°C per one percent change in the beryllium density factor. This effect is correlated to the change in the beryllium thermal conductivity.

Therefore, the blanket can accommodate more than 8% change in the density factor of all the beryllium zones from the design values.

Gap Conductance: Several analyses were performed to study the impact of the gap conductance on the thermal performance of the blanket. First, the gap conductance between the back plate of the first wall and the first beryllium zone is varied from 1000 to 10000 $W/m^2 \cdot K$ over the whole surface. The lower value of this range is corresponding to a gap thickness of 200 μm at this surface. Figure 7-22 shows the maximum temperatures of the different materials in the first breeder cell for this range of the gap conductance. For gaps of less than 100 μm, the maximum temperatures are less than the allowable for each material. Specifically, the maximum temperatures of the breeder and multiplier are 601 and 492°C respectively, for the 110 μm gap.

The impacts of a 50% uncertainty in the gap conductance value on the maximum temperature are shown in Fig. 7-23 for the first breeder cell. The gap conductance values are changed at the six interfaces of this cell simultaneously. In reality, if the gap conductance gets low on one side by lack of contact, it improves on the other. However for this assumed situation, the results show the maximum temperatures are 660 and 471 for the breeder and the multiplier materials, respectively. These temperatures are within the design guidelines for the blanket design.

References

[1] D.W. Stillman and J.D. Hallquist, "INGRID: A Three-Dimensional Mesh Generator for Modeling Nonlinear Systems," Lawrence Livermore National Laboratory Report, UCID-20506 (July 1985) also R. Rainsberger, Lawrence Livermore National Laboratory, private communication.

[2] A.B. Shapiro, "TOPAZ3D: A Three-Dimensional Finite Element Heat Transfer Code," Lawerence Livermore National Laboratory, UCID-20486, August 1985.

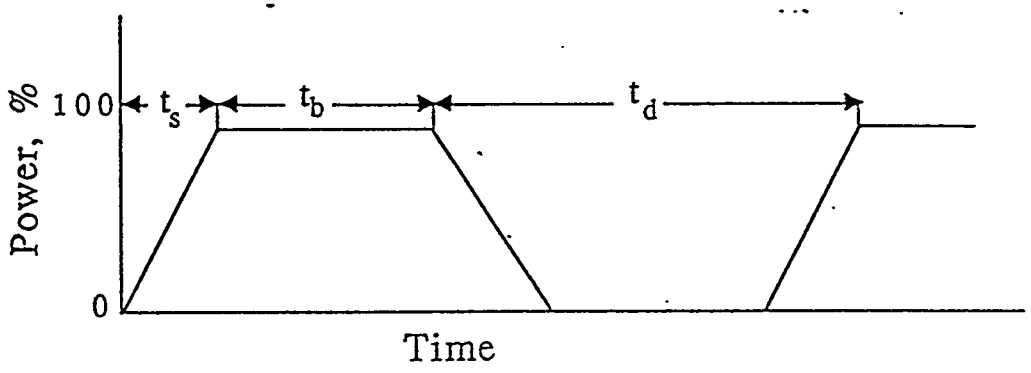

Parameter	Value, s
t_s	20
t_b	400 (physics), 2290 (Tech.)
t_d	200

Figure 7-1. Pulse parameters for the transient analyses of the blanket.

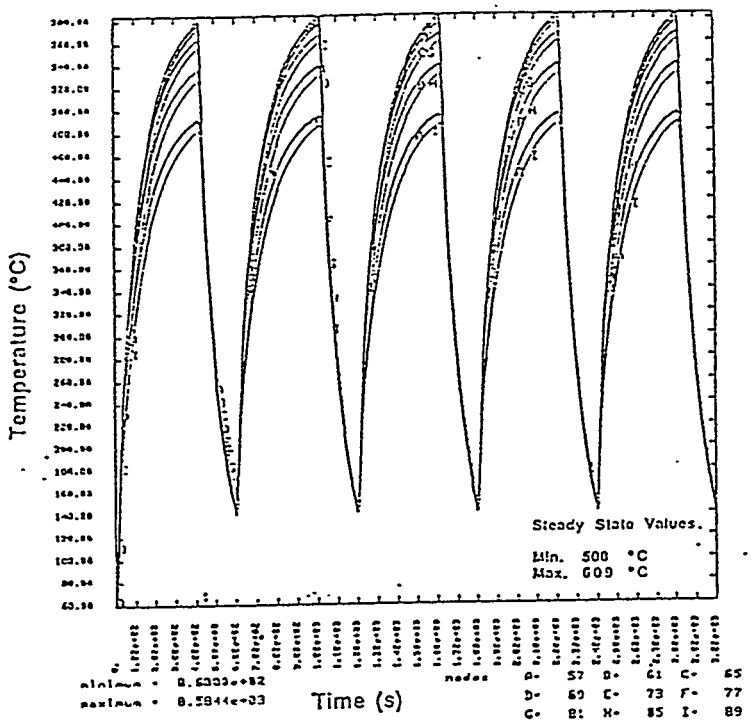

Fig. 7-2. Lowest temperature history of the first breeder zone during five physics pulses at the outboard midplane section.

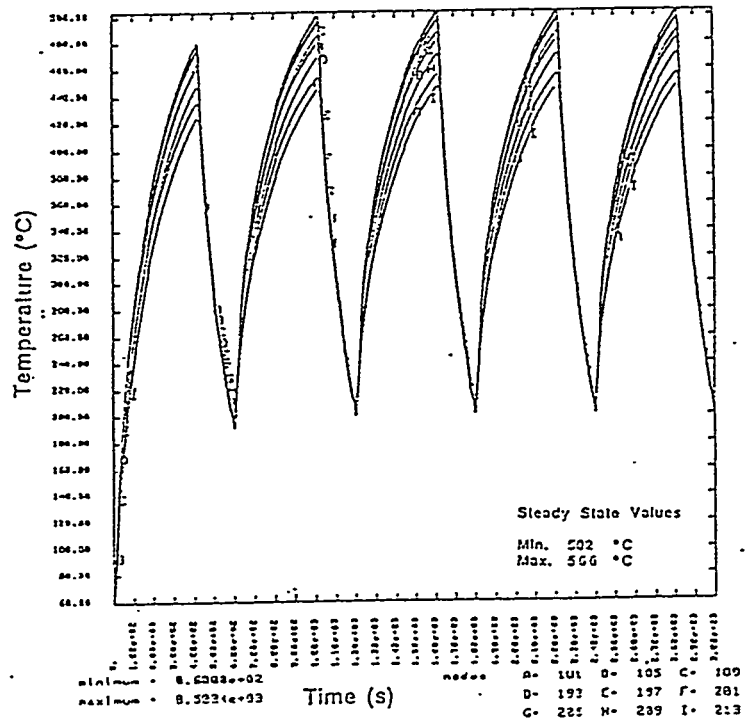

Fig. 7-3. Lowest temperature history of the second breeder zone during five physics pulses at the outboard midplane section.

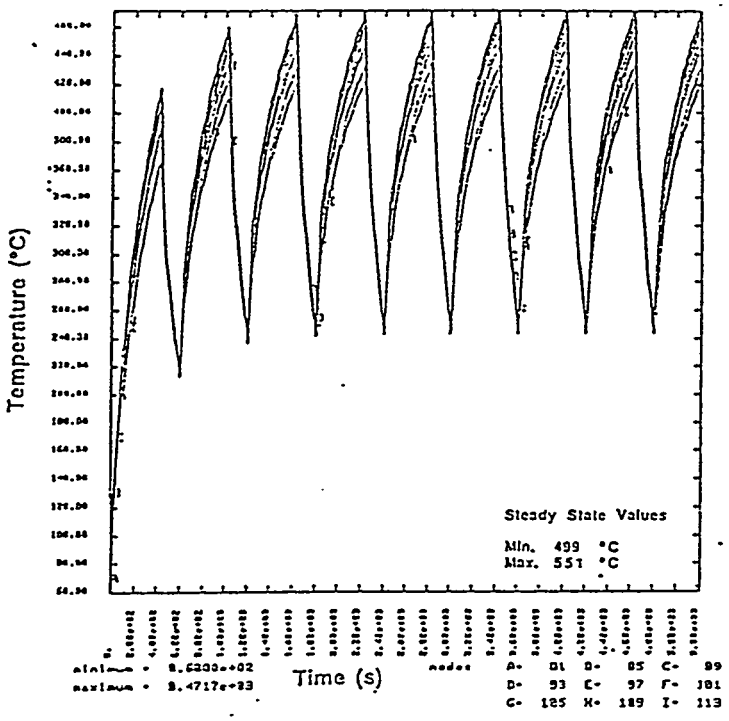

Fig. 7-4. Lowest temperature history of the first breeder zone during nine physics pulses at the outboard blanket at z = ±4.3 m.

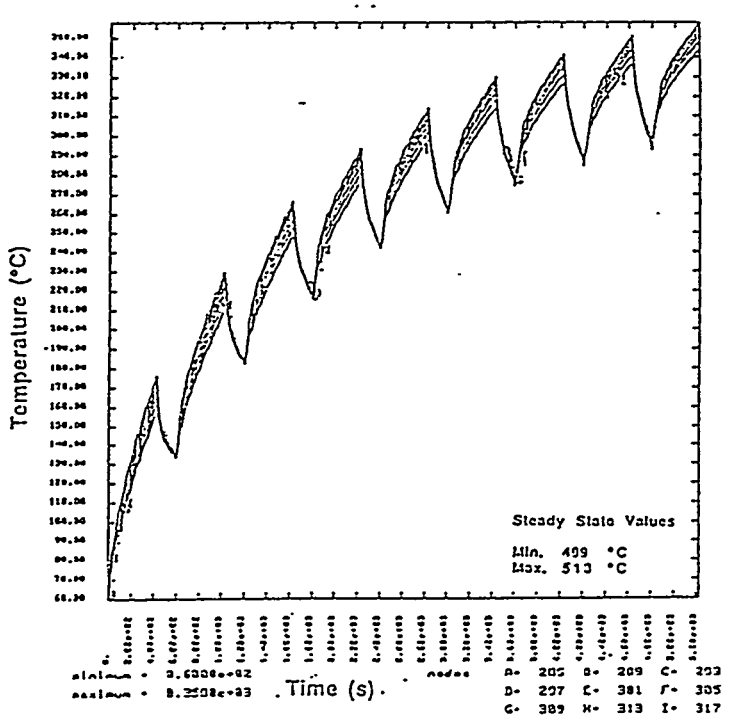

Fig. 7-5. Lowest temperature history of the second breeder zone during nine physics pulses at the outboard blanket at z = ±4.3 m.

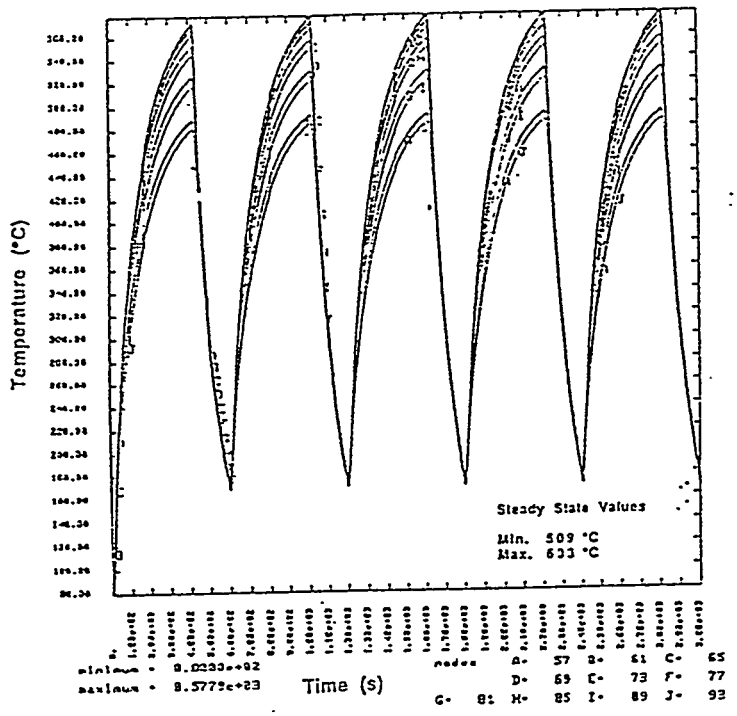

Fig. 7-6. Lowest temperature history of the inboard breeder plate during five physics pulses at the midplane section.

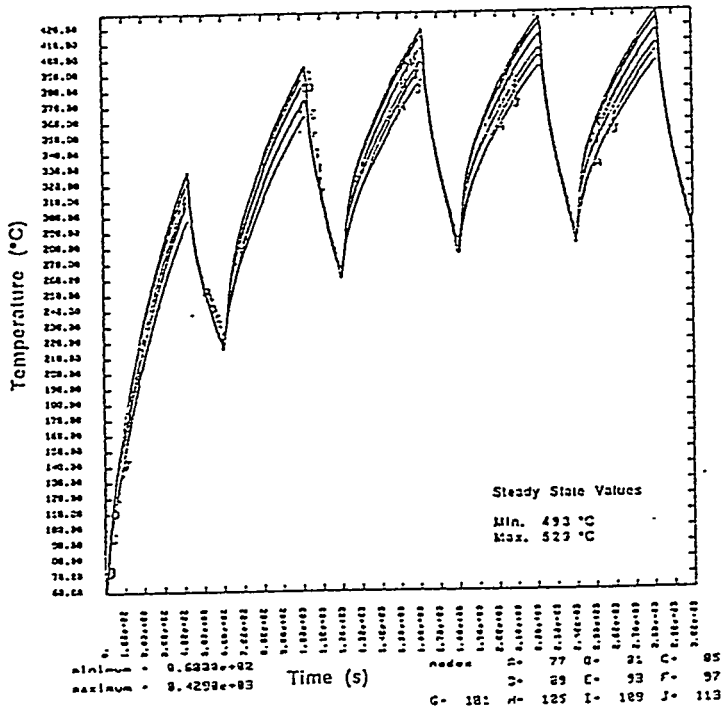

Fig. 7-7. Lowest temperature history of the inboard breeder plate during five physics pulses at the end of the blanket.

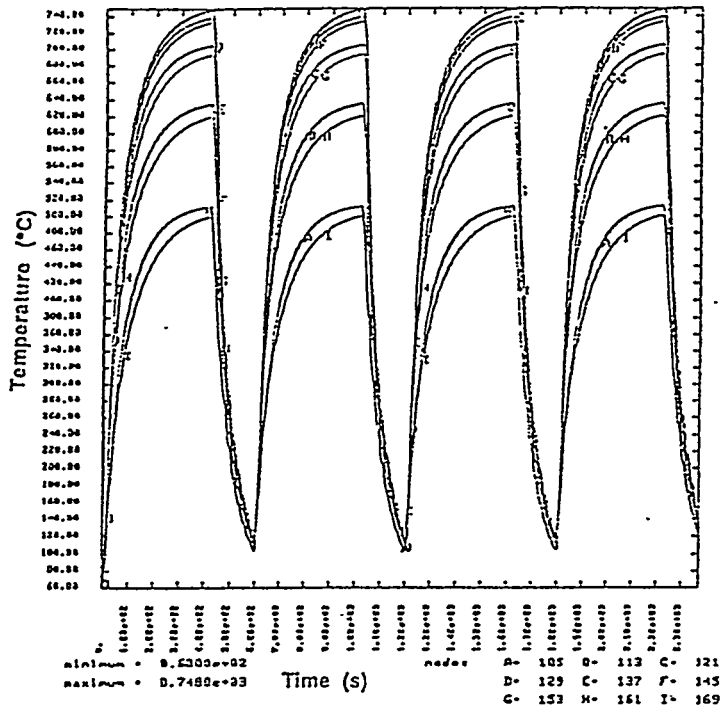

Fig. 7-8. Lowest temperature history of the first breeder zone during four physics pulses at the outboard midplane section for the single size lithium oxide pebbles.

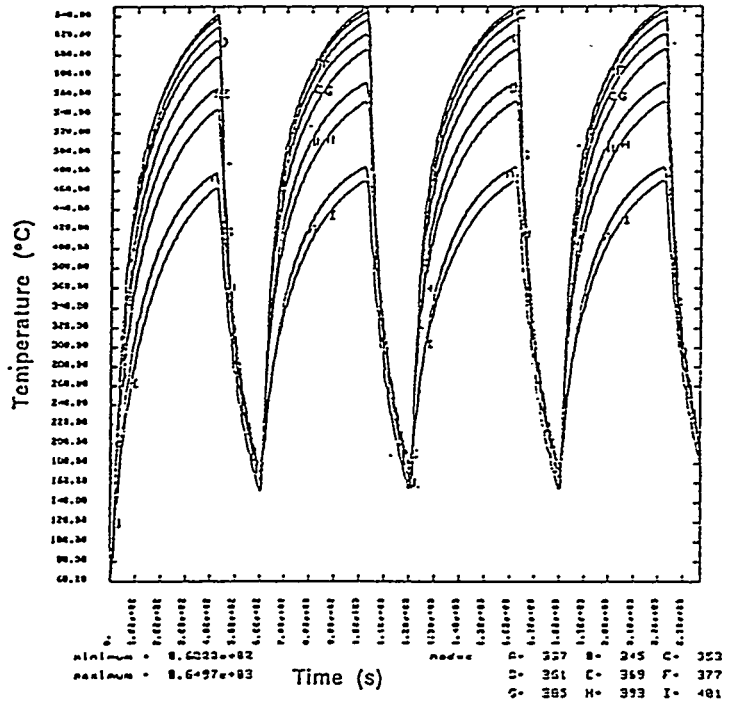

Fig. 7-9. Lowest temperature history of the second breeder zone during four physics pulses at the outboard midplane section for the single size lithium oxide pebbles.

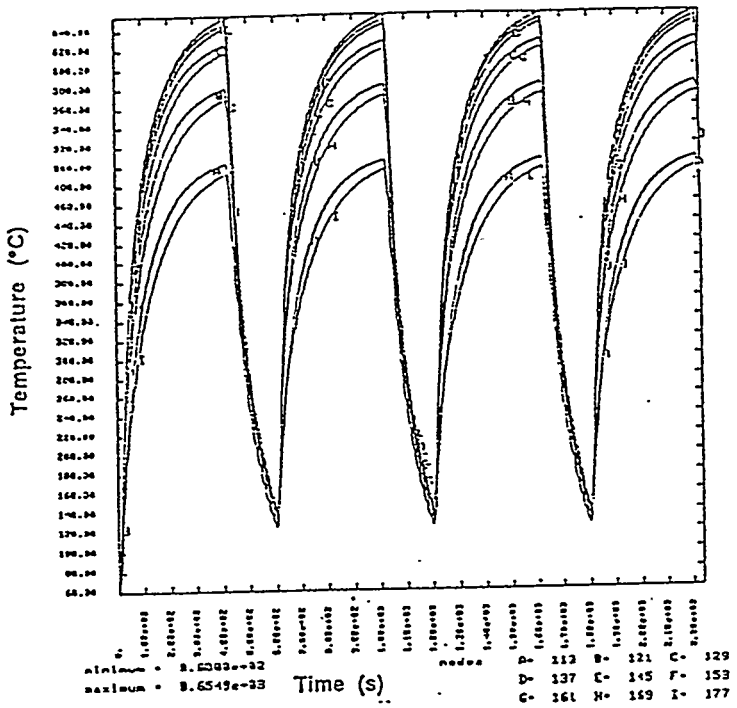

Fig. 7-10. Lowest temperature history of the first breeder zone during four physics pulses at the outboard midplane section for the two-size lithium oxide pebbles.

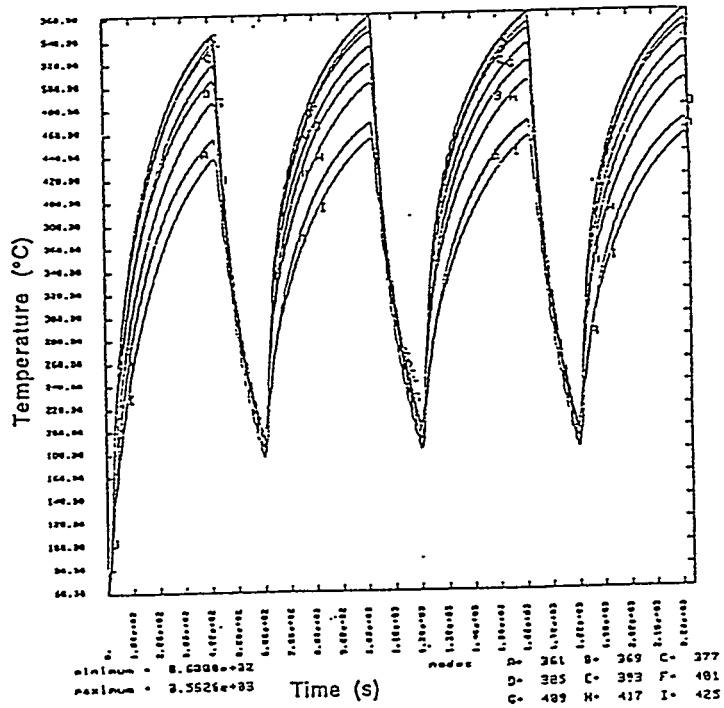

Fig. 7-11. Lowest temperature history of the second breeder zone during four physics pulses at the outboard midplane section for the two-size lithium oxide pebbles.

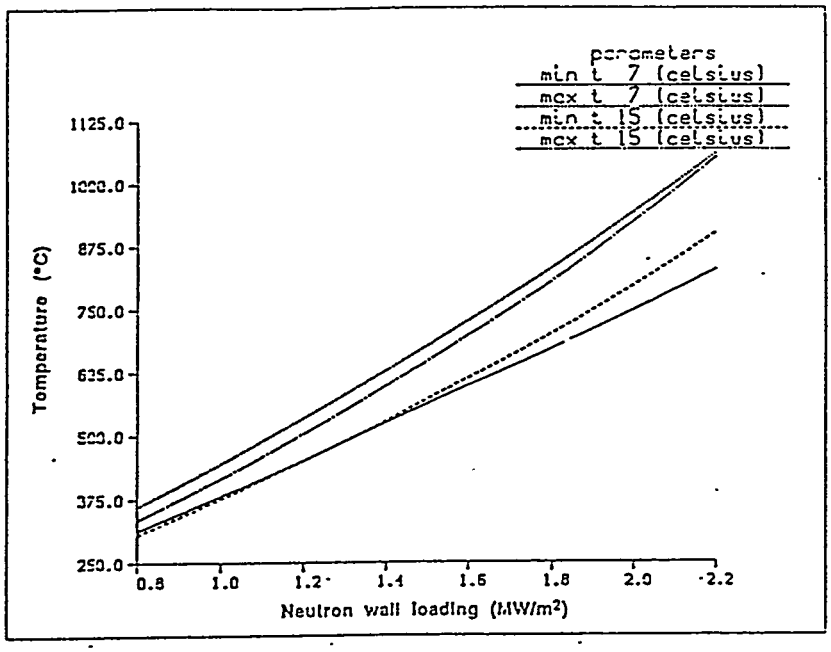

Fig. 7-12. Steady state extreme temperatures of the two breeder zones at the midplane as a function of the neutron wall loading during the technology phase.

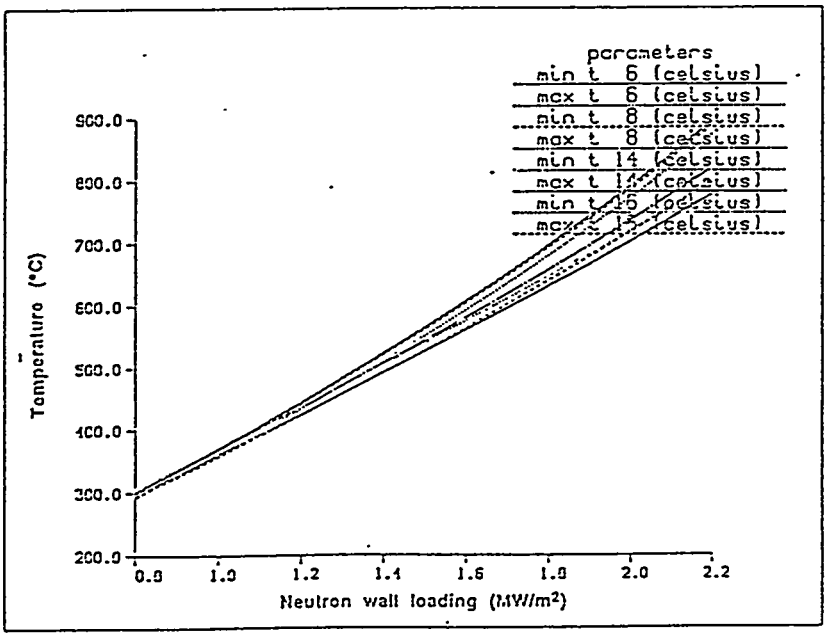

Fig. 7-13. Steady state extreme temperatures of the breeder clad at the midplane as a function of the neutron wall loading during the technology phase.

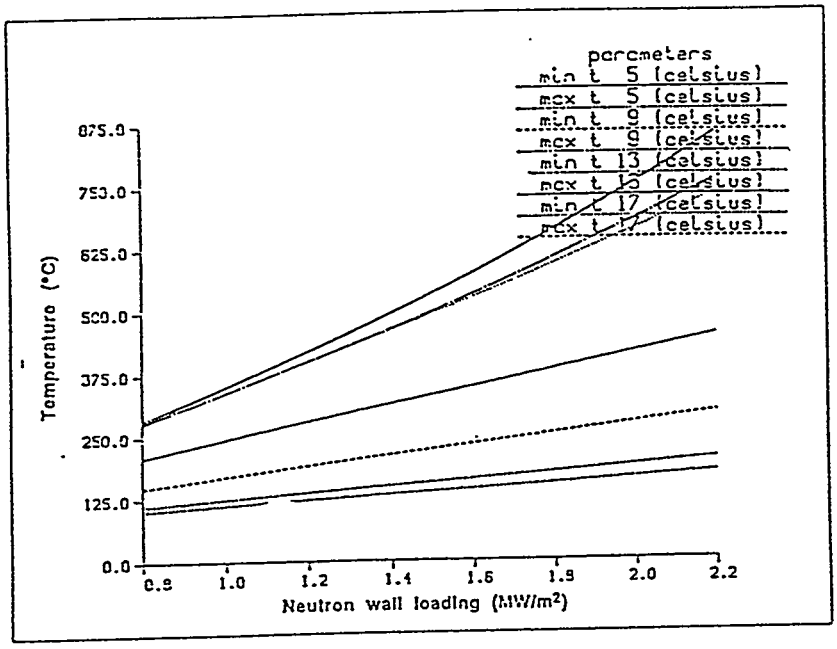

Fig. 7-14. Steady state extreme temperatures of the beryllium multiplier at the midplane as a function of the neutron wall loading during the technology phase.

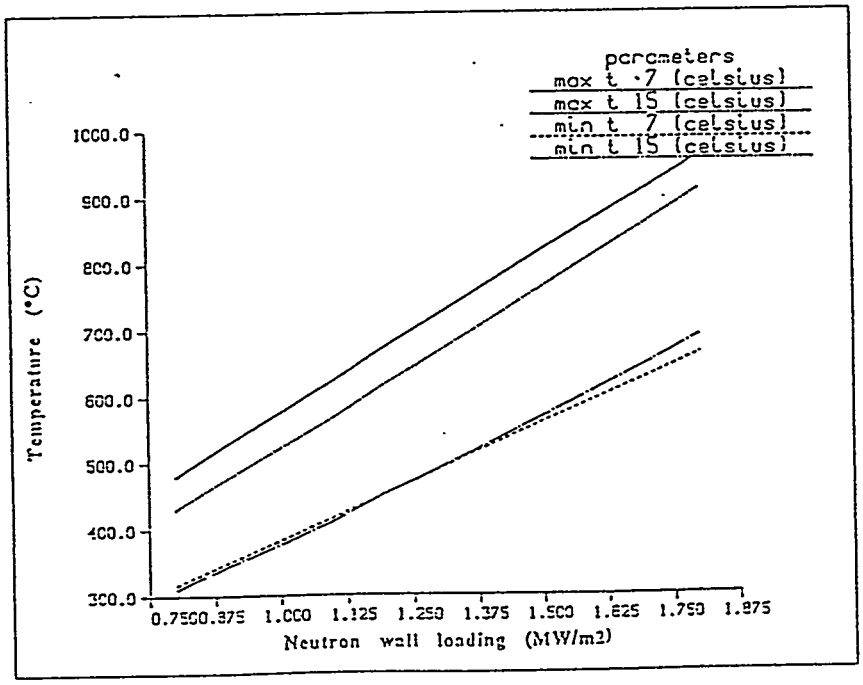

Fig. 7-15. Steady state extreme temperatures of the lithium oxide zones at the midplane as a function of the neutron wall loading during the technology phase for the single size pebbles.

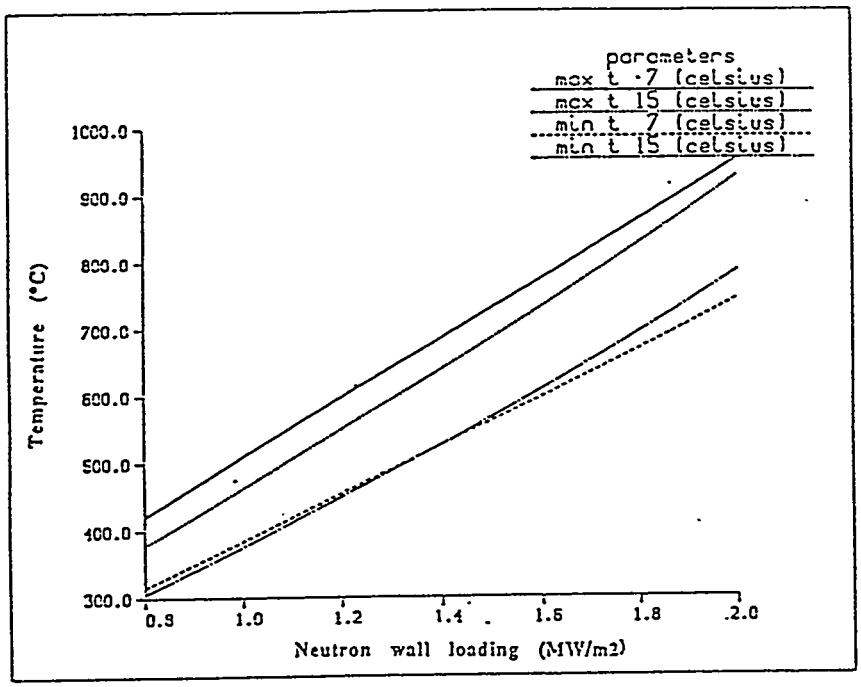

Fig. 7-16. Steady state extreme temperatures of the lithium oxide zones at the midplane as a function of the neutron wall loading during the technology phase for the pebbles with two sizes.

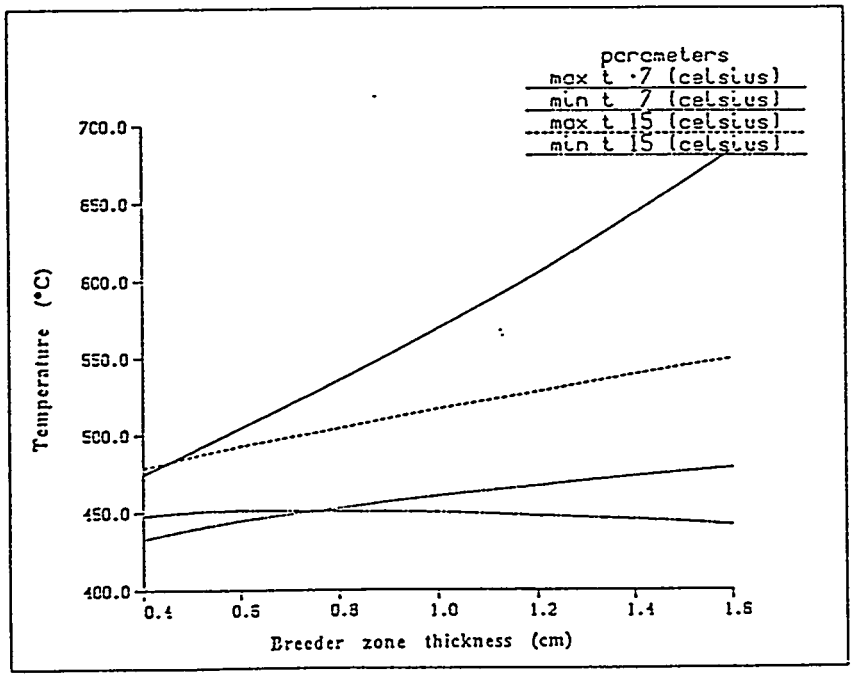

Fig. 7-17. Extreme temperatures of the breeder material as a function of the breeder zone thickness.

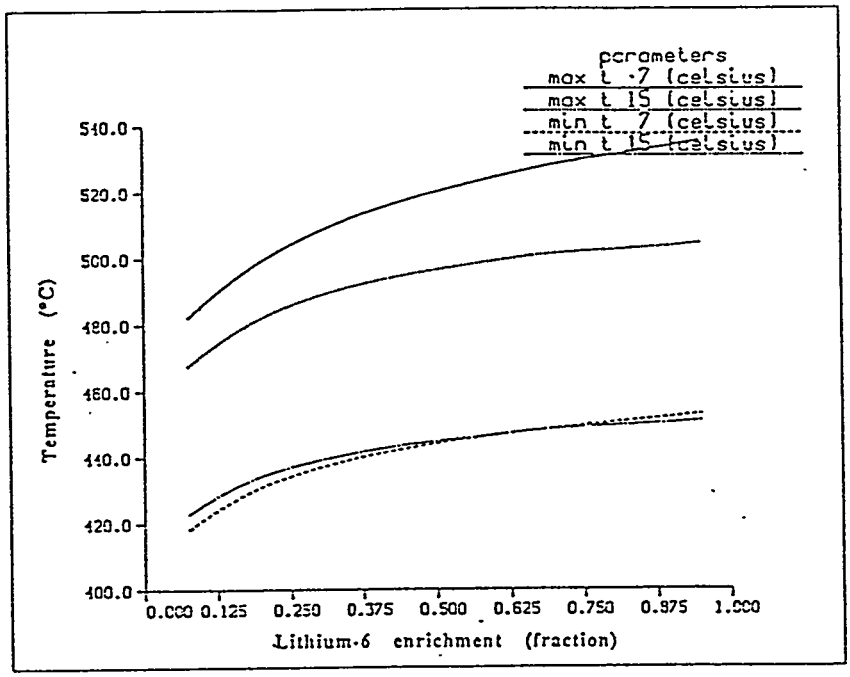

Fig. 7-18. Extreme temperatures of the breeder material as a function of the lithium-6 enrichment.

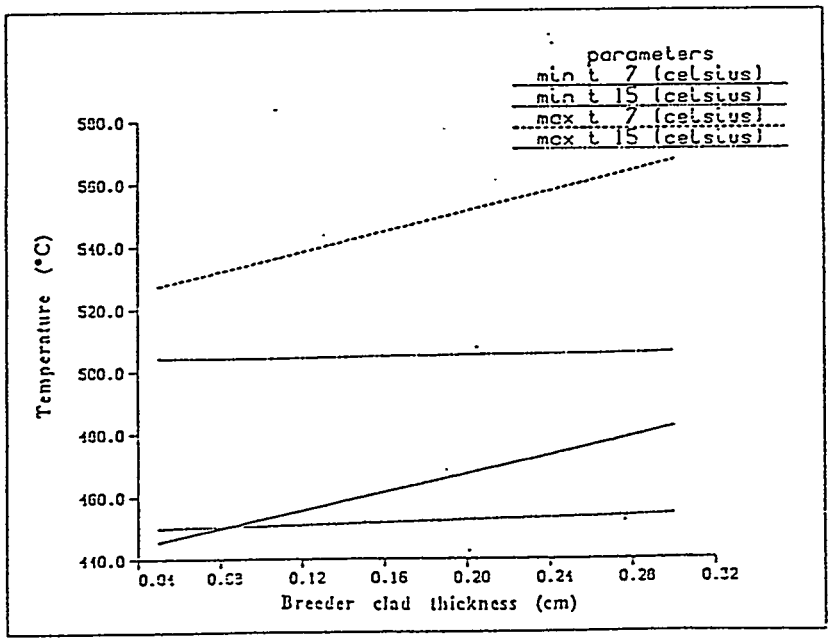

Fig. 7-19. Extreme temperatures of the breeder material of the blanket configuration with two breeder zones at the midplane as a function of the breeder clad thickness.

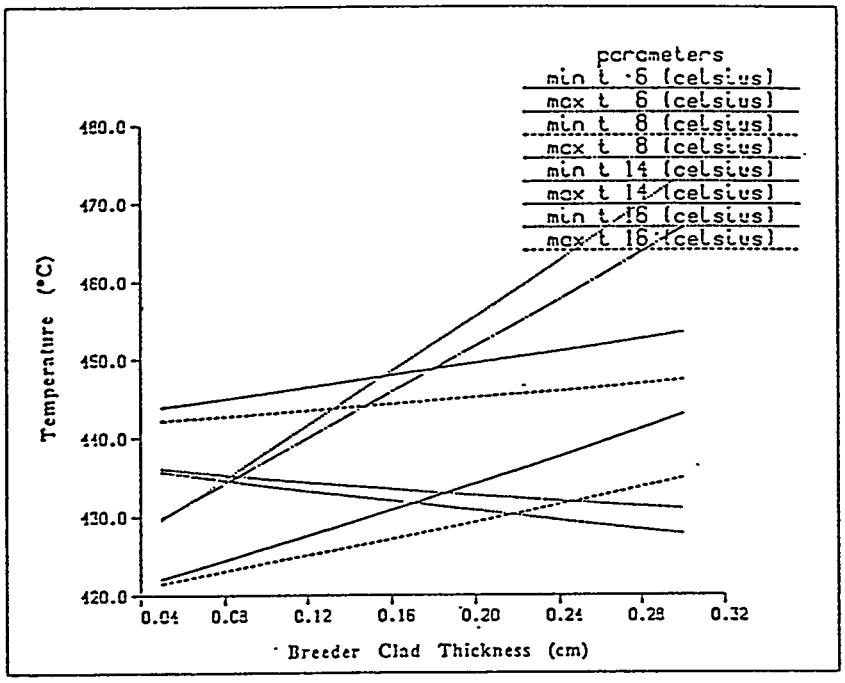

Fig. 7-20. Extreme temperatures of the breeder clad at the midplane as a function of the clad thickness.

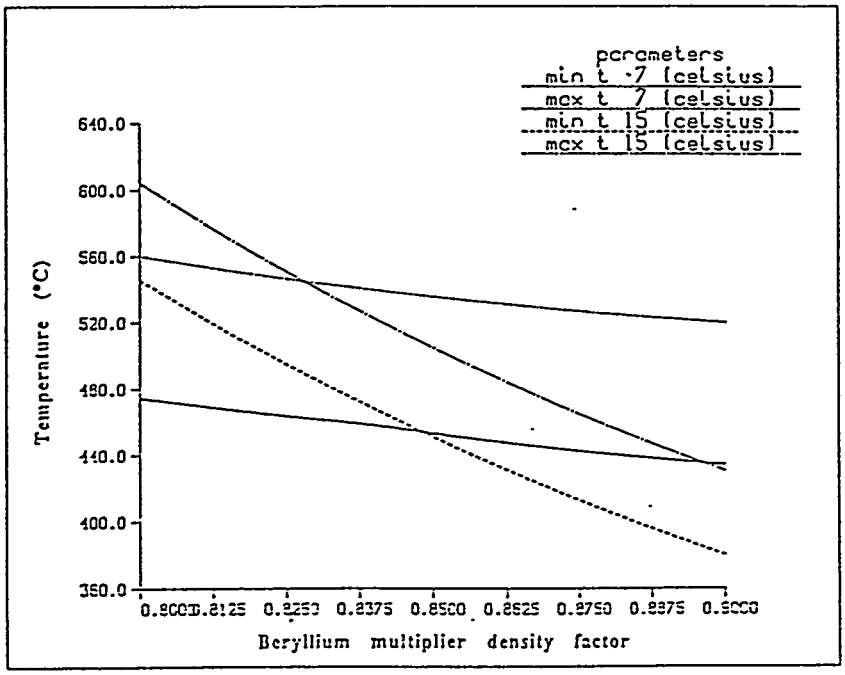

Fig. 7-21. Extreme temperature of the breeder material at the midplane as a function of the change in the beryllium multiplier density factor.

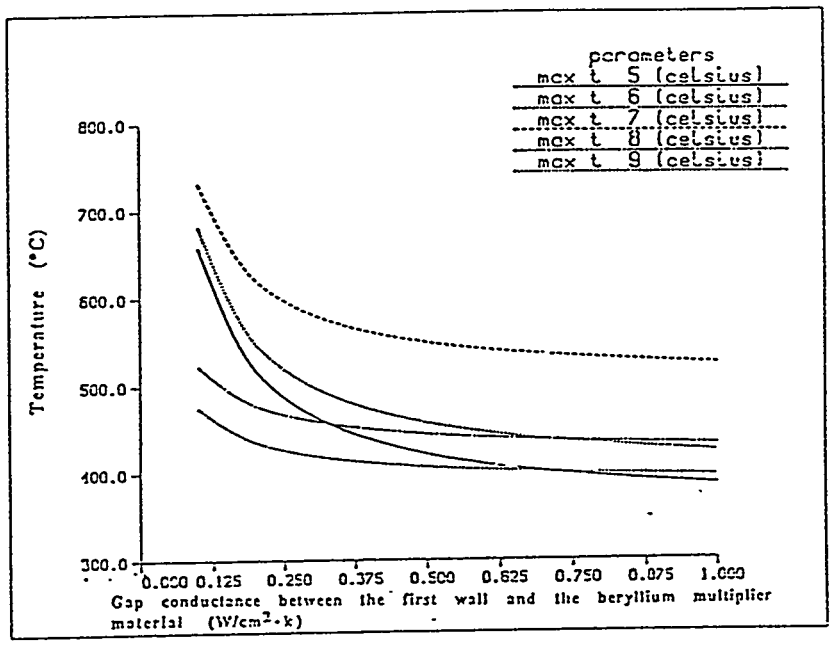

Fig. 7-22. Maximum temperatures of the breeder, clad, and multiplier materials of the first breeder zone of the blanket configuration at the midplane as a function of the gap conductance between the first wall and the beryllium multiplier material.

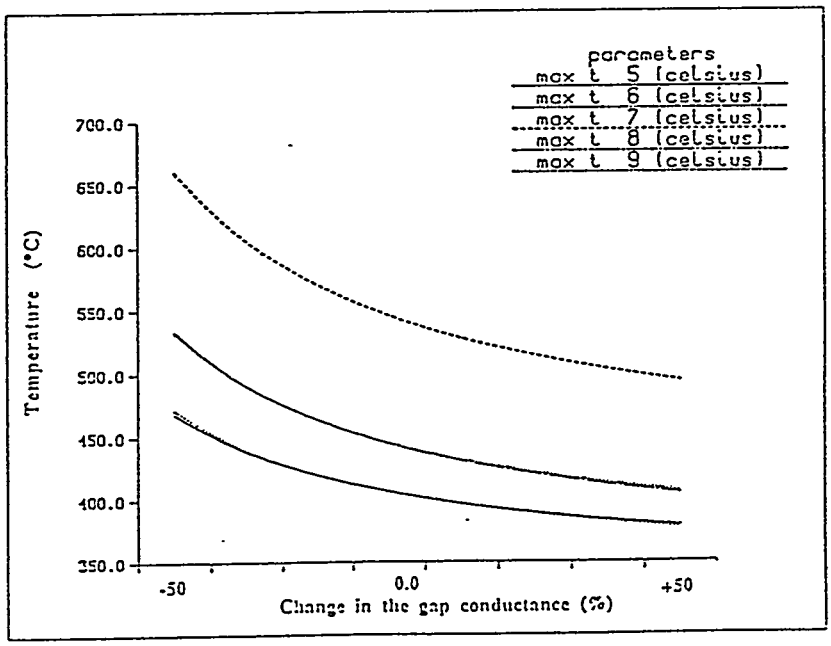

Fig. 7-23. Maximum temperatures of the breeder, clad, and multiplier materials of the first breeder zone of the blanket configuration at the midplane as a function of the change in the gap conductance at the six interfaces between breeder/steel and Be/steel.

Table 7-1.
Steady State Extreme Temperatures of the Different Blanket Materials for the Technology Phase with Two Breeder Zones at the Outboard Midplane, the Beginning of the Copper Stabilizer and the End of the Blanket

ZONE	MATERIAL (DF)	EXTREME TEMPERATURES,[a] °C 1.2 MW/m^2 Z = 0	0.958 MW/m^2 Z = ±2.7 m		0.6 MW/m^2 Z = ± 4.3 m
First Wall Layers[b]					
First wall	steel	77-191	74-168	74-168	69-132
Back wall	steel	82-225	81-222	82-228	79-203
Stabilizer	Cu			230-237	205-210
Blanket					
Multiplier	Be (0.85)	280-401	277-440	285-412	252-418
Clad	steel	426-438	462-472	432-442	432-439
Breeder	Li_2O (0.80)	453-537	484-559	455-522	448-492
Clad	steel	424-437	459-470	433-443	432-440
Multiplier	Be (0.85)	92-401	180-437	174-413	143-418
Coolant channel	steel	77-138	75-131	75-127	71-109
Coolant channel		70-109	68-101	68-99	65-84
Multiplier	Be (0.65)	138-421	124-454	121-431	97-440
Clad	steel	435-446	465-472	441-449	444-447
Breeder	Li_2O (0.80)	451-505	476-514	452-487	449-460
Clad	steel	434-443	465-471	442-447	446-447
Multiplier	Be (0.65)	123-422	106-457	104-434	309-444
Coolant channel	steel	68-99	66-879	66-86	63-303
Total first wall/blanket thickness		26.5	37.1	37.1	58.5
Local tritium breeding ratio		1.375	1.468	1.356	1.310

a-Poloidal sector (1/48 section) with the plasma minor radius.

b-The surface heat flux is 25% the DT neutron wall load value.

Table 7-2.
Steady State Extreme Temperatures for the Different Blanket Materials for the Technology Phase with One Breeder Plate at the Inboard Midplane and the End of the Blanket

ZONE	MATERIAL (DF)	EXTREME TEMPERATURE (C)	
		0.884 MW/m^2 Z = 0	0.325 MW/m^2 Z = ±3.4 m
First Wall			
First wall	steel	92-174	65-98
Back wall	steel	94-187	69-131
Blanket			
Multiplier	Be (0.65)	224-413	155-427
Clad	steel	433-440	435-438
Breeder	Li_2O (0.80)	452-526	442-472
Clad	steel	431-438	435-437
Multiplier	Be (0.65)	162-415	288-427
Coolant channel	steel	91-126	67-275
Total first wall/blanket thickness		10.9	18.5
Local tritium breeding ratio		0.755	0.895

Table 7-3
Steady State Extreme Temperatures of the Different Blanket Materials for the Physics Phase with Two Breeder Zones at the Outboard Midplane, the Beginning of the Copper Stabilizer and the End of the Blanket

ZONE	MATERIAL (DF)	EXTREME TEMPERATURES,[a] °C			
		1.535 MW/m^2 Z = 0	1.225 MW/m^2 Z = ±2.7 m		0.767 MW/m^2 Z = ± 4.3 m
First Wall Layers[b]					
Tile	C	291-396	251-332	252-331	188-236
First wall	steel	90-278	84-241	84-242	76-182
Back wall	steel	85-244	84-240	85-247	81-218
Stabilizer	Cu			249-257	219-226
Blanket					
Multiplier	Be (0.85)	305-449	300-492	310-460	272-465
Clad	steel	478-492	516-528	483-494	481-488
Breeder	Li_2O (0.80)	508-609	542-631	509-588	499-551
Clad	steel	475-490	513-526	484-496	482-490
Multiplier	Be (0.85)	206-449	193-490	186-462	152-466
Coolant channel	steel	79-147	77-139	76-135	72-115
Coolant channel	steel	71-115	69-105	69-104	65-87
Multiplier	Be (0.65)	146-470	131-508	128-483	101-491
Clad	steel	485-497	519-528	494-502	496-498
Breeder	Li_2O (0.80)	502-566	532-576	506-546	499-513
Clad	steel	484-494	520-527	494-501	496-498
Multiplier	Be (0.65)	130-471	111-511	109-486	336-494
Coolant channel	steel	69-103	66-91	66-90	63-331
Total first wall/blanket thickness		26.5	37.1	37.1	58.5
Local tritium breeding ratio		1.234	1.306	1.208	1.157

a-Poloidal sector (1/48 section) with the plasma minor radius.
b-The surface heat flux is 25% the DT neutron wall load value.

Table 7-4.
Steady State Extreme Temperatures for the Different Blanket Materials for the Physics Phase with One Breeder Zone at the Inboard Midplane and the End of the Blanket

ZONE	MATERIAL (DF)	EXTREME TEMPERATURE (C)	
		1.131 MW/m^2 Z = 0	0.416 MW/m^2 Z = ±4.1 m
First Wall			
Carbon wall	C	251-322	131-154
First wall	steel	100-239	69-126
Back wall	steel	95-200	70-138
Blanket			
Multiplier	Be (0.65)	241-465	165-477
Clad	steel	483-496	486-490
Breeder	Li_2O (0.80)	509-603	493-529
Clad	steel	485-493	484-487
Multiplier	Be (0.65)	172-463	313-476
Coolant channel	steel	93-132	68-298
Total first wall/blanket thickness		12.9	20.5
Local tritium breeding ratio		0.698	0.801

Table 7-5.
Steady State Extreme Temperatures of the Different Blanket Materials at the Outboard Midplane for the Technology Phase with Two Lithium Oxide Breeder Zones Using One or Two Size Pebbles

ZONE	MATERIAL (DF)	EXTREME TEMPERATURES[a] (°C)	
		One Size	Two Sizes
First Wall Layers[b]			
First wall	steel	77-191	77-191
Back wall	steel	79-203	81-216
Blanket			
Multiplier	Be (0.85)	249-327	267-369
Clad	steel	348-359	392-404
Breeder[c]	Li_2O	453-675	455-598
Clad	steel	346-359	391-404
Multiplier	Be (0.85)	179-327	187-370
Coolant channel	steel	75-131	76-135
Coolant channel	steel	70-108	70-109
Multiplier	Be (0.65)	137-364	138-397
Clad	steel	377-388	410-422
Breeder[c]	Li_2O	453-619	450-551
Clad	steel	380-389	410-419
Multiplier	Be (0.65)	125-367	124-398
Coolant channel	steel	68-100	68-99
Total first wall/blanket thickness		22.6	24.8
Local tritium breeding ratio		1.257	1.331

a- Poloidal sector (1/48 section) with the plasma minor radius.

b- The surface heat flux is 25% the DT neutron wall value.

c- The density factors for the one and two sizes lithium oxide pebbles are 0.6 and 0.8 respectively.

Table 7-6.
Steady State Extreme Temperatures for the Different Blanket Materials at the Outboard Midplane for the Physics Phase with Two Lithium Oxide Breeder Zones Using One or Two Size Pebbles

ZONE	MATERIAL (DF)	EXTREME TEMPERATURES[a] (°C)	
		One Size	Two Sizes
First Wall Layer[b]			
Tile	C	291-396	291-396
First wall	steel	90-278	90-278
Back wall	steel	81-220	83-234
Blanket			
Multiplier	Be (0.85)	271-364	291-412
Clad	steel	389-402	440-453
Breeder[c]	Li_2O	509-759	510-671
Clad	steel	386-400	438-452
Multiplier	Be (0.85)	193-364	201-414
Coolant channel	steel	77-139	78-144
Coolant channel	steel	71-114	71-114
Multiplier	Be (0.65)	145-405	146-442
Clad	steel	419-431	457-469
Breeder[c]	Li_2O	502-682	500-609
Clad	steel	421-432	457-467
Multiplier	Be (0.65)	132-408	131-443
Coolant channel	steel	69-105	69-103
Total first wall/blanket thickness		22.6	24.8
Local tritium breeding ratio		1.134	1.197

a- Poloidal sector (1/48 section) with the plasma minor radius.

b- The surface heat flux is 25% the DT neutron wall load value.

c- The density factors for the one and two sizes lithium oxide pebbles are 0.6 and 0.8, respectively.

Table 7-7.
Steady State Extreme Temperatures of the Different Blanket Materials for the Technology Phase at the Outboard Midplane with Two Breeder Zones and Two Zones of Beryllium Pebbles at the Front and Back of the Blanket

ZONE	MATERIAL (DF)	EXTREME TEMPERATURE (C)	
		1.2 MW/m^2 Z = 0	0.958 MW/m^2 Z = ±2.7 m
First Wall Layers			
First wall	steel	77-189	74-164
Back wall	steel	73-160	71-147
Blanket			
Multiplier	Be pebbles (0.82)	188-417	172-426
Clad	steel	439-450	444-454
Breeder	Li_2O (0.80)	464-547	465-536
Clad	steel	437-452	443-455
Multiplier	Be blocks (0.85)	205-413	192-422
Coolant channel	steel	79-147	77-139
Coolant channel	steel	76-135	74-125
Multiplier	Be blocks (0.85)	184-427	167-430
Clad	steel	444-450	444-452
Breeder	Li_2O (0.80)	462-520	456-497
Clad	steel	445-453	443-449
Multiplier	Be blocks (0.85)	325-431	344-433
Multiplier	Be pebbles (0.82)	125-300	106-327
Coolant channel	steel	68-100	66-88
Total first wall/blanket thickness		24.5	30.0

Table 7-8.
Steady State Extreme Temperatures for the Different Blanket Materials During the Technology Phase with Three Breeder Plates[a] at the Outboard Midplane and 2.7 m from the Midplane

ZONE	MATERIAL (DF)	EXTREME TEMPERATURE (C)	
		1.2 MW/m^2 Z = 0	0.6 MW/m^2 Z = 2.7 m
First Wall Layers			
First wall	steel	81-168	73-131
Back wall	steel	81-262	80-253
Blanket			
Multiplier	Be (0.85)	310-401	300-405
Clad	steel	424-436	427-437
Breeder	Li_2O (0.8)	452-546	451-535
Clad	steel	425-438	426-437
Multiplier	Be (0.85)	193-402	181-405
Coolant channel	steel	77-139	76-132
Coolant channel	steel	70-110	69-103
Multiplier	Be (0.65)	138-423	127-426
Clad	steel	436-447	437-446
Breeder	Li_2O (0.8)	454-521	451-505
Clad	steel	434-445	435-444
Multiplier	Be (0.65)	126-420	115-423
Coolant channel	steel	69-101	67- 94
Coolant channel	steel	66- 90	65- 83
Multiplier	Be (0.65)	107-442	97-442
Clad	steel	447-451	446-449
Breeder	Li_2O (0.8)	454-478	451-466
Clad	steel	447-450	449-451
Multiplier	Be (0.65)	355-441	350-446
Coolant channel/shield[b]	steel	65-347	63-346
Total first wall/blanket thickness[b]		45.1	61.8
Local tritium breeding ratio		1.634	1.650

a- The third breeder plate extends between the copper stabilizer loops in the poloidal direction.
b- Steel shield thickness is not included in the total FW/B thickness.

8.0 STRESS AND LIFETIME ANALYSIS

Structurally, the most vulnerable portions of the ITER outboard blanket are the first wall (FW) and the side walls (SW) connecting the FW to the shield. The ITER outboard blanket structure has been analyzed for stresses generated under normal operating and disruption conditions. All analyses are carried out using a multi-layer elastic shell element of the finite element program ANSYS. In all cases considered here, the first and side walls have been assumed to be a sandwich design consisting of a 5-mm (or 4-mm) thick plasma-facing front plate and a 5-mm (or 6-mm) thick back plate separated by 4-mm high coolant channels. The stiffening effects of the webs separating the adjacent coolant channels are ignored.

Because the toroidal span of the blanket box is small relative to its height, the stresses and deformation in the blanket components have been determined using a toroidal strip with a unit extent in the poloidal direction, ignoring the poloidal variation of the loadings. The peak stress is calculated by analyzing the toroidal strip lying at the location of the peak loading. The SW's are assumed to be rigidly attached to the shield, because the shield is much stiffer than the SW's.

The analysis assumes that the design limits for the ITER components are given by the ITER Design Criteria. Thus, the allowable primary membrane stress intensity (S_m) for annealed austenitic Type 316 Stainless Steel is 110 MPa. The maximum primary bending stress intensities for rectangular solid sections and for sandwich sections are taken as 165 MPa and 125 MPa, respectively.

8.1 Normal Operation

Normal operating conditions consist of a helium pressure of 0.1 MPa (one atm.) or 0.05 MPa (half atm.), a neutron wall loading of 1.2 MW/m^2, and an average surface heat flux of 0.25 MW/m^2 with a peak heat flux of 0.4 MW/m^2. Two criteria have to be satisfied by the first wall design during normal operation. First, the maximum stresses must be within the allowable limits as set forth in the ITER Design Criteria, and second, the maximum radial displacement of the first wall must be less than a preset design-dependent maximum. Depending on the initial configuration of the beryllium multiplier, the

maximum permissible displacement of the first wall could vary from ~100 μm to as much as ~ 1mm.

8.1.1 Beginning of Life

Primary Stresses

For a FW (4x4x6 mm) toroidal span of 0.8 m, the peak bending stress in the blanket box due to the 0.1 MPa internal pressure is ~ 150 MPa, which is approximately the maximum allowable bending stress. Hence, for an internal pressure of 0.1 MPa, the maximum unstiffened toroidal span allowed for the proposed FW configuration (4x4x6 mm) is 0.8 m. The maximum allowable span (unstiffened) can be increased to 1 m if the internal pressure is reduced to 0.05 MPa. However, from a practical viewpoint these designs are unacceptable, because they leave little margin for primary stresses due to disruptions.

The maximum radial displacement and primary stress intensity in the unstiffened outboard first wall (5x4x5 mm) due to helium pressure (0.1 MPa) loading are given in Fig. 8-1. Note that, if a maximum radial displacement of ≥ 500 μm is acceptable, then the maximum toroidal span of the first wall as determined by the allowable primary bending stress intensity of the material is 0.8 m for a pressure of 0.1 MPa and 1 m for a pressure of 0.05 MPa. As before, from a practical viewpoint these designs are unacceptable, because they leave little margin for primary stresses due to disruptions. Therefore, irrespective of the internal pressure, in the absence of any maximum displacement constraint, the maximum primary bending stress limit requires that each blanket segment (unstiffened) be divided into two sub-segments. On the other hand, if the maximum permissible radial displacement of the first wall is 100 μm, the toroidal span must be ≤ 0.34 m, i.e., each blanket segment has to be divided into 3 sub-segments.

An option to reduce the maximum radial displacement and primary stress of the first wall is to stiffen the first wall by using toroidal beams (Fig. 8-2) at poloidal spacings that could be varied in the poloidal direction. Figures 8-3 and 8-4 show the variations of the maximum radial displacement and maximum primary bending stress intensity, respectively, due to a helium pressure loading of 0.1 MPa as functions of the stiffener (3x3.3 cm beams) spacing for three toroidal spans. Although the maximum stresses are much less than the allowable primary bending stress intensity for the 0.5 m and 0.33 m spans, at

1 m span the maximum primary bending stress allowable can just be met at a stiffener spacing of 20 cm leaving no margin for disruption stresses. Thus, realistically, provided maximum displacements of ~1-2 mm can be accommodated by the design, a 1 m toroidal span may be acceptable if the helium pressure can be reduced to 0.05 MPa. On the other hand, a stringent criterion (e.g., ≤ 100 μm) for the maximum permissible radial displacement would rule out a toroidal span of 1 m. Under a similar displacement constraint, 0.5 m toroidal span would be acceptable, if the helium pressure can be reduced to 0.05 MPa. If the internal pressure cannot be reduced to 0.05 MPa, a toroidal span of 0.33 m will be necessary.

Although theoretically a toroidal span of 0.33 m with toroidal stiffening beams is acceptable (Fig. 8-3), it would entail dividing each blanket segment into three sub-segments, which is not very attractive from a design point of view. An alternative approach is to reinforce each blanket segment with toroidal stiffening beams at regular poloidal spacings as before, but, in addition, provide ties that connect the beams to the shield at as many locations as necessary. Alternatively, the blanket could be constructed out of rectangular or square modules with ties attaching the first wall to the shield. A typical square module (module size = beam spacing) with a single tie is shown in Fig. 8-5. The variations of the maximum radial displacement and stress intensity of the module with the module size for the case of the helium pressure (0.1 MPa) loading are shown in Fig. 8-6. If the maximum permissible radial displacement for the design is ≤ 500 μm, the maximum allowable primary bending stress intensity determines the maximum module size to be 1 m. However, in order to leave enough margin for accommodating primary stresses due to disruptions, either the helium pressure has to be reduced to 0.05 MPa or more ties have to be used. Similarly, to satisfy a more stringent permissible maximum displacement (e.g., ≤ 100 μm) criterion, either more ties (possibly four) or a module size of 0.5 m may be required.

Secondary Stresses

For the 4x4x6 mm design, the thermal stresses are first modeled by applying a linear temperature variation to the plasma-facing front plate of the first wall. The rest of the first wall is assumed to be maintained at the bulk coolant temperature, thus ignoring the heating effect of the beryllium

multiplier on the back plate of the first wall. The thermal stress intensity for this condition is found to vary linearly with the surface heat flux producing a maximum range of stress intensity of 330 MPa at a surface heat flux of ~0.4 MW/m^2. If primary stress due to 0.1 MPa (or 0.05 MPa) internal pressure is included, the 3 S_m limit is exceeded when the surface heat flux exceeds 0.22 MW/m^2 (or 0.31 MW/m^2) in which case an inelastic analysis will be needed.

In reality, the temperature of the back plate of the FW is not equal to the coolant temperature but is fixed by the heat transfer from the beryllium multiplier at a neutron wall loading of 1.2 MW/m^2. The temperature distribution in the plasma-facing front plate varies according to the surface heat flux. The maximum effective thermal stresses in the first and the side walls at the midplane for the 4x4x6 mm and 5x4x5 mm sandwich designs are shown in Table 8-1 for surface heat fluxes of 0.4 and 0.6 MW/m^2. Note that the 4x4x6 mm design is preferable at the higher heat flux. However, in all designs a 5mm thick copper layer is needed at the back of the first wall at certain poloidal locations, and there is some incentive to change this from a soft to a harder DS copper in order to take advantage of its superior strength. Table 8-2 shows a comparison of the maximum effective thermal stresses, with and without DS copper, at a surface heat flux of 0.25 MW/m^2. Note that the 5x4x5 mm design results in a lower maximum effective thermal stress than the 4x4x6 mm design, and the lowest maximum thermal stress occurs when DS copper is used.

Variations of the maximum effective stresses in the front and the back plates of the first wall together with the maximum radial displacement (positive towards the plasma) of the first wall are shown as functions of surface heat flux for toroidal spans of 0.33 m, 0.5 m, and 1 m in Figs. 8-7 through 8-9, respectively. In all cases, stresses due to a helium pressure are added on to the thermal stresses, the helium pressure being 0.1 MPa for the first two cases and 0.05 MPa for the last case. At a surface heat flux of 0.25 MW/m^2, the maximum effective stress occurs in the back plate, being equal to 445 MPa for a toroidal span of 0.33 m (stiffener spacing of 40 cms), 425 MPa for a toroidal span of 0.5 m (stiffener spacing of 25 cms), and 410 MPa for a toroidal span of 1 m (stiffener spacing of 20 cm). Because of the characteristics of the temperature distribution, the maximum displacement of

Table 8-1. Maximum effective thermal stresses (MPa) at the ITER outboard blanket at the midplane for surface heat fluxes of 0.4 and 0.6 MW/m^2 and a neutron wall loading of 1.2 MW/m^2. Results are shown for two sandwich designs, 4/6 mm and 5/5 mm. The $3S_m$ value for annealed stainless steel is 330 MPa. Significant cyclic plasticity will occur in the first wall of the 5/5 mm design if the surface heat flux reaches 0.6 MW/m^2.

	0.4 MW/m^2	0.6 MW/m^2
First wall, 4 mm plate	258	470
First wall, 6 mm plate	444	402
Side wall, 4 mm plate	270	380
Side wall, 6 mm plate	336	317
First wall, 5 mm plate	365	612
First wall, 5 mm back plate	342	281
Side wall, 5 mm plate	297	474
Side wall, 5 mm back plate	274	240

Table 8-2. Maximum effective thermal stresses (MPa) at the ITER outboard blanket at a poloidal distance of -1.8 m from the midplane for a surface heat flux of 0.25 MW/m^2 and a neutron wall loading of 1 MW/m^2. Results are shown for two sandwich designs, 4/6 mm and 5/5 mm, both using soft Cu and DS Cu. The $3S_m$ values for both annealed stainless steel and DS Cu are 330 MPa.

	With DS Cu	With Soft Cu
First wall, 4 mm plate	209	180
First wall, 6 mm plate	406	501
First wall, 5 mm Cu	336	0.00
Side wall, 4 mm plate	359	230
Side wall, 6 mm plate	477	240
First wall, 5 mm plate	228	216
First wall, 5 mm back plate	329	415
First wall, 5 mm Cu	300	0.00
Side wall, 5 mm plate	282	156
Side wall, 5 mm back plate	384	176

the first wall is inwards (away from plasma) in the first two cases, being equal to 120 μm and 62 μm, respectively. A maximum outwards displacement of 1280 μm occurs for a toroidal span of 1 m. At a surface heat flux of 0.4 MW/m^2, the maximum effective stresses in the front and the back plates equalize to 425 MPa, 390 MPa, and 380 MPa for toroidal spans of 0.33 m, 0.5 m, and 1 m, respectively. The maximum radial displacements for the three cases are 85 μm, 300 μm, and 2000 μm outwards (towards plasma), respectively. Since these maximum stresses exceed the 3 S_m limit (330 MPa) by a small margin (particularly, if only the thermal stress ranges are considered), they should be acceptable and will be demonstrated as such by future inelastic analyses.

Variations of the maximum radial displacement and effective stress in a 0.5 m and 1 m square module (with a single tie) with the surface heat flux are shown in Figs. 8-10 to 8-11 respectively. Helium pressures of 0.1 MPa and 0.05 MPa are included in the two cases, respectively. Because of the characteristics of the temperature distribution, the maximum effective stress occurs in the back plate for low surface heat flux (<0.4 MW/m^2) and in the front plate facing the plasma for surface heat flux >0.4 MW/m^2. Note that the 3 Sm criterion for the thermal stress range is satisfied up to a surface heat flux of 0.4 MW/m^2 in both cases. If the maximum surface heat flux exceeds 0.4 MW/m^2 significantly, inelastic analysis will be required. However, a stringent criterion (e.g., 100 μm) for maximum permissible radial displacement would limit the maximum surface heat flux for the 0.5 m square module to ~0.3 MW/m^2 and eliminate the 1-m square module design unless the number of ties from the first wall to the shield is increased to more than one (possibly 3-4).

Fatigue Analysis

Because a substantial portion of the stresses associated with the normal operating cycles of the blanket are of thermal origin, the process can be modeled as one of strain-controlled fatigue. For a toroidal span of 0.8 m (using 4x4x6 mm design) and a heat flux of 0.22 MW/m^2, the maximum plastic strain range is 0.05%. This corresponds to a fatigue life of a million cycles, which is adequate for ITER. For larger spans and higher heat fluxes, an elastic-plastic analysis must be carried out to guarantee that cyclic ratcheting does not occur.

8.1.2 End-of-life Results

Creep Relaxation

The end-of-life (EOL) results require consideration of both irradiation-induced creep and swelling. Irradiation-induced creep will act rapidly to relax the thermal stresses in the FW, with a characteristic decay exposure of 3 dpa. Unfortunately, these stresses reappear with reversed sign upon unloading. Hence, the stress relaxation has little effect on fatigue life of the component.

Swelling Stresses

Swelling stresses are caused by self-constraint of the material or surrounding materials. In the FW, the plasma-facing plate is at a higher temperature relative to the back plate, particularly at higher surface heat fluxes. Hence it lies in a relatively high swelling region. For this analysis, the plasma-facing front plate (4 mm thick) is assumed to swell by 3% by the EOL, while the rest of the first wall is assumed to undergo no swelling. Hence the restraint of the 6 mm back plate will lead to stresses throughout the FW. Because the swelling distribution will not be this severe, this is a conservative model and will yield an upper bound on the swelling stresses.

As creep relaxes the thermal stresses in the FW, the competition between self-restrained swelling and creep will lead to a steady-state swelling stress. For the ITER FW, the predicted steady-state swelling stress is less than 70 MPa, which is well below the primary stress limit. Further, this stress will not reverse upon unloading.

8.2 Disruption Conditions

Disruption conditions have been analyzed for two configurations of the stabilizer coils, one using a saddle coil stabilizer and the other using a twin loop stabilizer. The electromagnetic pressure distributions on the outboard first wall for these two configurations of the stabilizer coils are significantly different. In the first case, the radial pressure distribution on the first wall is approximately linear in the toroidal direction with a net integrated force of approximately zero across any toroidal section. The

poloidal location of the peak pressure (~0.5 MPa) is in the copper region where the toroidal span of the blanket is ~0.8 m. In contrast, when twin loop stabilizer coils are used, the radial pressure distribution in the toroidal direction no longer averages out to zero. A peak pressure of ~0.9 MPa, which is uniform in the toroidal direction, occurs at the midplane section of the blanket where the toroidal span is ~1 m. In other poloidal locations, the toroidal variation of pressure might be from peak to zero. These differences in the electromagnetic pressure distribution have a profound impact on the maximum stresses in the first wall of the outboard blanket.

Earlier transient dynamic analyses of the full outboard blanket structure had shown that the disruption transients were sufficiently slow so that the dynamic effects of the electromagnetic pressure loading on the maximum stresses of the blanket were minimal and that a good estimate for the maximum stress across any toroidal section of the blanket could be obtained from a quasi-static analysis of the section, thus minimizing the need for detailed transient dynamic analyses of the full outboard blanket structure. The stresses due to combined disruption pressure and helium pressure loadings have to satisfy the maximum primary stress intensity criteria. The interactions between cyclic stresses due to disruption pressure loadings and thermal stresses during normal operation, which might potentially lead to cyclic ratcheting of the first wall, require inelastic analysis and have not been carried out to date.

Due to the uncertainty of the disruption pressure distribution, the allowable peak pressure has been calculated parametrically for the 4x4x6 mm sandwich design (without stiffeners), using three generic pressure distributions. The first and most severe generic pressure distribution is the one of uniform toroidal pressure distribution. The second generic distribution consists of a peak pressure at one side wall diminishing linearly in the toroidal direction to zero at the other side wall. The third generic distribution like the second involves a linear pressure distribution in the toroidal direction. However, this case features a peak pressure at one side wall and a peak pressure of opposite sign at the other side wall with a zero pressure at the center. The allowable disruption pressures for various toroidal spans (without any stiffeners) are shown in Fig. 8-12. One way to increase the allowable disruption pressure is to segment the blanket

toroidally by attaching radial stiffeners to the FW (inside the blanket) and anchoring them to the shield. This effectively reduces the toroidal span of the FW without reducing the toroidal span of the blanket box. Figure 8-13 gives the maximum allowable toroidal span as a function of the disruption pressure (assumed uniform), assuming a uniform helium pressure of 0.1 MPa. It can be used to estimate the toroidal span required to withstand higher disruption pressures than those allowed by an unreinforced FW.

Design Using Saddle Coil Stabilizer

Because of the characteristics of the electromagnetic pressure distribution during disruptions using a saddle coil stabilizer, the maximum stress occurs in the first wall above the midplane in the copper region where the toroidal span is 0.8 m. A design using 1x2.5 cm toroidal beam stiffeners at various spacings was analyzed. Figures 8-14 and 8-15 show the variations of the maximum allowable peak pressure as a function of the beam spacing for the 5x4x5 mm and 4x4x6 mm designs, respectively, using either soft copper or a much stronger DS copper. Note that, if the peak pressure is limited to ~0.5 MPa, both designs using 5-mm thick DS copper (unstiffened by toroidal beams) can withstand the electromagnetic pressure without exceeding the primary stress limit. Further, if the designs can accommodate radial displacements on the order 2-3 mm at the midplane during normal operations, the blanket segments need not be divided into sub-segments or ties need not be provided.

Design Using Twin Loop Stabilizer Coil

When twin loop stabilizer coils are used, a maximum uniform pressure of ~ 0.9 MPa occurs during disruptions at or near the midplane of the outboard blanket. In order to minimize the resulting high stresses, a first option might be to reduce the toroidal span by dividing each blanket segment into two or more sub-segments that are either separate or integral with each other. Because of subsegmentation, the maximum uniform pressure at the midplane is expected to be reduced by ~30%. Table 8-3 shows the maximum stresses in the first wall, side wall, and the stiffening beam (3x3.3 cm) for various spacings of stiffeners. Note that the maximum stresses can be kept within the allowable limit by dividing each blanket segment into three separate sub-segments and using 3x3.3 cm stiffening beams at a spacing of 40 cm. The beam spacing can be increased or eliminated away from the midplane depending on the poloidal distribution of the pressure.

Table 8-3. ITER outboard blanket stresses at midplane using a 5×4×5 mm sandwich design. The toroidal span of 1 m is reduced by dividing each blanket segment into 2 or 3 sub-segments that are either separate or integral with each other. The first wall is stiffened by 3×3.3 cm beams at various poloidal spacings. The pressure loading is 0.73 MPa on the first wall and 0.1 MPa on the side walls.

Stiffener Spacing	No. of Sub-Segments	Maximum Stress in FW (MPa)		Maximum Stress in SW (MPa)		Maximum Stress in Beam (MPa)	
		Separ.	Integr.	Separ.	Integr.	Separ.	Integr.
15 cm	2	161	151	172	118	201	220
	3	67	74	72	58	91	77
25 cm	3	91	120	79	75	122	104
30 cm	3	103	---	96	---	131	---
40 cm	3	125	160	125	110	141	117
No beams	3	165	232	165	140		

If dividing each blanket segment into three sub-segments is not a practical alternative, the same effect can be achieved by providing toroidal stiffening beams at a poloidal spacing of 0.33 m and attaching each beam to the shield by a suitable number (3-4) of ties. Alternatively, a 0.5 m square modular design with a single tie to the shield, discussed earlier, can be selected. Since the pressure does not attenuate significantly in the poloidal direction within 0.5 m from the midplane, a uniform pressure of 0.73 MPa was assumed in the analysis. The resultant distributions of displacements and stresses in a module at the midplane are shown in Figs. 8-15 and 8-16, respectively. The maximum radial displacement is ~328 μm. The maximum primary bending stresses occur in the back plate of the first wall and are mostly within the allowable limit. Local stresses exceeding the allowable primary bending stress limit occur near the junction of the tie and the first wall. However, these stresses are secondary in nature and will be partially relieved by plastic yielding. To determine the full impact of such yielding,

a detailed inelastic analysis of the junction between the tie and the first wall will be needed. Of particular concern is the possibility of a significant radial gap developing between the beryllium blocks and the first wall because of plastic deformation of the first wall due to combined thermal and pressure loadings during disruptions. However, if necessary, additional ties may be provided to overcome this problem.

8.3 Conclusions

No Constraint on Displacements

If maximum displacements of ~4 mm under a 0.05 MPa helium pressure loading can be accommodated by the design, either a 4x4x6 mm or a 5x4x5 mm sandwich design (unreinforced) can be used. However, this does not leave any margin for disruption-induced primary stresses. The disruption pressure loadings on the outboard first wall for the twin loop stabilizer coils are far more severe from a stress viewpoint than those for the saddle stabilizer coils.

Design Using Saddle Coil Stabilizer

If DS copper is used, then the added stiffness due to DS copper is sufficient to take the disruption loading. Otherwise, with soft copper, necessary stiffness can be provided by 1x2.5 cm toroidal beams at 20 cm poloidal spacing. Nominal stiffening (e.g., 1x2.5 cm toroidal beams at a poloidal spacing of 30-40 cm) of the first wall in the non-copper region will be needed.

Design Using Twin Loop Stabilizer Coil

The maximum disruption stresses can be kept within the allowable limit by dividing each blanket segment into three separate sub-segments and using 3x3.3 cm stiffening beams at 40 cm poloidal spacing at the midplane and increasing or eliminating the beams away from the mid plane depending on the poloidal distribution of the pressure.

Alternatively, 3x3 cm toroidal beams have to be provided at 20 cm poloidal spacing with each beam connected to the shield at least at five locations.

Alternatively, the blanket (at the midplane) has to be constructed out of 0.5 m square modules with a single tie.

With Displacement Constraint During Normal Operations

If a maximum radial displacement (combined helium pressure and thermal) of 100 μm can be accommodated by the design under normal operating conditions, divide each blanket segment into three sub-segments and stiffen the first wall with 3x3.3 cm beams at 40 cm poloidal spacing.

A second alternative is to construct the blanket (at the midplane) out of 0.5 m square modules with a single tie.

A third alternative is to stiffen the blanket with a suitable number of toroidal beams and radial ties (arranged in a two-dimensional array) connecting the beams to the shield so that the average distance between the ties is ~ 0.33 m.

Thermal Stresses

The 5x4x5 mm design is preferred at surface heat fluxes $\leq$ 0.4 MW/m^2. Above 0.4 MW/m^2, the 4x4x6 mm design has smaller maximum thermal stress.

The maximum displacement of the 5x4x5 mm sandwich due to combined helium pressure and thermal loadings is radially inwards at a surface heat flux of 0.25 MW/m^2 and radially outwards at a surface heat flux of 0.4 MW/m^2.

The $3S_m$ (330 MPa) criterion for combined helium pressure and thermal-induced stress is exceeded in the back plate (5 mm) at a surface heat flux of ~0.2 MW/m^2. The fatigue life under such a loading is about one million. At a surface heat flux of 0.4 MW/m^2, the maximum stress intensity occurs in the plasma-facing front plate (5 mm) and is equal to ~400-450 MPa.

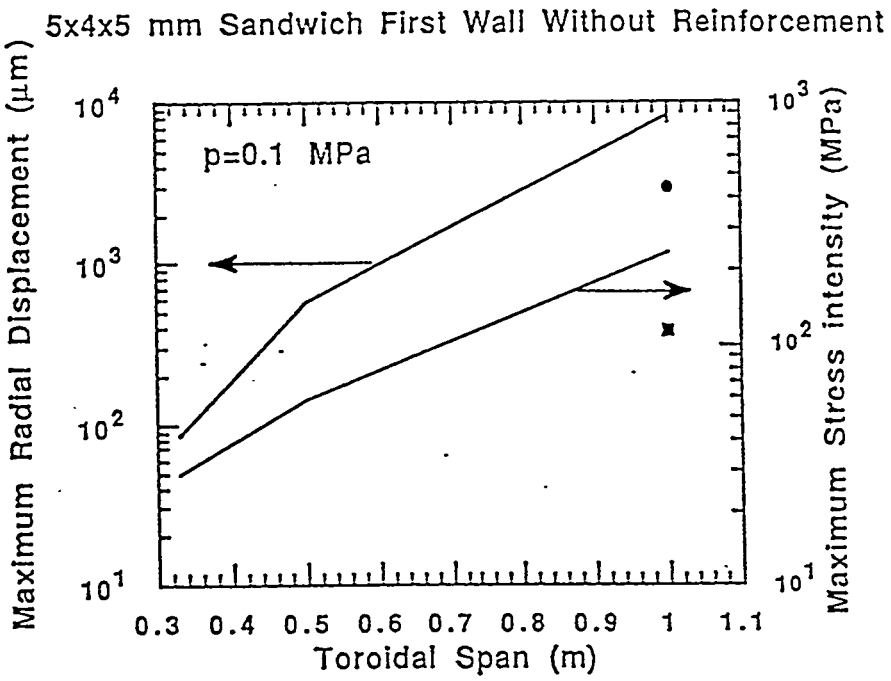

Fig. 8-1. Variation of the maximum radial displacement and maximum stress intensity in the first wall (without stiffeners) as functions of the toroidal span. Note that to satisfy the 100 μm maximum displacement criterion, the maximum permissible toroidal span is ≤ 0.34 m. Symbols refer to a case where the sandwich design is replaced by a solid wall of 2 cm thickness.

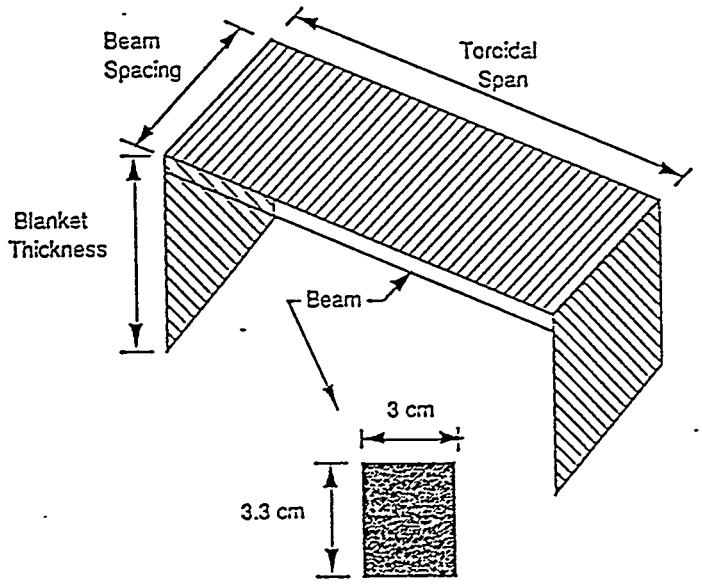

Fig. 8-2. Typical stiffened section of the ITER outboard blanket. In the case of the saddle coil stabilizer, the maximum disruption stress occurs at a section where the toroidal span and blanket thickness are 0.8 m and 0.5 m, respectively. In the case of the twin loop stabilizer, the maximum disruption stress occurs at the midplane section where the toroidal span and blanket thickness are 1 m and 0.3 m, respectively.

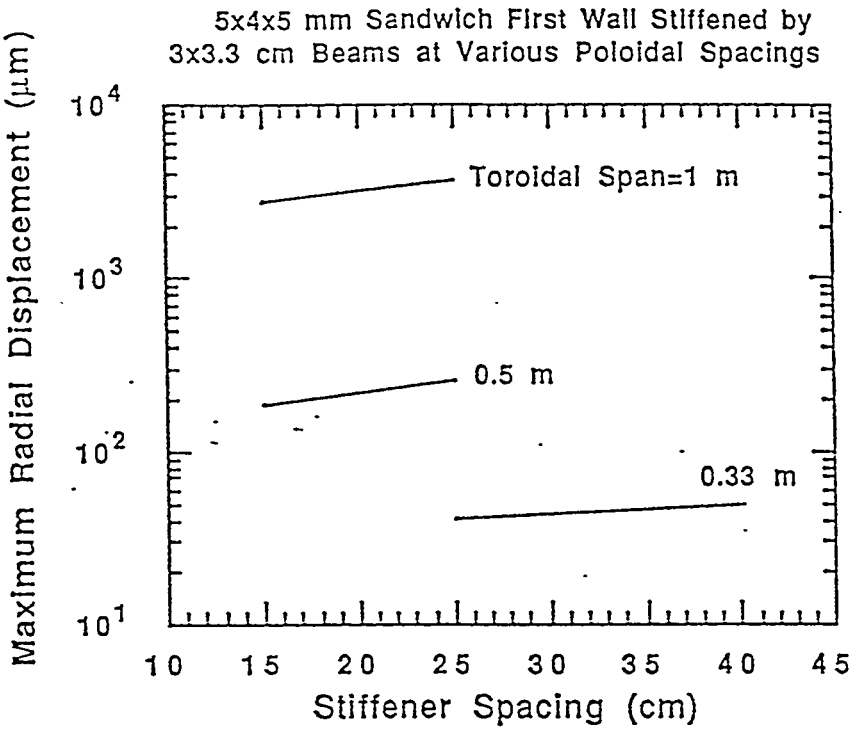

Fig. 8-3. Variation of the maximum radial displacement of the first wall stiffened by 3 × 3.3 cm beams with poloidal spacings due to a pressure of 0.1 MPa and for two toroidal spans.

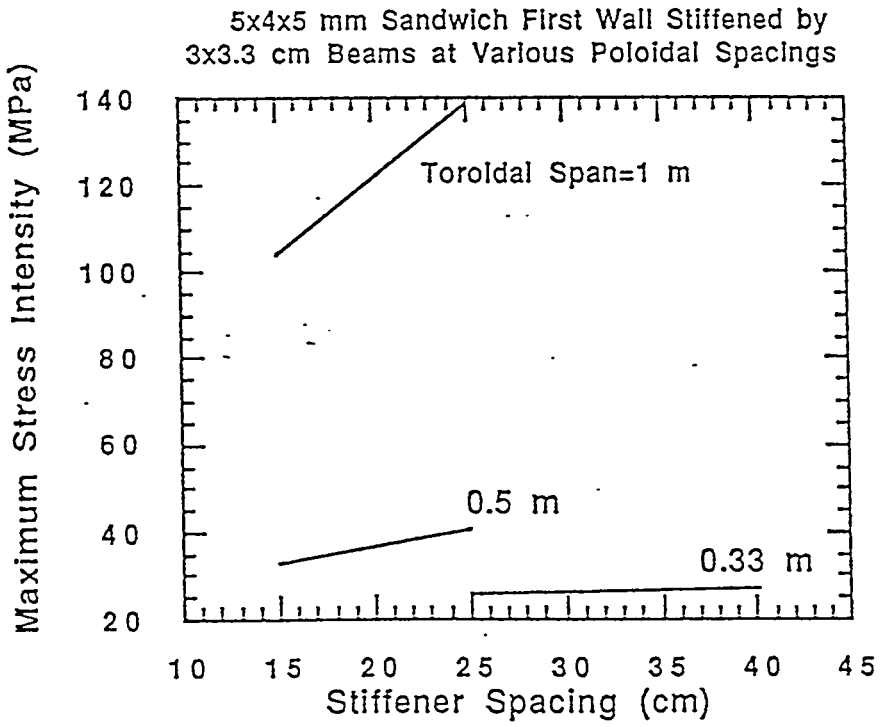

Fig. 8-4. Variation of the maximum stress intensity of the first wall stiffened by 3 × 3.3 cm beams with poloidal spacings due to a pressure of 0.1 MPa and for three toroidal spans.

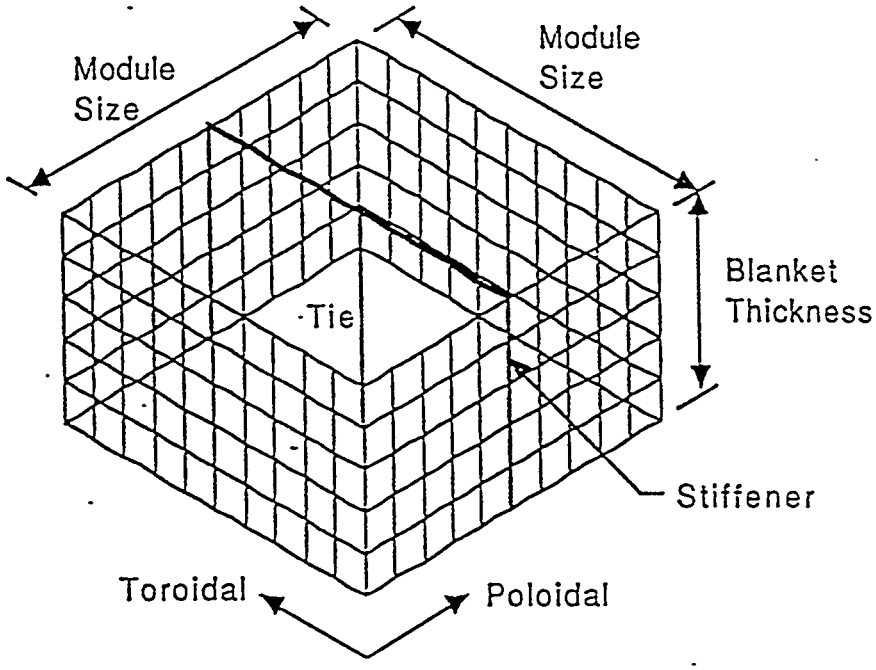

Fig. 8-5. Typical square module geometry (first wall not shown) with a single toroidal stiffening beam which is attached to the shield at the center for added rigidity.

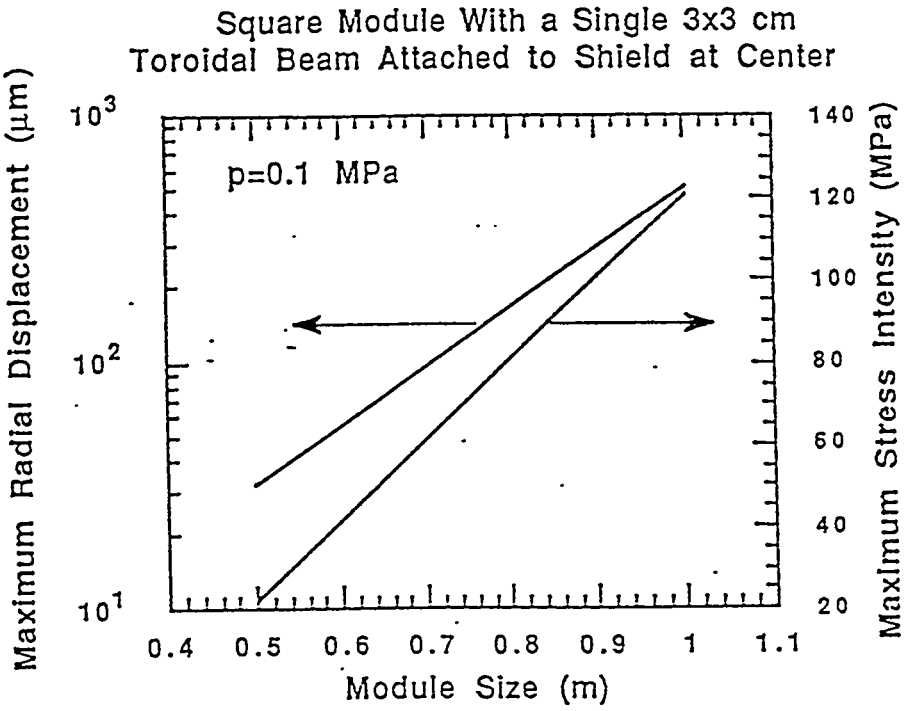

Fig. 8-6. Variation of the maximum radial displacement and maximum stress intensity in the first wall as functions of the module size. Note that to satisfy a 100 μm maximum displacement criterion, the maximum permissible module size is ≤ 0.7 m.

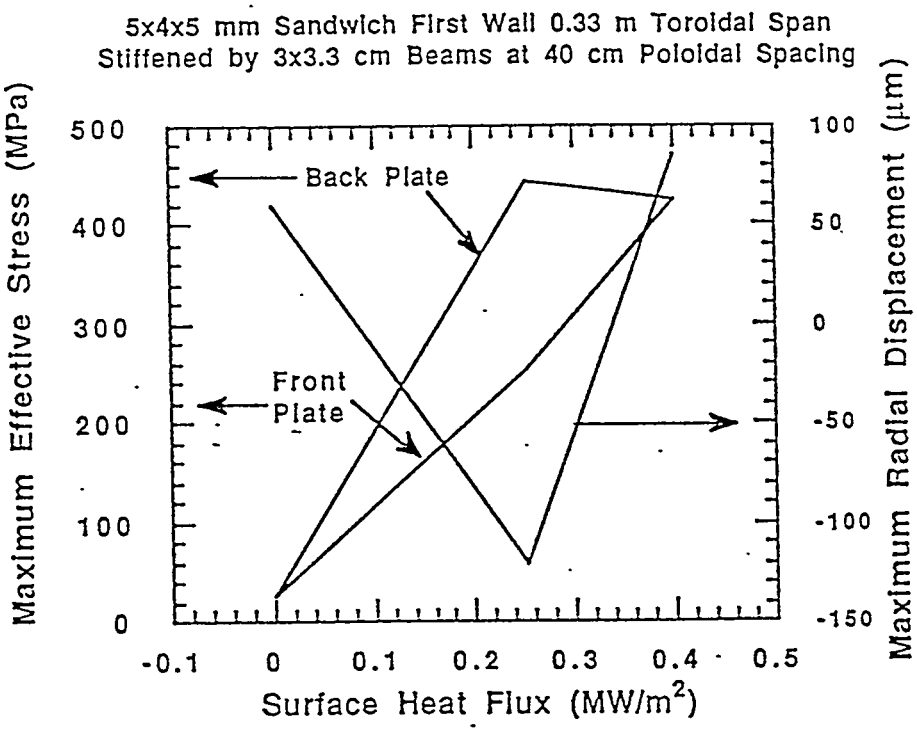

Fig. 8-7. Variation of the maximum radial displacement and maximum effective stress in the first wall of toroidal span 0.33 m stiffened by 3 × 3.3 cm beams at 40 cm spacing as functions of surface heat flux.

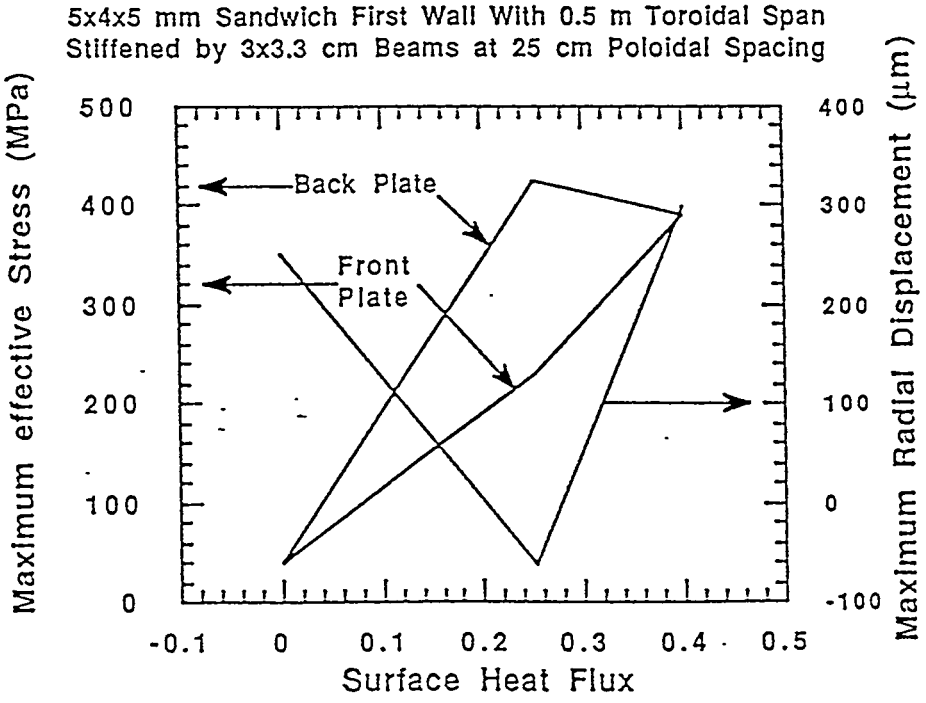

Fig. 8-8. Variation of the maximum radial displacement and maximum effective stress in the first wall of toroidal span 0.5 m stiffened by 3 × 3.3 cm beams at 25 cm spacing as functions of surface heat flux in MW/m^2.

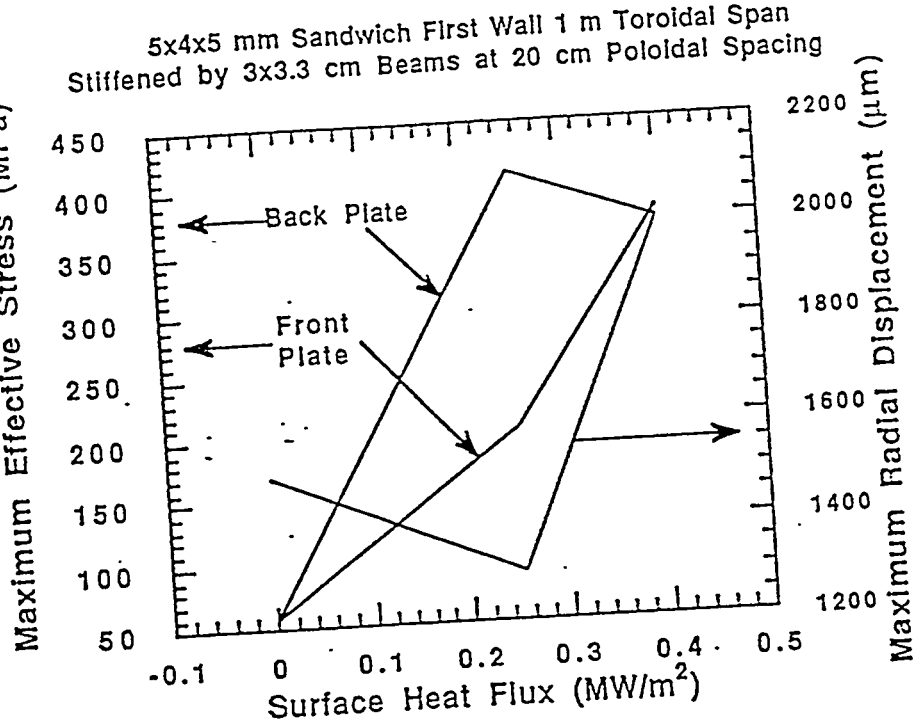

Fig. 8-9. Variation of the maximum radial displacement and maximum effective stress in the first wall of toroidal span 1 m stiffened by 3 × 3.3 cm beams at 20 cm spacing as functions of surface heat flux. Results include the effects of an internal pressure of 0.05 MPa.

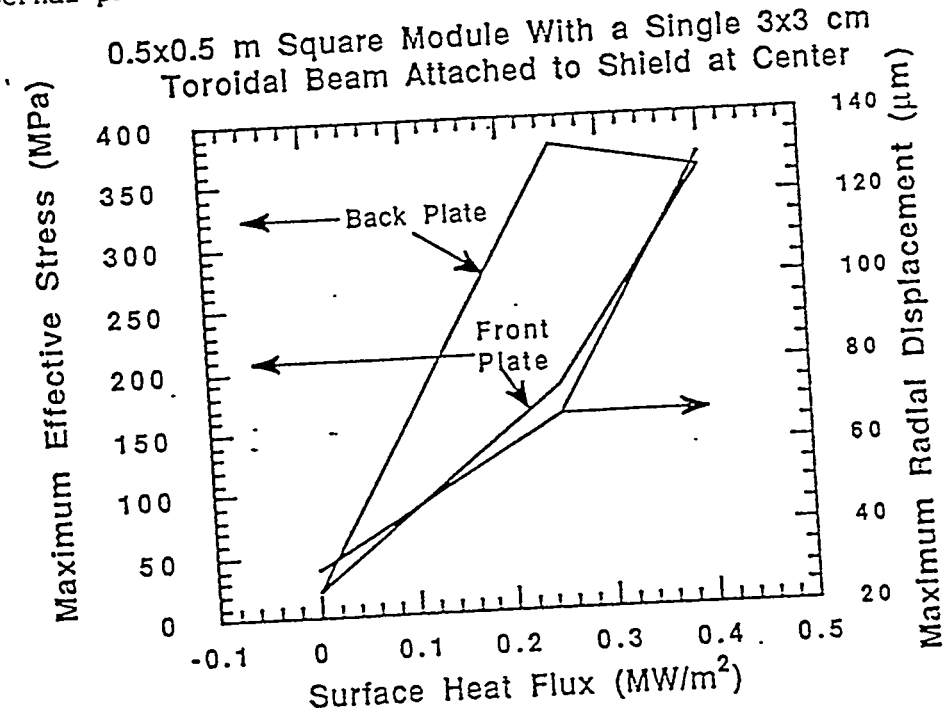

Fig. 8-10. Variation of the maximum radial displacement and maximum effective stress in the first wall of a 0.5 m square module with a single tie as functions of the surface heat flux. Note that to satisfy the 100 μm maximum displacement criterion, the maximum permissible heat flux is ≤ 0.33 MW/m^2.

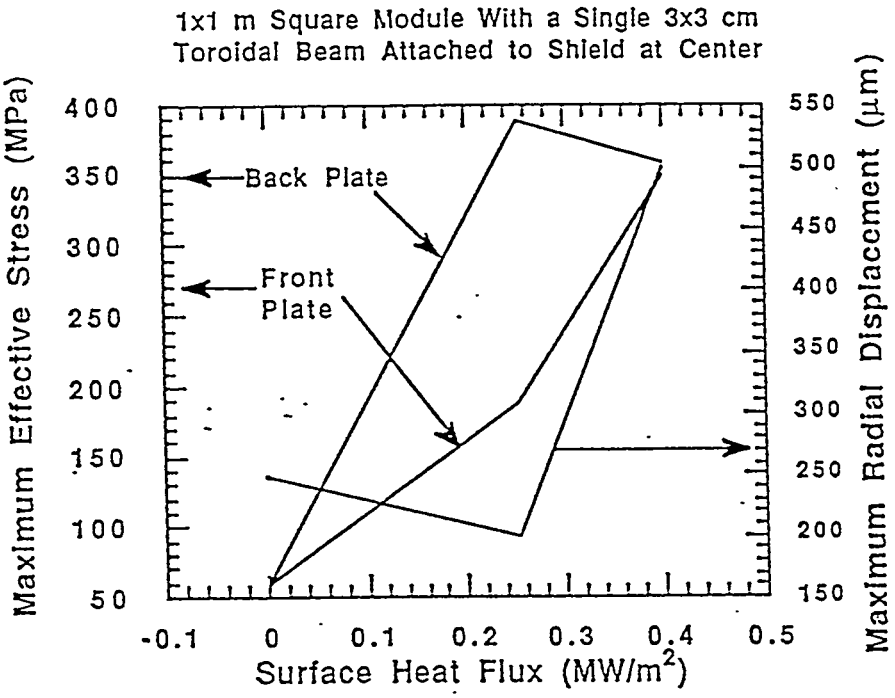

Fig. 8-11. Variation of the maximum radial displacement and maximum effective stress in the first wall of a 1 m square module with a single tie as functions of the surface heat flux.

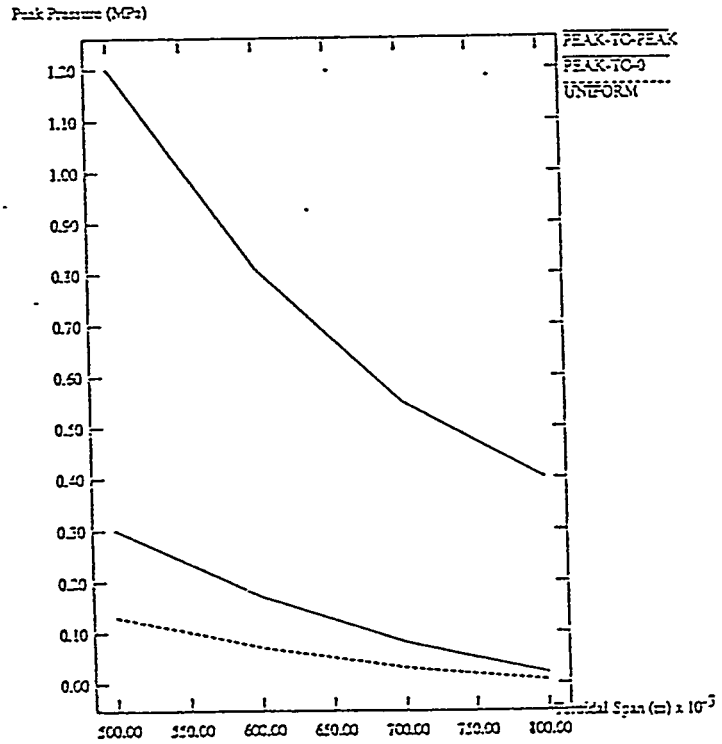

Fig. 8-12. Allowable disruption pressure for a 4/4/6 first wall, assuming a uniform 0.1 MPa internal blanket pressure. Each curve represents a different generic distribution of disruption pressure.

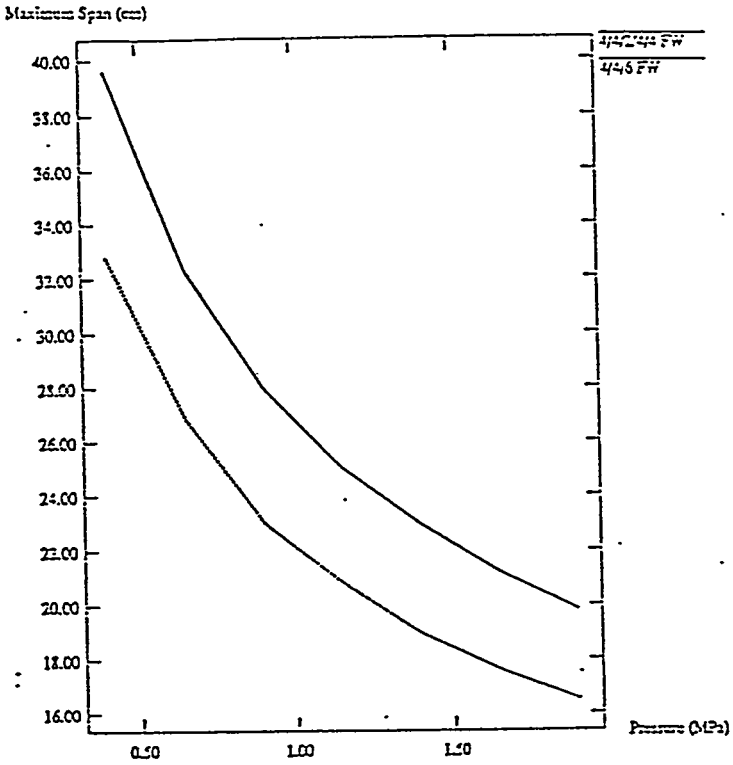

Fig. 8-13. Allowable toroidal span between stiffeners, assuming a 0.1 MPa uniform internal box pressure.

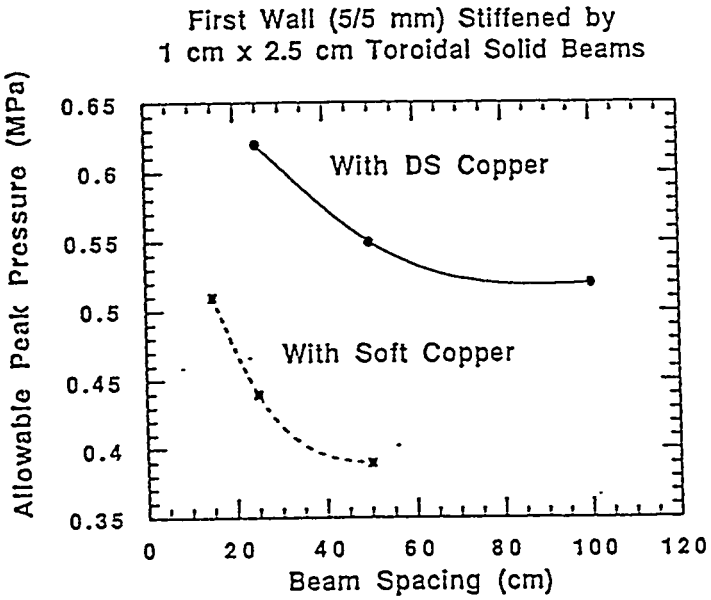

Fig. 8-14. Allowable peak electromagnetic pressure during disruptions for a design using saddle coil stabilizer as a function of stiffening beam spacing using either soft copper or DS copper. The first and side walls consist of two 5 mm thick stainless steel plates separated by 4 mm high coolant channels. No additional stiffening may be required if DS copper is used for the 5 mm copper layer. The toroidal span and radial blanket thickness at the location of maximum pressure are assumed to be 0.8 m and 0.5, respectively.

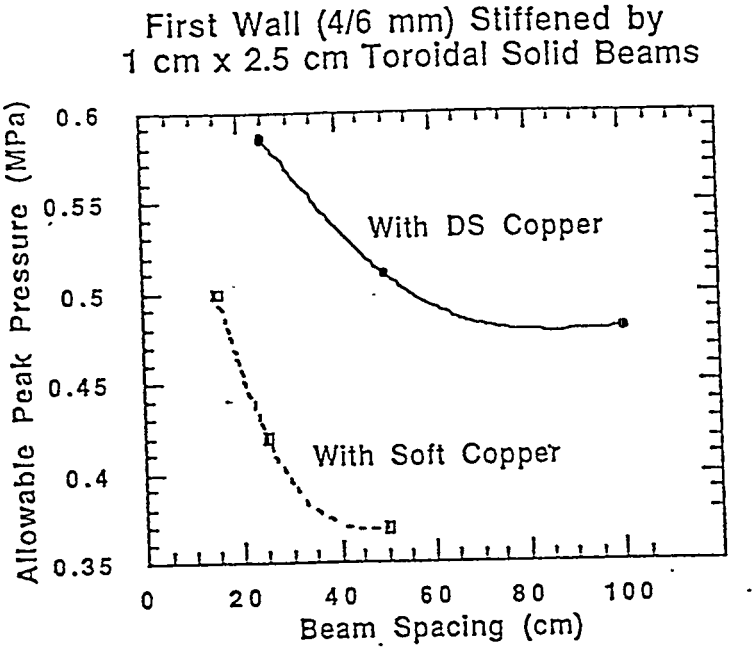

Fig. 8-15. Allowable peak electromagnetic pressure during disruptions as a function of stiffening beam spacing using either soft copper or DS copper. The first and side walls consist of two stainless steel plates, 4 mm and 6 mm thick, separated by 4 mm high coolant channels. Very little additional stiffening is required if DS copper is used for the 5 mm copper layer. The toroidal span and radial blanket thickness at the location of maximum pressure are assumed to be 0.8 m and 0.5 m, respectively. The spacing can be varied in the poloidal direction to take into account the poloidal variation of the electromagnetic loading.

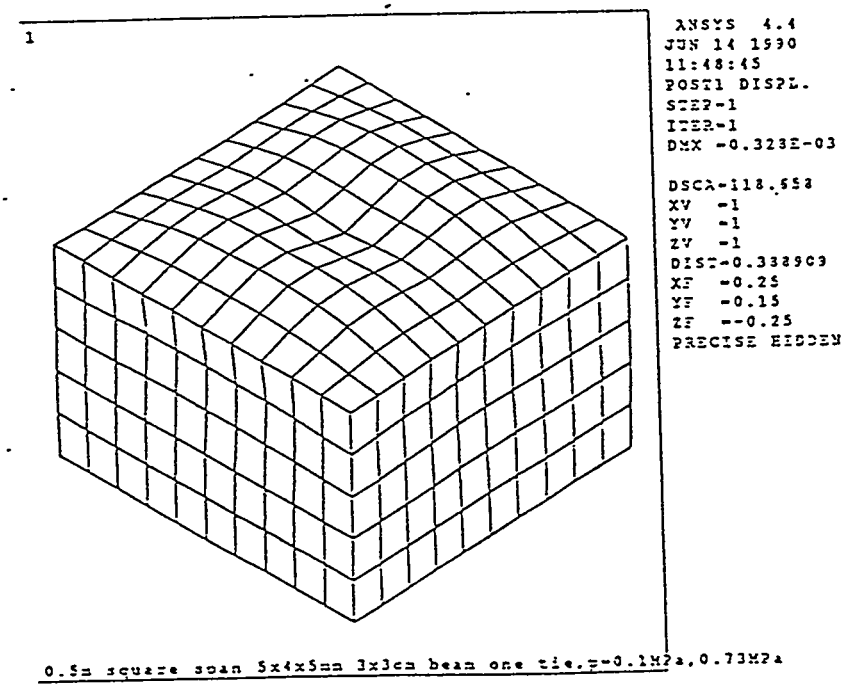

Fig. 8-16. Displaced shape of a typical 0.5 m square module of the ITER outboard first wall (using twin loop stabilizer coils) at the midplane during disruption using a single tie at the center.

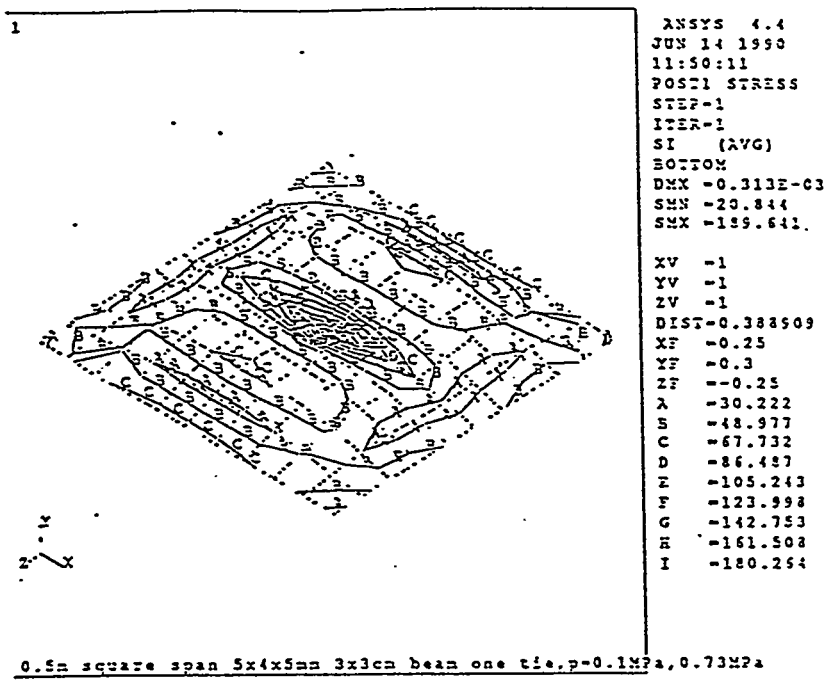

Fig. 8-17. Plot of the contours of effective stress in the back plate of a typical 0.5 m square module of the ITER outboard first wall (using twin loop stabilizer coils) at the midplane during disruption using a single tie at the center.

8.4 Blanket Components

Figures 8-18 through 8-20 show the blanket components in increasing levels of details with the alternating layers of Be, steel, and Li_2O. With average temperature differences from material-to-material, along with temperature gradients across each material, it is important to design the blanket to accommodate expansion without putting large displacement loads on the first wall. At the same time, reasonable integrity of heat-conducting interfaces should be maintained in the radial (thickness) direction to avoid excessive temperatures.

The toroidal span of an outboard module is ~1 m. From Fig. 8-18, it is shown that gas spaces are between the toroidal ends of the Be/steel/Li_2O layers and the side walls. As these gas regions are designed to allow ample flow of the He purge gas and to minimize toroidal heat flow, they can also be used to accommodate toroidal expansion of the Be/steel/Li_2O layers. However, the radial (i.e., heat transfer) direction has no planned sizable gaps, thus requiring a more careful deformation analysis and accommodation. During reactor start-up the main causes of deformation are thermal expansion for the blanket components and He pressure for the first wall. As time proceeds, the major cause of additional deformation is swelling of the Be and Li_2O.

Several cases were considered to determine what stresses would build up in the blanket components under the unrealistic case of total radial restraint. While this condition would be desirable from a heat transfer perspective, the resulting stresses would be higher than the compressive strengths of the blanket materials and high loads would be transferred to the first wall. Thus, this condition would be undesirable from a structural-integrity viewpoint. In the following analyses, the thermal and swelling deformations are quantified. The thermal deformation will be accommodated by as-fabricated gas-gap layers in the radial direction such that the gaps will be closed with low interfacial pressure or nearly closed at full power. An analysis is also performed to determine the amount of swelling deformation to be expected and the effects of such deformation on first-wall/blanket components.

Beginning of Life Results

Referring to Fig. 8-18, it is assumed that the side walls of the blanket box and region behind the last Be layer are relatively cool (~60°C). It is

also assumed that the thick shield region at the back of the blanket is rigid. The free thermal expansions for all other components are calculated relative to 60°C and reported in Table 8-4. Also reported in the Table is the deformation of the Be due to curvature in the presence of a temperature gradient. The Be will curve into the shape of a segment of a hollow sphere with the hot surface forming the outer boundary and the cold surface forming the inner boundary. Although detailed ANSYS calculations were performed to determine the Be displacement, a simple strength of materials formula, which was benchmarked to the ANSYS results, can be used to find the maximum radial (δ_{max}) distance between the center of the top (or bottom) surface and a top (or bottom) corner of the sphere:

$$\delta_{max} = a^2 \bar{\alpha}_m (T_{max} - \bar{T})/(2\ h) \qquad (8\text{-}1)$$

where a = the toroidal and poloidal dimension of the Be block, h = the radial thickness of the block, $\bar{\alpha}_m$ is the mean thermal expansion coefficient, T_{max} is the maximum Be temperature, and $\bar{T} = (T_{max} + T_{min})/2$ is the average Be temperature. The poloidal and toroidal expansion of each block (at the hot surface) due to the temperature gradient is given by

$$\tau_{max} \doteq \bar{\alpha}_m (T_{max} - \bar{T})\ (a/2) \qquad (8\text{-}2)$$

Clearly, the values for δ_{max} and τ_{max} are sensitive to the dimension a. The base case is calculated for a cubic block (a=h).

The results in Table 8-4 show that free expansion (relative to 60°C) of the blanket components between the first wall and the shield results in a total increase in radial thickness (Δh) of 1.5 mm. This could easily be accommodated by allowing a total fabricated clearance of 0.67 mm in the first breeder cell (front) and a 0.82 mm in the second breeder cell (back). The increase in toroidal length (ΔL) for each layer is also listed in Table 8-4. The Li_2O breeder, because of its large thermal expansion, has the largest increase in ΔL (12.9-13.6 mm). Thus, it would be sufficient to leave an extra 7 mm of space between each end of the Li_2O and the side walls to accommodate this.

The local gaps induced by Be curvature range from a maximum value of ~16 μm for the first row of Be blocks to 76 μm for the last row of Be blocks. These are reasonable in light of the assumed surface roughnesses of the first row (18 μm) and the last row (40 μm). If these gaps (due to the curvature of Be under a temperature gradient) prove to be a problem based on the heat transfer analysis, they can be reduced significantly be decreasing the poloidal/toroidal dimensions. For example, if the fourth-row blocks were reduced in size to 35 × 35 × 71 mm, the maximum gap would be reduced from 76 μm to 18 μm.

Under conditions of free thermal expansion of the blanket components, the only material which is under significant stress after full reactor power has been reached is the Li_2O breeder plates due to thermal stresses induced by the non-linear temperature profile. The tensile strength of Li_2O is estimated to be only ~20 MPa for 80% dense, 20-μm-grain diameter Li_2O at ~500°C. The maximum tensile thermal stress is calculated to be ~160 MPa for the first plate. Thus, some thermal-stress-induced cracking of the Li_2O (parallel to the heat flow path) may occur. If this proves to be undesirable, further segmenting of the Li_2O blocks may be in order.

End-of-Life Results

While it is preferable to provide as-fabricated clearance gaps to allow for thermal expansion, it is not desirable to build in extra space between the layers of material to accomodate swelling. Thermal expansion is essentially an instantaneous response to temperature increase. Swelling occurs relatively slowly in time. In this subsection the magnitudes of Li_2O and Be stress-free swelling are calculated. Several problems are solved to bound the stresses induced in these materials due to various restraint conditions. Finally, the overall stress-deformation of the blanket module is discussed.

In Table I of Section 4.2, the peak swelling of Li_2O observed in experiments is listed as 7% at 3 at. % Li burnup. However, at 500°C Li_2O was actually observed to densify by ~3% in closed capsule experiments. This may have been due to the presence of higher moisture levels in the closed capsules than are anticipated under ITER operating conditions. To be conservative, an end-of-life volumetric swelling value of 5% is recommended.

The correlation listed in Section 4.2 for Be swelling is a function of temperature and helium content. Also, the irradiation creep equation, which is needed for calculating stresses under the condition of restrained swelling, is a function of dpa. Both the dpa rate $\dot{D}$ and the helium production rate $\dot{G}_\alpha$ are listed in Table 8-5 as functions of radial position at the outboard core-midplane for the technology phase. The corresponding local swelling values are also listed for each position. The end-of-life swelling strain is highest (~2.6%) within the Be zone closest to the plasma. For most locations within the blanket, the swelling is low (<1%) and less than the thermal strain.

Table 8-6 summarizes the change in Be zone thicknesses due to both thermal expansion and swelling. Even if the Be were free to expand, there would be some stress induced by the non-linear swelling gradient. Also, there would be some restraint on the Be if no space were provided for this swelling. An upperbound analysis was performed to determine the swelling-induced stresses in the Be under the condition of complete radial restraint. As the stresses build up in time due to this restraint, they are partially relaxed by irradiation/thermal creep until an equilibrium stress is reached. The value of this stress is obtained by simply setting the swelling rate equal to the creep rate. It is listed in Table 8-6 along with an estimate of the minimum compression strength of Be. Notice that there is a factor of ~2 margin between this upperbound stress and the failure stress. Thus, regardless of any external- or self-restraint, the Be will not fail due to swelling induced stresses.

From the results in Table 8-6, it is clear that the total increase in Be layer thickness at the outboard core midplane due to swelling (1.10 mm) is about the same as the increase due to thermal expansion (1.24 mm). The major difference is that the thermal strains are accommodated by as-fabricated gaps resulting in no load transmitted to the first wall while the swelling strains will result in some load transmitted to the first wall. This is discussed in the next subsection.

Interaction between Blanket Components and First Wall

Be swelling results in an increase in blanket thickness of 1.1 mm over the life of the blanket. Li_2O swelling (assumed to be 5 vol. %) causes a free

increase in thickness of 0.27 mm. Thus a total of 1.37 mm of blanket expansion needs to be accommodated without causing excessive loading of the first wall. Toroidal accommodation of the swelling is relatively straightforward and is accomplished by as-fabricated spacing between the blanket and the side walls.

Analyses have been initiated (but not completed) to determine the first wall stresses due to blanket swelling. The effective stiffness (i.e., spring constant) of the blanket Be/SS/Li_2O layers has been calculated to be ~400 MPa/mm at the outboard core midplane position. As this stiffness is much higher than the stiffness of the first wall over its span in contact with the blanket, it can be assumed that the resulting interface pressure between blanket and first wall will be small. The driving force for differential swelling stresses is the difference between the blanket displacement ($\delta_b \leq$ 1.37 mm) and the initial pressure-induced expansion of the first wall (δ_f) which varies along its span. As δ_b increases in time, first-wall stresses will increase and will be partially relaxed by irradiation creep of the first wall. An equilibrium stress will be reached before the end-of-life. If this stress is higher than desirable, then several design options are available: increasing the geometric flexibility of the first wall, increasing the space between the blanket and side-walls, tapering the sintered Be blocks as they approach the side walls; and/or replacing the layer of sintered Be blocks near the first wall with a more flexible pebble bed. The optimum solution is obtained by iterating between the structural analysis and the thermal analysis until satisfactory performance is achieved.

As this analysis has not yet been completed, the recommended design solution is one which accounts for thermal expansion in the as-fabricated radial gaps and thermal/swelling expansion in the toroidal gaps between blanket components and the side walls. Table 8-7 summarizes these results. The radial clearance in the first breeder cell (δ_1) is 0.7 mm and the radial clearance in the second breeder cell(δ_2) is 0.83 mm.

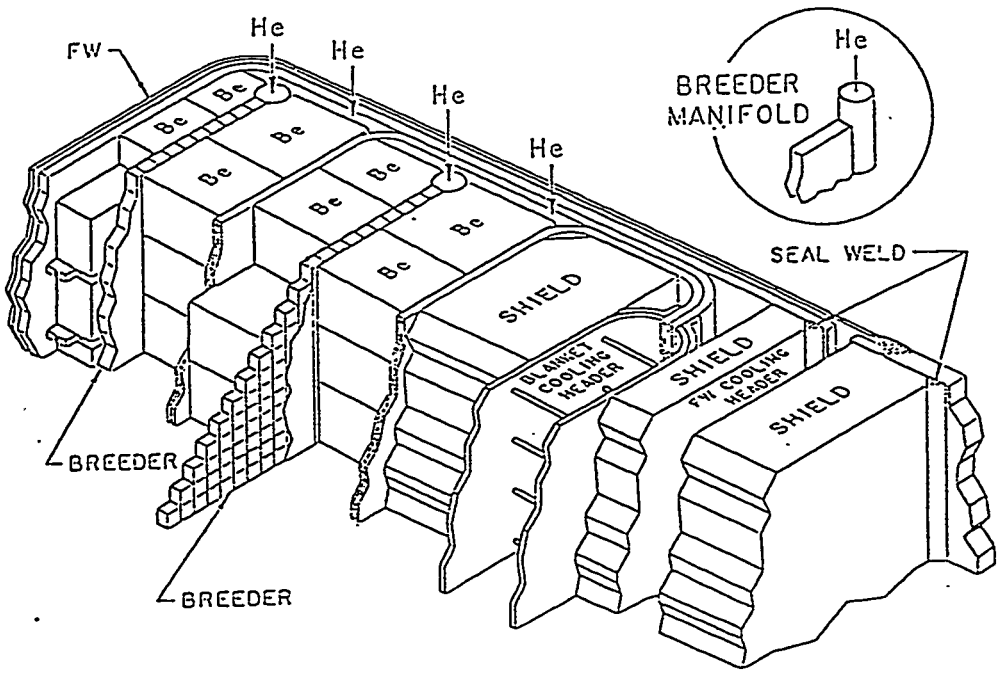

Figure 8-18. Isometric view of U.S. outboard blanket for ITER.

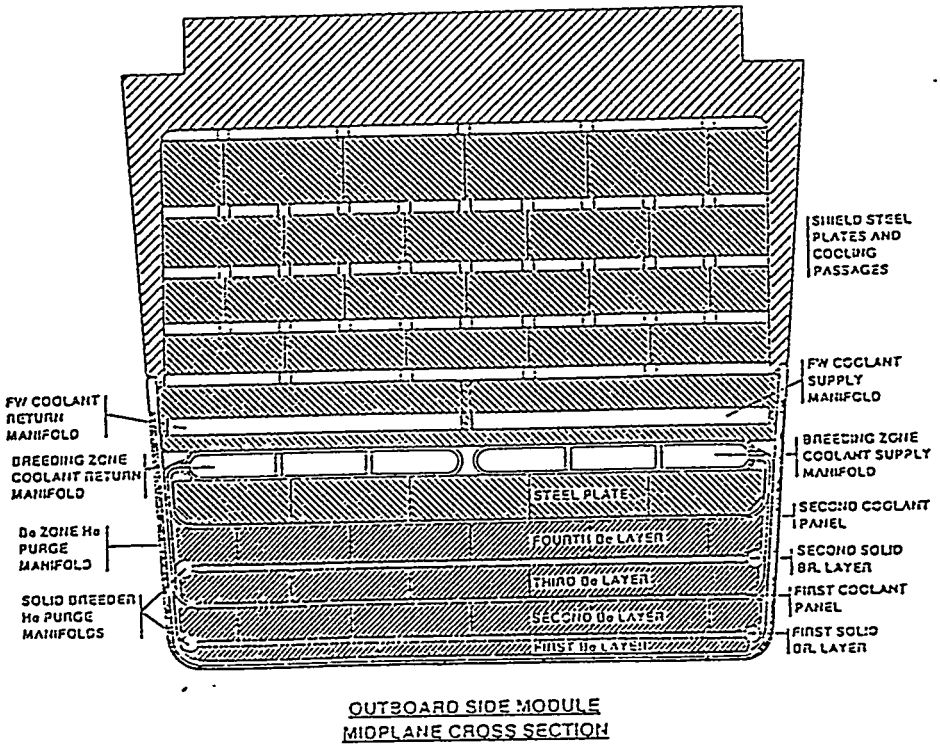

Figure 8-19. Midplane cross section of U.S. outboard blanket for ITER.

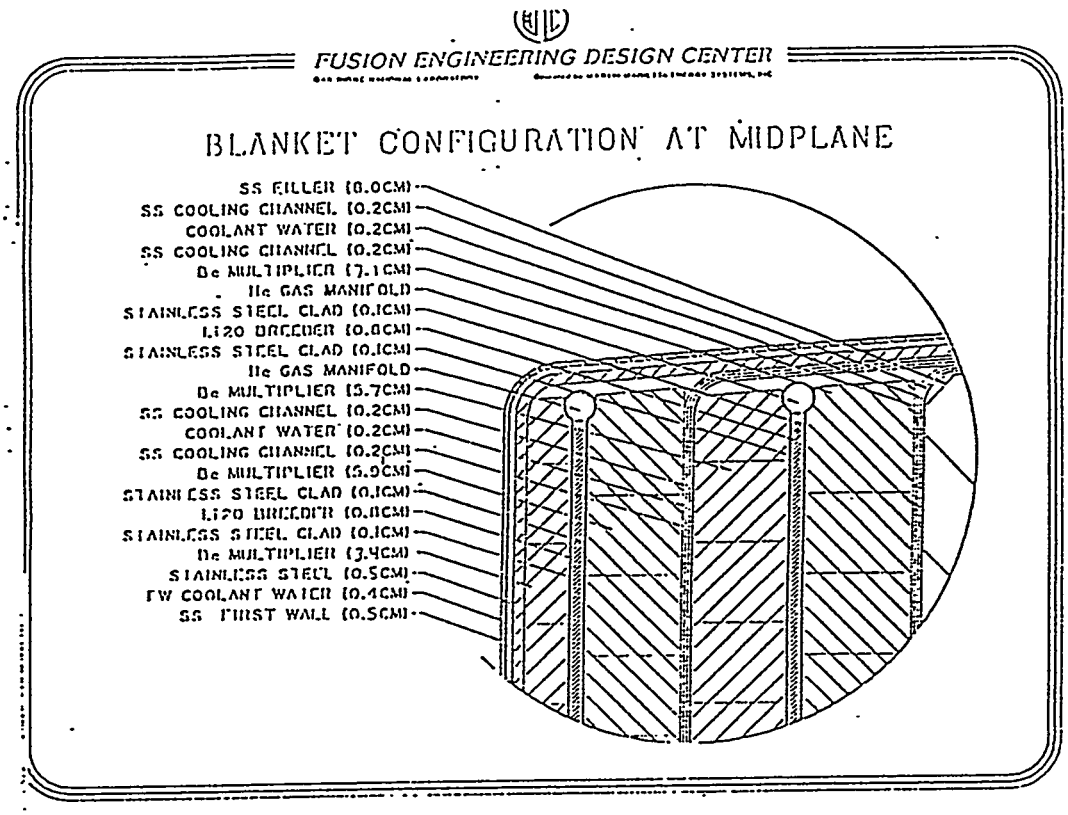

Figure 8-20. Blanket configuration at midplane.

Table 8-4.
Deformation Due to Free Thermal Expansion of Blanket Components at the Outboard Core Midplane Position for a 1 meter Toroidal Span

Layer (DF)	h, mm	T, °C		Thermal + Bending Expansion, mm		Maximum
		Min.	Max.	Δh	ΔL	Local Gap, μm
SS first wall	5	77	191	0.007	1.39	---
H_2O	4	---	---	---	---	---
SS back wall	5	82	225	0.009	1.80	---
Be (0.85)	34	280	401	0.214	6.27	15.6
SS clad	1	426	438	0.009	9.16	---
Li_2O (0.80)	8	453	537	0.109	13.63	---
SS clad	1	424	437	0.009	9.11	---
Be (0.85)	59	192	401	0.327	5.56	44.8
SS coolant channel	2	77	138	0.002	0.87	---
H_2O	2	---	---	---	---	---
SS coolant channel	2	70	109	0.001	0.53	---
Be (0.65)	57	138	421	0.312	5.46	57.4
SS clad	1	435	446	0.009	9.45	---
Li_2O (0.80)	8	451	505	0.103	12.87	---
SS clad	1	434	441	0.009	9.35	---
Be (0.65)	71	123	427	0.386	5.45	76.4
SS coolant channel	2	68	99	0.000	0.04	---
H_2O	2	---	---	---	---	---
SS coolant channel	2	60	60	0	0	---

Table 8-5. Be temperature, damage rate ($\dot{D}$), He production rate ($\dot{G}_\alpha$) and end-of-life swelling values ($\Delta V/V_o$) as a function of radial position (x) for the outboard core midplane at a technology-phase wall loading of 1.2 MW/m^2 for 3.792 effective full power years.

Be Zone	x, mm	T, °C	$\dot{D}$, dpa/y	$\dot{G}_\alpha$, appm/y	$\Delta V/V_o$, %
1	0	280	5.08	3961	1.50
	10	316	4.81	3698	1.53
	20	351	4.55	3452	1.73
	30	387	4.30	3222	2.26
	34	401	4.21	3137	2.59
2	0	401	4.09	2680	2.10
	10	366	3.88	2435	1.29
	20	330	3.67	2212	0.92
	30	295	3.48	2010	0.75
	40	259	3.30	1826	0.65
	50	224	3.13	1659	0.58
	59	192	2.98	1508	0.62
3	0	138	2.67	1331	0.46
	10	188	2.52	1238	0.43
	20	237	2.39	1151	0.40
	30	287	2.26	1070	0.38
	40	337	2.14	995	0.39
	50	386	2.02	925	0.47
	57	421	1.94	860	0.61
4	0	427	1.60	708	0.50
	10	384	1.51	653	0.31
	20	341	1.43	602	0.23
	30	299	1.35	555	0.19
	40	256	1.28	511	0.17
	50	213	1.21	471	0.16
	60	170	1.14	435	0.14
	70	127	1.08	401	0.13
	71	123	1.07	369	0.12

Table 8-6. Summary of results for increase in Be radial thickness at the outboard core midplane due to free thermal expansion and end-of-life swelling. Upperbound stresses due to complete radial restraint of swelling are also included.

Parameter	Be Zone			
	1	2	3	4
h_o, mm	34	59	57	71
ρ, % TD	85	85	65	65
$\bar{D}$, dpa	17.6	13.3	8.67	5.00
$\bar{G}_\alpha$ 10^3 appm	13.4	7.73	4.09	1.97
$\bar{T}$, °C	341	297	280	275
Thermal Δh, mm	0.214	0.327	0.312	0.386
Swelling Δh, mm	0.577	0.313	0.142	0.0717
Constrained swelling stress, MPa	74.4	45.8	24.1	19.3
Minimum failure strength, MPa	129	132	49	49

Table 8-7.

Summary of recommended as-fabricated radial clearances (δ) to accommodate blanket thermal expansion and as-fabricated toroidal spaces (τ) between blanket components and side-walls to accommodate thermal and end-of-life swelling expansion at the outboard core-midplane position.

Layer (DF)	h, mm	$\bar{T}$, °C	Radial Thermal Expansion, mm	Min. Toroidal Clearance τ, mm
SS first wall	5	134	0.007	0.70
H_2O	4	60	---	---
SS back wall	5	154	0.009	0.90
Be (0.85)	34	341	0.214	11.6
SS clad	1	432	0.009	4.6
Li_2O (0.8)	8	509	0.109	14.7
SS clad	1	431	0.009	4.6
Be (0.85)	59	297	0.327	5.4
δ_1 clearance	0.70	---	---	---
SS coolant channel	2	108	0.002	0.4
H_2O	2	60	---	---
SS coolant channel	2	90	0.001	0.3
Be (0.65)	57	280	0.312	4.0
SS clad	1	441	0.009	4.7
Li_2O (0.80)	8	487	0.103	14.7
SS clad	1	438	0.009	4.7
Be (0.65)	71	275	0.386	3.2
δ_2 clearance	0.83	---	---	---
SS coolant channel	2	84	0.000	0.02
H_2O	2	60	---	---
SS coolant channel	2	60	0	0

8.5 Thermal Performance under Deformation

The as-fabricated gaps (see Section 8.4) are designed so that the Li_2O breeder and Be will be in nominal (i.e., low interface pressure) contact with stainless steel layers once full reactor power is achieved. It is important to examine the sensitivity of the heat transfer coefficients at the interfaces and the overall thermal performance of the blanket to deformation and uncertainties in interface conditions. In particular, conditions which may cause a low heat transfer coefficient are explored. It is showed in Section 7 that because of the low heat fluxes involved, uncertainties in the higher values of gap conductance ($\gtrsim$ 4000 W/m^2-K) have little impact on the breeder temperatures.

In the previous section, the Be blocks were designed such that the maximum gap between the thermally-curved Be and the stainless steel was on the order of the surface toughness. The effects of this curvature on the heat transfer are now explored, along with the possibility of hot gas gaps being present. The assumed gas pressure is 0.1 MPa for these sensitivity calculations.

From Section 4.2, the equation for the heat transfer coefficient for Be/SS interfaces in marginal contact (at surface roughness heights) or with a hot gas gap (G) is

$$H = 3.366 \times 10^3 \left[(G + 2 + 110\ P) + 6.95 \times 10^{-3}\ T_g^{1.168}\right]^{-1} T_g^{0.668} \qquad (8\text{-}3)$$

where H is in W/m^2-K, T_g = average interface temperature, G = hot gap in μm, and P = porosity volume fraction (used to estimate the roughness).

It is useful to evaluate the effect of hot gap size on the effective conductivity of the whole Be region (radial thickness = h). Let $\bar{k}_b$ be in the average conductivity of the porous Be material, H_h be the heat transfer coefficient at the hot (T_h) Be/SS interface and H_c be the heat transfer coefficient at the cold (T_c) Be/SS interface. The effective thermal conductivity is defined in terms of the heat flux (q'') and the steel interface temperatures (T_h, T_c) as

$$k_{eff} \equiv \frac{hq''}{T_h - T_c} \ ,$$

where

$$k_{eff} = \left[1/\bar{k}_b + (1/h)(1/H_c + 1/H_h)\right]^{-1} .$$

The reference case for analysis is for zero hot gap (G=0). The sensitivity study is performed by letting G vary and investigating the effect on k_{eff}. Table 8-8 shows the effect of hot gap size, G, on k_{eff}. Highlighted in the table are the hot gap sizes caused by the average gas gaps due to Be curvature.

Table 8-8.

Sensitivity of the effective conductivity (k_{eff}) for the SS/Be/SS zones as a function of hot gap size. These are ratioed to the k_{eff} for zero gap size (k^o_{eff}) for the four regions (51.31, 63.05, 27.92, and 29.22 W/m-K, respectively.)

G, μm	k_{eff}/k^o_{eff} #1	#2	#3	#4
0	1	1	1	1
1	0.989	0.991	0.996	0.996
2	0.976	0.982	0.991	0.992
5	0.942	0.955	0.978	0.981
7.8	0.911	---	---	---
10	0.890	0.915	0.957	0.964
20	0.801	0.843	0.918	0.930
22.4	---	0.827	---	---
28.7	---	---	0.887	---
38.2	---	---	---	0.874
50	0.618	0.682	0.818	0.841
100	0.447	0.517	0.692	0.725
200	0.288	0.349	0.529	0.569
500	0.139	0.176	0.310	0.346

From Table 8-8, it is clear that the effect of Be curvature on the total heat transfer from the SS/Be/SS region is relatively small. It is ~9% for the first zone, ~17% for the second zone, ~11% for the third zone and ~13% for the fourth zone. These numbers can further be reduced if the poloidal and toroidal dimensions (a) of the Be blocks were to be reduced to $a/h < 1$.

Table 8-8 can also be used to estimate the maximum hot gap allowed in the design. Obviously, region 4 can tolerate the largest hot gap with only a small effect on the breeder temperatures. This type of calculation is done more rigorously in Section 7.

The first wall will tend to deform away from the first Be layer, which is the most critical with regard to heat transfer and is the most sensitive to hot gaps. An attractive design solution to this problem is to use a Be binary pebble bed for this first region. The pebbles will tend to redistribute as the first wall expands, thereby eliminating any hot gaps between the first wall and the first Be region.

8.6 Mechanical Behavior of Blanket Support System During Bakeout, Operation, Fault Conditions

The concept proposed for the blanket structural support system ties all the blanket/shield modules together. The inboard blanket/shield modules form one cylindrical structure and the outboard blanket/shield modules form a second cylindrical structure. All the electromagnetic loads are reacted internally within these cylinders except the net vertical force. The vertical force is carried into the lower portion of the vacuum vessel, then into the gravity support and finally to ground. A sketch of the inboard structural cylinder concept is shown in Fig. 8-21 and a schematic of the vertical support is shown in Fig. 8-22. The vertical support provides some restraint in the toroidal direction to prevent ratcheting of the blanket/shield structure about its axis and to keep the structure centered. The cylinder is allowed to move radially, however and there is no other connection between the blanket assemblies and the vacuum vessel. The following sections describe the implications of various thermal conditions on the blanket structure.

8.6.1 Bakeout

During bakeout, the blanket/shield module temperature is raised to 350°C, while the vacuum vessel temperature is raised to only about 150°C. This causes the blanket/shield assemblies to grow vertically about 50 mm. Since the support is at the bottom only, there is no restraint to vertical growth and there are no induced stresses. In addition to vertical growth, the inboard blanket/shield cylinder assembly grows radially about 17 mm and the outboard assembly grows 45 mm. Since there is no radial restraint on the cylinder, there should be no induced stresses. If the blanket/shield module tempertures are not raised uniformly during bakeout, high thermal stresses could result. It should also be noted that these movements are from the nominal average operating temperature of 70°C on the outboard and 85°C on the inboard so the total range of movement from room temperature is greater. Table 8-9 summarizes thermal growth values.

Table 8-8. Thermal Growth of Blanket/Shield Modules

Component	Radius at 100°C (operat.)	Radius at 250°C (bakeout)	Radius at 20°C (install.)	Height* @ 100°C (operat.)	Height* @ 250°C (bakeout)	Height* @ 20°C (install.)
Inboard Blanket/ Shield	3710 (85°C)	3710+17 (350°C)	3710-4 (20°C)	10503 (85°C)	10503+47 (350°C)	10503-12 (20°C)
Outboard Blanket/ Shield	9600 (70°C)	9600+45 (350°C)	9600-8 (20°C)	11756 (70°C)	11756+56 (350°C)	11756-10 (20°C)

* Height is measured from vertical support to inner bore of vacuum vessel.

8.6.2 Normal operation

During normal operation, cooling water is introduced at about 60°C into the shield, flows poloidally and feeds into the blanket and first wall. The water flows toroidally through these components and exits at a temperature of about 100°C. The coolant temperature rise in the shield is very slight, on the order of 2°C. The effective temperature distribution, then, is constant in the poloidal direction and has minor radial gradients through the shield where the bulk of the structural mass is. The blanket and first wall see a toroidal gradient of 40°C in the coolant, and a radial gradient of up to 250°C in the first wall stainless steel skin. The gradient between the exit water manifold and the shield creates a shearing stress at this interface and a corresponding poloidal compressive stress in the side wall and first wall of the blanket. The overall distortion of the shield structure should be small, resulting in minimal stress in the structural connections between shield modules.

8.6.3 Fault conditions

Many fault conditions can hypothesized, including loss of coolant to the entire blanket/shield array, loss of coolant to a single blanket/shield assembly, blockage in a flow circuit that effects part of the blanket or shield, etc. Each fault condition would have a unique temperature peak and distribution, so only a general discussion is possible, here, selecting a possible condition and examining the implications.

One typical problem would be a small leak in one blanket/shield module that would cause the machine to be shut down until a repair could be made. The coolant pressure would have to be relieved as quickly as possible to avoied backing water up into the blanket cavity that contains the beryllium or spraying water into the plasma confinement volume. Only accessible leaks could be repaired without removing the module, and these would only be repairable during the early stages of operation, before the radiation damage level exceeds the re-welding limit. Only in rare cases would it be possible to leave the blanket/shield module in the machine. The temperature of the affected module could become very high, would probably have a radial gradient, and could damage the module and the connecting structure to adjacent modules.

In order to prevent damage to the connecting structure, it would be desirable to remove the vertical shear restraint and let adjacent modules slide relative to each other. Unfortunately, this requires that the substantial electromagnetic shear load that occurs during a plasma disruption be carried back into the vacuum vessel. None of the vacuum vessel concepts proposed thus far are capable of carrying this load. The present philosophy is to accept damage to the module that loses coolant and to the structural connections to adjacent modules, but to limit the damage to the adjacent modules themselves.

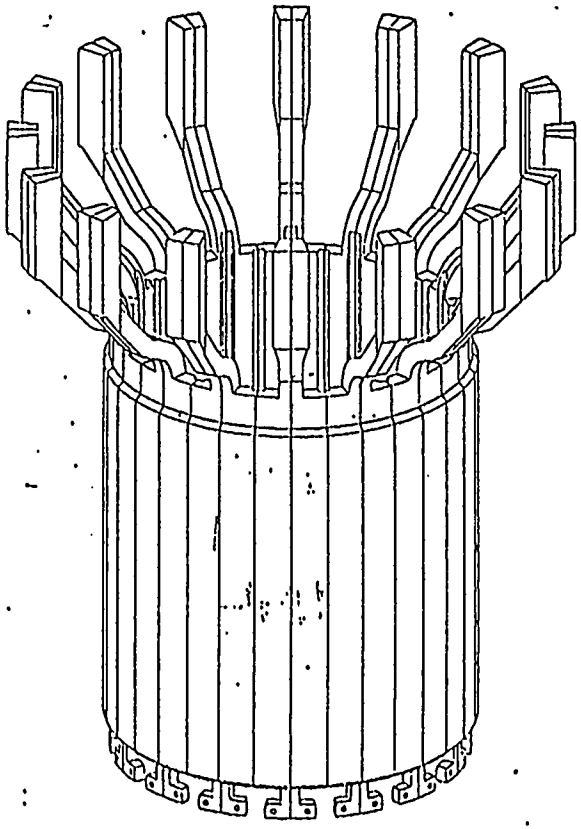

Figure 8-21. Inboard shield/blanket assembly.

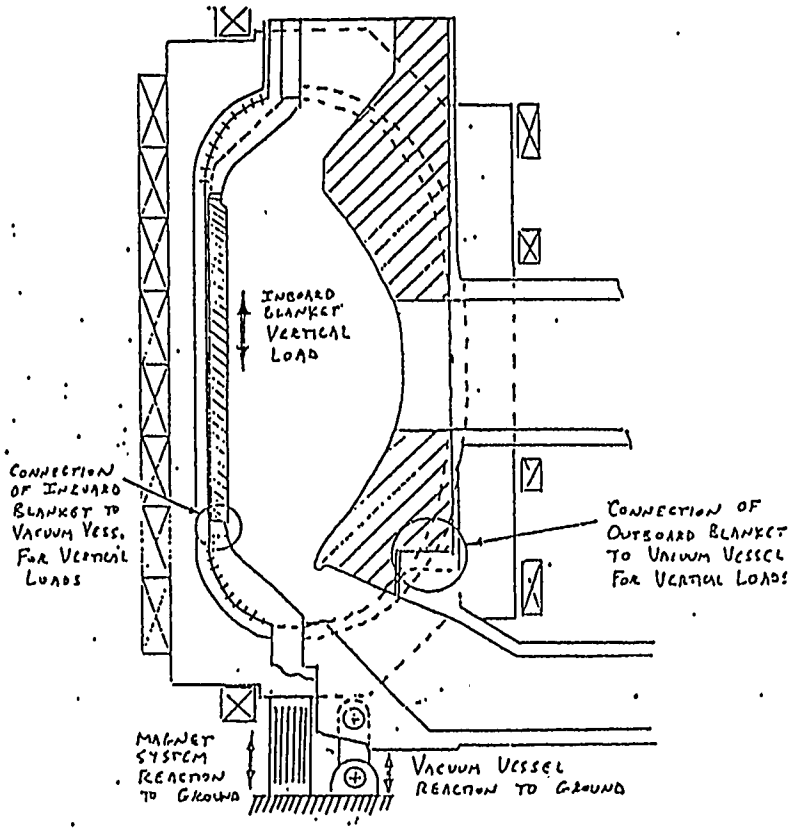

Figure 8-22. Vertical support schematic.

9.0 HYDRAULICS ANALYSIS

The hydraulics analysis for the blanket is given. In addition, thermal-hydraulics analysis for the water-cooled shield and first wall/side walls are given in this section for inboard and outboard regions. The detailed geometry of the coolant systems is recommended based on thermal and mechanical considerations. Several analyses were performed to optimize temperature distribution, thermal stresses and pressure drop in the shield, first wall and side walls. In the shield thermal hydraulics analysis, the temperature distribution, overall coolant routing, thermal stresses and pressure drops have been calculated for both inboard and outboard regions. Coolant channel thicknesses in the shield have been optimized to minimize the pressure drop in the coolant loop without affecting shield performance. Different routes for the coolant were investigated to reduce the maximum temperature in the shielding material. In all cases, the maximum thermal stresses are within the prescribed limits for the material at the maximum operating temperatures. A multilayer configuration is employed for the design of the blanket and shield. The optimum configuration of the shield has been determined from one-dimensional neutronics calculations. The blanket/shield radial build varies poloidally depending on the neutron wall loading. The temperature distribution of the blanket is calculated in Section 7.0. Several radial build configurations of the shield have been thermally analyzed. Thermal stresses in the shielding material determine the thickness of the different layers. The way the coolant is routed in the blanket and shield determines, to a large extent, the pressure drop results. Toroidal routes result in very low pressure losses while the reverse is true for poloidal routes. In the toroidal coolant routing the flow cross sectional area is larger which gives a lower flow velocity. Also, toroidal routing provides a shorter coolant path. The coolant runs poloidally in the inboard blanket/shield and outboard shield, while it runs toroidally in the outboard first wall and blanket. The coolant is supplied and collected at the top of the reactor except for the central lower outboard modules where the supply and the return have to be from the bottom. In this section, the thermal analysis is done for the technology phase and linear scale-up may be used for physics phase calculations. The following are the assumptions used in the hydraulics analysis.

- 1-D thermal analysis
- The coolant is supplied to the first wall, blanket or shield at 60°C.
- The coolant returns upward and is collected at 100°C.
- The vertical extent of the blanket/shield is 8 meters for nuclear heating calculations, while it is 10 meters for pressure drop calculations.
- The coolant velocity in the coolant feed pipes to the FW, blanket or shield is 4.5 m/s.

9.1 Inboard Thermal Hydraulics Analysis

9.1.1 First wall & side walls

The inboard blanket consists of 32 modules. Each module has three sectors separated by an electrical insulator layer. Each sector has a first wall and two side walls. The first wall and the side walls are designed in the form of steel/water/steel layers. Figure 9-1 is a schematic which shows the general configuration of one sector of the inboard blanket/shield. Coolant channels are formed in the steel walls. For each sector the first wall has 6 coolant channels while each side wall has 5 coolant channels. Half of the coolant passing in the first wall, say through the left 3 coolant channels, returns back in the left side wall through the 5 channels (see Figs. 9-1 and 9-2 and the mechanical design section). The first wall/side wall coolant routes can use a single or double coolant loop. The change in width of the first wall and side walls at the top and the bottom of the blanket has been considered in the pressure drop calculations. The results of the thermal-hydraulics analysis for 0.5 cm FW channel thickness are given in Table 9-1.

9.1.2 Inboard shield

The shield consists of alternating layers of 316 stainless steel and water. Nuclear heating results obtained from one-dimensional neutronics

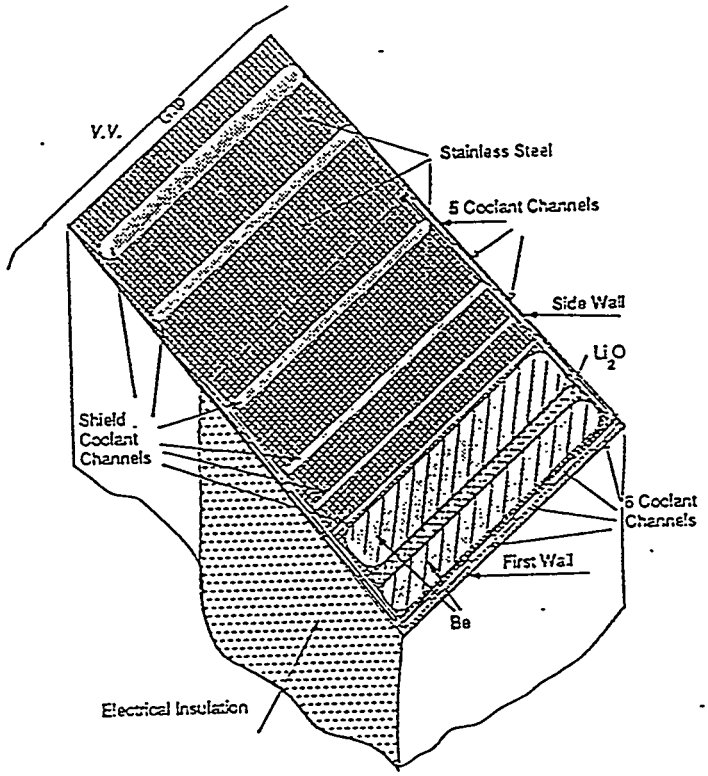

Figure 9-1. A schematic layout for 1/96 (one sector) of inboard blanket and shield.

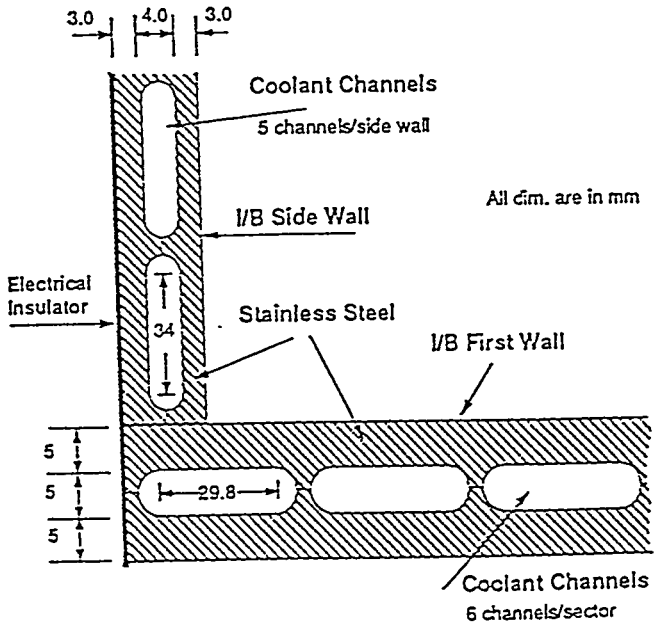

Figure 9-2. A schematic of the first wall and side wall coolant channels.

Table 9-1. Inboard Thermal-Hydraulics Parameters for FW/Side Wall.

Nuclear heating carried by the first wall channel	41.7 kW/cm
Nuclear heating carried by the side wall channel	10.9 kW/cm
Temperature rise in first wall coolant	31.7°C
Temperature rise in side wall coolant	8.3°C
Max. velocity in the first wall channel (at the midplane)	7.08 m/s
Max. velocity in the side wall channel (at the midplane)	4.02 m/s
Average velocity in the first wall channel	6.70 m/s
Average velocity in the side wall channel	3.02 m/s
Hydraulic diameter of the first wall coolant channel	0.896 cm
Hydraulic diameter of the side wall coolant channel	0.738 cm
Number of coolant channels in one first wall sector (at midplane)	6
Number of coolant channels in one side wall sector (at midplane)	5
Pressure drop along the first wall channel	4.20 atm
Pressure drop along the side wall coolant channel	1.35 atm
Total pressure drop in FW/side wall coolant system	5.55 atm
Volumetric flow rate to one inboard module (FW)	21.5 liter/s
Total volumetric flow rate to inboard side (FW)	687.84 liter/s
Coolant feed pipe diameter to one inboard module (FW)	7.8 cm

calculations have been utilized to perform the thermal analyses for the inboard shield. Figure 9-3 is a nuclear heating distribution at the midplane and the top of the inboard blanket/shield. Figure 9-4 is a simple plane schematic of the radial build of the inboard blanket/shield. It gives the coolant routes, coolant velocity, temperature rise in the coolant from top to bottom, pressure drop, steel maximum temperature and steel maximum thermal stresses at the reactor midplane. Figure 9-5 is a simple plane schematic of the radial build of the inboard blanket/shield at the top of the reactor. It gives the temperature of the coolant at the top of the blanket/shield, steel maximum temperature and steel maximum thermal stresses. Figures 9-6 and

9-7 are the temperature distributions at the midplane and at the top of the inboard blanket/shield, respectively. Figure 9-8 shows a plot of the effect of the first wall coolant channel thickness on the pressure drop in the first wall alone. The coolant feeding pipe diameter to each inboard module is 8.3 cm and the total volumetric flow rate to each inboard module is 24.4 liter/s. Hence, the total volumetric flow rate to the 32 modules is 781 liter/s.

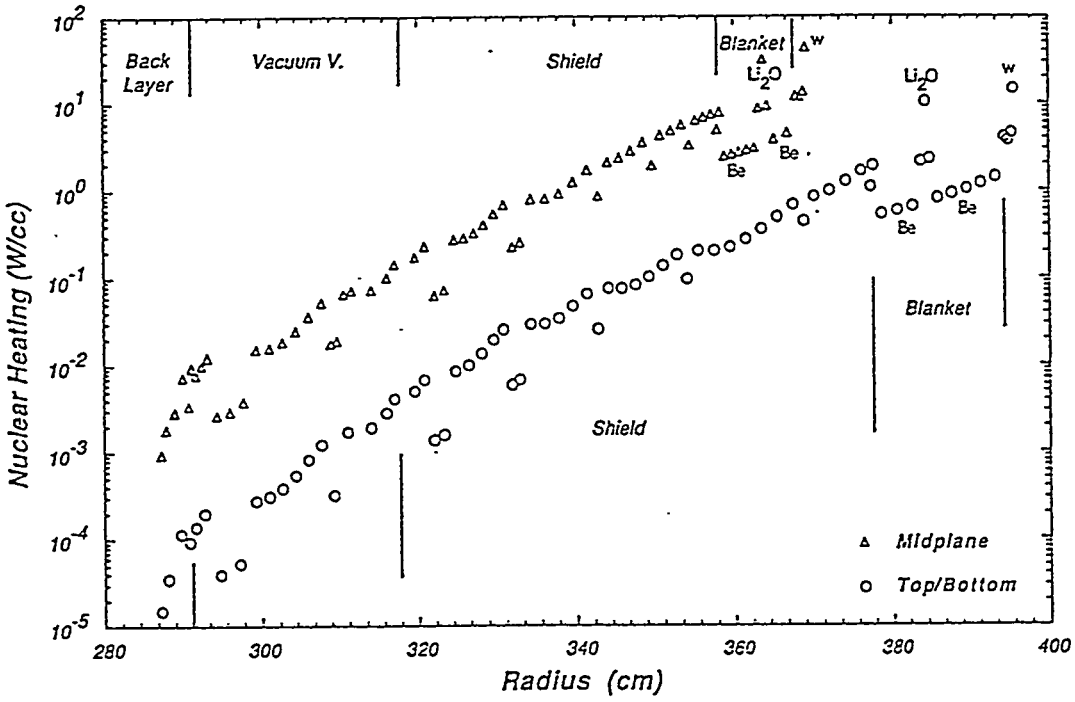

Figure 9-3. Nuclear heating distribution in inboard blanket/shield.

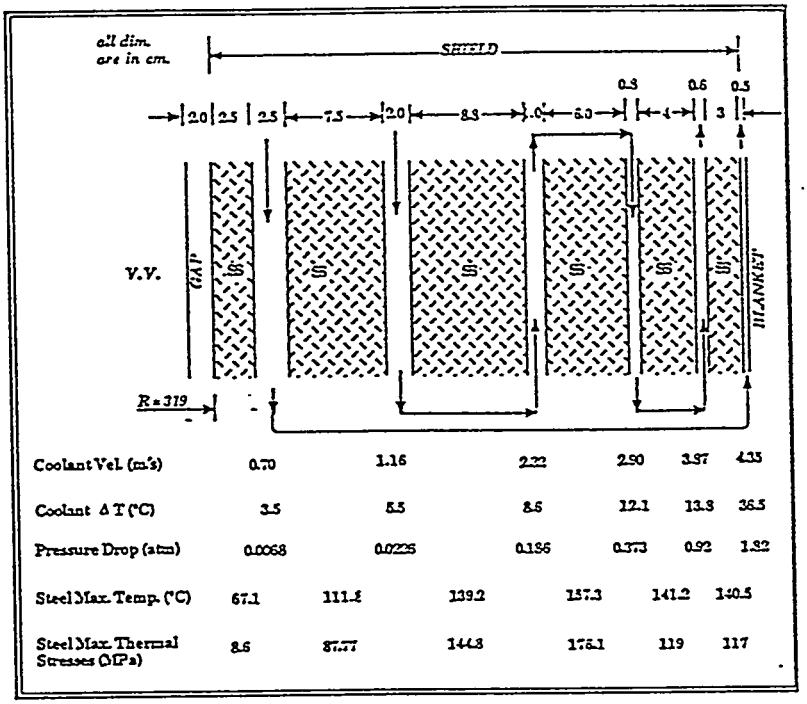

Figure 9-4. A schematic of the radial build-up of the inboard blanket/ shield at midplane.

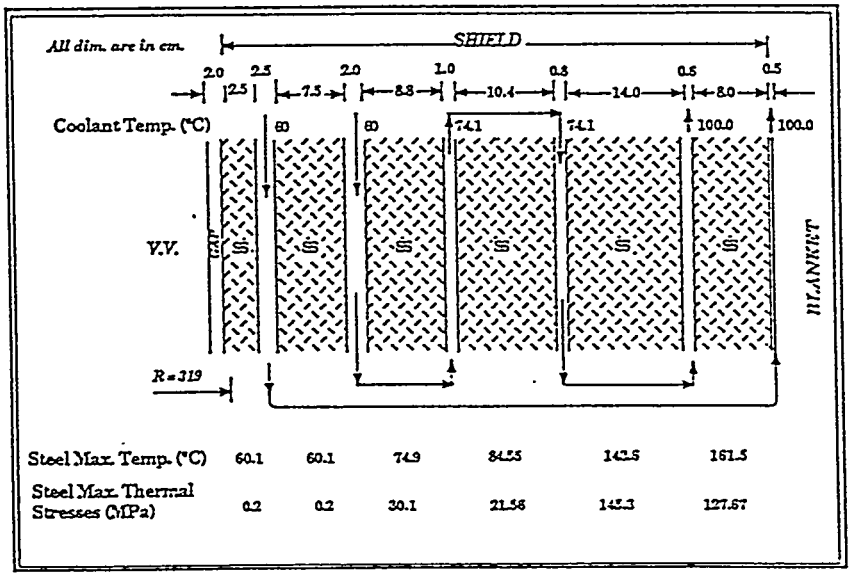

Figure 9-5. A schematic of the radial build-up of the inboard blanket/ shield at the top.

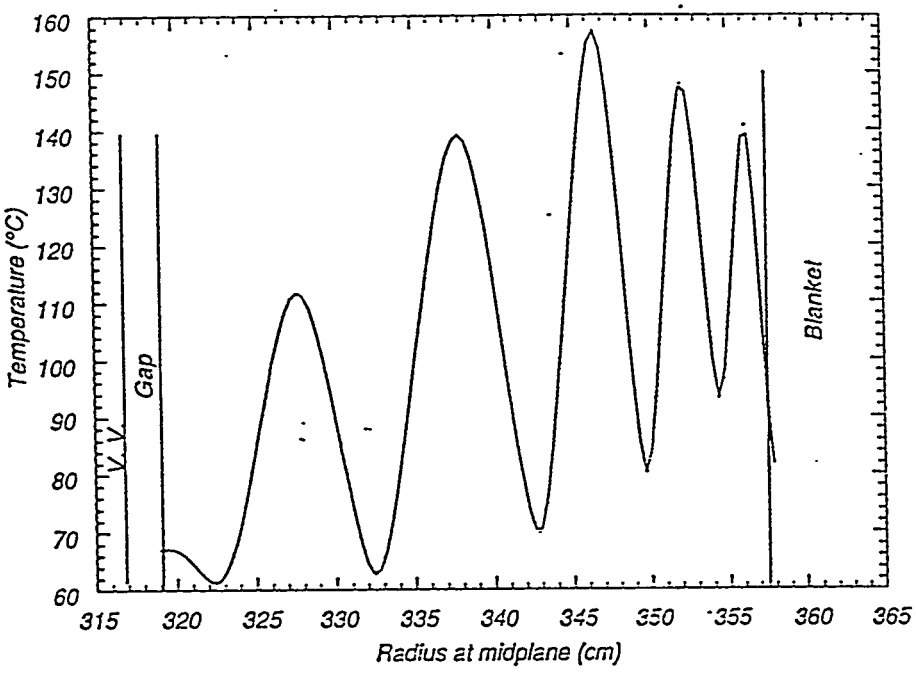

Figure 9-6. The temperature distribution at the midplane of the inboard shield.

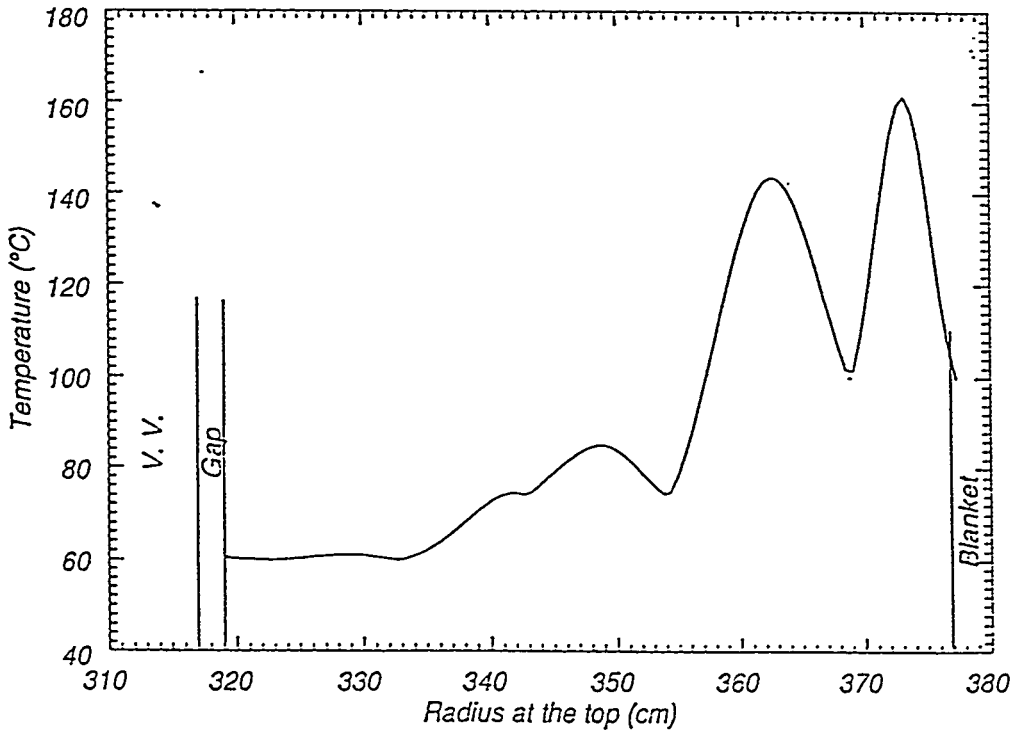

Figure 9-7. The temperature distribution at the top of the inboard shield.

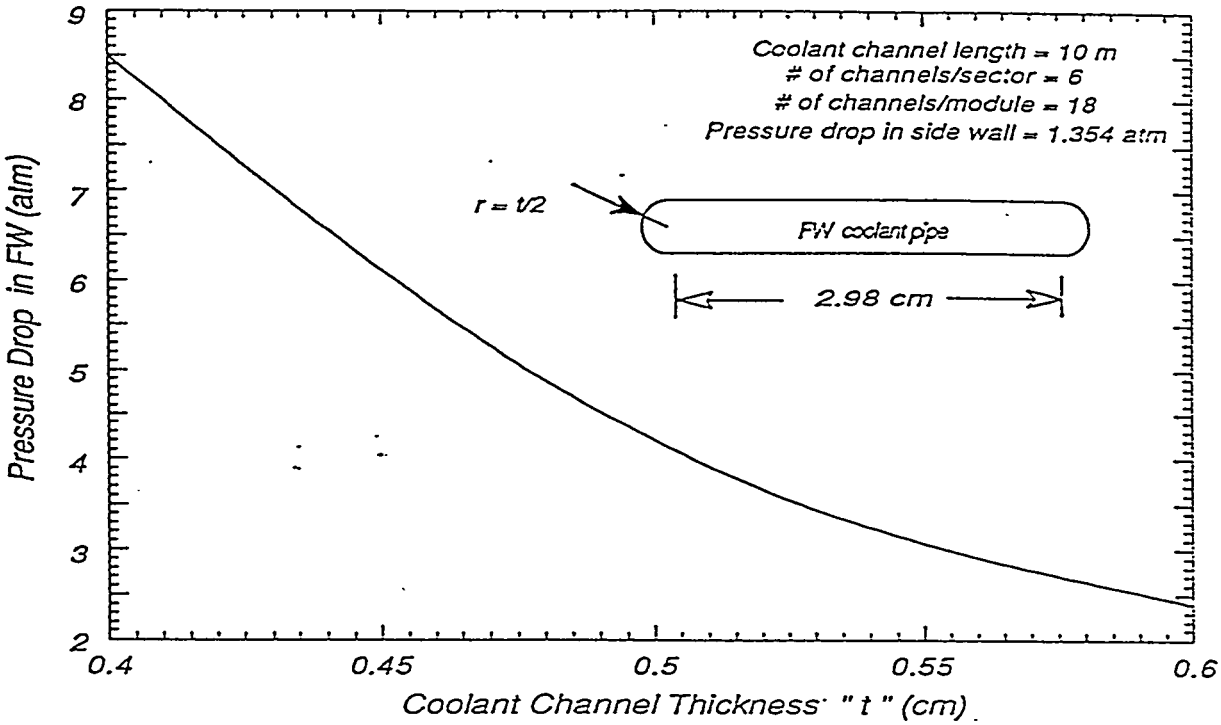

Figure 9-8. The effect of the FW coolant channel thickness on the pressure drop in the FW alone.

9.2 Outboard Thermal Hydraulics Analysis

The outboard blanket consists of 48 equal segments. Each segment has three modules, one central and two side modules. The central module is divided into an upper and lower module. All coolant connections (except for the lower central module, it is on the bottom) are at the top. The first wall is designed in the form of a steel/water/steel layer and the coolant channels are oriented toroidally. The first wall coolant is totally separate and independent from either the breeding zone or shield coolant. The first wall manifolds are located behind the breeding zone manifold and run poloidally. The first wall manifolds vary in toroidal width and have 30 mm radial depth. The first wall coolant traverses the first wall in the toroidal direction, then collects in the return manifold and exits the module at the top through the return pipe. The breeding zone consists of beryllium plates interleaved with solid breeder plates and cooling system. The details of the breeding zone can be found in the neutronics section. Each breeding zone is cooled from both sides. The cooling panels are 6 mm thick steel and have 2 mm × 22 mm cooling channels oriented toroidally. The coolant traverses the breeding zone in the

toroidal direction, then collects in the return manifold and then routed through the shield. The shield zone consists of steel plates with increasing thickness in the outward radial direction but with constant thickness in the poloidal direction. The plates are separated by coolant channels oriented poloidally. For the general configuration of the outboard blanket/shield see the mechanical design section. Figure 9-9 shows the radial build-up of one outboard module, general coolant routing, maximum steel temperature and maximum thermal stresses in steel. Figure 9-10 shows a plot of the nuclear heating for the outboard blanket/shield at midplane. Figure 9-11 shows a plot of the temperature distribution for the outboard shield at midplane. The results of the thermal-hydraulics analysis for outboard region are given in Table 9-2.

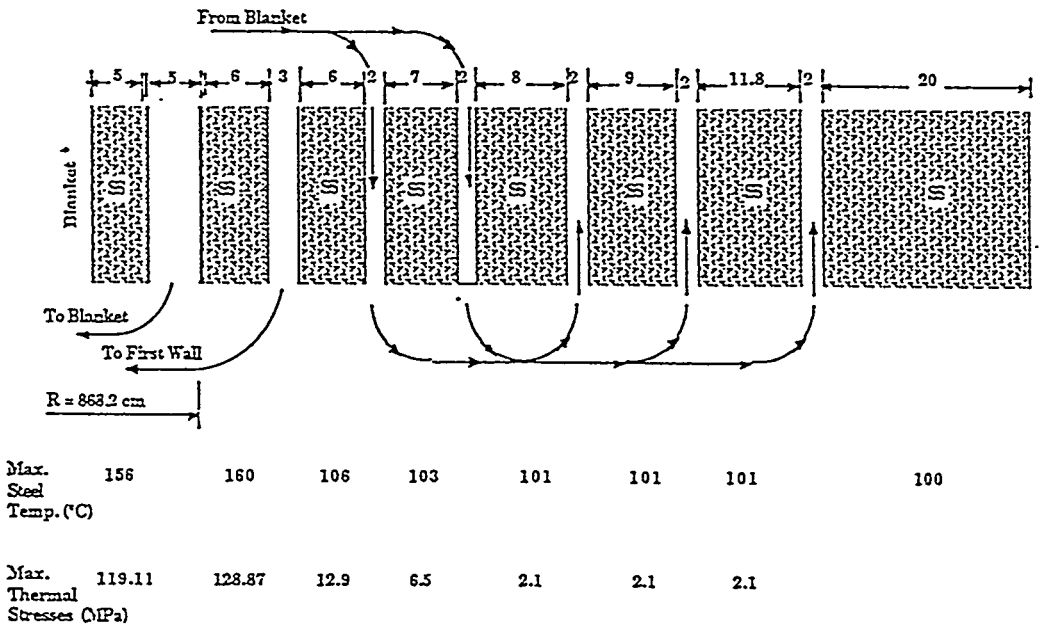

Figure 9-9. Outboard shield layout.

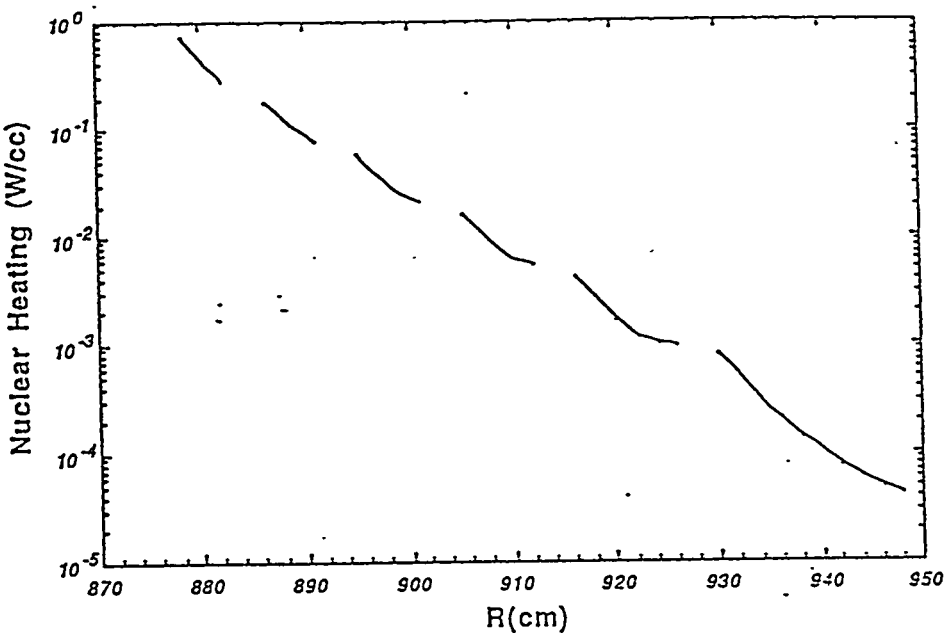

Figure 9-10. Nuclear heating in OB shield at midplane.

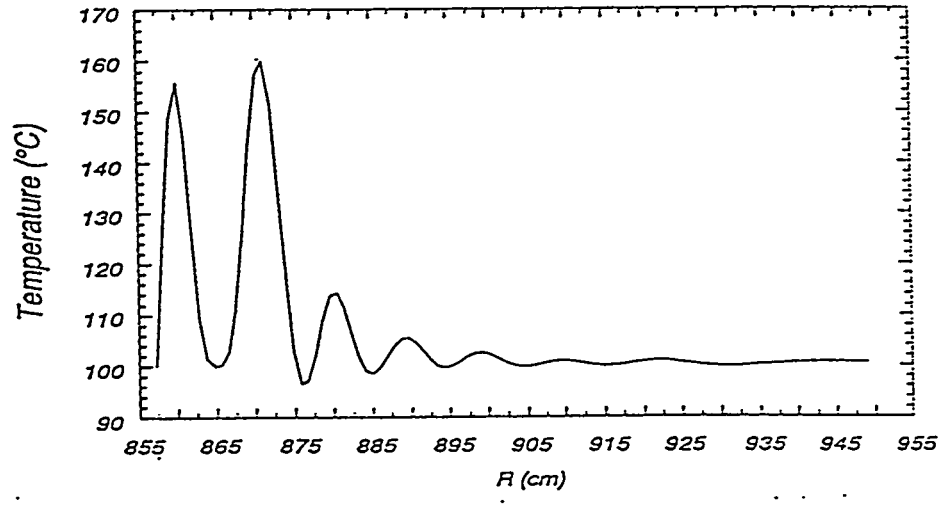

Figure 9-11. Temperature distribution for OB shield at midplane.

Table 9-2. Outboard Thermal-Hydraulics Parameters.

First wall	
Average Velocity	1.62 m/s
Pressure Drop	0.0686 atm
First wall header	
Maximum Velocity	5.7 m/s
Pressure Drop (One Side)	0.107 atm
Total Pressure Drop in the First Wall Coolant System	0.283 atm
Total Volumetric Flow Rate/Module	90.6 liter/s
Total Volumetric Flow Rate	2900 liter/s
Coolant Feed Pipe Diameter to One Inboard Module (FW)	16.0 cm
Blanket	
Average Velocity	
First Channel	2.1 m/s
Second Channel	1.2 m/s
Pressure Drop	
First Channel	0.194 atm
Second Channel	0.0739 atm
Shield	
Coolant Parameters	
All Channels Width	2.0 cm
Inlet Temperature	
(a) First (Two) Channels	99.2°C
(b) Next (Three) Channels	99.8°C
Exit Temperature	
(a) First (Two) Channels	99.8°C
(b) Next (Three) Channels	100°C
Velocity	
(a) First (Two) Channels	2.17 m/s
(b) Next (Three) Channels	1.45 m/s
Pressure Drop	
(a) First (Two) Channels	0.122 atm
(b) Next (Three) Channels	0.058 atm
Total Pressure Drop	0.18 atm
Total Volumetric Flow Rate/Module	92.0 liter/s
Total Volumetric Flow Rate	2944.3 liter/s
Coolant Feed Pipe Diameter to One Outboard Module	16.13 cm
Coolant Manifold	
Maximum Velocity	3.87 m/s
Pressure Drop (One Side)	0.027 atm
Total Pressure Drop in Blanket/Shield Coolant System	0.503 atm

10. TRITIUM RECOVERY AND INVENTORY ANALYSIS

10.1 Purge Flow Hydraulics

The purge flow rate is determined by the maximum tritium and moisture partial pressures allowed in the purge stream. The performance of Li_2O is particularly sensitive to moisture (H_2O + HTO + T_2O) partial pressure. Precipitation of separate phase LiOH(T) will occur if the temperature is low enough and the moisture partial pressure is high enough. Figure 10-1 shows the solubility limit for OH(T) in Li_2O and the corresponding saturation pressure [1]. The formation of separate phase LiOH(T) is undesirable because it acts as a trap for tritium and it has a low melting temperature (471°C). Vaporization of LiOH(T) can also cause mass transfer and corrosion problems.

Given the inlet moisture impurity level in the purge and the tritium generation rate, the outlet moisture flow rate is determined with the assumption that one oxygen atom is released from Li_2O for every two tritium atoms released. Let $\dot{n}_{He}$ be the local purge flow rate in moles (He)/m^2(Li_2O)-s, where m^2 (Li_2O) refers to the breeder cross-sectional area perpendicular to the purge flow direction (toroidal). Also, let $\dot{n}_m^o = \dot{n}_m^i + L\,\dot{g}_{T_2}$ be the purge outlet molar flow rate of moisture in moles (H_2O + HTO + T_2O)/m^2(Li_2O)-s, where $\dot{n}_m^i$ is the inlet moisture flow rate, L is the flow length in m and $\dot{g}_{T_2}$ is the molar generation rate of T_2 in moles (T_2)/m^3(Li_2O)-s. Then for a specified maximum moisture pressure, P_m^o, the required He flow rate is

$$\dot{n}_{He} = \dot{n}_m^o \left(P_{He}^o / P_m^o\right) \quad , \tag{10.1-1}$$

where P_{He}^o is the outlet He purge pressure.

For ITER applications, P_m^o is chosen as ~10 Pa which corresponds to a critical LiOH precipitation temperature of ~360°C, well below the minimum breeder design temperature. For an exit helium pressure of ~1 atm (0.1 MPa), a maximum generation rate of 3.76×10^{-5} moles (T_2)/m^3(Li_2O)-s over a 1-m flow length, and an inlet moisture impurity level of 1 vppm, the required He flow rate is 0.38 moles (He)/m^2 (Li_2O)-s. If this flow rate is maintained

throughout all breeder regions, then the total He flow rate required is 3.14 moles (He)/s.

The next step in the purge flow hydraulics analysis is to choose a breeder permeability to give the desired pressure drop in the purge flow direction. The relationship between permeability (K_e) and purge pressure drop (ΔP) for a desired flow rate ($\dot{n}_{He}$) is given by a modified form of Darcy's law:

$$K_e = \frac{\dot{n}_{He}\ R\ T\ \mu\ L}{\Delta P\ (P_o + \Delta P/2)}\ ,\ m^2 \qquad (10.1\text{-}2)$$

where

R = 8.314×10^{-6} m^3-MPa/mol-K
T = temperature in K
μ = $5.714 \times 10^{-13}\ T^{0.64}$ MPa-s (He viscosity)
L = 1 m (assumed flow length)
P_o = He exit pressure in MPa

As a sample calculation, for $P_o = \Delta P = 0.1$ MPa and $T = 723$ K, the required permeability is $K_e \sim 6 \times 10^{-12}$ m^2. In the next two sections, the purge flow geometries are described for the sintered-product design and the common ITER design (pebble bed).

10.1.1 Sintered-product design

The permeability of 80% dense Li_2O with 20-μm grain diameter and 5 μm average pore diameter is calculated to be $\sim 4 \times 10^{-14}$ m^2 [1]. This value is much too low to give a reasonable pressure drop at the desired flow rate over a 1-m flow path. Figure 10-2 shows a schematic of the sintered-product breeder plates with semi-circular purge channels fabricated at the Li_2O/steel interface. The relationship between permeability (K_e), purge hole diameter (d_p in m) and number of holes (n_h) per m^2 of Li_2O cross-section is [1]

$$K_e = 9.15 \times 10^{-3}\ n_h\ d_p^4,\ m^2\ . \qquad (10.1\text{-}3)$$

Combining Eq. (10.1-2) and (10.1-3), gives the required purge hole diameter as a function of purge temperature, purge outlet pressure, and purge pressure drop:

$$d_p = 1.185 \times 10^{-4}\ T^{0.41}\ [n_h\ \Delta P\ (P_o + \Delta P/2)]^{-0.25} \qquad (10.1\text{-}4)$$

For sample design calculations, assume $n_h = 10^4$ complete holes/m^2 (1 hole/cm^2) and T = 723 K. Then for P_o = 0.1 and ΔP = 0.13, $d_p = 4.6 \times 10^{-4}$ m (0.46 mm). If a lower outlet pressure and pressure drop are required, then the purge hole diameter must be increased. For example, for P_o = 0.05 MPa and ΔP = 0.017 MPa, then $d_p = 1 \times 10^{-3}$ m (1 mm). Thus, $0.46 \leq d_p \leq 1$ mm should cover all of the design ranges of interest.

The pumping power associated with the required flow rate is quite small. The relationship between pumping power loss through the entire breeder region and the pressure drop is

$$W_p = \dot{N}_{He}\ RT\ \ell n\ (1 + \Delta P/P_o) \qquad (10.1\text{-}5)$$

For $\dot{N}_{He}$ (total molar He flow rate) = 3.14 moles/s, the pumping power is 0.0157 MW (15.7 kW) for the case P_o = 0.1 MPa and ΔP = 0.13 MPa; and 0.00552 MW (5.52 kW) for the case P_o = 0.05 MPa and ΔP = 0.017 MPa.

Consideration has been given to reducing the average gas pressure in order to alleviate the stress on the first wall. Thus, two outlet pressure cases are analyzed: the previously assumed 0.1 MPa case and a 0.05-MPa case. Figure 10-3 shows the pressure drop as a function of the helium flow rate for 2 different groove sizes for the two above cases. The results show the substantial reduction in pressure drop when the groove size is increased from 0.5 to 1 mm, which is to be expected from the exponential dependence of the pressure drop on d_p. Reducing the outlet pressure causes a noticeable increase in the pressure drop.

From Fig. 10-3, for an outlet pressure of 0.1 MPa and a helium flow rate of 0.4 moles/s-m^3 breeder (corresponding to a maximum tritium moisture pressure of ~10 Pa), the pressure drop is about 0.1 MPa, which would translate to an inlet pressure of about 0.2 MPa for a 0.5-mm groove diameter. For an

outlet pressure of 0.05 MPa, a 0.5-mm groove diameter would result in an unacceptable pressure drop. The groove diameter would have to be increased to about 1 mm, which reduces the pressure drop to about 0.017 MPa.

Figure 10-4 illustrates more clearly the sensitivity of the pressure drop to the groove diameter for a typical flow rate of 0.4 moles/m^3 (solid breeder)-s. Two outlet pressure cases are shown: 0.05 MPa and 0.04 MPa, which would result in an average purge pressure of about 0.05 MPa for a pressure drop of about 0.02 MPa. The total pumping power (Wp) through the breeder (or multiplier) can be found by integrating PdQ from inlet to outlet to give

$$Wp = NRT \ln (P_i/P_o) = NRT \ln(1+\Delta P/P_o) \qquad (10.1\text{-}6)$$

The relative pumping power corresponding to the pressure drop of Fig. 10-4 is illustrated in Fig. 10-5. The pumping power is more sensitive to changes in the outlet pressure than the pressure drop as it tends to increase with both decreasing outlet pressure and the corresponding increase in pressure drop.

Achieving Uniform Pressure Drop and Tritium Partial Pressure

The helium purge enters the plate from the inlet manifold. Although it is not a design requirement, there is flexibility to achieve the same pressure drop over the breeder regions and the same tritium partial pressure for the same gas pressure if it proves desirable. This can be done by tailoring the groove sizes based on the local tritium generation rate. Tailoring the groove size enables the permeability and, thus, the flow resistance to be set to the desired values. A sample calculation has been done for a uniform tritium partial pressure of 3.8 Pa and purge inlet and outlet pressures of 0.067 and 0.05 MPa respectively. The helium flow rates and groove sizes required to achieve this are listed in Table 10-1 for two different poloidal locations for the Technology Phase. The helium flow rates range from 0.24 moles/s-m^2 for the top inboard to 1.87 moles/s-m^2 for the midplane outboard with corresponding groove diameters of 0.82 mm and 1.1 mm respectively. For the Physics Phase, for the given groove sizes and helium flow rates, the inlet and outlet pressures will stay the same. However, because of the increase in tritium generation rate of about 18%, the tritium partial pressure will increase to 4.5 Pa.

Table 10-1. Groove Hole Diameters at Different Blanket Modules

Poloidal Location	Helium Flow Rate (moles/s-m^2)	Groove Diameter (mm)
Inboard		
Midplane	0.562	1.02
Top	0.245	0.82
Outboard Plate 1		
Midplane	1.873	1.10
Top	1.171	0.98
Outboard Plate 2		
Midplane	1.461	1.01
Top	0.390	0.72

Purge Flow Effect on Tritium Inventory

To ascertain the effect of a change of purge flow rate on the tritium inventory, the steady state tritium inventory was calculated for the first outboard region as a function of the tritium partial pressure in the purge (set by the purge flow rate for a constant tritium generation rate). The calculations were done using the MISTRAL code for the corresponding steady state temperature profile and tritium generation rate. The tritium inventory results include the components due to bulk diffusion, surface coverage, pore diffusion, and LiOT precipitation based on the critical moisture pressure, but do not include solubility. The values will then be lower than the reference inventory values which take into consideration inventories in both outboard regions and in the inboard region, and which account for solubility. Thus, for this sample case, the relative variation in tritium is more important than the absolute tritium inventory values.

The results are summarized in Fig. 10-6 for the Technology Phase. The results for the Physics Phase are similar, except that the tritium inventory tends to be slightly lower due to the higher solid breeder temperature. The major inventory component in all the cases is the surface coverage. It is interesting to note that the tritium inventory varies virtually in direct proportion with the tritium partial pressure in the purge (i.e., in indirect proportion with the purge flow rate), except at partial pressures of about 1

Pa or lower where the inventory becomes less sensitive to changes in the tritium partial pressure. For the chosen solid breeder operating temperature, the inventory is low enough that the purge flow rate can be set to a very low value without the inventory becoming a major concern. For example, for a low flow rate corresponding to a tritium partial pressure of the order of 100 Pa, the total inventory would probably still be of the order of 10 g which is acceptable. However, the concern is that at lower temperature a correspondingly high moisture pressure could cause the critical moisture pressure for LiOT precipitation to be exceeded, resulting in most of the tritium being trapped as LiOT. This could result if for some reason the solid breeder operating temperature is noticeably lower than the design value. To guard against such an eventuality, it seems prudent to keep the design value of the tritium partial pressure in the purge to the order of 10 Pa or lower.

Summary for Sintered-Product Design

- For the sintered-product design, the purge flows through grooves along the sintered solid breeder blocks. The purge pressure drop is strongly dependent on the groove size. Groove diameters of 0.46-1.0 mm give reasonable pressure drops for a range of operating conditions.

- For an effective distribution of one cylindrical groove per cm^2, the pressure drop is about 0.1 MPa for an outlet pressure of 0.1 MPa, a groove diameter of 0.5 mm, and an helium flow rate of 0.4 moles/s-m^3 solid breeder.

- For an outlet pressure of 0.04 MPa, the pressure drop is 0.02 MPa for a groove diameter of 1 mm. This results in an average purge pressure of about 0.05 MPa, which significantly reduces the stress on, and deflection of, the first wall.

- If it is desirable to have uniform pressure drop and tritium partial pressure at every reactor location, then the groove size can be tailored for each poloidal region to accomplish this. However, it is not a design requirement.

- The steady state tritium inventory varies virtually in direct proportion with the tritium partial pressure in the purge (and, hence, in indirect proportion with the purge flow rate). For the design value of the solid breeder operating temperature range, the inventory is low enough to provide flexibility in setting the purge tritium partial pressure and the flow rate.

- It is advisable, however, not to operate with too high a tritium partial pressure in the purge since, if for some reason the solid breeder temperature is much lower than the design value, the critical moisture pressure causing LiOT to precipitate could be exceeded. A design moisture partial pressure value of the order of 10 Pa seems reasonable.

Be Purge

The Be regions are also purged with He. The tritium generation rate in the Be is quite small compared to the generation rate in the breeder (~1%). Also, based on current analyses ~80% of the generated tritium will be retained in the Be. As the Be is not sensitive to moisture content and releases very little tritium, there is no rigid design constraint for the purge flow rate in the Be. The main functions of the purge are to guard against tritium buildup in the Be porosity during over-power transients and to maintain low moisture pressures at the Be/steel/Li_2O interface in case of H_2O leaks at the Be/steel/coolant interface. Thus, it is really off-normal and accident events which set the desired Be flow rate. The only steady-state criterion is based on maintaining a proper tritium/protium partial pressure to minimize permeation from the breeder region to the Be region.

The measured permeability of 85% dense Be fabricated by cold-isostatic-pressing followed by sintering is [2] ~2.3×10^{-14} m^2. For 74% dense Be (the lowest density tested), the permeability is ~1.4×10^{-13} m^2. Extrapolation of these results to 65% dense material gives ~1×10^{-12} m^2. For the slow He flow rates anticipated for the Be purge, these permeabilities are high enough to purge the Be through its interconnected porosity, with no special purge grooves needed.

As a reference case, assume that the desired Be purge flow rate is 1/100 of the breeder flow rate. This would give an average pressure drop across the 85% dense Be of

$$\Delta P = \frac{4.677 \times 10^{-8}\ T^{1.64}}{P_o + \Delta P/2} \qquad (10.1\text{-}6a)$$

and across the 65% dense Be of

$$\Delta P = \frac{7.215 \times 10^{-12}\ T^{1.64}}{P_o + \Delta P/2} \qquad (10.1\text{-}6b)$$

Both of these equations give $\Delta P << 0.1$ MPa and negligibly small pumping powers. Thus, there is considerable flexibility in going to higher flow rates if off-normal and accident analyses dictate that it would be desirable.

10.1.2 ITER common design

The ITER common design assumes an Li_2O packed bed configuration. A detailed hydraulic analysis of flow in such a configuration can be made based on the continuity and non-Darcian [3] equations for the velocity distribution and pressure drop. The modified Darcy equation describing the fluid motion accounts for friction caused by macroscopic shear (Brinkman effect) and for flow inertia (Forchheimer effect). Key parameters involved in this equation include the permeability (k) and the inertia coefficient (C), which depend on the characteristics of the packed bed. For a matrix consisting of packed spheres of diameter d_s, the permeability and the inertia coefficients are described as [3]:

$$k = d_s^2 \phi^3 / (150\ (1 - \phi)^2)$$

$$C = (1.75/\sqrt{175})\phi^{-3/2} \qquad (10.1\text{-}7)$$

where ϕ is the porosity of the packed bed. For the binary bed, Cheng's expression was also used based on an effective particle diameter [defined later in equation (10.1-10)].

A 2-dimensional computer program [4] using the SIMPLE numerical algorithm was written to solve the velocity profile and pressure distribution in a packed bed. To account for the wall effect on the packing the porosity distribution in the packed bed is required. For a single bed, a distribution suggested by Cheng et al. [5] was assumed for the analysis. The velocity distribution was then calculated for single size beds with average particle diameter of 1 mm and for a binary bed with average particle diameters of 1 mm and 0.15 mm. For both cases, the bed width was assumed to be 0.8 cm. The results are summarized in Fig. 10-7, which shows the corresponding velocity profiles for a purge flow rate of 0.4 mol/s-m^3 (sb) in the outboard region 1 of the common ITER design. The result indicates that there is a high velocity jet near the wall region due to the higher porosity close to the wall. This velocity profile is beneficial since it results in a region near the clad where the local tritium partial pressure will be the lowest, thus minimizing tritium permeation through the clad and where the heat transfer will be enhanced, thus increasing the wall conductance [6]. It can be seen that the velocity jet is thinner for the binary bed due to the smaller effective particle diameter.

The fully developed pressure gradient through the packed bed calculated from the code was compared to the Blake-Kozeny correlation [7]. This correlation was developed for laminar flow and is written as:

$$\frac{\Delta P}{\Delta L} = 175 \frac{(1-\alpha)^2}{\alpha^3} \frac{\mu_f v_o}{(\phi d_s)^2} \qquad (10.1\text{-}8)$$

v_o = superficial velocity
α = porosity
ϕ = 1 for sphere
d_s = particle diameter

The difference between the two calculations is about 10% and the total pressure drop for a 1-meter long breeder packed bed is 320 Pa for a superficial velocity of 1 cm/s. When the system pressure drop becomes larger,

the velocity varies along the flow path. To account for this effect, Eq. (10.1-8) is rewritten in terms of molar flow rate as:

$$\frac{\Delta P}{\Delta L} = 175 \frac{(1-\alpha)^2}{\alpha^3} \frac{\mu_f N R T}{(\phi d_s)^2 A_b (P_o+\Delta P/2)} \qquad (10.1\text{-}9)$$

For a packed bed with 80% packing fraction, binary mixtures with particle diameter ratios >5 are required. To estimate the pressure drop for a helium gas flowing through such a binary packed bed, an equivalent particle diameter must be used in equation (10.1-9). Such an equivalent diameter, $\bar{d}_s$, can be defined as:

$$\bar{d}_s = \frac{1}{\sum \frac{w_{fi}}{d_{si}}} \qquad (10.1\text{-}10)$$

where w_{fi} = weight fraction of particle i.

Figures 10-8 and 10-9 show the calculated pressure drop as a function of purge volumetric flow rate for a plate 8 mm thick and gas outlet pressures of 0.05 MPa and 0.1 MPa respectively. Results for both single-size and binary mixture packed beds are shown in each figure. It can be seen that the pressure drop for the case of the binary mixture is substantially higher than for the single-size case.

Thus, if the average purge pressure has to be minimized because of first wall stress and deflection constraints, a single-size bed is preferable. For an outlet pressure of 0.05 MPa in the case, the pressure drop is about 0.002 MPa for a typical helium flow rate of 0.4 mol/s per m^3 of solid breeder, resulting in a moderate average purge pressure of about 0.051 MPa. For a binary bed, the pressure drop in this case jumps to about 0.1 MPa. It seems preferable to operate the binary bed case with an outlet pressure of 0.1 MPa. The pressure drop in this case is about 0.06 MPa and the average purge pressure is about 0.13 MPa.

Summary for ITER Common Design

- The pressure drop as a function of helium flow rate has been calculated for single-size and binary beds. For a typical flow rate, the velocity profile has also been calculated for both beds.

- The velocity profile shows a high velocity region near the walls where the porosity increases. The thickness of this region is dependent on the particle size and tends to be smaller for binary beds. This particular profile results in a lower tritium partial pressure at the clad and thus in lower tritium permeation through the clad, which is beneficial. In addition, the velocity jet enhances heat transfer at the clad, resulting in higher wall conductance.

- The pressure drop associated with the binary bed is substantially larger than for the single-size bed.

- The binary bed has advantages of higher packing fraction and thermal conductivity and is recommended for the design. Acceptable inlet and outlet pressures would then be about 0.16 MPa and 0.1 MPa for a typical helium flow rate of 0.4 mol/s per m^3 of solid breeder.

- If it is desired to reduce the average purge pressure to about 0.05 MPa because of first wall stress and deflection, use of the single-size bed is preferable. Inlet and outlet pressures would then be 0.052 and 0.05 MPa respectively. However, for the binary particle case, which is better for heat transfer and tritium breeding, the volume fractions and diameter ratios could be optimized to also reduce the average purge pressure.

References

[1] M.C. Billone, "Purge Flow Design Analysis and Tritium Inventory Calculations for ITER Li_2O Solid Breeder Blankets," Argonne National Laboratory Report ANL/FPP/TM-245 (to be published).

[2] S.N. Rosenwasser, D.M. Goddard, and M.J. Hovan, "Development of Porous Be," McDonnell Douglas Report AFML-TR-71-241, January 1972.

[3] S. Ergun, Chemical Engineering Prog. 48,89 (1952).

[4] A.Y. Ying et al., "Characteristics of Helium Purge Flow in Solid Breeder Pebble Bed and its Impact on Design Considerations," submitted to 16th Symposium on Fusion Technology, September 3-7, 1990.

[5] P. Cheng, C.T. Hsu, "Fully-Developed, Forced Convective Flow Through an Annular Packed-Sphere Bed with Wall Effects," Int. J. Heat Mass Transfer, Vol. 29, No. 12, (1986) pp. 1843-1853.

[6] A.R. Raffray, "Packed Bed Wall Conductance," write-up for U.S. ITER Blanket Homework, UCLA, June 1990.

[7] S.U. Patankar, "Numerical Heat Transfer and Fluid Flow."

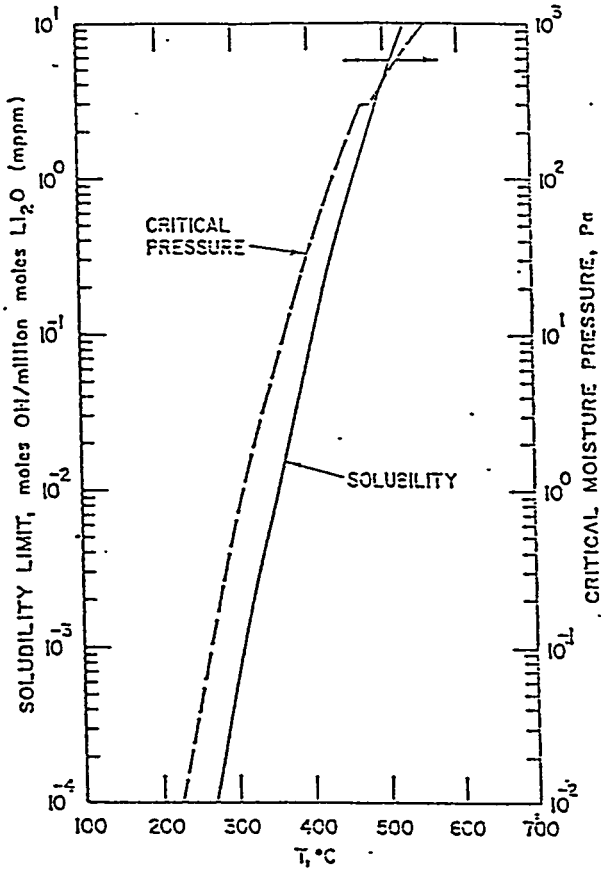

Fig. 10-1. Hydroxide solubility limit & critical moisture pressrue in Li_2O.

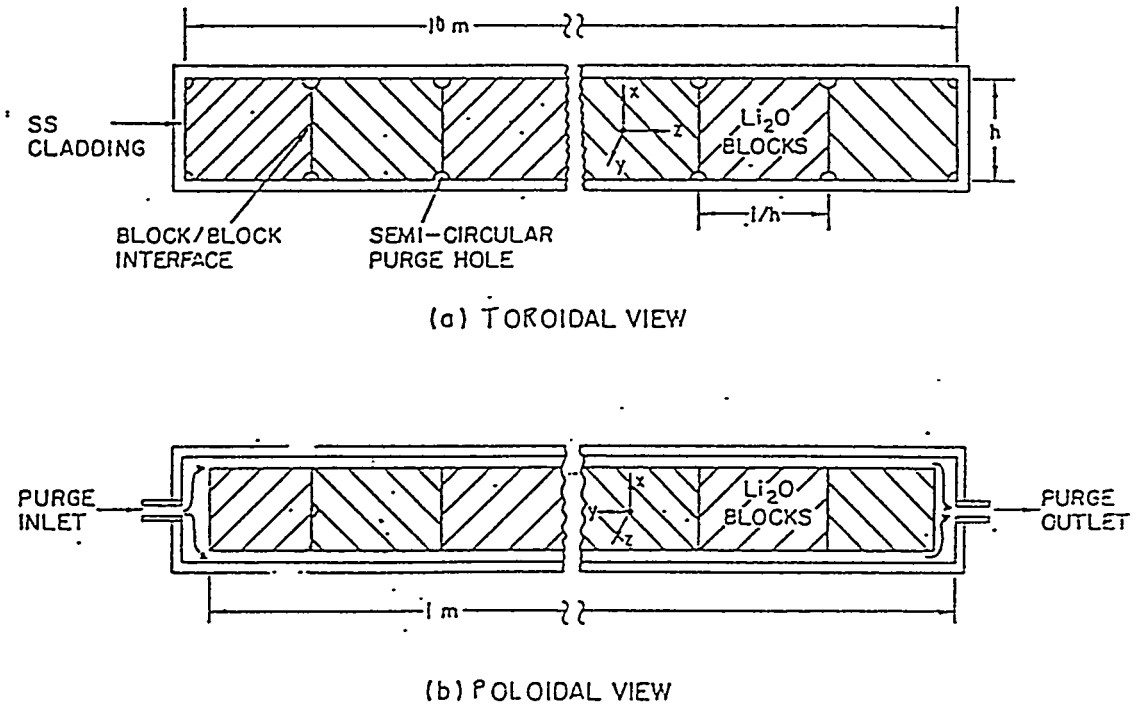

Fig. 10-2. Schematic of Li_2O breeder plates for sintered-product design.

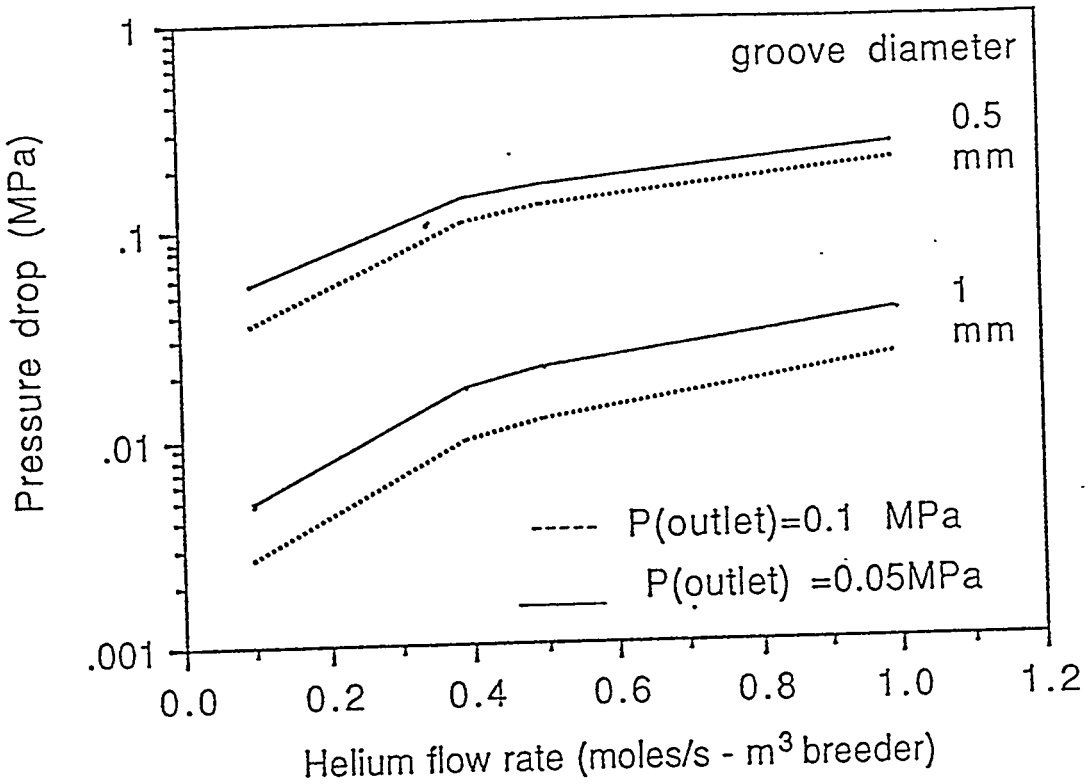

Fig. 10-3. Purge pressure drop as a function of flow rate for different outlet pressures and groove diameters.

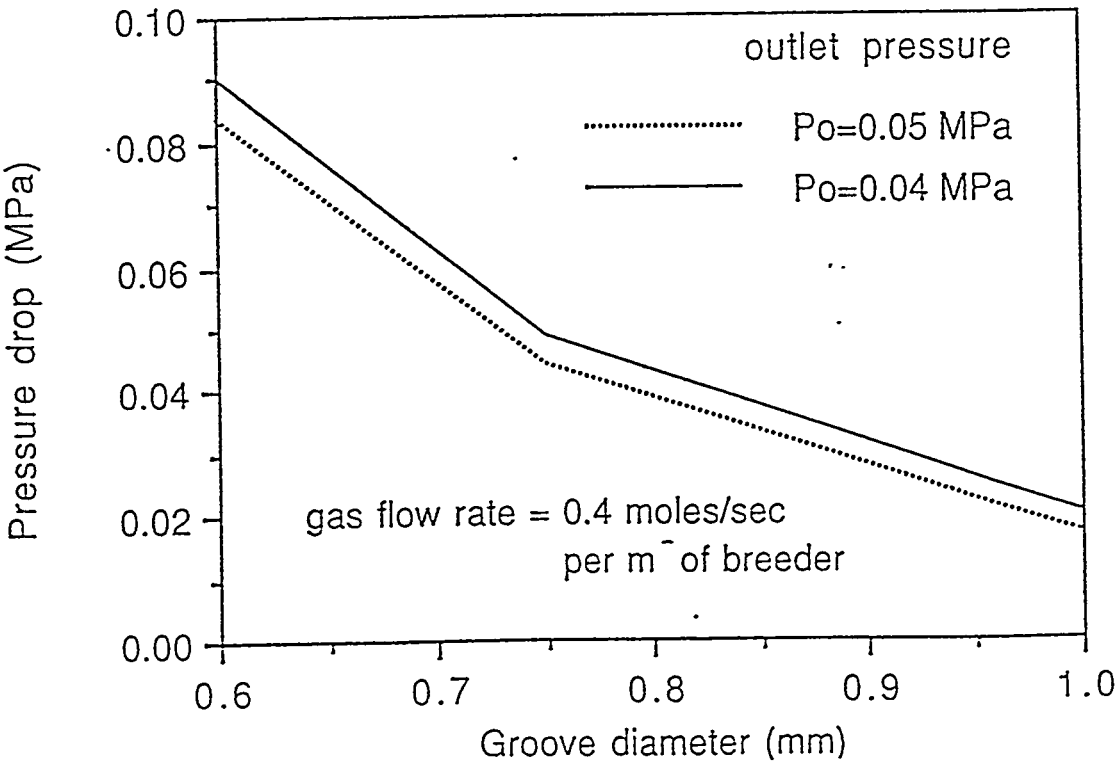

Fig. 10-4. Purge pressure drop as a function of groove diameter for two different outlet pressures.

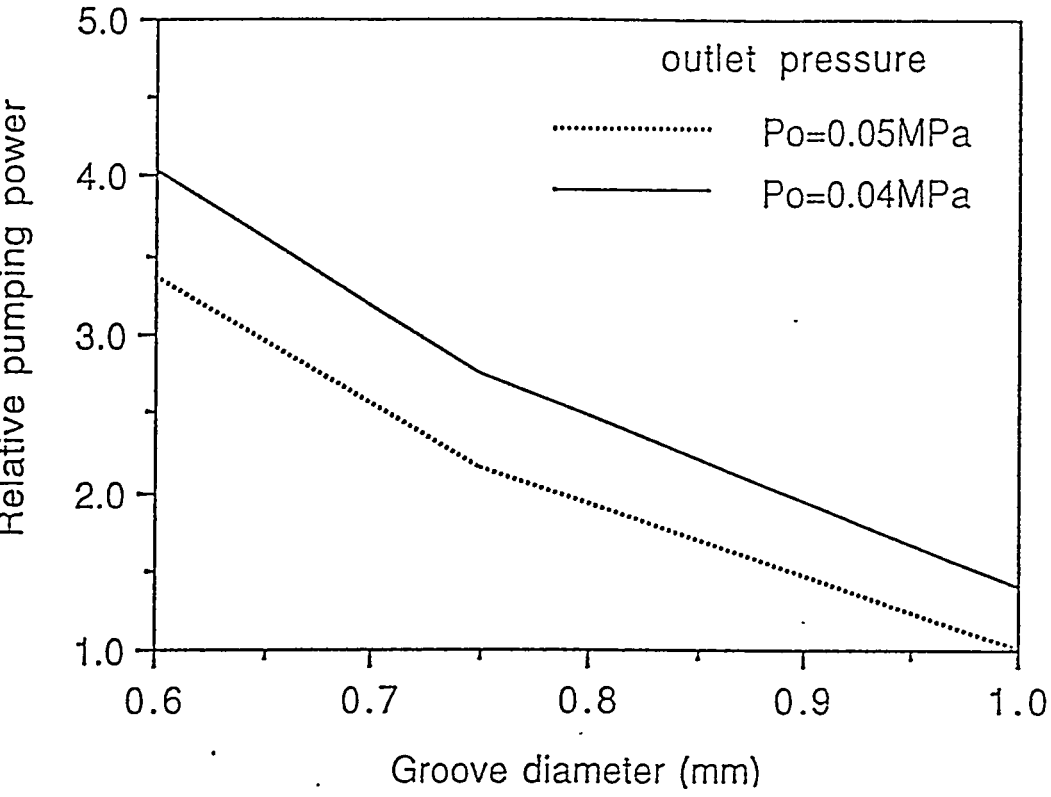

0-5. Pumping power as a function of groove diameter for two different outlet pressures (He flow rate = 0.4 moles/sec per m^3 of solid breeder volume).

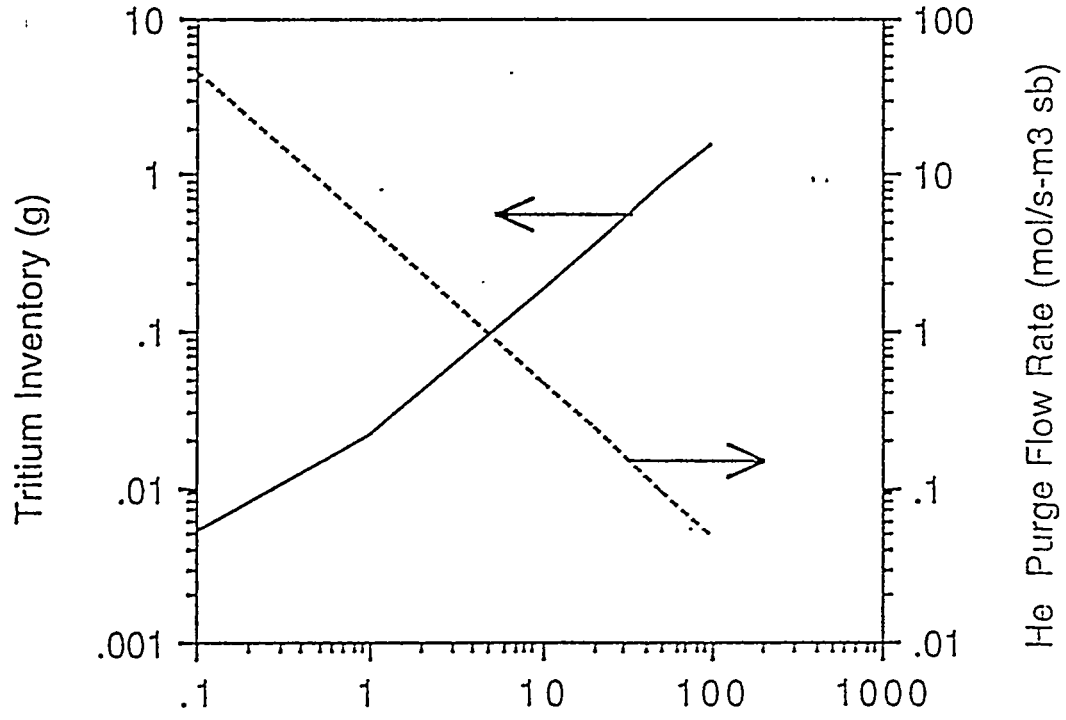

0-6. Tritium inventory as a function of tritium partial pressure in the purge for the outboard region 1 of the sintered-product breeder blanket during the technology phase. The He purge flow rate corresponding to the tritium partial pressure is also shown.

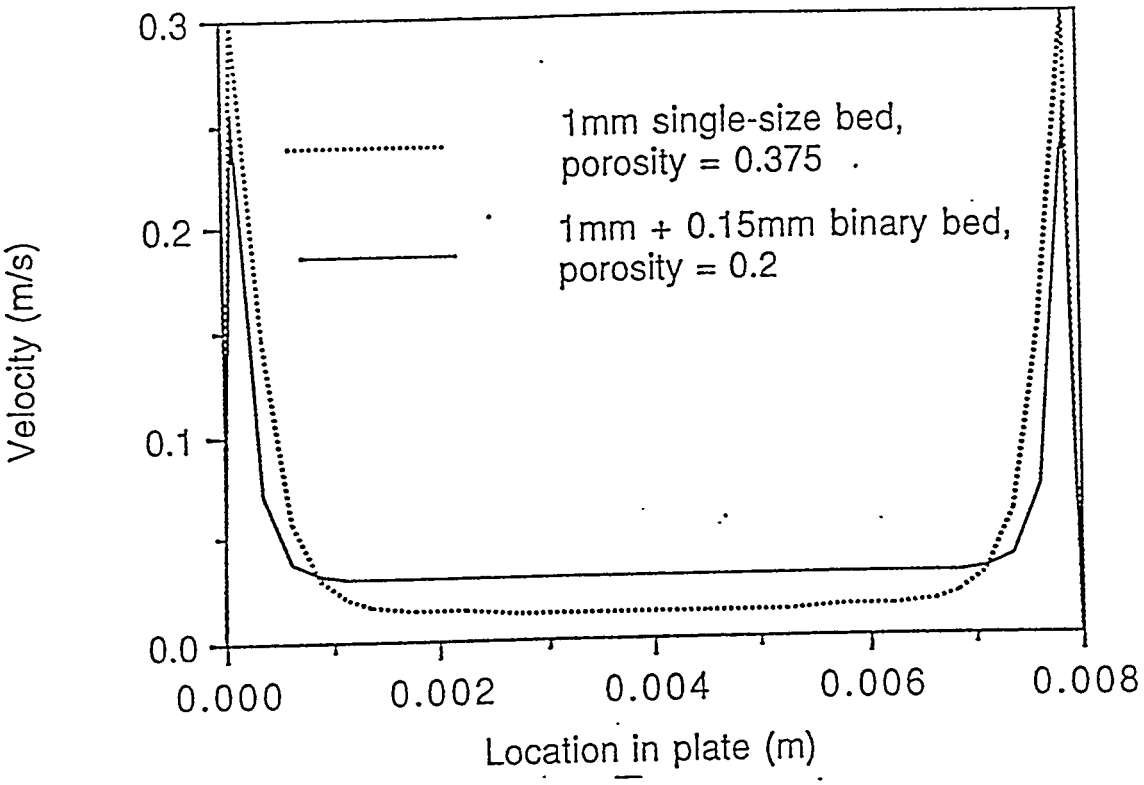

Fig. 10-7. Velocity profile for single-size and binary packed beds.

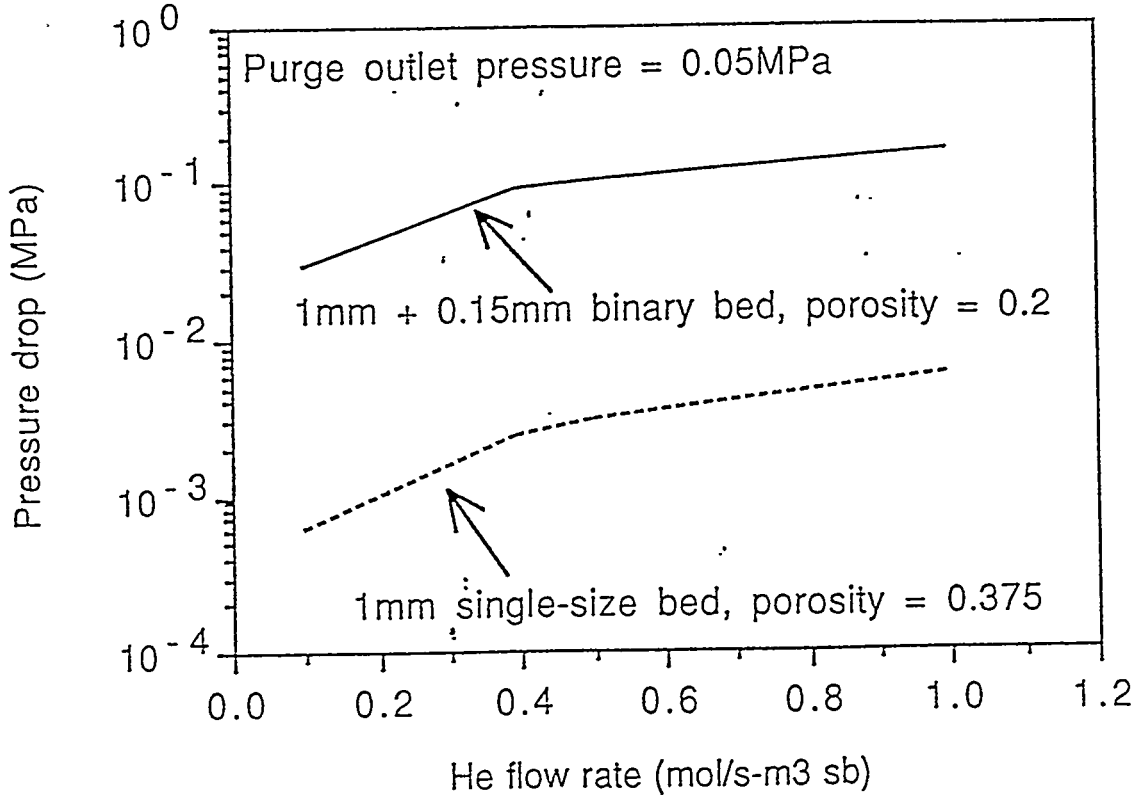

Fig. 10-8. Pressure drop as a function of the He flow rate for single-size and binary beds for an outlet pressure of 0.05 MPa.

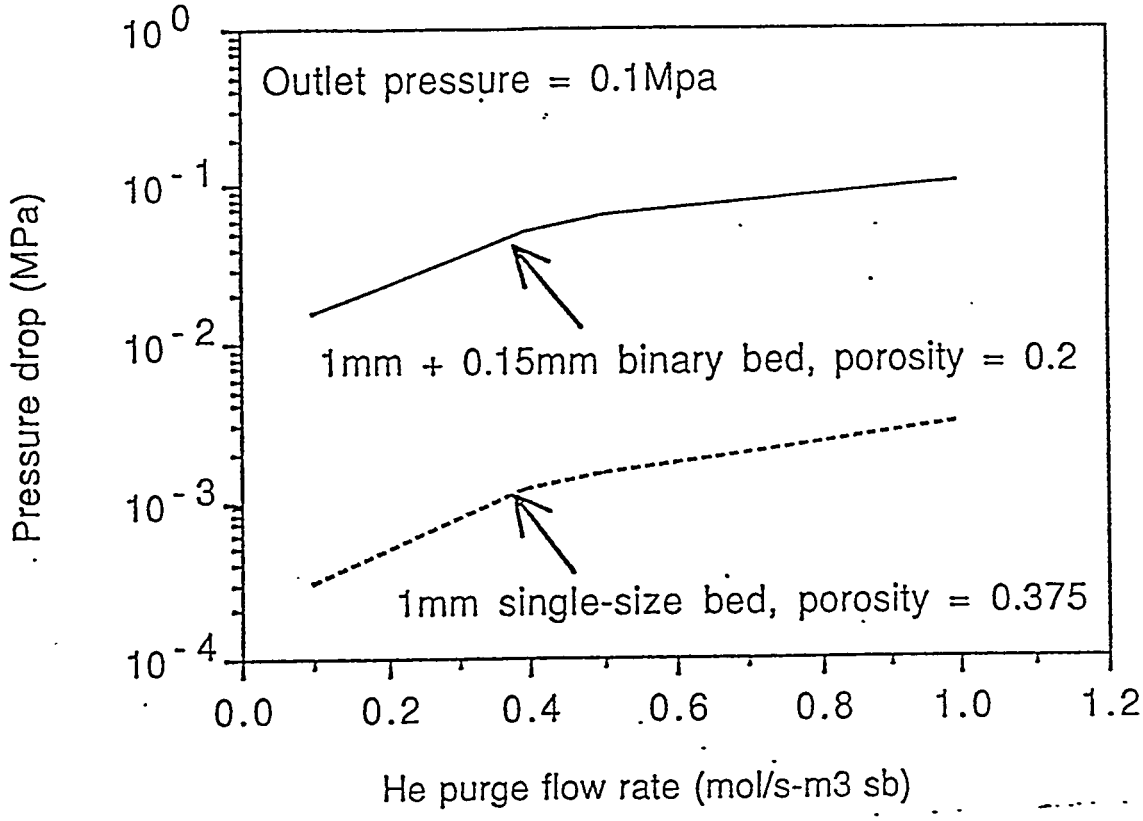

Fig. 10-9. Pressure drop as a function of the He flow rate for single-size and binary beds for an outlet pressure of 0.1 MPa.

10.2 Purge Flow Chemistry and Composition

The He purge is assumed to be relatively dry (~1 vppm moisture) at the inlet to the breeder purge holes. The inlet moisture level can be in the range of 1-5 vppm and still have relatively little impact on the solid breeder performance. For an exit He pressure of 0.1 MPa, this range of initial moisture levels would correspond to only 0.1-0.5 Pa, which is small compared to the design limit of 10 Pa. Thus, most of the moisture in the purge exit is from the oxygen released from the breeder at the same rate as the tritium (T_2) molar release rate.

In-reactor purge flow experiments have been performed to investigate the tritium release kinetics as a function of protium (H_2) levels in the He purge. Excellent tritium release has been achieved with protium levels of 0.1-1% in 1-atm He purge. For Li_2O, the protium reduces the HTO and T_2O levels in the purge, and thereby reduces the dissolved OT in the Li_2O. In addition, the higher the protium level, the higher the OH concentration at the breeder pore-solid interface. This tends to enhance the desorption of tritiated molecules (e.g., HTO) from the surface.

A mathematical model [1] has been developed based on thermodynamic equilibrium to determine mole fractions of H_2, HT, H_2O, HTO, and T_2O in the purge as a function of molar tritium release rate, inlet H_2 flow rate, inlet H_2O flow rate, temperature and position. Figure 10-10 shows the results of model calculations at 400°C for purge exit molar flow rates of the gas species as a function of inlet molar flow rate of H_2. All results are normalized to the molar generation rate of T_2, which at steady-state is assumed to be equal to the release rate to the purge. Tables 10-2 through 10-4 show the numerical results for 400°C, 500°C, and 600°C, respectively. Notice that going from no H_2 to a H_2/T_2 ratio of 20 has a dramatic effect on the HTO + T_2O level in the purge exit, while the sum of HTO + T_2O decreases more slowly as H_2/T_2 is increased to levels >20. Because it is desirable to minimize tritium inventory due to adsorption/solubility of moisture and to also minimize the amount of protium added to facilitate tritium processing, the minimum H_2/T_2 ratio for design is chosen to have a value of 20. This corresponds to a protium level of ~0.2 vol. % in the inlet He purge.

At temperatures above ~550°C under ITER conditions, tritium solubility tends to be the dominant inventory component. It is clear from Fig. 10-10 how

protium swamping would help decrease the solubility. However, at lower temperatures (360-550°C) desorption tends to be the rate limiting tritium release mechanism. It is less clear how to quantify this because of the large scatter in the data for H_2 adsorption/solubility on/in Li_2O. This is shown in Fig. 10-11 for hydrogen isotopes. The data of O'Hira et al. are considered to be the most reliable because of their direct measurement of hydrogen isotopes in the samples. However, even taking the mean of their two curves leaves a factor of 4 uncertainty in the analysis. Thus, while the 0.2% H_2 level (460 Pa at purge inlet and 200 Pa at purge outlet) seems reasonable, it may not be optimum, given the factor of 4 uncertainty in the adsorption/ solubility data.

Below ~360°C (depending on the ratio of He flow rate to tritium generation rate), precipitation of separate-phase LiOT is the dominant tritium retention mechanism. For a given generation rate, this temperature can be lowered by increasing the He flow rate. For example, an increase of a factor of 10 in flow rate will reduce the precipitation temperature to ~310°C.

Calculations were performed to determine the local and global purge-gas component partial pressures and flow rates during the technology phase. The results are shown in Table 10-5. The case corresponds to a tritium generation rate of 18.4 moles (T_2)/day and a He flow rate of 2.80×10^5 moles (He)/day, giving an average He/T_2 ratio of 1.52×10^4 and a minimum local value of 1.04×10^4. The total H_2 flow rate is 560 moles (H_2)/day, giving an average H_2/T_2 ratio of 30.4 and a minimum local value of 21. The peak moisture pressure (10.7 Pa) occurs at the purge outlet of outboard plate #1 at the core midplane. These values are all reasonable with respect to the nominal design goals and guidelines.

The results in Table 10-5 are for the sintered-product design. For the same tritium generation rate, He purge flow rate and, H_2 flow rate, the ITER common design will differ only in the average purge temperature. The reference design has an average purge temperature of 450°C (equal to the breeder T_{min}) while the common design has an average purge temperature equal to the average breeder temperature (550°C for the binary bed and 600°C for the single-size bed). As can be seen by comparing Tables 10-2 through 10-4, the total moisture pressure will be the same, the total tritium pressure will be

the same, and there will be only a slight redistribution in HT, HTO, and T_2O components with the HT decreasing, the HTO increasing, and the T_2O decreasing.

References

[1] M.C. Billone, "Purge Flow Design Analysis and Tritium Inventory Calculations for ITER Li_2O Solid Breeder Blankets," Argonne National Laboratory Report ANL/FPP/TM-245, to be published.

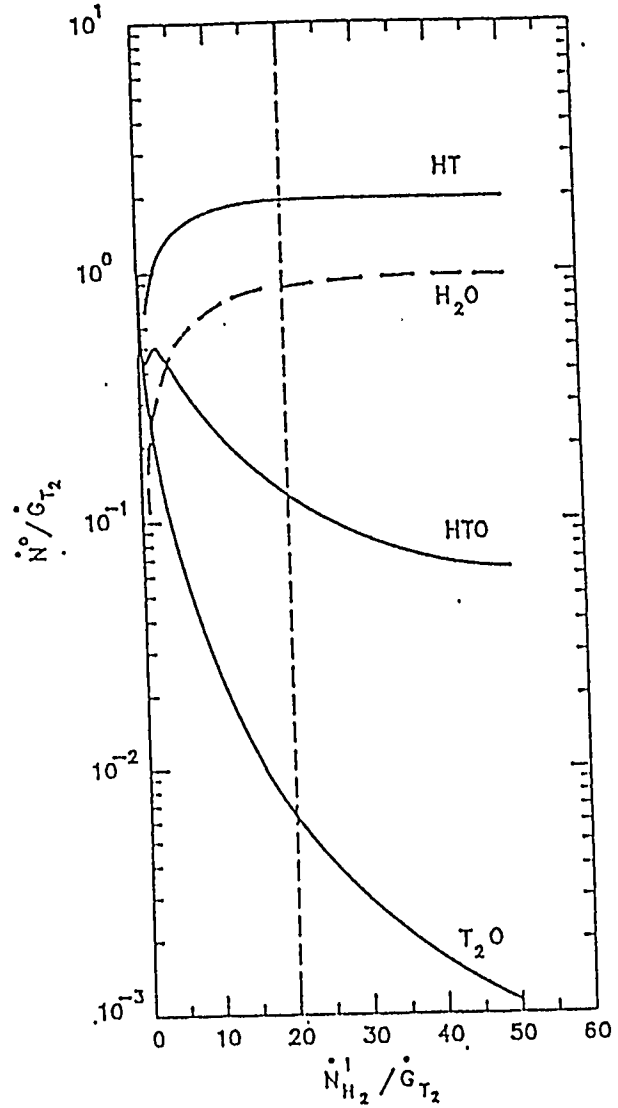

Fig. 10-10. Effect of protium purging on chemistry of purge gases. Calculation performed for 400°C.

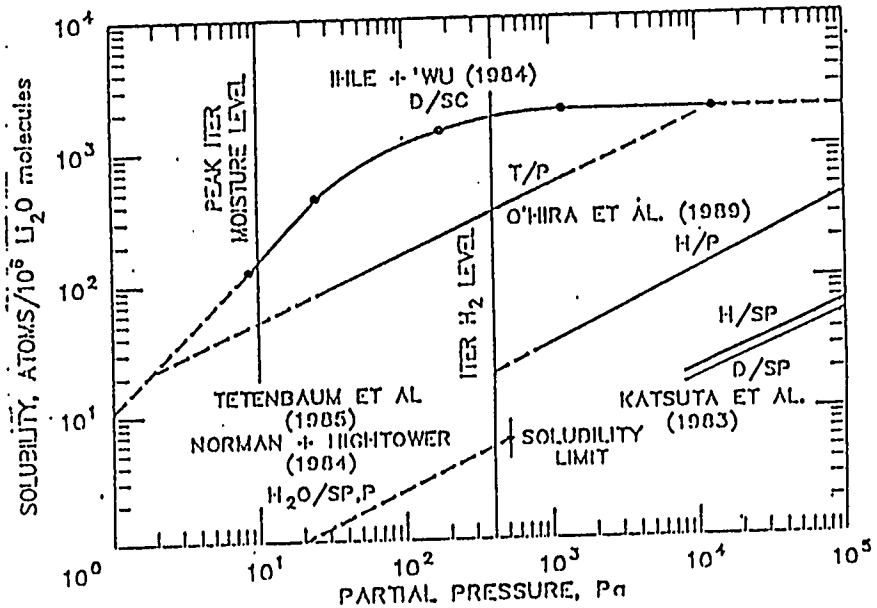

Fig. 10-11. Summary of experimental results for protium (H), deuterium (D), and tritium (T) solubility in single crystal (SC), sintered product (SP) and powdered (P) Li_2O at 515°C.

Table 10-2.
Molar Flow Rate Ratios of Purge Outlet Constituents (H_2, HT, H_2O, HTO, T_2O) at 400°C as a Function of Inlet-H_2 to Generated-T_2 Ratio. All Outlet Flow Rates are Normalized to the Molar T_2 Generation Rate.

Inlet H_2	Outlet				
	H_2	HT	H_2O	HTO	T_2O
1	0.3132	0.6868	0.1174	0.4519	0.4306
2	0.9662	1.0338	0.2666	0.5005	0.2328
3	1.7614	1.2386	0.3830	0.4726	0.1444
4	2.6273	1.3727	0.4706	0.4315	0.0979
5	3.5330	1.4670	0.5376	0.3917	0.0706
6	4.4632	1.5368	0.5901	0.3565	0.0533
7	5.4095	1.5905	0.6322	0.3261	0.0417
8	6.3669	1.6331	0.6666	0.2999	0.0335
9	7.3323	1.6677	0.6952	0.2774	0.0275
10	8.3036	1.6964	0.7193	0.2578	0.0229
15	13.2120	1.7880	0.7991	0.1898	0.0111
20	18.1629	1.8371	0.8437	0.1497	0.00660
25	23.1322	1.8678	0.8721	0.1236	0.00432
30	28.1113	1.8887	0.8918	0.1051	0.00311
40	38.0845	1.9155	0.9173	0.0809	0.00179
50	48.0681	1.4319	0.9331	0.0658	0.00116

Table 10-3.
Molar Flow Rate Ratios of Purge Outlet Constituents (H_2, HT, H_2O, HTO, T_2O) at 500°C as a Function of Inlet-H_2 to Generated-T_2 Ratio. All Outlet Flow Rates are Normalized to the Molar T_2 Generation Rate.

Inlet	Outlet				
H_2	H_2	HT	H_2O	HTO	T_2O
1	0.2909	0.7091	0.1246	0.4600	0.4155
2	0.9281	1.0719	0.2858	0.5002	0.2139
3	1.7184	1.2816	0.4095	0.4627	0.1279
4	2.5840	1.4160	0.5003	0.4154	0.0843
5	3.4912	1.5088	0.5683	0.3722	0.0595
6	4.4236	1.5764	0.6207	0.3351	0.0443
7	5.3721	1.6279	0.6620	0.3040	0.0341
8	6.3318	1.6682	0.6953	0.2775	0.0271
9	7.2992	1.7008	0.7228	0.2552	0.0220
10	8.2725	1.7275	0.7458	0.2359	0.0183
15	13.1882	1.8118	0.8205	0.1708	0.00872
20	18.1437	1.8563	0.8614	0.1335	0.00511
25	23.1162	1.8838	0.8872	0.1095	0.00335
30	28.0975	1.9025	0.9048	0.0928	0.00234
40	38.0738	1.9262	0.9276	0.0711	0.00137
50	48.0593	1.9407	0.9415	0.0576	0.000832

Table 10-4.
Molar Flow Rate Ratios of Purge Outlet Constituents (H_2, HT, H_2O, HTO, T_2O) at 600°C as a Function of Inlet-H_2 to Generated-T_2 Ratio. All Outlet Flow Rates are Normalized to the Molar T_2 Generation Rate.

Inlet H_2	Outlet				
	H_2	HT	H_2O	HTO	T_2O
1	0.2713	0.7287	0.1316	0.4654	0.4029
2	0.8935	1.1065	0.3048	0.4968	0.1983
3	1.6791	1.3209	0.4352	0.4505	0.1143
4	2.5447	1.4553	0.5287	0.3978	0.0734
5	3.4536	1.5464	0.5973	0.3518	0.0509
6	4.3881	1.6119	0.6491	0.3137	0.0372
7	5.3389	1.6611	0.6894	0.2822	0.0283
8	6.3007	1.6993	0.7216	0.2560	0.0223
9	7.2701	1.7299	0.7479	0.2341	0.0180
10	8.2451	1.7549	0.7697	0.2156	0.0148
15	13.1675	1.8325	0.8394	0.1537	0.00689
20	18.1271	1.8729	0.8768	0.1193	0.00392
25	23.1024	1.8976	0.9001	0.0973	0.00254
30	28.0858	1.9142	0.9160	0.0821	0.00184
40	38.0647	1.9353	0.9363	0.0626	0.00103
50	48.0519	1.9481	0.9487	0.0506	0.00629

Table 10-5.
Summary of Purge Flow Analysis for the Sintered-Product Concept During the ITER Technology Phase with a He Flow Rate of 3.24 moles/s (2.80×10^5 moles/day) an Inlet Pressure of 0.23 MPa, an Exit Pressure of 0.1 MPa, and 0.2% H_2 at Purge Inlet

Parameter	Location[a]	Exit Values				
		H_2	HT	H_2O	HTO	T_2O
Partial Pressure, Pa	IB Midplane	190	13.3	6.29	0.720	0.0204
	IB Average	190	12.9	6.11	0.678	0.0189
	IB Top	196	5.96	2.91	0.146	0.0018
	OB1 Midplane	185	18.0	9.33	1.33	0.0527
	OB1 Average	186	17.0	7.91	1.17	0.0439
	OB1 Top	191	12.7	5.52	0.548	0.0136
	OB2 Midplane	190	13.0	6.15	0.686	0.0192
	OB2 Average	194	8.44	4.07	0.288	0.0051
	OB2 Top	199	3.57	1.76	0.0514	0.0004
Total Flow Rate, moles/day	IB	86.1	5.86	2.77	0.308	0.009
	OB	439	28.8	13.6	1.63	0.054
	Total	525	34.7	16.4	1.94	0.063

a- Inboard (IB), outboard plate #1 (OB1) closest to the plasma, and outboard plate #2 (OB2) farthest from the plasma.

10.3 Transient Tritium Release Rate

10.3.1 Introduction

Because of the pulsed nature of operation for the physics and technology phases, it is important to perform a transient tritium release analysis. In the next section, Tables 10-10 to 10-12 give information about the power ramp, flat-burn, and total cycle times for the physics and technology phases. The physics phase is assumed to have a ramp-up (and ramp-down) time of 20 s with a flat-burn time of 400 s in between up and down ramps. The total physics cycle time, including time at zero power, is 600 s. Further, it is assumed that the physics phase consists of 5000 of these cycles. The technology phase consists of 20-s ramps, 2290-s flat-burn time and 2490-s total cycle time.

In the tritium analysis, there are three sets of response times. The first two are the tritium generation rate and temperature inputs to the analysis. The third is due to the tritium response time of the Li_2O itself. For this type of problem, the generation rate has the fastest time constant ; the thermal response lags the generation rate and the tritium response lags the thermal response.

Transient temperature profiles were generated by the TOPAZ code and are described in Section 7. Table 10-6 summarizes the beginning of cycle breeder minimum and maximum temperatures, the end-of-flat-burn minimum and maximum temperatures and the time-averaged values of these temperatures from the beginning of the up-ramp to the end of flat-burn. The results are shown for the "equilibrium" thermal cycle. For the long technology-phase pulses, steady temperatures are achieved before the end of the first flat burn. The equilibrium thermal cycle starts with the beginning of the second pulse for most locations and is maintained for every succeeding pulse. The only minor exception to this is the second breeder plate at the top of the blanket which requires an addition pulse to reach the equilibrium cycle. Also notice that the thermal response time of the breeder and surrounding Be and steel layers is fast enough to reach the steady-state heat-transfer temperatures at all locations except for the second breeder plate at the top of the outboard blanket, which falls only 16°C below this value.

For the physics phase, the equilibrium thermal cycle is achieved somewhere between the second and tenth reactor cycle, depending on location. The

thermal response time at every location is too long for the steady-state (heat-transfer) physics temperatures to be achieved at the end of the 400 s flat burn. However, as the physics-phase heating rate is higher than for the technology phase, the end-of-flat-burn temperatures are higher for the physics phase than the steady-state technology temperatures.

Qualitatively, what can be expected for the tritium release rate during pulsed operation is that the release rate will be lower than the generation rate during the early part of the cycle when the temperatures are low. As the breeder temperature increases, the release rate will increase and may exceed the generation rate. Finally, an "equilibrium" tritium-release-rate cycle will be achieved during which the time-averaged release rate will equal the generation rate.

The analysis of the transient tritium release from the sintered-product solid breeder blanket was performed using the MISTRAL code [1]. The model on which the code is based is briefly described below. The cases considered are then highlighted, followed by a discussion of the results and a summary section.

10.3.1 Model description

MISTRAL is based on the mechanisms shown in Fig. 10-12. The tritium atom generated in the solid breeder bulk diffuses with an activation energy E_{diff}. When it gets to the surface it adsorbs with an activation energy of E_{β}. On the surface it combines with another atom or radical to desorb with energy E_{des}. Tritium in the pore (gas phase) can also adsorb back with an activation energy E_{ads}. Figure 10-12 illustrates the surface processes of adsorption from the bulk, adsorption from the pore and desorption to the pore. Note that in the model the flux associated with an adsorbed tritium atom entering the bulk (dissolution flux) with an activation energy of E_{diss} is neglected.

A schematic of the complete model is shown in Fig. 10-13. The pore length is based on the physical solid breeder dimension and on the tortuosity factor associated with the solid breeder microstructure. A spatial temperature gradient across the solid breeder can be incorporated by specifying the temperature at different pore locations.

In the original model [1], the assumed species in the pore were H_2, T_2, and HT. However, because of concern about LiOT precipitation in Li_2O being substantial at low temperature and high moisture partial pressure, the code was modified to include H_2O, T_2O, and HTO also in the pore. It was assumed that all oxygen in the pore comes from the desorbing molecules (T_2O and HTO) in the ratio: 1 oxygen atom to 2 tritium atoms.

The LiOT precipitation calculation proceeds as follows: first, the critical moisture pressure, P_m^c, above which LiOT precipitation occurs, is calculated for the given local temperature, T_c:

$$P_m^c = \begin{cases} (3.469 \times 10^{11}\ \text{Pa}) \exp\left(-1.552 \times 10^4/T_c\right) & \text{for } T_c \le 744\ \text{K} \\ (1.89 \times 10^8\ \text{Pa}) \exp\left(-1.010 \times 10^4/T_c\right) & \text{for } T_c > 744\ \text{K} \end{cases}$$

Then, the corresponding sum of the partial pressure of H_2O, T_2O, and HTO is computed. If this total moisture pressure is higher than the critical moisture pressure, it is assumed that all tritium in the bulk precipitates in LiOT form. Otherwise, no precipitation is assumed to occur and the code proceeds with the normal solution of the tritium release equations [1]. A key assumption at this stage is that LiOT precipitation and dissociation in the bulk occur instantaneously. For LiOT precipitation, this is conservative, since it results in higher tritium inventories. For LiOT dissociation, this results in the desorption activation energy effectively controlling the characteristic time for an effective dissociation/desorption process.

10.3.2 Cases considered

In the interest of time and computational efficiency, the following strategy was adopted. The calculations would be done only for the outboard region 1 of the blanket based on the latest blanket operating parameters. Previous calculations had shown that the tritium release results for that case were representative of those for the outboard region 2 and for the inboard region. However, if warranted by unusual tritium release behavior or concern that for some reason the tritium release from the other regions would behave differently following the results for region 1, runs would also be done for other regions.

The main parameters used in the calculations are shown in Table 10-7 and the cases considered are shown in Table 10-8. To assess the effect of the tritium concentration in the purge, the two limiting cases of zero tritium concentration (which would occur at the entrance to the solid breeder region) and of tritium concentration correspondingly to the steady state level (which is more representative of the conditions at the purge exit) are analyzed for both the technology and physics phase.

10.3.3 Results

The transient tritium release results for the technology and physics phase are discussed below. Since the cases associated with the assumption of steady-state-like tritium partial pressure in the purge (i.e., Case 2 for the technology and physics phases) are more conservative, they are discussed in more detail.

Technology Phase

The tritium generation rate and maximum temperature profile histories for the cycles of operation during the technology phase are shown in Figs. 10-14 and 10-15. The histories of the maximum and minimum temperatures across the solid breeder are used a input in the code and the spatial temperature distribution at each time step is estimated from them, based on a parabolic profile.

The tritium release rate for an effective tritium partial pressure of 20 Pa in the purge ise shown in Fig. 10-16. The tritium release exhibits a characteristic initial peak at the start of the burn time due to the combined effects of the generation rate starting and the temperature rising. This is followed by a return to a normalized release of 1 during the rest of the burn time. The release falls to zero during the dwell time. The tritium release profile reaches a quasi-steady-state within a couple of cycles only.

The tritium release results for zero tritium partial pressure in the purge (Case 1) are shown in Fig. 10-17. Because of the lower moisture pressure, less tritium is trapped during the up-ramp and the peak release rate is only ~1.3 times the generation rate.

Physics Phase

The normalized tritium generation and maximum temperature histories for the Li_2O outboard region 1 during the physics phase are shown in Figs. 10-18 and 10-19.

The tritium release history is shown in Fig. 10-20 for the more conservative case with a 20 Pa tritium partial pressure in the pore (Case 2). The results are similar to those for the technology phase with the normalized release peaking at the outset of the burn time and then approaching one before going to zero during the dwell time.

When the tritium partial pressure in the purge was set to zero (Case 1), it resulted in an ever lower tritium release peak; a behavior similar to that observed for the technology phase cases.

Summary

- The effect of LiOT precipitation has been included in the MISTRAL code for ITER Li_2O blanket tritium release calculations. The assumption is that all bulk tritium precipitates when the total moisture partial pressure exceeds the critical precipitation partial pressure at the given temperature.

- The calculations were done for the Li_2O outboard region 1 of the blanket which is thought to be generally representative of the other regions also based on previous calculations. Nothing in the new results seems to contradict that.

- The focus of the calculations was on the more conservative cases where the tritium partial pressure in the purge is assumed to be at the steady-state level (about 20 Pa).

- For both the technology and physics phases, the following observations emerge from the results:

  - The tritium release exhibits a characteristic initial peak at the start of the burn time due to the combined effects of the generation

rate starting and the temperature rising. This is followed by a return to a value equivalent to the generation rate during the rest of the burn time, and by a drop to zero release during the dwell time. The tritium release cycle approaches its quasi-steady-state behavior quite rapidly, within two or three cycles, at the outboard core-midplane position.

- LiOT precipitation does not occur during the burn time because the moisture pressure is significantly lower than the critical moisture pressure for both phases based on the operating temperature data. During the dwell time, the occurrence of precipitation does not really affect the tritium behavior since the tritium release would virtually stop in any case due to the combination of no tritium generation and very slow diffusion at low temperature.

- While release peaks of ~1.3 to 5.0 times the generation rate occurred locally along the purge flow direction at the outboard core midplane (plate #1), it should be emphasized that the tritium recovery and processing systems do not see these local peaks. The tritium content at the purge exit is an integrated value for the release rates along the purge flow path. Also, the magnitudes, duration, and time-of-occurrence of the peaks varies poloidally as the heating rate decreases and as the thermal response time of the breeder/Be layers decreases. The peak in integrated release rate for the whole outboard breeder is estimated to be <2 times the generation rate. Thus, the tritium recovery/processing system should be designed for no more than a factor of 2 release rate above the steady-state value for pulsed operation.

10.3.4 ITER common design results

Similar results are expected for the ITER common design with Li_2O pebbles replacing the sintered product. This is because the breeder minimum temperature history is controlled by the thermal response time of the Be zones. Thus, the time history for T_{min} remains the same. The higher values for T_{max} for the common design will result in a somewhat faster tritium response time than for the reference design.

References

[1] G. Federici, A.R. Raffray, and M.A. Abdou, "MISTRAL: A Comprehensive Model for Tritium Transport in Lithium-Base Ceramics - Parts I and II," accepted for publication in The Journal of Nuclear Materials.

Table 10-6. Summary of Li_2O Breeder Temperatures for Technology and Physics Phase Equilibrium Thermal Cycles

Phase	Location[a]	T, °C		
		Inboard	OB1	OB2
Technology	Midplane			
	BOC T_{min}	147	138	203
	AVG T_{min}	437	437	430
	EOB T_{min}	452	453	451
	SS T_{min}	452	453	451
	BOC T_{max}	154	140	204
	AVG T_{max}	510	519	482
	EOB T_{max}	527	536	505
	SS T_{max}	527	536	505
	Top			
	BOC T_{min}	254	237	319
	AVG T_{min}	424	430	394
	EOB T_{min}	442	448	433
	SS T_{min}	442	448	449
	BOC T_{max}	257	238	319
	AVG T_{max}	453	473	404
	EOB T_{max}	472	492	444
	SS T_{max}	472	492	460
Physics	Midplane			
	BOC T_{min}	170	142	200
	AVG T_{min}	393	387	358
	EOB T_{min}	487	487	448
	SS T_{min}	509	508	502
	BOC T_{max}	177	150	208
	AVG T_{max}	458	460	396
	EOB T_{max}	576	584	503
	SS T_{max}	603	609	566
	Top			
	BOC T_{min}	280	243	308
	AVG T_{min}	396	352	335
	EOB T_{min}	397	424	360
	SS T_{min}	493	499	499
	BOC T_{max}	290	248	311
	AVG T_{max}	370	386	345
	EOB T_{max}	429	472	371
	SS T_{max}	529	551	513

[a]Beginning of cycle (BOC), time-averaged (AVG), end of flat burn (EOB), and steady state (SS)

Table 10-7.
Main Parameters Used for Transient Tritium Calculations
for the Sintered-Product Li_2O Solid Breeder for Outboard Region 1

Thickness (mm)	8
T Generation Rate (atoms/s-m^3):	
Physics Phase	2.31×10^{19}
Technology Phase	2.01×10^{19}
Total Porosity (%)	20
Open Porosity (%)	18
Average Grain Size, (μm)	20
BET Surface Area (m^2/kg)	5
Li_2O Theoretical Density (kg/m^3)	1905
Grain Diffusion Coefficient:	
Pre-exponential (m^2/s)	6.81×10^{-7}
Activation Energy (kJ/mol)	84.8
Desorption Activation Energy (kJ/mol)	122
Pore Diffusion Coefficients for Tritium & Hydrogen (m^2/s):	
Reduced form: see Ref. [1]	
Oxidized form: $(3.5 \times 10^{-5}$ Pa/P)$T^{2.334}$	

Table 10-8.
Cases Considered for Tritium Release Calculations

Technology Phase	
Total cycle time	2490 s
Flat burn time	2290 s
Ramp time	20 s
Dwell time	200 s
Case 1. Tritium concentration in purge = 0	
Case 2. Tritium concentration in purge = steady state level ≡ 20 Pa	
Physics Phase	
Total cycle time	600 s
Flat burn time	400 s
Ramp time	20 s
Dwell time	200 s
Case 1. Tritium concentration in purge = 0	
Case 2. Tritium concentration in purge = steady state level ≡ 20 Pa	

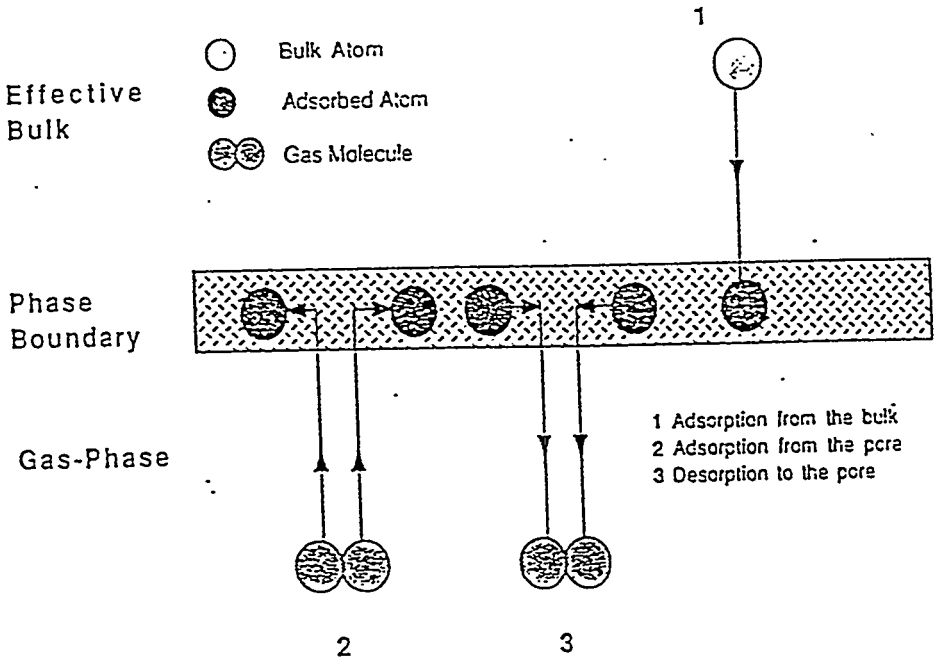

Figure 10-12. Schematic of the surface processes included in the model.

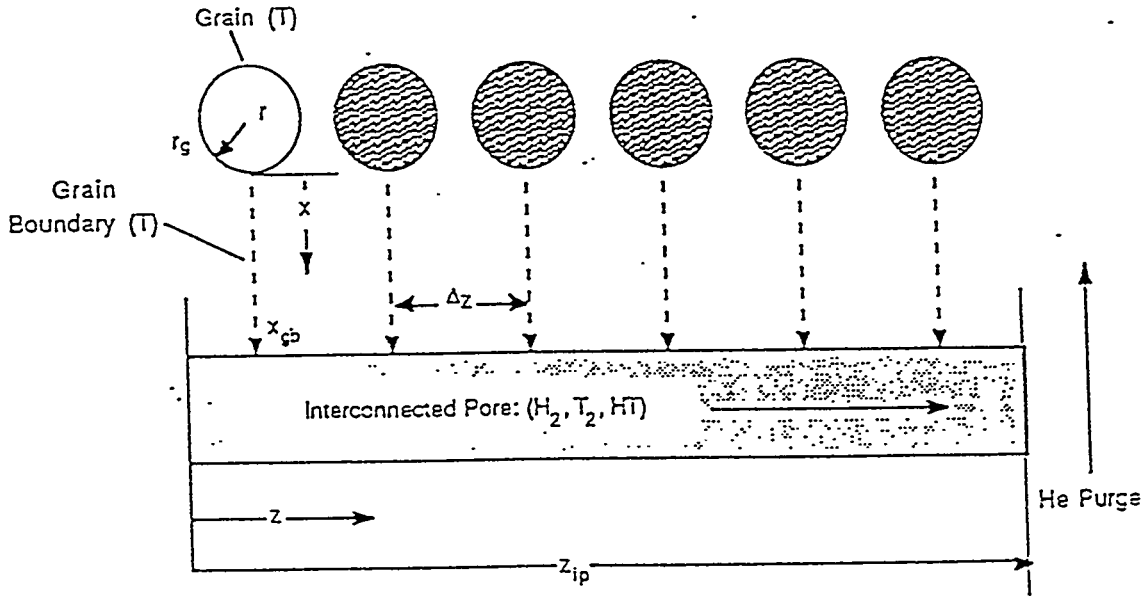

Figure 10-13. Schematic diagram of the multiregion model.

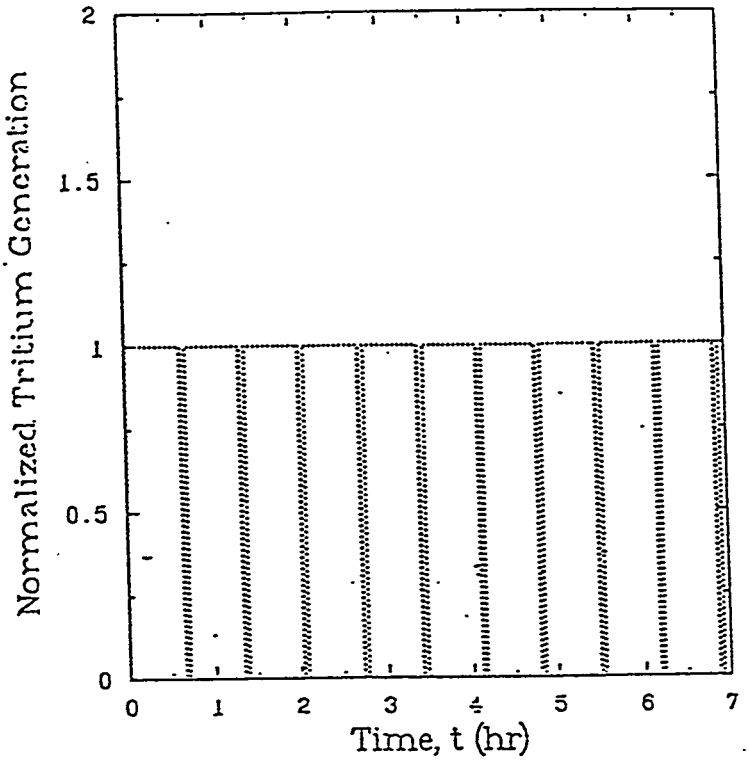

Figure 10-14. Normalized tritium generation history during technology phase.

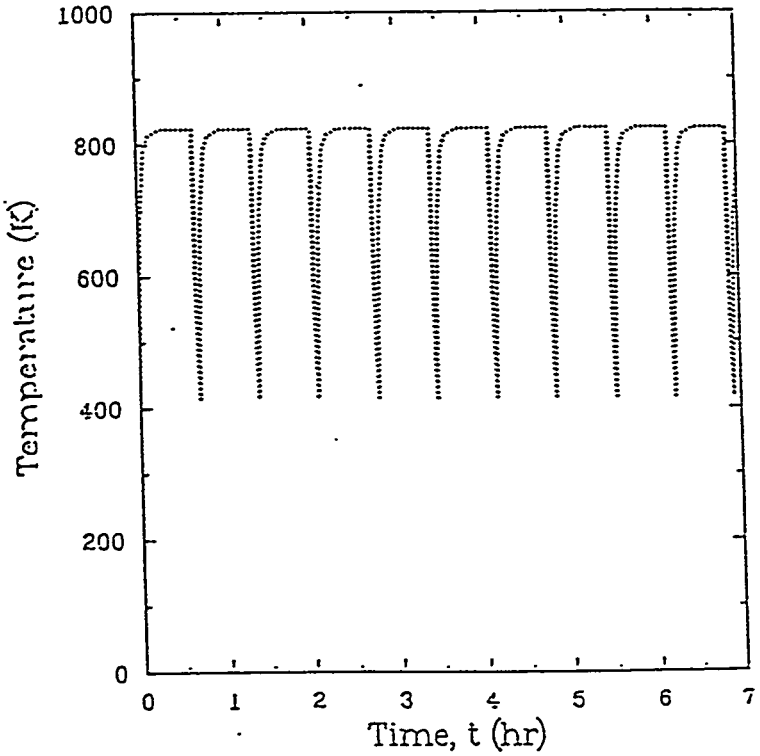

Figure 10-15. Maximum Li_2O temperature history for the outboard Li_2O region 1 for the technology phase.

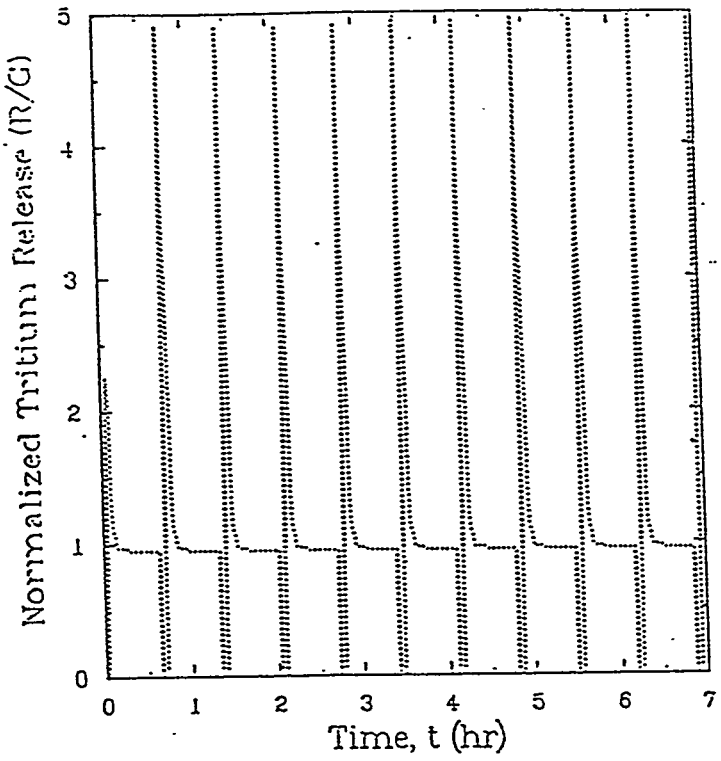

Figure 10-16. Tritium release history for the outboard Li_2O region 1 during the technology phase with a 20 Pa tritium partial pressure in the purge.

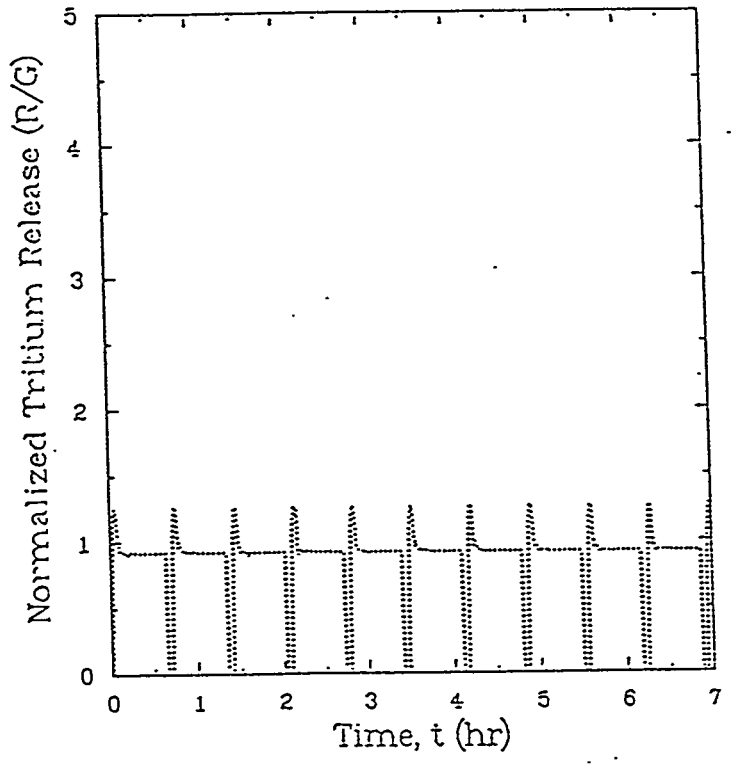

Figure 10-17. Tritium release history in the Li_2O outboard region 1 during the technology phase with zero tritium partial pressure in the purge.

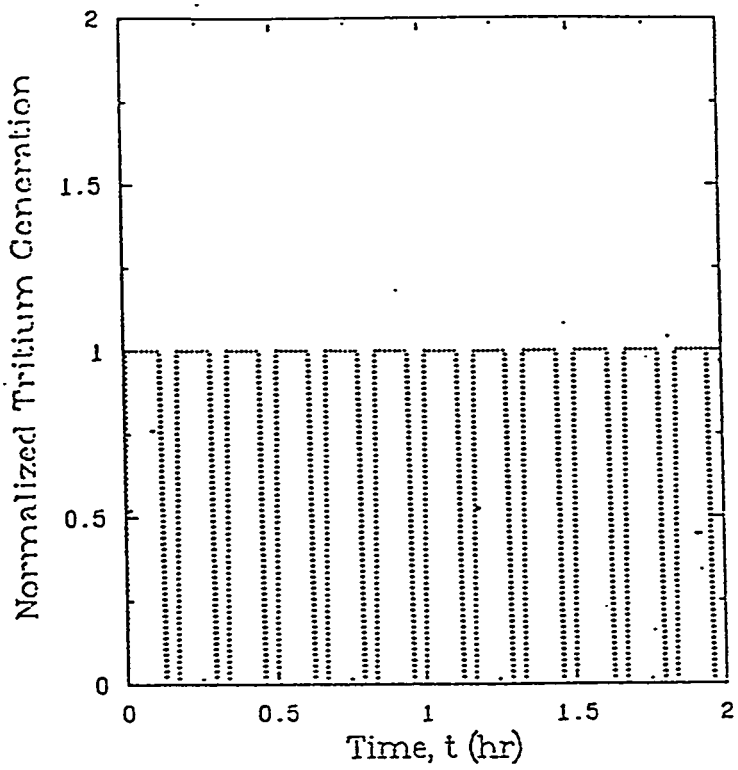

Figure 10-18. Normalized tritium generation history for the Li_2O outboard region 1 during the physics phase.

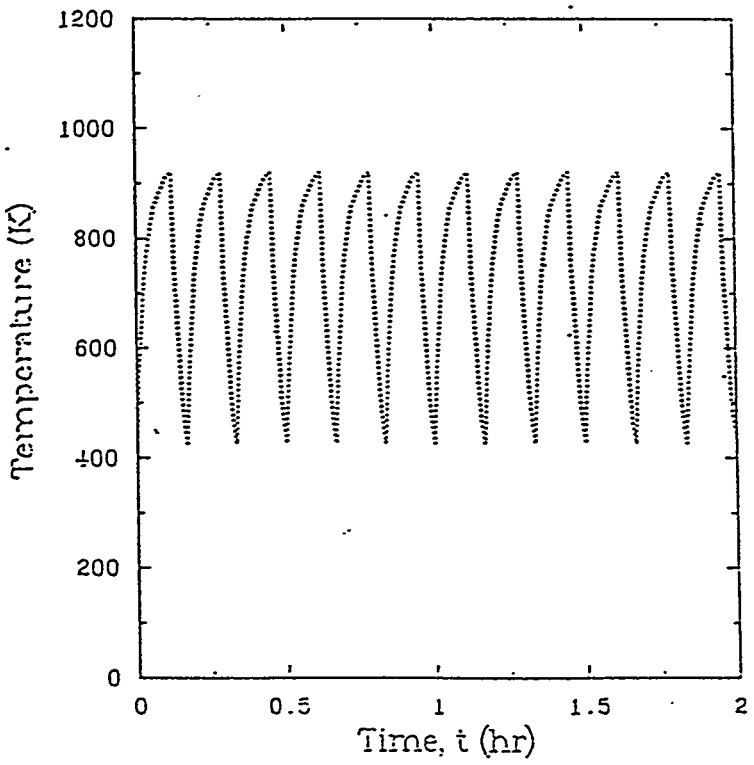

Figure 10-19. Maximum temperature history for the Li_2O outboard region 1 during the physics phase.

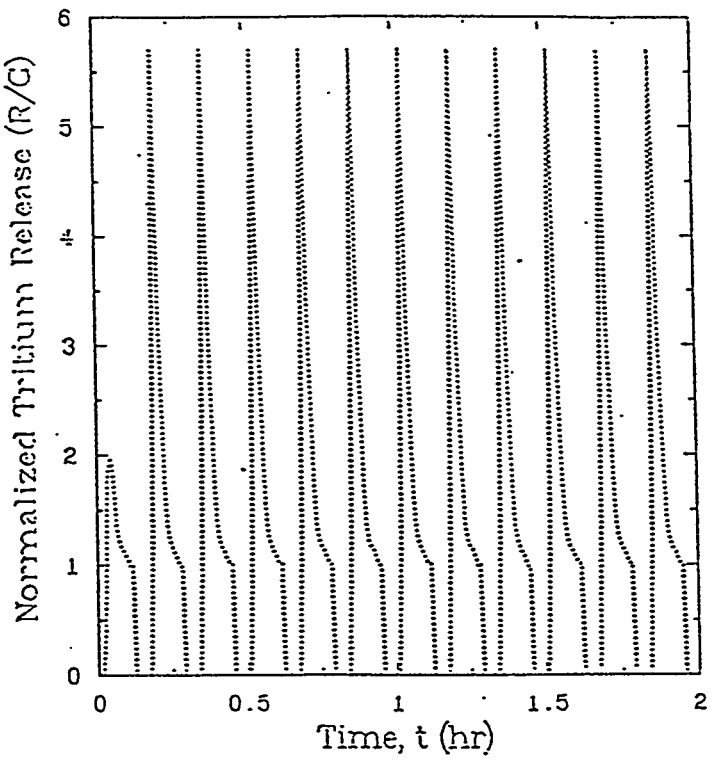

Figure 10-20. Normalized release history in the Li_2O outboard region 1 during the physics phase with a 20 Pa tritium partial pressure in the purge.

10.4 Steady State Tritium Inventory

Detailed models have been developed to describe tritium retention in Li_2O solid breeders [1]. Bulk diffusion, desorption, adsorption/solubility and precipitation (separate phase LiOT) mechanisms are included in the analysis. In the following, tritium inventories under steady-state operating conditions are calculated for both the sintered-product and the common (pebble bed) designs.

10.4.1 Sintered-product

Table 10-9 contains the breeder plate fabrication and Li_2O model parameters used in the tritium retention/release analysis. In addition to the parameters in Table 10-9, the purge flow rate, inlet pressure, and outlet pressure needs to be specified. The total reactor flow rate is 3.24 moles (He)/s. It is based on keeping the maximum local moisture pressure (H_2O + HTO + T_2O) to be $\leq$ 10 Pa. Locally, this flow rate corresponds to 0.392 moles (He)/s-m^3 (Li_2O). For the baseline case, the He inlet/outlet pressures are ~0.2/0.1 MPa with small local variations due to variations in purge temperature. This is achieved by fabricating semi-circular grooves of 0.46-mm diameter every 1 cm^2 of breeder cross-section in the poloidal direction. The purge flow is toroidal and thus has a flow path of ~1 m.

Table 10-10 contains the global ITER parameters. The masses were obtained from the volumes calculated from the 3-D tritium breeding ratio (TBR) analysis. The tritium generation rates are consistent with the net TBR values for inboard and outboard. Notice that although the physics phase has a fusion power ~1.28 greater than the technology phase, the generated tritium is only a factor of ~1.14 greater because of the lower breeding ratio during the physics phase.

Tables 10-11 and 10-12 give the local tritium generation rates and steady-state breeder temperatures for the physics and technology phases, respectively. The local tritium generation rates are derived from the average three-dimensional values by scaling according to the local neutron wall loading and the local TBR. The steady-state temperatures are obtained from TOPAZ (see Section 7).

The detailed tritium inventory results for the sintered-product design are presented in Table 10-13. Local tritium concentrations are given in weight parts tritium per million weight parts Li_2O (wppm). Total inboard (IB), outboard (OB) and combined inboard/outboard inventories are given in grams. For each breeder plate, calculations were performed at the peak tritium-generation-rate position (midplane), the minimum tritium-generation-rate region (top or bottom), and an intermediate position corresponding to the location of the average tritium generation rate (average). Each of these regions has different temperature profiles (see Tables 10-11 and 10-12). The approach used to calculate the total inventories was to compare the value of the "average-position" inventory concentration to the mean concentration of the top and midplane positions. The larger of these two numbers was then multiplied by the appropriate masses of each breeder plate from Table 10-11 or 10-12 to obtain the inventory in grams.

The inventory for the physics (higher temperature) phase under assumed steady-state operating conditions is only ~3 g with solubility being the dominant component. The corresponding inventory for the technology (lower-temperature) phase is ~14 g with desorption being the dominant inventory component. Both these results seem reasonable. The technology-phase results are more relevant to pulsed operation, however, than the physics-phase results because of the long length of the technology phase pulses.

The baseline case shown in Table 10-13 is for a He inlet pressure of 0.236 MPa and an outlet pressure 0.101 MPa. Because of concerns about the structural response of the first wall to such gas pressures, the inventory calculations were re-run with 0.067 MPa inlet pressure and 0.05 MPa outlet pressure, keeping the He and H_2 flow rates the same. The resulting reduction in H_2 pressure causes a change in tritium inventory. The physics phase inventory remains low (1.6 g) while the technology phase inventory increases to ~24 g due to the increased desorption component. If the average H_2 pressure had been kept the same (by increasing the H_2 content of the low pressure He to 0.58 vol. %) then the results for the reduced-He-pressure case would be essentially the same as for the refrence case.

Another set of calculations was performed to determine the uncertainty in the tritium-inventory results due to the uncertainty in H_2, HT, T_2 adsorption/solubility (see Fig. 10-11). The hydrogen isotope solubility was

varied (up and down) by a factor of 4 to determine the effects of this parameter on the total inventory. Increasing the hydrogen isotope solubility tends to increase the tritium solubility component and to decrease the desorption component. The results of the uncertainty analysis are shown in Table 10-14 along with the results of the lower He pressure case and the baseline He pressure case.

10.4.2 ITER common design

The primary difference between the common design and the reference design, with regard to tritium inventory analysis, is the higher average breeder and purge temperatures. Under these conditions, the solubility component will increase and the desorption component will decrease. The Li_2O temperature profiles for single-size and binary pebble beds are shown in Table 10-15 for technology phase outboard breeder region #1 (closest to the plasma) at the core midplane. Also, shown in the table are the estimated average partial pressures of H_2, HT, H_2O, and T_2O. These were used to generate the inventory components for the common design. The results are on the same order as for the sintered-product design. Extrapolating these results to the whole reactor leads to 14 g for the sintered-product design, 9 g for the binary-pebble-bed common design and 10 g for the single-size-pebble-bed common design.

References

[1] M.C. Billone, "Purge Flow Design Analysis and Tritium Inventory Calculations for ITER Solid Breeder Blankets," Argonne National Laboratory Report ANL/FPP/TM-245 (to be published).

Table 10-9. Li_2O Breeder Plate and Model Parameters for Sintered-Product Tritium Analysis

Parameter	Value
Plate thickness, mm	8 (OB), 10 (IB)
Theoretical density, g/cm^3	1.905
Li-6 enrichment, %	95
Grain radius, μm	10
Specific surface area, m^2/g	0.05
Total porosity, %	20
Interconnected porosity, %	18
Average pore radius, μm	2.5
Breeder permeability, 10^{-12} m^2	0.04
Purge permeability, 10^{-12} m^2	4.0
H_2 content in He purge, %	0.2
Lattice diffusivity, m^2/s	$6.81\times10^{-7}\ \exp(-84.8\ kJ\cdot mol^{-1}/RT)$
Grain boundary diffusivity, m^2/s	
Surface desorption rate constant s^{-1}	$\exp(19 - 122\ kJ\cdot mol^{-1}/RT)$
Effective pore diffusivity,(a) m^2/s	
HT (P in Pa)	$(1.52\times10^{-5}/P)\ [1 + (3.87/P)\ T^{1.323}]^{-1}\ T^{1.823}$
HTO (P in Pa)	$(1.16\times10^{-6}/P)\ [1 + (0.661/P)\ T^{1.834}]^{-1}\ T^{2.334}$
Tritium solubility	$86.5\ \exp(-2950/T)\ P_{HT}/P_{H_2}^{0.5}$
appm (Li_2O)	$+\ 10^{6-A}\ B(9.869\times10^{-6}\ P_{H_2O})^B\ (P_{HTO}/P_{H_2O})$
	$A = 17.667 - 2.502\times10^{-2}\ T + 9.62\times10^{-6}\ T^2$
	$B = 0.427 + 1.7\times10^{-4}\ T$
Critical moisture pressure for LiOH(T) precipitation, Pa	
$T \leq 744K$	$(3.49\times10^{11})\ \exp(-1.552\times10^{4}/T)$
$T > 744K$	$(1.89\times10^{8})\ \exp(-1.010\times10^{4}/T)$

(a) To be used with a source term per unit total volume and a diffusion length = plate halfwidth.

Table 10-10. ITER Reactor Parameters

Parameter	Inboard	Outboard	Total
Effective FW area for breeder, m^2	136	408	544
Li_2O mass, MT	2.07	10.53	12.6
Be mass, MT	19.0	186.7	206
Fusion power, MW			
Physics	--	--	1100
Technology	--	--	860
Tritium generation rate, g/day			
Physics	21.5	105.6	127
Technology	18.5	92.7	111
Effective full power operating time, days			
Physics	--	--	$\leq$24.3
Technology	--	--	$\leq$1360
Physics times, s			
Cycle, s	--	--	600
Ramp, s	--	--	20
Flat burn, s	--	--	400
Technology times,			
Cycle, s	--	--	2490
Ramp, s	--	--	20
Flat burn, s	--	--	2290

Table 10-11.
Local ITER Parameters for Tritium Analysis
During the Physics Phase

Parameter	Inboard	Outboard #1	Outboard #2
Li_2O mass, MT	2.07	4.97	5.56
Neutron wall Loading, MW/m^2			
Midplane	1.130	1.535	
Average	1.000	1.279	
Top	0.416	0.767	
Tritium generation rate, wppm/day			
Midplane	10.93	15.05	9.27
Average	10.39	13.87	9.11
Top	4.62	9.11	2.65
Breeder SS T_{min}, °C			
Midplane	509	508	502
Average	506	505	501
Top	493	499	499
Breeder SS T_{max}, °C			
Midplane	603	609	566
Average	589	589	554
Top	529	551	513

Table 10-12.
Local ITER Parameters for Tritium Analysis
During the Technology Phase.

Parameter	Inboard	Outboard #1	Outboard #2
Li_2O mass, MT	2.07	4.97	5.56
Neutron wall loading, MW/m^2			
Midplane	0.884	1.200	
Average	0.785	1.000	
Top	0.325	0.600	
Tritium generation rate, wppm/day			
Midplane	9.23	12.80	9.02
Average	8.96	12.00	5.74
Top	4.02	8.00	2.38
Breeder SS T_{min}, °C			
Midplane	452	453	451
Average	450	451	451
Top	442	448	449
Breeder SS T_{max}, °C			
Midplane	527	536	505
Average	517	520	496
Top	472	492	460

Table 10-13.

Local and Global Results for Tritium Inventory in Li_2O Under Steady-State Physics and Technology Phase Operating Temperatures and Generation Rates for the Sintered-Product

Phase	Location[a]		Tritium Inventory, wppm				
			Desorp.	Sol.	Diff.	Gas Phase	Total
Physics	IB	Midplane	0.000	0.224	2.41E-4	7.66E-4	0.225
	IB	Average	0.000	0.202	2.61E-4	7.33E-4	0.203
	IB	Top	0.000	0.072	2.16E-4	3.35E-4	0.072
	OB1	Midplane	0.000	0.311	3.20E-4	1.05E-3	0.312
	OB1	Average	0.000	0.266	3.51E-4	9.78E-4	0.267
	OB1	Top	0.000	0.152	3.32E-4	6.53E-4	0.153
	OB2	Midplane	0.000	0.165	2.90E-4	6.60E-4	0.166
	OB2	Average	0.000	0.155	3.19E-4	6.52E-4	0.156
	OB2	Top	0.000	0.040	1.41E-4	1.93E-4	0.040
	Total	IB (grams)	0.00	0.42	0.00	0.00	0.42
	Total	OB (grams)	0.00	2.18	0.00	0.01	2.19
	Total	IB+OB (grams)	0.00	2.60	0.00	0.01	2.61
Technology	IB	Midplane	0.658	0.129	5.96E-4	6.76E-4	0.788
	IB	Average	0.815	0.120	6.45E-4	6.60E-4	0.936
	IB	Top	0.202	0.045	4.93E-4	3.03E-4	0.248
	OB1	Midplane	1.281	0.183	7.57E-4	9.33E-4	1.466
	OB1	Average	1.551	0.161	8.34E-4	8.82E-4	1.714
	OB1	Top	1.114	0.097	7.52E-4	5.96E-4	1.212
	OB2	Midplane	0.962	0.115	7.24E-4	8.50E-4	1.079
	OB2	Average	0.192	0.072	5.05E-4	4.27E-4	0.265
	OB2	Top	0.000	0.026	3.20E-4	1.80E-4	0.027
	Total	IB (grams)	1.69	0.25	0.00	0.00	1.94
	Total	OB (grams)	10.4	1.20	0.01	0.01	11.6
	Total	IB+OB (grams)	12.1	1.45	0.01	0.01	13.6

a- Inboard (IB), outboard plate #1 (OB1) closest to plasma, and outboard plate #2 (OB2) farthest from plasma.

Table 10-14.
Effects of Uncertainties and He Purge Pressure on the Tritium Inventory Results

Phase	Case	Tritium Inventory, g Inboard	Outboard	Total
Physics	Baseline:			
	Upper Bound	1.54	8.30	9.48
	Nominal	0.42	2.18	2.61
	Lower bound	0.35	2.18	2.53
	Low He Pressure/0.2% H_2 (0.067 MPa in, 0.05 MPa out)	0.25	1.33	1.58
Technology	Baseline:			
	Upper bound	6.87	37.8	44.7
	Nominal	1.94	11.6	13.6
	Lower bound	0.97	4.70	5.67
	Low He Pressure/0.2% H_2 (0.067 MPa in, 0.05 MPa out)	3.68	20.3	23.9

Table 10-15.
Temperatures, Gas Compositions, and Tritium Inventories in Li_2O for the Common (Pebble-bed) Design as Compared to the Sintered-Product Design for the Outboard Core Midplane Plate #1 During the Technology Phase

Parameter	Reference	Common Single-Size	Common Binary
Breeder T_{min}, °C	453	453	455
Purge $\bar{T}$, °C	453	600	551
Breeder T_{max}, °C	536	675	599
$\bar{P}_{H_2}$, Pa	320	200	250
$\bar{P}_{HT}$, Pa	9.0	9.1	9.1
$\bar{P}_{H_2O}$, Pa	4.7	4.8	4.9
$\bar{P}_{HTO}$, Pa	0.67	0.56	0.60
$\bar{P}_{T_2O}$, Pa	0.026	0.020	0.023
Inventory, wppm	1.466	0.982	1.043

10.5 Transient Tritium Inventory

10.5.1 Sintered-product design

The transient tritium transport model (MISTRAL) and the generation-rate and temperature histories for physics and technology cases are discussed in Section 10.3 for the sintered-product design. The corresponding inventory results are presented in this section.

Technology Phase

The tritium inventory components in outboard breeder plate #1 at the core midplane were calculated for technology phase pulses. The results are shown in Fig. 10-21 for a local region near the purge outlet, where an upperbound (i.e., steady-state) purge tritium pressure of 20 Pa was assumed. The inventory is dominated by the surface coverage (i.e., adsorption/desorption component) whose plot in the figure coincides nearly exactly with the total inventory. It oscillates between maximum and minimum values of 5.0×10^{-2} and 8.3×10^{-3} wppm (1 wppm = 13 g if extrapolated to the whole reactor).

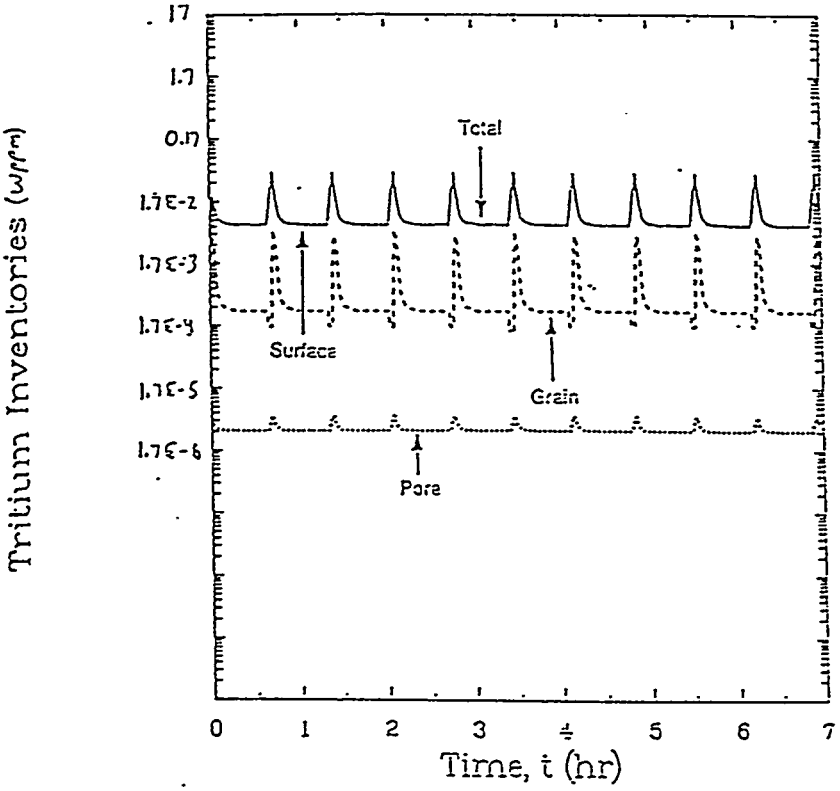

Figure 10-21. Tritium inventory history for the outboard Li_2O region 1 during the technology phase with a 20 Pa tritium partial pressure in the purge (1 wppm = 13 g).

The bulk (grain) inventory is quite low because LiOT precipitation does not occur during the burn time for the temperature and moisture pressure operating conditions. Figures 10-22 and 10-23 show the moisture pressure histories at the beginning and end of the interconnected pore system. The critical moisture pressure above which LiOT precipitation occurs is always higher than the calculated moisture pressure during the burn time. Because of the sharp drop in temperature during the dwell time, the critical moisture pressure decreases to below the moisture level. However, since, there is no tritium generation and no tritium release during the dwell because of very slow diffusion at the low temperature, LiOT precipitation does not really affect the overall tritium release and inventory behavior.

The tritium inventory results for the case near the purge inlet (i.e., zero tritium purge pressure) were lower than for the purge outlet case. The inventory oscillated around 3.3×10^{-3} wppm, which is substantially lower than the 1.7×10^{-2} wppm for the purge outlet position.

The lower inventory in the pore also results in a lower moisture pressure, well below the critical moisture pressure. Note that in this case the moisture partial pressure is lower than the critical one during the burn time, but also during most of the dwell time because of the very low pore concentrations set by the zero tritium partial pressure condition at the purge. This can be explained by the absolute pore concentrations between the burn and dwell times being also much more marked than before.

Physics Phase

The local inventory at the purge outlet of the outboard core-midplane breeder plate #1 is shown in Fig. 10-24. The results are similar to those of the technology phase in that the surface inventory is the dominant component. The maximum and minimum local inventories at this position are 3.3×10^{-2} wppm and 5.0×10^{-3} wppm. Figure 10-25 shows the calculated vs. critical moisture pressure for this case at the breeder centerline (z=0).

Near the purge inlet, the tritium pressure in the purge is zero. There is a very small increase in tritium and moisture pressure through the interconnected porosity to the breeder centerline. The calculated local inventories were ~1/5 of those calculated at the purge outlet position.

Summary

- The effect of LiOT precipitation has been included in the MISTRAL code for ITER Li_2O blanket inventory calculations. The assumption is that all bulk tritium precipitates when the total moisture partial pressure exceeds the critical precipitation partial pressure at the given temperature.

- The calculations were done for the Li_2O outboard region 1 of the blanket which is thought to be generally representative of the other regions also based on previous calculations. Nothing in the new results seems to contradict that.

- The focus of the calculations was on the more conservative cases where the tritium partial pressure in the purge is assumed to be at the steady-state level (about 20 Pa).

- For both the technology and physics phases, the following observations emerge from the results:

  - The inventory is dominated by surface coverage and is small, with a maximum local value of <0.17 wppm for the technology and physics phases, respectively, with a tritium partial pressure in the purge of 20 Pa. With zero tritium partial pressure in the purge, the inventory is even smaller. The slightly lower inventory in the physics phase is due to the higher operating temperature.

  - LiOT precipitation does not occur during the burn time because the moisture pressure is significantly lower than the critical moisture pressure for both phases based on the operating temperature data. During the dwell time, the occurrence of precipitation does not really affect the tritium behavior since the tritium release would virtually stop in any case due to the combination of no tritium generation and very slow diffusion at low temperature.

10.5.2 ITER common design results

In both the sintered-product and common designs, the thermal response time for the Li_2O breeder is dominated by the thermal lag in the Be. Thus, the time history for the breeder T_{min} will be the same. The maximum breeder temperature (T_{max}) will be higher than for the reference sintered-product Li_2O design. Thus, the tritium response time for the Li_2O pebble-bed common design is expected to be faster than for the layered design. The resulting inventory during pulsed operation will be even lower for the pebble-bed design.

10.5.3 Discussion

There is an apparent discrepancy in the "steady-state" inventory results presented in 10.5 and the transient results given in this section. One would expect higher inventories during pulsed operation than during steady state operation. The difference is more in the degree of conservatism in the modeling parameters than in the models. MISTRAL was validated to Li_2O transient release data such as summarized in Fig. 4-4 of Section 4. In this sense, MISTRAL represents a best-fit to the transient data. The steady-state model parameters were developed with considerable conservatism to encompass uncertainties in models, model parameters, and long-time extrapolation. When the residency time implied by these steady-state models is compared to measured residency times, the steady-state models give a much longer residency time (i.e., higher inventory) than data from short-term transient tests. Another reason for the higher inventories calculated with the steady-state models is that these models include a solubility component. This apparent discrepancy is not significant in that Li_2O inventories are small regardless of the degree of conservatism used in either approach.

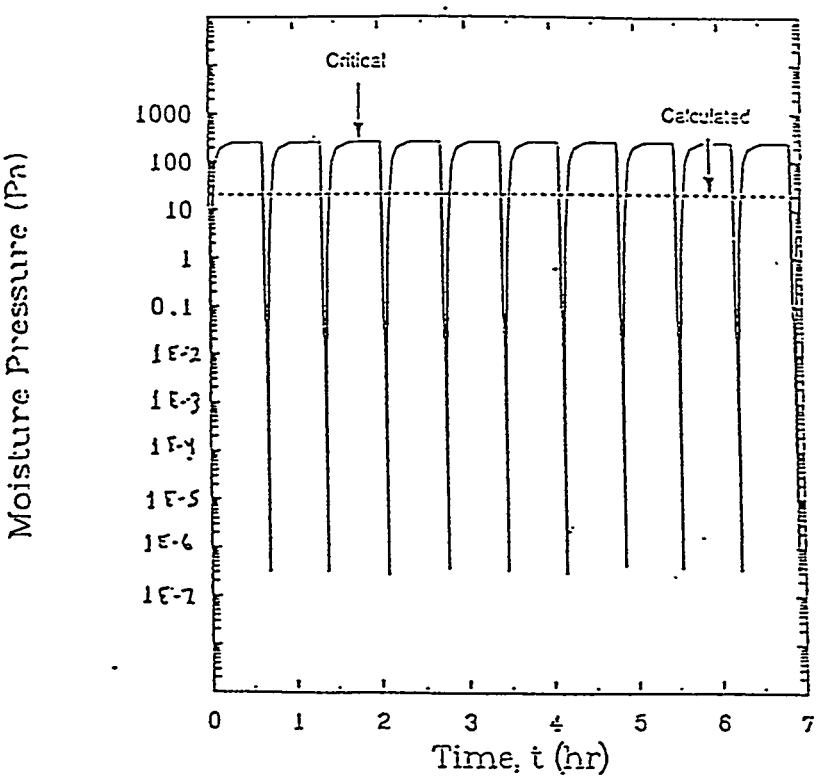

Figure 10-22. Critical and calculated moisture pressure histories at pore location z=0 in the Li_2O outboard region 1 during the technology phase with a 20 Pa tritium partial pressure in the purge.

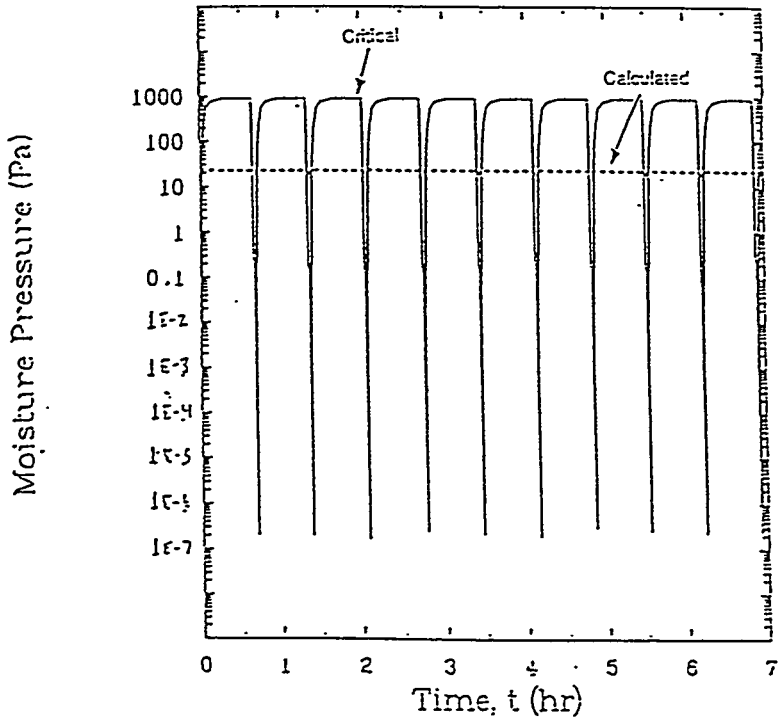

Figure 10-23. Critical and calculated moisture pressure histories at pore location $z=z_{ip}$ in the Li_2O outboard region 1 during the technology phase with a 20 Pa tritium partial pressure in the purge.

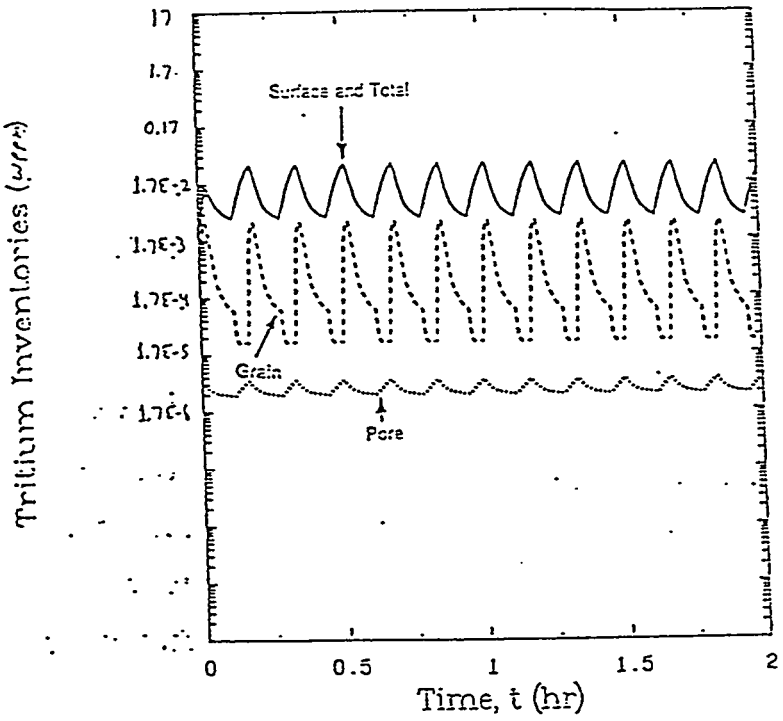

Figure 10-24. Tritium inventory history in the Li_2O outboard region 1 during the physics phase with a 20 Pa tritium partial pressure in the purge.

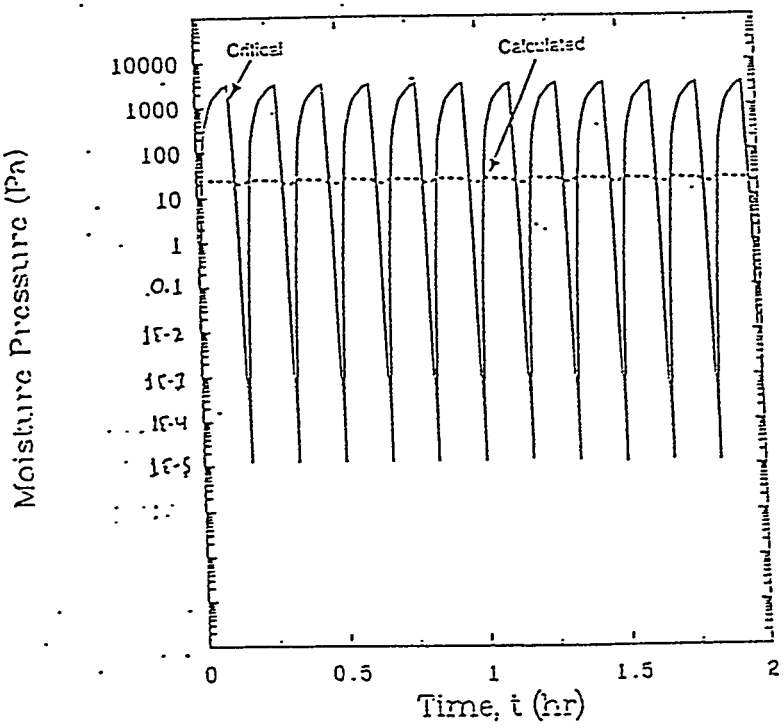

Figure 10-25. Critical and calculated moisture pressure histories at pore location z=0 in the Li_2O outboard region 1 during the physics phase with a 20 Pa tritium partial pressure in the purge.

11.0 ACTIVATION ANALYSIS

Full activation calculations have been made for the physics phase and the technology phases of ITER. The radioactivity code RACC [1] and the 46 neutron groups fluxes generated by the neutron transport code ONEDANT [2] are used for the calculations. The different activation responses are calculated for one pulse of each phase, at the end of the physics phase and at the end-of-life assuming a continuous operation. The fluence goals are 24.3 full power days (FPD) and 1360 FPD for the physics and the technology phases, respectively. The pulse burn times of the physics and the technology phases are 600 and 2310 seconds, respectively.

The neutron transport calculations are based on one-dimensional cylindrical toroidal geometry. The plasma source is assumed uniform. However, the neutron fluxes have been normalized to account correctly for the different average neutron wall loadings on the inboard and the outboard first walls. For the technology phase, the average neutron wall loading values are .59 MW/m^2 and .895 MW/m^2 for the inboard and outboard first walls, respectively. The corresponding wall loadings in the physics phase are 1.279 times these values.

The radial build at midplane is given in Table 11-1. The only differences between the two phases for the activation analyses are the protection method of the FW and the thicknesses of the scrapeoff layers. The FW has a 2 cm graphite tile in the physics phase while a 0.05 cm tungsten is used in the technology phase. Table 11-2 lists the densities and the compositions of the materials used in these calculations.

The total activity, the decay heat generation rate (DHGR), the integrated decay heat (IDH), and the air-biological hazard potential (BHP-air) are shown in Figs. 11-1 through 11-4 as a function of the time after shutdown for both phases. The responses are shown for one DT plasma shot (600 s physics and 2310 s technology) and at the end of two phases assuming a continuous operations. The responses are given per one cm of the vertical length of the reactor.

The activation levels at shutdown are 2.233 and 1.493 MCi/cm at the end of the technology and the physics phases, respectively. After one pulse only, the corresponding values are .783 and .806 MCi/cm. It should be emphasized

that the calculation with the continuous operation assumption over-estimates the short-term activation levels. For those isotopes with half-lifes in the order of the pulse duration or shorter than the time between pulses, their activities will never reach saturation within one pulse. In this case, the activation levels at the end of operation will be close to the end of one-pulse operation.

For one pulse, the DHGRs are 8.58 and 8.63 KW/cm for the technology and the physics phases, respectively. At the end of the physics phase, the DHGR is 15.65 KW/cm compared to 15.57 KW/cm at the end-of-life.

Figures 11-5 and 11-6 show the specific activities and the specific DHGR of the inboard and the outboard first walls including the carbon tile or the tungsten coating after the full operation of the two phases. At shutdown, the activation concentration (Ci/cc) in the tungsten coating of the technology phase is about 6 times that in the first walls. The radioactivity in the graphite tile of the phases is negligible. The DHGR concentration (W/cc) in the tungsten is about 4 times that of the first walls.

References

[1] J. Jung, "Theory and Use of the Radioactivity Code RACC," Argonne National Laboratory Report ANL/FPP/TM-122 (1979).

[2] R. O'Dell et al., "User's Manual for ONEDANT," Los Alamos National Laboratory Report LA-9184-M (1982).

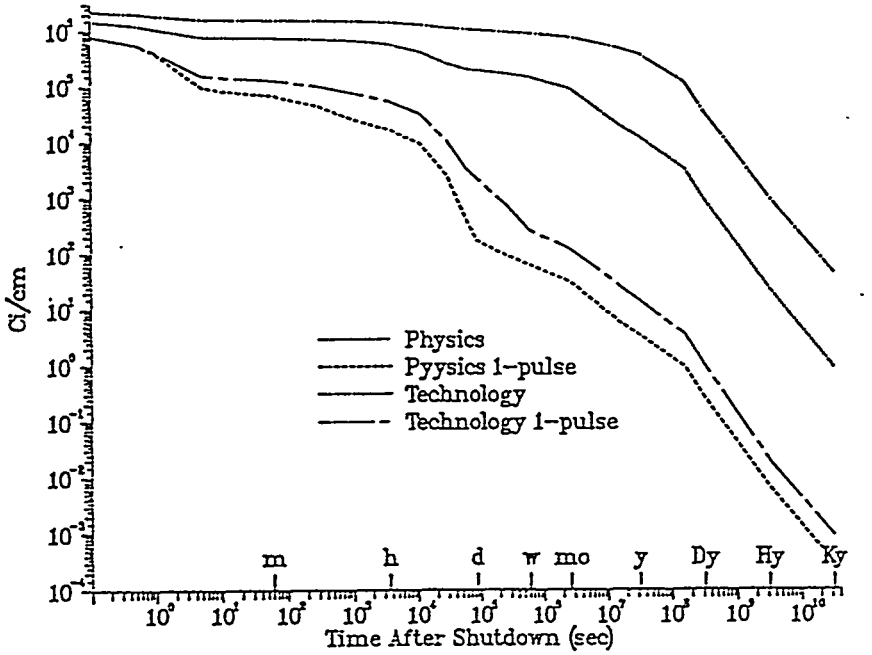

Figure 11-1. ITER total activity.

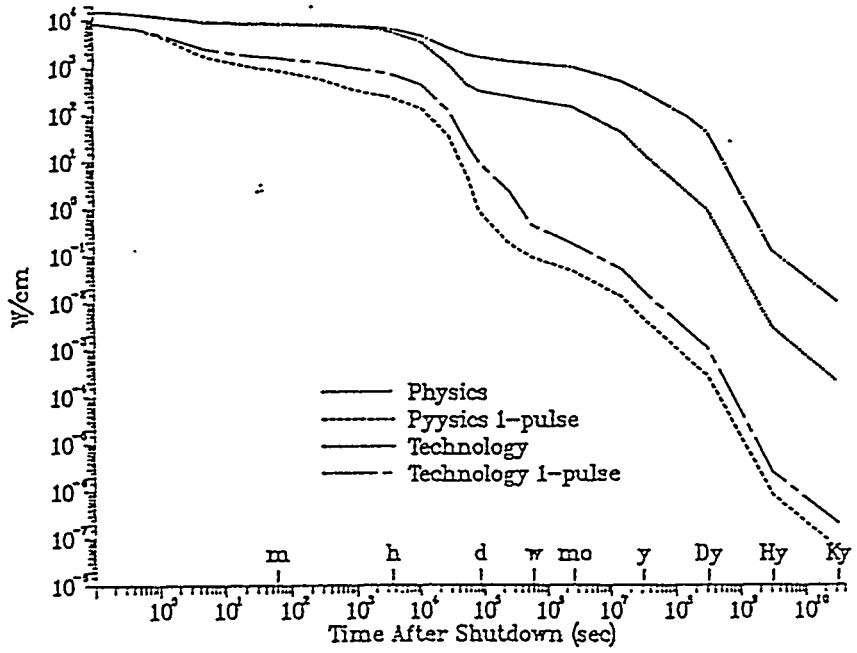

Figure 11-2. ITER decay heat (generation rate).

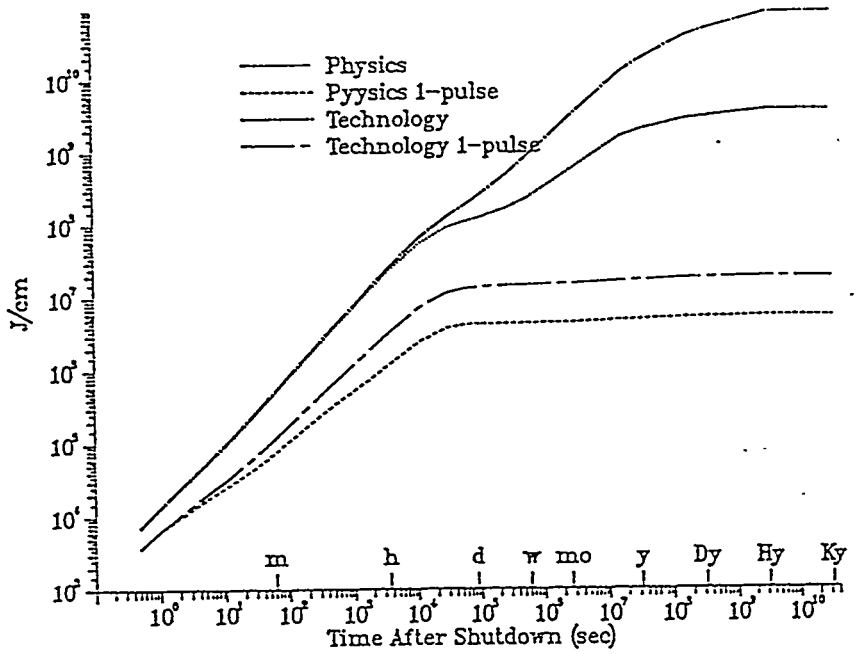

Figure 11-3. ITER decay heat (integrated).

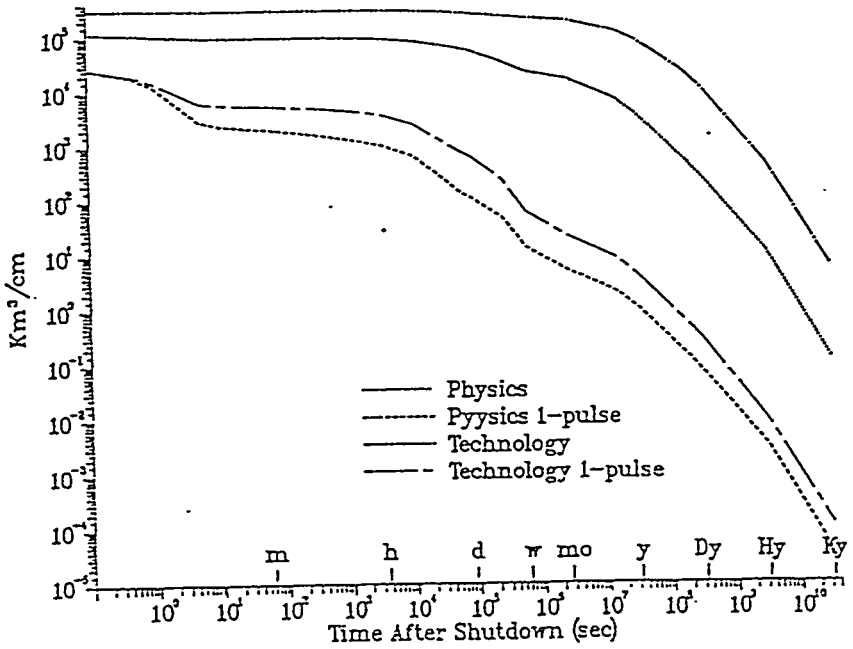

Figure 11-4. ITER BHP-air.

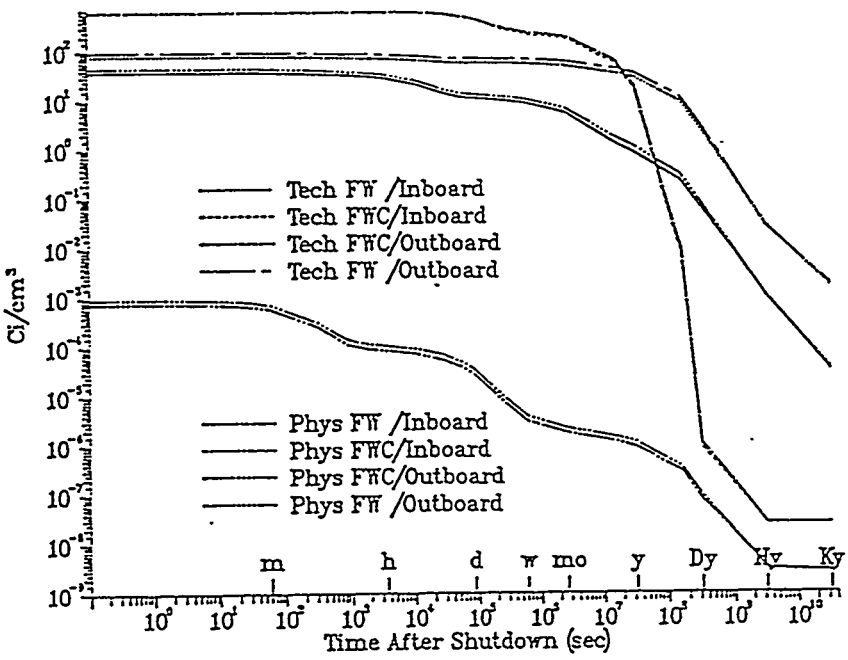

Figure 11-5. FW/coating specific activity.

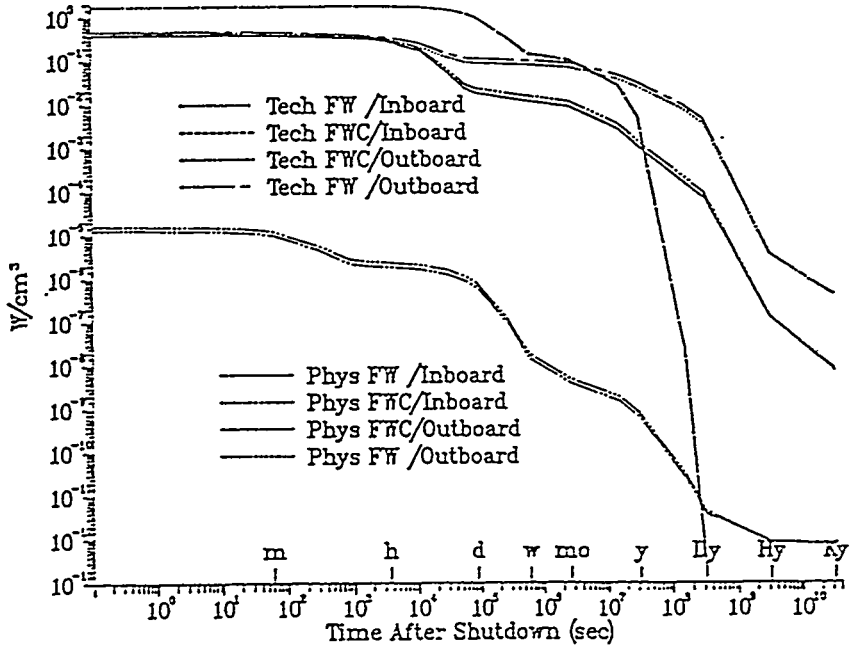

Figure 11-6. FW/coating specific decay heat (generation rate).

Table 11-1. Radial Build

No.	Inner Radius	Thickness	Outer Radius	Material
1	0.00	213.00	213.00	vacuum
2	213.00	29.00	242.00	case(316SSc)
3	242.00	0.70	242.70	R-epoxy
4	242.70	30.60	273.30	magnet(a)
5	273.30	0.70	274.00	R-epoxy
6	274.00	0.40	274.40	cc(b)
7	274.40	5.60	280.00	case(316SSc)
8	280.00	3.00	283.00	vacuum
9	283.00	0.67	283.67	therm. insul.(c)
10	283.67	3.33	287.00	vacuum
11	287.00	0.30	287.30	316SS1
12	287.30	3.00	290.30	Pb
13	290.30	1.00	291.30	b4c80
14	291.30	2.20	293.50	316SS1
15	293.50	4.00	297.50	H2O
16	297.50	11.00	308.50	316SS1
17	308.50	1.50	310.00	H2O
18	310.00	2.00	312.00	316SS1
19	312.00	1.00	313.00	vacuum
20	313.00	4.00	317.00	316SS1 85%
21	317.00	2.00	319.00	vacuum
22	319.00	2.50	321.50	316SS1
23	321.50	2.50	324.00	H2O
24	324.00	7.50	331.50	316SS1
25	331.50	2.00	333.50	H2O
26	333.50	8.80	342.30	316SS1
27	342.30	1.00	343.30	H2O
28	343.30	6.00	349.30	316SS1
29	349.30	0.80	350.10	H2O

Table 11-1. Radial Build (continued)

No.	Inner Radius	Thickness	Outer Radius	Material
30	350.10	4.00	354.10	316SS1
31	354.10	0.60	354.70	H2O
32	354.70	2.70	357.40	316SS1
33	357.40	0.50	357.90	H2O
34	357.90	0.20	358.10	316SS1
35	358.10	4.80	362.90	Be 65%
36	362.90	0.10	363.00	316SS1
37	363.00	1.00	364.00	li2o.
38	364.00	0.10	364.10	316SS1
39	364.10	3.40	367.50	Be 65%
40	367.50	0.50	368.00	316SS1
41	368.00	0.50	368.50	H2O
42	368.50	0.50	369.00	316SS1
....	.....	.....		.....
43 Physics	369.00	2.00	371.00	gh451
43 Technology	369.00	0.05	369.05	w
44 Physics	371.00	14.00	385.00	vacuum
44 Technology	369.05	15.95	385.00	vacuum
45	385.00	430.00	815.00	plasma
46 Physics	815.00	15.00	830.00	vacuum
46 Technology	815.00	16.95	831.95	vacuum
47 Physics	830.00	2.00	832.00	gh451
47 Technology	831.95	0.05	832.00	w
....	.....	.....		.....
48	832.00	0.50	832.50	316SS1
49	832.50	0.40	832.90	H2O
50	832.90	0.50	833.40	316SS1
51	833.40	3.40	836.80	Be 85%
52	836.80	0.10	836.90	316SS1

Table 11-1. Radial Build (continued)

No.	Inner Radius	Thickness	Outer Radius	Material
53	836.90	0.80	837.70	li2o.
54	837.70	0.10	837.80	316SS1
55	837.80	5.90	843.70	Be 85%
56	843.70	0.20	843.90	316SS1
57	843.90	0.20	844.10	H2O
58	844.10	0.20	844.30	316SS1
59	844.30	5.70	850.00	Be 65%
60	850.00	0.10	850.10	316SS1
61	850.10	0.80	850.90	li2o.
62	850.90	0.10	851.00	316SS1
63	851.00	7.10	858.10	Be 65%
64	858.10	0.20	858.30	316SS1
65	858.30	0.20	858.50	H2O
66	858.50	8.40	866.90	316SS1
67	866.90	5.00	871.90	H2O
68	871.90	3.40	875.30	316SS1
69	875.30	3.00	878.30	H2O
70	878.30	6.00	884.30	316SS1
71	884.30	2.00	886.30	H2O
72	886.30	7.00	893.30	316SS1
73	893.30	2.00	895.30	H2O
74	895.30	8.00	903.30	316SS1
75	903.30	2.00	905.30	H2O
76	905.30	9.00	914.30	316SS1
77	914.30	2.00	916.30	H2O
78	916.30	11.80	928.10	316SS1
79	928.10	2.00	930.10	H2O
80	930.10	20.00	950.10	316SS1
81	950.10	2.00	952.10	vacuum

Table 11-1. Radial Build (continued)

No.	Inner Radius	Thickness	Outer Radius	Material
82	952.10	4.00	956.10	316SS1 85%
83	956.10	1.00	957.10	vacuum
84	957.10	18.50	975.60	316SS1
85	975.60	5.00	980.60	H20
86	980.60	1.50	982.10	316SS1
87	982.10	3.00	985.10	Pb
88	985.10	4.90	990.00	vacuum
89	990.00	44.00	1034.00	case(316SSc)
90	1034.00	0.70	1034.70	R-epoxy
91	1034.70	30.60	1065.30	magnet(a)
92	1065.30	0.70	1066.00	R-epoxy
93	1066.00	40.00	1106.00	case(316SSc)
94	1106.00	194.00	1300.00	vacuum
95	1300.00	7.00	1307.00	cryostat(316SS1)
96	1307.00	263.00	1570.00	vacuum
97	1570.00	200.00	1770.00	Bio. Shield(d)

(a) magnet	: 316SS1w	0.3160, Cu	0.2600, Nb3Sn	0.0250,
	bronze	0.0640, V	0.0060, lhe	0.2110,
	r-epxy	0.1180		
(b) cc	: 316SSc	0.6300, lhe	0.3700	
(c) therm. insul	: 316SSc	0.7500, ln	0.2500	
(d) Bio. Shield	: conc	0.8700, c1020	0.0800, H20	0.0500

Table 11-2. Material Composition

	atom/barn-cm ss316-L 7.855		atom/barn-cm ss316lw 7.855		atom/barn-cm ss316c 7.855		atom/barn-cm c1020 7.93		atom/barn-cm conc 2.321	
H	-	-	-	-	-	-	-	-	0.75	1.040-2
B	0.001	4.375-6	0.001	4.375-6	0.001	4.375-6	-	-	-	-
C	0.018	7.089-5	0.01	3.938-5	0.034	1.339-4	0.2	7.952-4	5.55	6.458-3
N	0.07	2.364-4	0.19	6.417-4	0.2	6.754-4	-	-	0.01	9.979-6
O	0.002	5.913-6	0.002	5.913-6	0.002	5.913-6	-	-	49.29	4.306-2
Na	-	-	-	-	-	-	-	-	0.42	2.553-4
Mg	-	-	-	-	-	-	-	-	1.48	8.509-4
Al	0.3	5.260-4	0.3	5.260-4	0.3	5.260-4	-	-	2.06	1.067-3
Si	0.46	7.748-4	0.1	1.684-4	0.5	8.421-4	0.25	4.251-4	15.7	7.813-3
P	0.026	3.971-5	0.003	4.582-6	0.026	3.971-5	-	-	-	-
S	0.01	1.475-5	0.0014	2.065-6	0.01	1.475-5	-	-	0.17	7.410-5
K	0.0005	6.049-7	0.0005	6.049-7	0.0005	6.049-7	-	-	0.75	2.681-4
Ca	-	-	-	-	-	-	-	-	22.95	8.004-3
Ti	0.04	3.952-5	0.04	3.952-5	0.04	3.952-5	-	-	0.05	1.460-5
V	0.004	3.714-6	0.004	3.714-6	0.004	3.714-6	-	-	-	-
Cr	17.1	1.556-2	17.17	1.562-2	17.36	1.579-2	-	-	-	-
Mn	1.7	1.463-3	1.48	1.273-3	1.04	8.947-4	0.45	3.908-4	-	-
Fe	64.4265	5.457-2	66.3331	5.618-2	66.0305	5.593-2	99.1	8.474-2	0.82	2.052-4
Co	0.03	2.408-5	0.03	2.408-5	0.03	2.408-5	-	-	-	-

Table 11-2. Material Composition (continued)

	atom/barn-cm		atom/barn-cm		atom/barn-cm		atom/barn-cm			atom/barn-cm		
	ss316-L		ss316lw		ss316c		c1020			conc		
	7.855		7.855		7.855		7.93			2.321		
Ni	13.2	:1.064-2	12.14	:9.785-3	11.78	:9.495-3	-	:	-	-	:	-
Cu	0.1	:7.444-5	0.1	:7.444-5	0.1	:7.444-5	-	:	-	-	:	-
As	0.0005	:3.157-7	0.0005	:3.157-7	0.0005	:3.157-7	-	:	-	-	:	-
Zr	0.002	:1.039-6	0.002	:1.039-6	0.002	:1.039-6	-	:	-	-	:	-
Nb	0.002	:1.018-6	0.055	:2.800-5	0.002	:1.018-6	-	:	-	-	:	-
Mo	2.5	:1.233-3	2.03	:1.001-3	2.53	:1.248-3	-	:	-	-	:	-
Ag	0.0002	:8.771-8	0.0002	:8.771-8	0.0002	:8.771-8	-	:	-	-	:	-
Cd	0.0002	:8.415-8	0.0002	:8.415-8	0.0002	:8.415-8	-	:	-	-	:	-
Sn	0.002	:7.968-7	0.002	:7.968-7	0.002	:7.968-7	-	:	-	-	:	-
Sb	0.0005	:1.942-7	0.0005	:1.942-7	0.0005	:1.942-7	-	:	-	-	:	-
Ba	0.0005	:1.722-7	0.0005	:1.722-7	0.0005	:1.722-7	-	:	-	-	:	-
Tb	0.0005	:1.488-7	0.0005	:1.488-7	0.0005	:1.488-7	-	:	-	-	:	-
Ta	0.0005	:1.307-7	0.0005	:1.307-7	0.0005	:1.307-7	-	:	-	-	:	-
W	0.001	:2.573-7	0.001	:2.573-7	0.001	:2.573-7	-	:	-	-	:	-
Ir	0.0005	:1.230-7	0.0005	:1.230-7	0.0005	:1.230-7	-	:	-	-	:	-
Pb	0.0008	:1.826-7	0.0008	:1.826-7	0.0008	:1.826-7	-	:	-	-	:	-
Bi	0.0008	:1.811-7	0.0008	:1.811-7	0.0008	:1.811-7	-	:	-	-	:	-

Table 11-2. Material Composition (continued)

	atom/barn-cm		atom/barn-cm		atom/barn-cm		atom/barn-cm		atom/barn-cm	
	li2o98		be100		b4c80		pb_w		g-h451	
	1.52402		1.85		2.01697		11.35303		1.74	
Li6	39.61991	:6.045-2	-	: -	-	: -	-	: -	-	: -
Li7	4.86447	:6.363-3	-	: -	-	: -	-	: -	-	: -
Be	1.	w:1.018-7	100.	:1.236-1	-	: -	-	: -	-	: -
B	1.	w:8.488-8	-	: -	-	: -	-	: -	0.000002	:1.938-7
B10	-	: -	-	: -	14.34393	:1.740-2	-	: -	-	: -
B11	-	: -	-	: -	63.90082	:7.050-2	-	: -	-	: -
C	100.	w:7.641-6	-	: -	21.75525	:2.200-2	-	: -	99.9927	:8.723-2
N	2.	w:1.310-7	-	: -	-	: -	-	: -	-	: -
O	55.46493	:3.182-2	-	: -	-	: -	-	: -	-	: -
F	0.1	w:4.831-9	-	: -	-	: -	-	: -	-	: -
Na	60.	w:2.395-6	-	: -	-	: -	-	: -	0.00001	:4.558-7
Mg	10.	w:3.775-7	-	: -	-	: -	-	: -	0.000001	:4.310-8
Al	50.	w:1.701-6	-	: -	-	: -	-	: -	0.000004	:1.553-7
Si	50.	w:1.634-6	-	: -	-	: -	-	: -	0.000021	:7.835-7
P	1.	w:2.963-8	-	: -	-	: -	-	: -	-	: -
S	0.1	w:2.862-9	-	: -	-	: -	-	: -	0.000001	:3.268-8
Cl	10.	w:2.588-7	-	: -	-	: -	-	: -	-	: -
K	20.	w:4.694-7	-	: -	-	: -	-	: -	-	: -
Ca	100.	w:2.290-6	-	: -	-	: -	-	: -	0.000022	:5.752-7

* v = wppm.

Table 11-2. Material Composition (continued)

	atom/barn-cm li2o98 1.52402		atom/barn-cm be100 1.85		atom/barn-cm b4c80 2.01697		atom/barn-cm pb_w 11.35303		atom/barn-cm g-h451 1.74	
Ti	10.	w:1.917-7	-	-	-	-	-	-	0.000001	:2.189-8
V	1.	w:1.802-8	-	-	-	-	-	-	0.000001	:2.057-8
Cr	1.	w:1.765-8	-	-	-	-	-	-	-	-
Mn	1.	w:1.669-8	-	-	-	-	-	-	-	-
Fe	50.	w:8.217-7	-	-	-	-	-	-	0.000003	:5.629-8
Co	0.2	w:3.115-9	-	-	-	-	-	-	-	-
Ni	10.	w:1.564-7	-	-	-	-	-	-	-	-
Cu	10.	w:1.444-7	-	-	-	-	-	-	-	-
Zn	10.	w:1.404-7	-	-	-	-	-	-	-	-
As	0.1	w:1.225-9	-	-	-	-	-	-	-	-
Br	0.1	w:1.149-9	-	-	-	-	-	-	-	-
Zr	1.	w:1.008-8	-	-	-	-	-	-	-	-
Mo	0.1	w:9.571-10	-	-	-	-	-	-	-	-
Cd	0.1	w:8.164-10	-	-	-	-	-	-	-	-
Sn	1.	w:7.730-9	-	-	-	-	-	-	-	-
Sb	1.	w:7.538-9	-	-	-	-	-	-	-	-
Ba	5.	w:3.342-8	-	-	-	-	-	-	-	-
Pb	0.1	w:4.429-10	-	-	-	-	100.	:3.299-2	0.000007	:3.540-8

* w = wppm.

Table 11-2. Material Composition (continued)

	atom/barn-cm		atom/barn-cm		atom/barn-cm		atom/barn-cm		atom/barn-cm	
	w		r-epxy		nb3sn		bronze		cu_ITR	
	17.40441		1.90061		8.90099		8.80043		8.7499	
H-1	-	-	1.90459	2.163-2	-	-	-	-	-	-
C	-	-	19.85491	1.892-2	-	-	-	-	-	-
N	-	-	2.52097	2.060-3	-	-	-	-	-	-
O16	-	-	37.81571	2.706-2	-	-	-	-	-	-
Mg	-	-	2.52747	1.190-3	-	-	-	-	-	-
Al	-	-	9.2645	3.930-3	-	-	-	-	-	-
Si	-	-	19.63073	8.000-3	-	-	-	-	-	-
S	-	-	1.42867	5.100-4	-	-	-	-	-	-
Cu	-	-	5.05245	9.100-4	-	-	91.9973	7.672-2	100.	8.292-2
Nb	-	-	-	-	70.12733	4.046-2	-	-	-	-
Sn	-	-	-	-	29.87267	1.349-2	8.0027	3.572-3	-	-
W182	26.28274	1.514-2	-	-	-	-	-	-	-	-
W183	14.27852	8.180-3	-	-	-	-	-	-	-	-
W184	30.67894	1.748-2	-	-	-	-	-	-	-	-
W186	28.75981	1.621-2	-	-	-	-	-	-	-	-

Table 11-2. Material Composition (continued)

	atom/barn-cm			atom/barn-cm			atom/barn-cm			atom/barn-cm			atom/barn-cm
	v			lhe			ln			h2o			
	6.09992			0.14011			0.80802			1.			
H	-	:	-	-	:	-	-	:	-	11.19016	:6.685-2		
He	-	:	-	100.	:2.108-2		-	:	-	-	:	-	
N	-	:	-	-	:	-	100.	:3.474-2		-	:	-	
O	-	:	-	-	:	-	-	:	-	88.80984	:3.343-2		
V	100.	:7.211-2		-	:	-	-	:	-	-	:	-	

12.0 LOFA ANALYSIS FOR THE SINTERED-PRODUCT SOLID BREEDER BLANKET

12.1 Introduction

The loss of flow accident (LOFA) considered in the present analysis is assumed to result from the simultaneous failure of all pumps due to either catastrophic mechanical failure or loss of power. Both of these occurrences tend to be fairly unlikely. Note that in both cases, corrective action can be taken to avoid or limit damages, for example through the use of back-up pumps and back-up generators. The objective here is to assess the need for corrective action following different LOFA scenarios and, if so, to characterize the time available for implementing the corrective action before irreversible damage could occur, caused by boiling water overpressurization, for example.

For the proposed ITER blanket design, the coolant duct is laid in the toroidal-radial plane, and natural convection does not help much when the pump becomes unavailable. The issues of LOFA then become whether the plasma can be shut down rapidly enough that the power flow mismatch during the transient does not lead to unacceptable coolant temperatures or whether corrective measures are required for removal of afterheat (decay heat + energy stored inside the blanket module). To determine the coolant flow rate history following the accident, the effects of the fluid inertia and the pump inertia following the loss of power need to be included in the hydraulic model. Once a determination of the flow coastdown has been made, the resultant transient coolant temperature is estimated. The flow characteristics and coolant temperature history are then incorporated into the TOPAZ2D transient code to evaluate the blanket module temperature distributions. Parametric studies are carried out to evaluate the required pump inertias to prevent the water from boiling inside the blanket module in the absence of corrective measures as a function of the time required for plasma shut down.

12.2 LOFA due to Catastrophic Mechanical Pump Failure

For the case of catastrophic mechanical pump failure, it is assumed that the flow stops completely at the initiation of the LOFA. The heat transport mechanism within the blanket is mostly conduction due to the small Grashof number ($<<$ 2000). The coolant temperature histories under this type of

accident were estimated using the TOPAZ code [1] for different times following the initiation of the LOFA during which the plasma stays on. This is shown in Fig. 12-1. It indicates that the coolant reaches the boiling point (461 K at 15 atm) after about 15 seconds if the plasma stays on for 10 seconds after LOFA and after about 20 seconds if the plasma stays on for 1 second after LOFA. The results also show that the temperature increase rate varies with blanket location due to the different time constants.

From the results, even if the plasma is turned off quasi-instantaneously following such a LOFA, only about 20 seconds are available before the water coolant reaches its boiling point for corrective action to be taken, such as to put back-up pumps on line or to start an emergency cooling system or passive release to the water pressure.

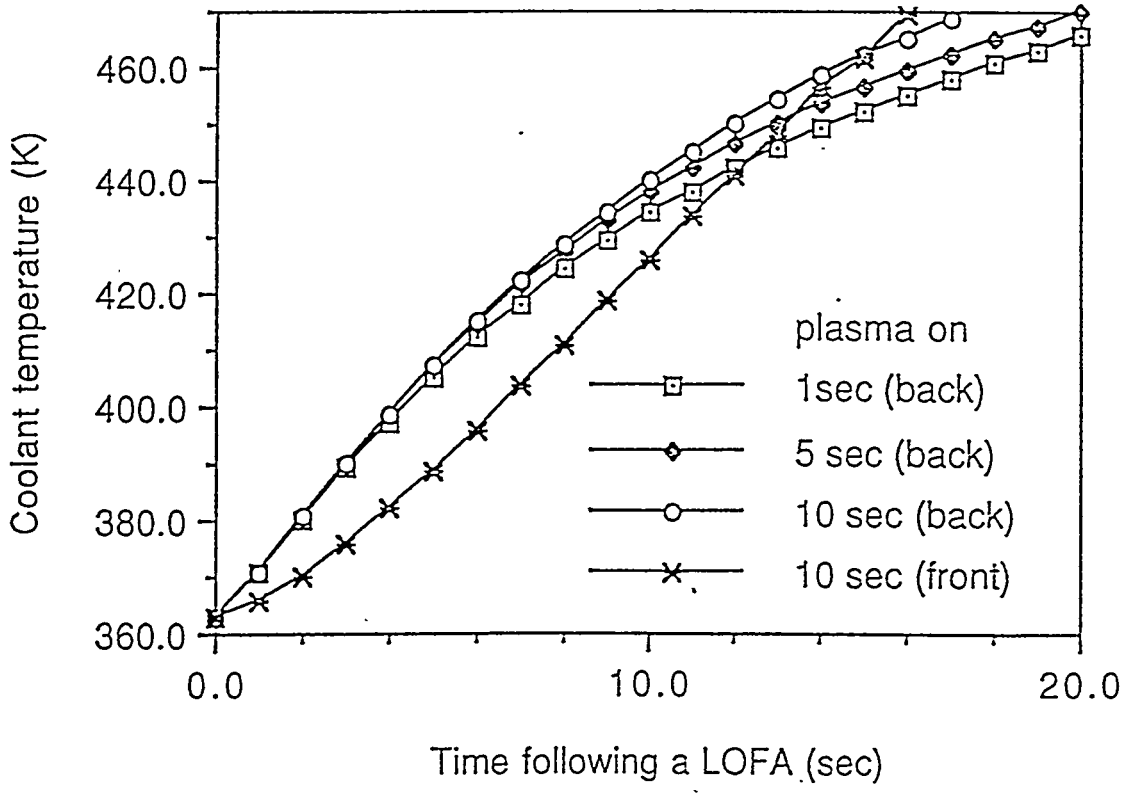

Figure 12-1. Coolant Temperature History Following a LOFA with Complete Flow Stoppage for Different Times During Which the Plasma Stays On

12.3 LOFA Due to Loss of Power

12.3.1 Flow Transient

To determine the flow transient, pressure drop flow relationships along with Kirchhoff's laws [2] are applied to the hydraulic systems, which include the blanket modules, inlet/outlet coolant pipes, and coolant pump. Kirchhoff's law states that the sum of the pressure drops around any channel loop is equal to zero. The resultant flow transient equation can be written as [2]:

$$t_l \frac{d}{dt}\left(\frac{W}{W_o}\right) + \left(\frac{W}{W_o}\right)^2 = \frac{1}{(1+t/t_p)^2} \qquad (12\text{-}1)$$

where t_l is the loop half-time, W is the mass flow rate, W_o is the mass flow rate prior to the LOFA and t_p is the pump half-time. The loop half-time is given by:

$$t_l = \frac{2\,\bar{m}}{W_o\,\tilde{k}_{pr}\,(A/L)_{sys}}$$

where $\bar{m}$ is the average water density, $\tilde{k}_{pr}$ is the appropriate friction coefficient for the entire primary system, which accounts for the series and parallel flow paths within the blanket module and the loop, and $(A/L)_{sys}$ is the effective ratio of area to length for the system.

The pump half-time is given by:

$$t_p = \frac{I}{C\,\omega_o} \qquad (12\text{-}3)$$

where I is the moment of inertia of the pump, C is a loss coefficient relating the windage torque, and ω_o is the initial pump speed.

Usually, the coolant pumps for reactor applications are designed with sufficiently large flywheels and the pump inertia tends to be much larger than that of the fluid. Hence $t_p >> t_l$. In this case, it is reasonable to ignore the first term in Eq. (12-1) and approximate the flow coastdown by

$$W(t) = \frac{W_o}{1 + t/t_p} \tag{12-4}$$

In general, the pump half-time for fission reactors is of the order of several seconds.

12.3.2 Temperature Transient

Once a determination of the flow coastdown has been made, it is necessary to evaluate the resultant transient in the coolant temperature. Since the average blanket temperature drop is much larger than the coolant temperature rise, it is reasonable to neglect the changes in heat stored in the coolant channels. Under this approximation, the thermal model for the coolant can be decoupled from the blanket element and the temperature rise of the coolant can be estimated from the following expression, under the assumption that the plasma remains full power and that the heat flux to the coolant stays constant (i.e., during a time much smaller than the thermal time constant of the system):

$$\Delta T_c(t) = \Delta T_c(0) \frac{W_o}{W(t)} \tag{12-5}$$

If the plasma power drops immediately to zero following the LOFA, the coolant temperature rise (neglecting the decay heat) across the blanket module will depend on the thermal time constant of the system as heat is transferred from the high temperature blanket elements to the ccolant. The coolant temperature rise then can be approximately expressed as:

$$\Delta T_c(t) = \Delta T_c(0) \frac{W_o}{W(t)} e^{-t/\tau} \tag{12-6}$$

where τ is the thermal time constant associated with the blanket elements and is estimated from [2]:

$$\tau = R_{sys} \sum (M C_p) \qquad (12\text{-}7)$$

where R_{sys} is the system thermal resistance, and M and C_p are the mass and specific heat of the blanket elements. The thermal time constants for the front and back portions of the midplane of the outboard blanket module have been estimated to be 600 and 1000 seconds respectively. A thermal time constant of the blanket module longer than the pump half-time results in a peak in the coolant temperature rise since the energy stored in the blanket elements is not transferred to the coolant until after the flow deterioration has become large. The results are illustrated in Fig. 12-2, which shows the coolant temperature rise as a function of time for different pump half times and for a blanket thermal time constant of 600 seconds. The calculation assumes that the secondary heat removal system is still under operation. It is interesting to see that if the pumps can be designed with sufficiently large flywheels with corresponding pump half-times of the order of 40 seconds or more, it is possible to remove the heat stored inside the blanket element using the decreasing flow and prevent the coolant from boiling.

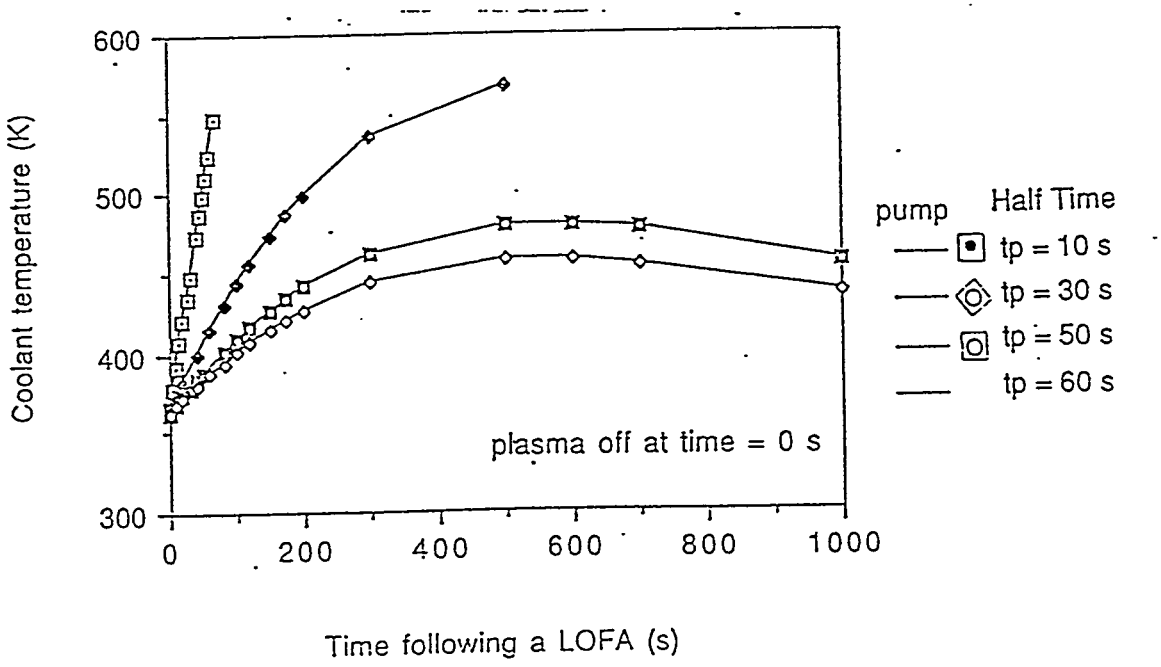

Figure 12-2. Coolant Temperature at Exit of Breeder Region Following a LOFA for Different Pump Half-Times (for a blanket thermal time constant of 600 s and with the plasma immediately turned off following the LOFA).

12.3.3 Transient Temperature Distribution

The temperature distributions for the beryllium, SS cladding, and breeder were estimated using TOPAZ2D computer code. Natural circulation is negligible in the blanket design due to the small channel width and temperature difference (Grashof number is much less than 2000.) Convective boundary conditions based on the decreasing flow rate were applied at the coolant boundaries. The corresponding heat transfer coefficients were calculated from the following correlation for thin rectangular channel [3]:

$$h = \frac{k}{D_e}\left[0.116\ (R_e^{2/3} - 125)\left(1 + \left(\frac{D_e}{L}\right)^{2/3}\right) P_r^{1/3}\right] \qquad (12\text{-}8)$$

for $R_e > 10{,}000$

and, from [4]

$$h = \frac{k}{De}\left(0.0395\ Re^{0.75}\ Pr^{0.33}\right)$$

for $3 \times 10^3 < Re < 1 \times 10^4$ (12-9)

The breeder (sintered-product) and clad surface temperature histories are shown in Fig. 12-3 for the mid-plane and outboard blanket region 1. For this example, the plasma was assumed to stay on for 10 seconds following the LOFA. The figure shows that the breeder and Be maintain their temperatures while the plasma is on but that the breeder temperature then falls much faster when the plasma is off. The coolant temperature continuously rises but will not reach the boiling point for the 50-seconds pump half time.

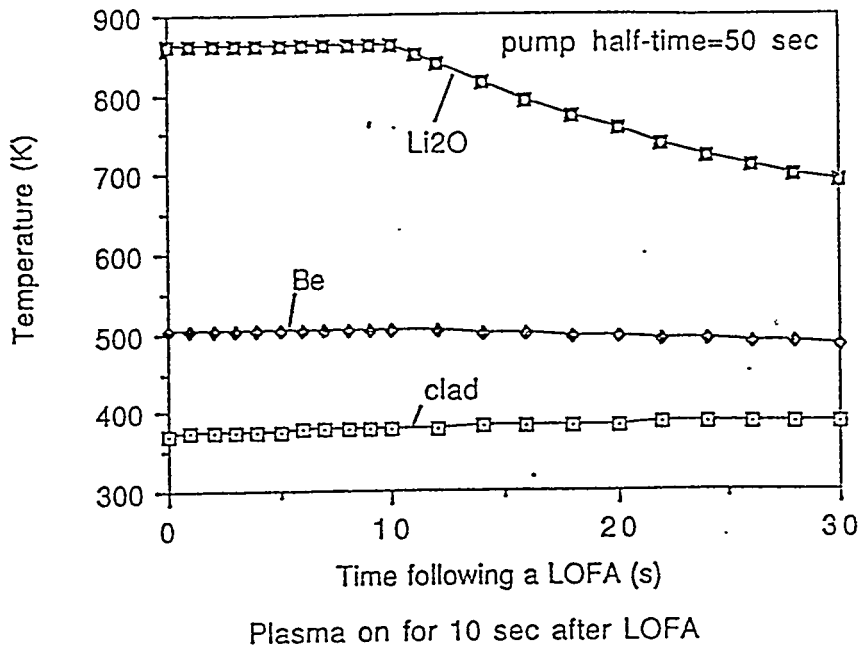

Figure 12-3. Temperature Histories of Clad, Be in the Mid-plane Outboard Blanket, and Li_2O Following a LOFA Assuming the Plasma Stays on for 10 s.

12.4 Summary

- For the US ITER blanket with coolant flowing in the radial/toroidal plane, natural convection does not offer much help following a LOFA.

- In the extreme case of catastrophic pump failure where the flow stops completely, the water coolant will reach its boiling point within about 20 seconds even if the plasma is shut off quasi-instantaneously following the LOFA. To prevent this, corrective action such as putting back-up pumps on line or starting an emergency heat removal system would need to be implemented within these 20 seconds.

- In the case of a loss of power accident, the pump inertia can be helpful. For example, for an estimated blanket thermal time constant of 600 seconds, the coolant will not reach its boiling point if the pump can be designed with a sufficiently large flywheel with a corresponding pump half-time of about 40 seconds or more, assuming the plasma is shut down

instantaneously following the LOFA. A finite time for plasma shut-down would require an higher pump half-time to prevent water from boiling. Even if the pump inertia is lower, it can extend quite appreciably the allowable time prior to the implementation of corrective action such as starting back-up generators.

References

[1] A.B. Shapiro, TOPAZ - A Finite Element Heat Conduction Code for Analyzing 2-D Solids.

[2] E.E. Lewis, Nuclear Power Reactor Safety, John Wiley & Sons, Inc., 1977.

[3] E.R. Eckert and R.M. Drake, Jr., Heat and Mass Transfer, McGraw-Hill, New York, 1964.

[4] A. Soria et al., "Programs in the Studies of Passive Heat Removal in the Next European TORUS Under Accident Conditions," Fusion Technology, 16, 474 (1989).